university of groningen

University Medical Center Groningen

University of Groningen

The conductive geothermal field as an energy and economic entity

Daniilidis, Alexandros

IMPORTANT NOTE: You are advised to consult the publisher's version (publisher's PDF) if you wish to cite from it. Please check the document version below.

Document Version
Publisher's PDF, also known as Version of record

Publication date:
2017

Link to publication in University of Groningen/UMCG research database

Citation for published version (APA):
Daniilidis, A. (2017). The conductive geothermal field as an energy and economic entity: Effects and implications for the province of Groningen, North-East Netherlands [Groningen]: University of Groningen

Copyright
Other than for strictly personal use, it is not permitted to download or to forward/distribute the text or part of it without the consent of the author(s) and/or copyright holder(s), unless the work is under an open content license (like Creative Commons).

Take-down policy
If you believe that this document breaches copyright please contact us providing details, and we will remove access to the work immediately and investigate your claim.

Downloaded from the University of Groningen/UMCG research database (Pure): http://www.rug.nl/research/portal. For technical reasons the number of authors shown on this cover page is limited to 10 maximum.

Download date: 11-02-2018

The conductive geothermal field as an energy and economic entity

Effects and implications for the province of Groningen, North-East Netherlands

Alexandros Daniilidis

The conductive geothermal field as an energy and economic entity

Effects and implications for the province of Groningen, North-East Netherlands

This work formed part of the Flexiheat project and was supported by Samenwerkingsverband Noord Nederland (SNN) and the Dutch Ministry of Economic Affairs

The research reported in this thesis was carried out at the Geo-energy group, which is part of the Energy and Sustainability Research Institute Groningen (ESRIG) of the University of Groningen, according to the requirements of the graduate school of the faculty of Science and Engineering, University of Groningen

The printing of this thesis was partially supported by the graduate school of the faculty of Science and Engineering.

ISBN: 978-94-028-0796-7

Copyright © 2017, Alexandros Daniilidis

Cover design and layout: Alexandros Daniilidis

The cover data represent the modelled hourly heat demand data in the Groningen geothermal system.

university of groningen

The conductive geothermal field as an energy and economic entity

Effects and implications for the province of Groningen, North-East Netherlands

PhD thesis

to obtain the degree of PhD at the
University of Groningen
on the authority of the
Rector Magnificus Prof. E. Sterken
and in accordance with
the decision by the College of Deans.

This thesis will be defended in public on

Friday October 27th at 16.15 hours

by

Alexandros Daniilidis

born on September 26th 1983
in Stockholm, Sweden

Supervisor

Prof. M.A. Herber

Assessment Committee

Prof. H.A.J. Meijer

Prof. D.M.J. Smeulders

Prof. D. Bruhn

“The antique people are down in the dungeons
Run by machines and afraid of the tax
Their heads in the grave and their hands on their eyes
Hauling their hearts around circular tracks
Pretending forever their masquerade towers
Are not really riddled with widening cracks
And I wave goodbye to iron
And smile hello to the air”

Tim Buckley, 1967

Contents

Summary

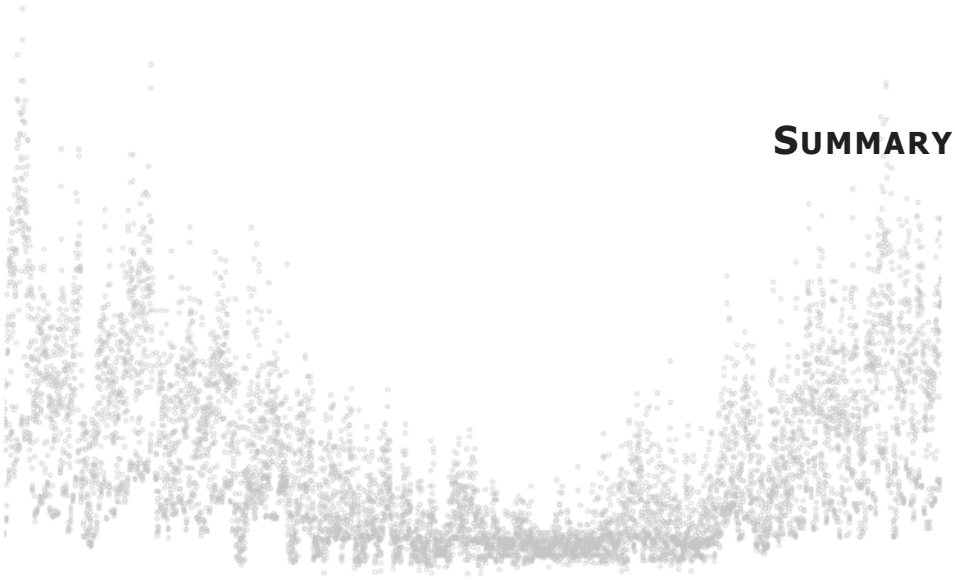

Geothermal sources provide renewable energy that can be used for electricity or heat generation (**Chapter 1**). This thesis is aimed at identifying and analyzing potential geothermal fields in the conduction-dominated geological setting of NE Netherlands in two different ways. The first consists of exploring and harvesting the high heat flow through salt. The second is a step-wise, incremental approach in outlining, assessing, characterizing and evaluating the development of the Groningen geothermal system.

The high thermal conductivity of salt in comparison with other sediments is significant for the temperature field in a conductive geological setting (**Chapter 2**) as it describes a locally higher geothermal gradient. The presence of this anomaly lowers the threshold for accessing the heat resource (in terms of capacity, time and, most critically for geothermal projects, cost) and enhances the renewability of the resource.

In the study area, salt causes temperature anomalies proportional to its thickness. A critical minimum thickness was identified (~600m). Temperature differences up to 25°C were modelled between the top of the salt structure and the surrounding strata at the same depth. If a suitably permeable formation is overlying this sweet spot, up to 40% more energy can be extracted, while the field recovery time is only being prolonged by 13%. In the Dutch context, the provinces of Drenthe and Groningen are likely candidates for application of this principle, as local salt thickness can exceed 800m.

Just as any subsurface development, geothermal projects are subject to uncertainties. In this thesis a comprehensive analysis is devoted to assess not only individual uncertainties,

but also their interaction. In order to cover ranges of uncertainties the approach is based on stochastics. The combined uncertainty associated with reservoir initial state (pressure and gas saturation levels), geology (reservoir and fault permeability) and operations (flow rate levels and re-injection temperature) are analyzed for the Groningen geothermal system (**Chapter 3**). The reservoir initial state principally affects the pressure difference between the producer well and a hydrostatic reservoir, as well as the produced gas volume. Pressure depletion dictates the required pump depth, while gas saturation potentially contributes to the project finances but also complicates the pump installation and operation.

Of the geological parameters, reservoir permeability is tightly connected to the pressure difference between the wells. Fault permeability affects the drainage area and thus has a temporal effect on the produced temperature. Of the operational parameters, the chosen flow rate controls the produced thermal power, the well pressure difference and the producer temperature. The injection temperature also affects the produced thermal power over time.

System complexity is increased when the geothermal resource is coupled with the demand pattern of the surface system (**Chapter 4**). This introduces seasonal load factors, together with uncertainty regarding the robustness of supply, as well as possible geochemical implications. For the Groningen case, it is shown that coupling the seasonal surface demand with the subsurface supply causes no adverse geochemical effects on the reservoir and energy generation during a production time of 50 years. Moreover, the seasonally variable production enables a more efficient use of the geothermal resource by delaying the propagation of the cold front. This variability is found to affect only the rate and not the nature of the changes in the chemical reservoir properties.

The geochemical behavior of the reservoir is mostly affected by flow rate, and secondarily by the injection pH and injection temperature. In the Rotliegend Sandstone, anhydrite and dolomite are identified as the two key minerals. Anhydrite dissolves during the first years of production leading to increased permeability around the injector well. The flow rate control strategy influences the rate of dissolution, but the investigated flow rate control strategies all result in the dissolution of the same volume fraction. Dolomite has an effect on the permeability at a later time and its change rate is primarily affected by pH and secondarily by temperature. Acidic pH and lower temperatures favor dolomite dissolution while a neutral pH and higher temperatures favor precipitation.

Bringing together technical and economic uncertainties provides a comprehensive overview of geothermal field development (**Chapter 5**). A probabilistic, techno-economic model incorporates uncertainty for both the geological and the economic parameters.

The Expected Monetary Value (EMV) shows a 50% probability for marginal profits at the end of a 40 years period, mostly affected by the success rate of drilling the wells. However, even if both wells are successfully drilled, still a net deficit remains as a possible outcome. The Net Present Value (NPV) is mostly sensitive to operational and initial state parameters, while the Levelised Cost of Heat (LCOH) is principally affected by geological and operational parameters. This difference suggests that the LCOH and NPV indexes should be used in tandem for a more insightful financial assessment.

The seasonality of the load factor and its importance on the economic outlook highlight the significance of seasonal storage or additional seasonal loading. These, together with the temporal decoupling of the surface and subsurface capital investments, can significantly improve the economic outlook of similar projects. A subsidy scheme with a shorter duration but more impact directly after the drilling phase would be more effective in offsetting the high initial investment costs.

Geothermal development is put into context with regard to the political and economic zeitgeist (**Chapter 6**). When discussed, renewable energy is usually equated to electricity, but heating and cooling amount to half of the EU energy consumption and three quarters of household consumption.

A better understanding of conductive, direct-use geothermal systems could be derived through a structured, systematic data supply. This direction seems attainable for the Dutch geothermal developments in near future and could pioneer the integrated assessment and monitoring of geothermal resources.

SAMENVATTING

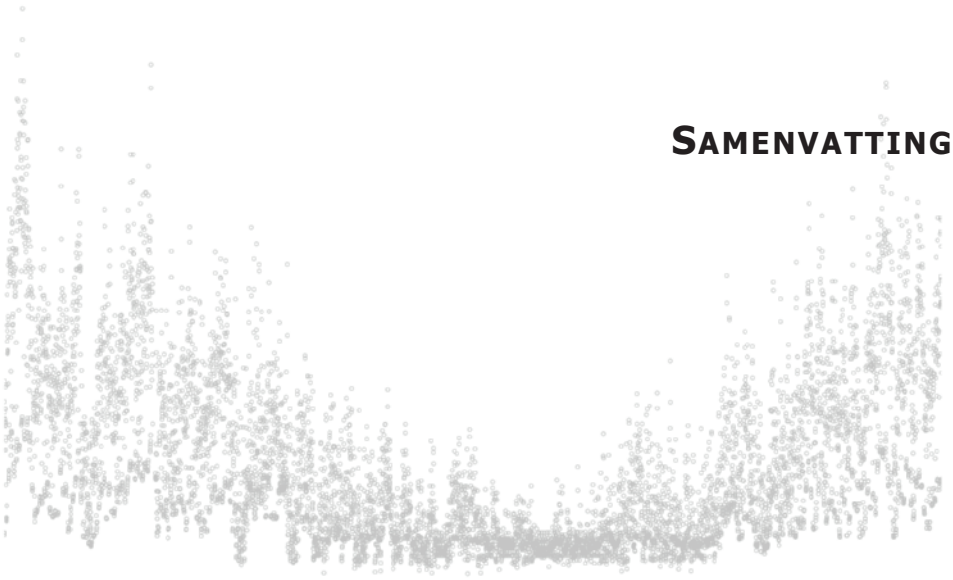

Geothermische bronnen leveren hernieuwbare energie die direct als warmte wordt toegepast danwel gebruikt voor het opwekken van elektriciteit (**Hoofdstuk 1**). Dit proefschrift richt zich op het identificeren en analyseren van mogelijke geothermische 'velden' onder de geologische condities in noordoost Nederland, waar de ondergrondse warmtestroom voornamelijk plaats vindt door geleiding. Dit potentieel wordt op twee manieren beschouwd: allereerst door de sterke warmtestroom door zoutlagen te onderzoeken en benutten. De tweede casus wordt behandeld door een gepland geothermisch systeem in de stad Groningen stap voor stap te omschrijven, karakteriseren en zowel technisch als economisch te evalueren.

De warmtegeleiding in zoutlagen is drie tot vier maal hoger in vergelijking met andere sedimenten. Dit heeft een significant effect op de temperatuurverdeling in een sedimentair geologisch bekken, daar het lokaal kan resulteren in een hogere geothermische gradient (**Hoofdstuk 2**). De aanwezigheid van een dergelijke anomalie maakt exploitatie van de geothermische warmtebron aantrekkelijker vanwege lagere boorkosten.

In het studiegebied van noordoost Groningen worden door het zout temperatuur anomaliën veroorzaakt, die evenredig zijn met de dikte van de zoutlaag, waarbij in deze studie een kritische dikte van minimaal 600m is geïdentificeerd. Door middel van modellering werden temperatuurverschillen tot wel 25˚C aangetoond tussen de top van het zout en de omliggende lagen op dezelfde diepte. Als er een voldoend permeabele laag boven deze 'sweet spot' aanwezig is, kan er tot 40% meer energie worden onttrokken, terwijl de hersteltijd met slechts 13% wordt verlengd. In Nederland bevinden zich in de

provincies Groningen en Drenthe diverse lokaties waar dit principe kan worden toegepast, aangezien de dikte van het zout op verschillende plekken meer dan 800m is.

Geothermische projecten zijn, net als elke ondergrondse ontwikkeling, onderhevig aan onzekerheden. In dit proefschrift wordt hier een uitgebreide analyse aan gewijd, niet alleen in termen van afzonderlijke onzekerheden, maar ook middels hun onderlinge interactie. De gecombineerde onzekerheid, die samenhangt met de aanvangstoestand van het reservoir (druk niveau en gas in oplossing), de geologie (permeabiliteit van reservoir en breuken) en de operationele condities (stroomsnelheden en her-injectie temperatuuur) is geanalyseerd voor het Groningse geothermische project (**Hoofdstuk 3**). De aanvangstoestand van het reservoir bepaalt meerendeels het drukverschil tussen de productieput en een hydrostatisch reservoir, alsmede de mee geproduceerde hoeveelheid gas. De mate waarin de druk gedepleteerd is bepaalt de vereiste pompdiepte, terwijl het opgeloste gas enerzijds mogelijk kan bijdragen aan de winstgevendheid van het project, maar ook een complicerende factor kan zijn voor de operatie fase en het installeren van de pomp.

Onder de geologische parameters is de reservoir permeabiliteit nauw verbonden met het druk verschil tussen de twee putten van het geothermisch doublet. De doorlaatbaarheid van de omliggende breukzones beïnvloedt de omvang van het gedraineerde gebied en heeft derhalve een effect op het tijdsverloop van de temperatuur van het geproduceerde water. Onder de operationele parameters is de gekozen stroomsnelheid bepalend voor het geproduceerde thermisch vermogen, het drukverschil tussen de putten en het temperatuur verloop bij de productieput. Tenslotte bepaalt de injectie temperatuur eveneens het geproduceerde vermogen.

De complexiteit van het systeem neemt toe wanneer de geothermische bron wordt gekoppeld met het energie vraagpatroon van het warmtenet (**Hoofdstuk 4**). Hiermee wordt een seizoensafhankelijke belasting geïntroduceerd, die een nieuwe onzekerheid met zich mee brengt aangaande leveringszekerheid en mogelijke extra geochemische effecten. Voor het Groningen systeem wordt in dit proefschrift aangetoond dat over een productie periode van 50 jaar in de meeste productie scenarios een seizoensafhankelijke warmtevraag geen nadelige geochemische effecten voor reservoir en energie productie oplevert. Bovendien maakt seizoensafhankelijke productie het mogelijk een meer efficiënt gebruik van de geothermische bron te maken, aangezien het voortschrijden van het koudefront wordt vertraagd. Deze variatie heeft alleen effect op de reactiesnelheid maar niet op de soorten van geochemische eigenschappen van het reservoir.

Het geochemisch gedrag van het reservoir wordt voornamelijk bepaald door de stroomsnelheid en in de tweede plaats door pH en temperatuur van het injectiewater. De mineralen anhydriet en dolomiet blijken het meest te worden beïnvloed in het Rotliegend

zandsteen reservoir. Anhydriet lost op in de eerste productie jaren, waardoor de permeabiliteit rond de injectie put toeneemt. De oplossingssnelheid wordt bepaald door de stroomsnelheid, maar alle onderzochte productie scenarios resulteren in het oplossen van een gelijke volume fractie. Het effect van dolomiet op de permeabiliteit treedt op in een later stadium van de productie, voornamelijk bepaald door de pH en in de tweede plaats temperatuur. Hoge zuurgraad en lagere temperaturen bevorderen het oplossen van dolomiet, terwijl bij neutrale pH en hogere temperaturen het mineraal neerslaat uit oplossing.

Door de technische en economische onzekerheden bij elkaar te brengen wordt een compleet overzicht van een geothermische ontwikkeling verkregen (**Hoofdstuk 5**). Hiertoe is een probabilistisch techno-economisch model ontworpen dat de onzekerheden bevat die gepaard gaan met zowel de geologische als economische factoren.

De ' Expected Monetary Value' (EMV) is de waarde van een project waarin de risico's zijn meeberekend. De EMV van het Groningen project geeft een 50% kans op een marginale winst aan het eind van een productieperiode van 40 jaar, waarbij het succesvol boren van de twee putten in het doublet de grootste invloed heeft. Echter, ook als beide putten succesvol zijn, is een netto verlies nog steeds een van de mogelijke uitkomsten. De 'Net Present Value' (NPV) wordt berekend zonder risico's maar is wel zeer gevoelig voor de keuze van operationele parameters (bv stroomsnelheid), alsmede de begincondities van het reservoir (bv. druk). Anderzijds wordt de 'Levelised Cost Of Heat' (LCOH) vooral beïnvloed door geologische (bv permeabiliteit) en operationele (bv injectie temperatuur) parameters. Gezien dit verschil tussen de verschillende indicatoren verdient het aanbeveling zowel EMV, NPV als LCOH in combinatie te gebruiken voor een meer volledige economische evaluatie.

De seizoensafhankelijkheid van de warmtevraag en haar effect op de economische verwachtingen van het project laten duidelijk zien hoe belangrijk tijdelijke warmte opslag en/of additionele belasting van de bron zijn om een 'vlak' productieprofiel te kunnen bewerkstelligen. Dit laatste kan, samen met een ontkoppeling in de tijd van boven- en ondergrondse kapitaal investeringen, de economische verwachtingen van gelijksoortige projecten aanzienlijk verbeteren. In dit licht zal ook, in tegenstelling tot de huidige SDE+ regeling, een subsidie verlening met een kortere looptijd, maar optredend onmiddellijk na de boor fase, meer effectief zijn in het compenseren voor de hoge initiële investeringen die inherent zijn aan een geothermisch project.

In het laatste deel van dit proefschrift (**Hoofdstuk 6**) wordt de ontwikkeling van geothermische energie in context bezien van de politieke en economische 'zeitgeist'. Veelal wordt met hernieuwbare energie verwezen naar electriciteit, maar verwarming en

koeling zijn verantwoordelijk voor de helft van de energievraag van de EU en drie-kwart van de huishoudelijke consumptie.

Het verzamelen van meer gestructureerde en systematische gegevens zal leiden tot een beter begrip van geothermische systemen op basis van ondergrondse warmtegeleiding met directe toepassing voor verwarming. De ontwikkelingen van geothermische projecten in Nederland maken dit mogelijk in de nabije toekomst en daardoor wordt een voortrekkersrol mogelijk gemaakt op het gebied van een integrale evaluatie en monitoring van geothermische energiebronnen.

Chapter 1

Introduction & Thesis Outline

Introduction

Fossil fuels are depleted at an ever-growing pace, the energy intensity per capita is growing, the world population is increasing and climate change is expected to pick up pace. The combination of these parameters makes future energy supply a challenge at multiple levels. To battle this issue the energy sources need to be diversified and a gradual switch to more sustainable ways of energy generation has to prevail. As a renewable source with a non-intermittent nature, geothermal energy can be one of the pathways towards this goal.

Geothermal energy has been used for many centuries and in a wide variety of applications. The most common use consists of hot water for balneology and in more modern times for spa's (Barbier, 2002; Lund, 2007). Electricity production using geothermal energy on an experimental basis began in 1904. The first commercial power plant with a capacity of 250kW$_e$ started production in 1913 in Larderello, Italy (Barbier, 2002; Lund, 2007; Tester *et al.*, 2006). The first municipal heating system based on geothermal energy started operating in Reykjavik, Iceland, in 1930 (Barbier, 2002).

With its low environmental impact, continuous nature and invariability, geothermal energy appears to be a financially competitive source of sustainable, renewable, base-load electricity and thermal energy provider (Goldstein *et al.*, 2011a). Today it offers an alternative to fossil fuels that meets both current and future environmental standards, while keeping security of energy supply intact.

Geothermal energy

Principle

Heat generation

The heat generated at the mantle of the earth originates from the decay of naturally occurring radioactive isotopes with half-lives in the same order of magnitude as the 4.5 billion years old planet of the earth (Barbier, 2002; Olasolo et al., 2016; Rybach, 2007). These isotopes include: ^{40}K, ^{232}Th, ^{235}U and ^{238}U (Barbier, 2002; Tester *et al.*, 2006). The heat generated by radioactive decay in the earth's mantle and core slowly reaches towards the surface via two mechanisms: conduction and convection (Axelsson et al., 2005; Goldstein et al., 2011b; IGA, 2001; Moeck, 2014; Tester et al., 2006). In the case of conduction, mainly for solids, heat is transferred through the random kinetic energy between neighbouring molecules without the transfer of matter. In the case of convection, heat is transferred through a geothermal fluid flow (in most cases an aqueous solution or a gas) due to buoyancy. Buoyancy is caused by thermal expansion that reduces the viscosity of the fluid and also includes mass transfer (Barbier, 2002; Hanano, 2004).

Owing to the transfer of mass, convection is some 10 times (Garg and Kassoy, 1981) more efficient than conduction in transferring thermal energy (Axelsson, 2010).

Therefore, aquifers or a mechanically circulated fluid are essential parts for most geothermal fields (Barbier, 2002). Using a fluid, the heat is extracted by means of convection and is replenished through naturally occurring conduction and/or convection (Ungemach *et al.*, 2005). As a result of fluid convection, the upper and lower parts of a reservoir have a similar temperature and therefore the reservoir itself has a low temperature gradient (Barbier, 2002).

The average geothermal gradient for continental crust, is in the order of 30°C/km (Barbier, 2002; Fridleifsson et al., 2008; Banks, 2012) with values ranging between 10°C/km and 100°C/km for ancient continental crust and areas of active volcanism respectively (Barbier, 2002). The world average heat flow is estimated at 82mW/m^2, which amounts to a total thermal output of 4x10^{13}W (Uyeda, 1988). However, there is a wide variety of heat flow levels, between 57mW/m^2 (Barbier, 2002) , 59mW/m^2 (Tester *et al.*, 2006) and 65mW/m^2 (Goldstein *et al.*, 2011b; Stefansson, 2005) for the continental crust and between 99mW/m^2 (Barbier, 2002) and 101mW/m^2 (Stefansson, 2005) for the oceanic crust. .

Production of geothermal energy is established via drilling, using methods and techniques often used by the oil and gas industry (Tester *et al.*, 2006). In most geothermal systems a minimum of one producer and one injector well are present, while combinations of multiple injecting and producing wells are more common in high enthalpy fields. Thermal energy is extracted by means of a coupled heat transport system and is subject to reservoir properties such as hydrologic, lithologic and geologic conditions (Tester *et al.*, 2006).

The presence of geothermal energy is mostly associated with geologic and/or tectonic phenomena and therefore it is commonly found on tectonic plate boundaries or areas of plutonic and volcanic activity (Tester *et al.*, 2006). This however does not exclude the exploitation of geothermal energy in other regions as well.

Geothermal prospects are usually dispersed, making geothermal a distributed energy source for local and domestic uses, which could contribute to the security of energy supply (Lund, 2007). It is currently documented that low temperature geothermal reservoirs are present at depths accessible by drilling in most parts of the world (Barbier, 2002).

Geothermal system and reservoir

Geothermal systems have recently been classified based on the geological control in geothermal plays. Derived from petroleum geology, a play is used to describe a

combination of certain geological characteristics. For a petroleum system these are a source rock, a reservoir rock and a trap (Allen and Allen, 2005a). In the case of a geothermal system the play is defined by the elements of the heat source, the geological controls on the heat migration/pathway, the heat/fluid storage capacity and the potential for an economic recovery of the heat in place (HIP) (Moeck, 2014).

Consequently, two major geothermal play types can be distinguished based on the mechanism that controls the heat source. These are convection dominated systems and conduction dominated systems (Moeck, 2014). The former usually coincide with igneous activity, often referred to as high enthalpy systems, while the latter are mostly encountered in intra-continental systems and sedimentary basins.

The geothermal storage medium can be defined as the geothermal reservoir. A geothermal reservoir consists of a large body of hot permeable rock at a depth reachable through drilling, which contains large amounts of fluid (water or steam), enabling the transfer of heat to the surface (Barbier, 2002). If the fluid is absent it can be introduced by injection. A geothermal reservoir is defined as "the hot part of the geothermal system that can be exploited either by extracting the contained fluid (water, steam or various gases) or using anyhow its heat" (Grant *et al.*, 1982). The part of the geothermal reservoir that can support production of either heat or electricity constitutes the geothermal field (Barbier, 2002).

The fluids in geothermal reservoirs can be identified by means of resistivity surveys due to their significantly reduced electrical resistance compared to their surroundings (Magnusdottir and Horne, 2011), depending on the brine salinity. Reservoir engineering for geothermal resources includes the estimation of heat in place (HIP), reservoir performance, well deliverability, heat recovery, water injection and reservoir lifetime (Ungemach *et al.*, 2005). Information for geothermal resources can be derived from different sources (Hurter and Schellschmidt, 2003). Such sources include geophysical surveys, which aid to determine structure (faults) and spatial distribution of reservoir formations, borehole data, which provide information on stratigraphy, porosity and temperature, as well as cores for permeability measurements.

When performing reservoir engineering for a geothermal application two points are of importance. Firstly, determination of the reservoir volume through the interpretation of the system structure (Goldstein et al., 2011b; O'Sullivan et al., 2001) and the variations in well productivity (Juliusson and Horne, 2010). These dictate the plant size based on a number of conditions (formation temperature, heat recovery rate etc.) (Stefánsson, 1992). Secondly, the aim is to design a safe and efficient operation for the project lifetime (Goldstein et al., 2011b; O'Sullivan et al., 2001). Understanding the spatial variability of reservoir properties (i.e. porosity and permeability) is of utmost importance to estimate the fluid flow through the host formation (Salimi and Wolf, 2011). In order to understand

the nature of a geothermal reservoir, well data remain the most valuable source of information over any other (Stefánsson, 1992).

The reservoir impedance (or resistance to flow) can be divided in three main parts: impedance close to the injection well, main reservoir impedance and impedance at the production well (Murphy *et al.*, 1999). Usually, the greater part of the impedance is spatially located close to the injection well, suggesting that larger reservoirs or a greater spacing between production and injection well can increase the amount of produced heat with little effect on the required pumping power (Murphy *et al.*, 1999). However, larger well spacing can only increase the amount of produced energy if well connectivity is not disturbed by structural or facies discontinuities and inhomogeneity (Crooijmans et al., 2016; Willems et al., 2017b).

The refresh rate of the hydrothermal system dictates the production level, but this can be further extended by reinjection of the used water stream (Tester *et al.*, 2006). Stepwise development based on the utilization of the previous step to slowly approach equilibrium is suggested as a way of reducing over investment risk (Stefansson and Axelsson, 2005) when developing geothermal fields.

Regarding low enthalpy, conduction dominated geothermal reservoirs, a number of conditions should be met for successful economic utilization (Legarth *et al.*, 2005). These include high mass flow rates, connection of a maximum inflow area to the wellbore for an efficient fluid production and, if present, stimulation must achieve the maximum possible reservoir thickness. These conditions can be summarized under the term transmissivity, meaning the rate that the reservoir can facilitate flow.

Renewability and sustainability

Geothermal energy is often listed among the renewable sources of energy. However, the renewability of any resource largely depends on the timeframe under which it is examined, together with the rate at which the resource is utilized and replenished (Barbier, 2002).

Towards this end, Axelsson et.al (2005) make an important distinction between two often mixed up terms. Renewability concerns the nature of the resource, while sustainability refers to the way the resource is utilized (Axelsson et al., 2005; Stefansson and Axelsson, 2005). If the production levels are kept below a certain threshold for which the system can reach equilibrium, utilization can be sustained for longer periods of time (Axelsson *et al.*, 2005), e.g. 100 years or more. Historical examples for both sustainable and unsustainable geothermal utilization can be found in literature (Axelsson *et al.*, 2005).

A geothermal resource has two aspects, an energy flow and the energy stored (Axelsson, 2010). Each aspect has a different replenishing rate since the energy flow can be considered fully renewable, while stored energy is renewed at a slower pace, especially if heat conduction is the dominant mechanism (Axelsson *et al.*, 2005; Axelsson, 2010). In most geothermal applications, the limiting factor for production is water flow i.e. the energy flow and not the availability of the stored thermal energy (Axelsson *et al.*, 2005).

Without considering economic aspects, possible environmental issues and technological advances, which could be context and time dependent, Axelsson et.al. (2001) propose that there exists a certain base level of energy production from any geothermal system, termed E_0. Below this energy production level the resource can be used sustainably for a period between 100 and 300 years. This level relates to the total extracted energy and is dependent on the nature of the resource, leaving out load factors and efficiency. Exceeding the amount of the base energy level leads to excessive production and depletion of the resource. Sustainable utilization of geothermal sources can only be achieved when the exploitation rate is equal or lower than the regeneration rate over the same time period (Cataldi, 2001). Consequently, on the scale of technological and societal systems and unlike fossil fuel reserves, geothermal systems can be considered renewable (Rybach, 2003).

Axelsson (2010) suggests that a sustainable production of geothermal heat can be achieved either through: constant production below the sustainable limit, a step-wise increase in production, intermittent excessive production or reduced production after a shorter period of heavy production. Intermittent excessive production (on a seasonal basis) will be further examined in the course of the project. In recent years field management options of alternating the injection and production wells have also been suggested as ways of extending the lifetime of a geothermal field.

Types of geothermal energy

Geothermal fields can be split into two main categories depending on their enthalpy level (Lokhorst and Wong, 2007): high enthalpy and low enthalpy. Based on that distinction they can be used for base-load electricity generation and/or for direct heating uses (Tester *et al.*, 2006) respectively.

Four types of geothermal systems are identified: hydrothermal, hot dry rock, geo-pressured and magmatic (Barbier, 2002). Nonetheless, most developed geothermal systems are of the hydrothermal type (Barbier, 2002; Fridleifsson et al., 2008).

A hydrothermal system consists of the heat source, a reservoir and the recharge area of the reservoir (Barbier, 2002; Fridleifsson et al., 2008; Sausse et al., 2010). Through the recharge area, water reaches the heat source and can sometimes also circulate back to the

surface. In turn, hydrothermal systems can be distinguished in water and vapour dominated fields (Barbier, 2002; Hanano, 2004).

Water dominated geothermal fields can produce water of up to 100°C at the surface and are of economic interest if the reservoir is found not deeper than 2km, can produce at high flow rates (150t/h) and maintain a low water salt content (60g/kg) (Barbier, 2002). The geothermal systems discussed in this thesis belong to the water dominated type of systems.

Wet steam fields produce water at the surface at temperatures exceeding 100°C and steam in shallower and lower pressure parts of the reservoir (Barbier, 2002). The increase in pressure is usually caused by the presence of a cap rock and manifests itself at the surface as boiling springs and geysers (Barbier, 2002). If the produced temperature is lower than 150°C, a second fluid with a lower boiling point is used to generate vapour in a binary or organic Rankine Cycle (Barbier, 2002; DiPippo, 2005; Franco and Vaccaro, 2012; Lund, 2007).

Vapour dominated fields generate dry saturated or even superheated steam and the presence of a cap-rock is essential to their existence (Barbier, 2002). The steam generally includes quantities of CO_2 and H_2S and the heat transfer is higher than in water dominated fields. Due to the higher temperatures, vapour dominated fields are more suitable for electricity production (Barbier, 2002).

Applicable to water dominated, wet steam and vapour dominated fields two different methods can be used for electricity generation. The first one is flash steam (single or double) and the second is a binary cycle. In the flash steam and in high temperature fields, a different fluid (e.g. propane, pentane or ammonia) is used when the temperature in the field is not high enough to produce large amounts of steam from water (Barbier, 2002; DiPippo, 2005; Jalilinasrabady *et al.*, 2012). This can be carried out in either one or two separate pressure phases (single flash, double flash). A binary cycle is used when the field is not hot enough to produce steam from water at surface conditions. A working fluid , with a lower boiling point, is used to extract the heat from the field and to power the generator (Barbier, 2002; DiPippo, 2005).

Hot dry rock systems are expected to be widely utilized in the near future through a technique that has come to be known as Enhanced Geothermal Systems (EGS) (Olasolo et al., 2016). According to the EGS principle, a fracture network is artificially created or enlarged in low permeability sediments or basement heat bearing rock in order to reduce hydraulic resistance (Mégel et al., 2006; Tester et al., 2006; Fridleifsson et al., 2008; Sausse et al., 2010). Enhancing the fracture network is carried out through the process of stimulation, which can be either hydraulic or chemical (Tester *et al.*, 2006); in recent

years, the option of thermal stimulation has also been explored (Siratovich et al., 2015). The purpose of hydraulic fracturing is to increase well injectivity/productivity by injecting water at high rates and pressure, targeting deepest flow paths (so as to maximize temperature) and lastly to homogenize permeability in order to avoid thermal short circuits (Mégel *et al.*, 2006). Chemical fracturing aims for the same result, using acids that erode the rock or other materials in existing fractures (Tester *et al.*, 2006). Thermal fracturing is achieved through the injection of cold water inducing steep thermal gradients. These gradients in turn lead to thermal stress and cracking mostly due to the anisotropic behaviour of heterogeneous rocks (Siratovich et al., 2015).

In all EGS systems water is circulated and steam or hot water is produced. The appeal of EGS lies in their large potential over a wide geographic spread across the world (Barbier, 2002) and their very low environmental impact. Recently two projects have been made commercial namely the Desert Peak in the US and Soultz-sous-Forêts in Europe.

Potential, Economics and Emissions

Global geothermal potential for electricity is between 2800TWh/yr and 86000TWh/yr (Goldstein *et al.*, 2011b).About 41% of the installed capacity for geothermal power generation is generated by single flash type plants (Bertani, 2016). Notably, while the installed capacity of heat systems is 5.5 times that of power systems (**Table 1.1**); nonetheless, the annually produced heat is only 2.2 times that of power, highlighting the effect of the load factors of heat producing systems (**Table 1.1**). At the same time the higher thermal power compared to electric power also highlights the energy sector in which geothermal can have a more significant contribution.

Table 1.1. Summary of key world geothermal data for power and heat.

	Power	Heat
Technical potential	1.2TW (incl 70% chance of 1TW EGS) (Bertani, 2012)	$10TW_{th}$ (Bertani, 2012)
Installed capacity	12.7GW (Bertani, 2016)	$71GW_{th}$ (Lund and Boyd, 2016)
Annual production	74TWh (Bertani, 2016)	$165TWh_{th}$ (Lund and Boyd, 2016)

More than half of the heat is generated by means of geothermal heat pumps (Lund and Boyd, 2016) and more than 70% of the global geothermal resources have an output of 150°C or less, produced from water dominated fields (Franco and Vaccaro, 2012); this highlights the importance of geothermal heat in the energy landscape. While several other renewable energy technologies exist for the production of power, geothermal heat

production is uniquely positioned as a renewable, environmentally friendly energy source.

Drilling expenses constitute a significant component of the overall cost of any geothermal application (Barbier, 2002; Goldstein et al., 2011b; Hurter and Schellschmidt, 2003; Johnston et al., 2011; Stefánsson, 1992; Stefánsson, 2002; Tester et al., 2006). Moreover, even though geologic conditions are variable, trajectories more complex and larger diameters are used, geothermal wells are comparable in terms of cost with hydrocarbon wells (Lukawski et al., 2014). Costs for geothermal electricity in the US range between 2-10$cents/kWh (Barbier, 2002). The MIT study (Tester *et al.*, 2006) further suggested for the USA a Levelized Cost Of Electricity (LCOE) between 2.5 and 4.4 cents per kWh for high grade and 6.5 to 11 cents per kWh for low grade EGS, using a flow rate of 80kg/s. The numbers are derived in the case of mature EGS technology with a setup of 1 injector and 3 producer wells. The results appear to be more sensitive to the production well flow rate and surface plant capital costs, while stimulation costs appear to have a very low impact. Economic factors such as the ratio of bond over the equity debt and the equity rate of return are the most sensitive economic factors. Systematic cost estimations for direct use geothermal heat are not so widespread, in part due to the fact that heat is mostly an immature, unregulated market; nonetheless, current Levelised Cost Of Heat (LCOH) values in the US are estimated at 0.63$cents/$kWh_{th}$ (Beckers Koenraad F. et al., 2014). Economic aspects for direct use geothermal heat are further discussed in Chapter 5 of this thesis.

Regarding greenhouse gas emissions, due to the absence of a combustion process in a geothermal application (heat or power), the associated emissions are mostly determined by the chemical composition of the reservoir (Goldstein *et al.*, 2011b). Geothermal electricity generation, which usually utilizes higher temperature fields, can range between 13g to 740g CO_2/kWh_e (Fridleifsson, 2001; Goldstein et al., 2011b). Emissions from direct use applications are only a fraction, because of the lower gas content of low temperature geothermal fields (Fridleifsson, 2001); however, direct venting of CH_4 (hundred times stronger greenhouse gas compared to CO_2) might still occur. Nonetheless, emissions of CO_2 equivalents from LCA studies suggest between 14g and 202g of CO_2eq /kWh_{th} for direct use purposes (Goldstein *et al.*, 2011b).

The specific energy of hot water amounts to circa 1% of the specific energy of oil and gas (10kWh/kg) (Orzol *et al.*, 2005). This difference in contained energy is attributed to the fact that only the latent heat of a geothermal fluid is used, while for hydrocarbons the chemical energy stored is released during combustion. Electricity generation is also limited by conversion efficiency (25%-50%), mostly due to the lower temperatures of geothermal fluids compared to combustion temperatures of fossil fuels (Tester *et al.*, 2006). Direct use however does not require any energy conversions.

Geothermal energy in the Netherlands

An initial estimation of Heat In Place (HIP) mentioned 90,000PJ on the Dutch onshore (Lokhorst and Wong, 2007). Recently more thorough assessments based on formation depth, thickness, porosity, permeability and temperature suggest the existence of as much as 820,000PJ of HIP while the Recoverable Heat (RH) under technical and economic criteria is estimated at 85,000PJ (Kramers et al., 2012). With the total energy supply for the Netherlands in the order 3,250PJ for 2011 (CBS, November 16, 2012) there is in principle significant potential for direct use geothermal development.

Initial interest for geothermal applications in the Netherlands focused on storage of thermal energy, mostly for large applications such as commercial buildings (Lund *et al.*, 2011). The most widespread use of geothermal energy is via heat pumps, less than 500m deep (Lokhorst and Wong, 2007; Lund et al., 2011). The demand for geothermal direct heat applications mostly stems from agricultural and district heating systems (Ministry of Economic Affairs, 2012). In recent years, the Netherlands finds itself amongst the world leading countries in terms of annual geothermal energy used directly (Lund and Boyd, 2016).

Governmental annual reports suggest that in recent times, for three consecutive years, the amount of licence applications regarding geothermal energy was notably greater than for any other subsurface activity (Ministry of Economic Affairs, 2010; Ministry of Economic Affairs, 2011; Ministry of Economic Affairs, 2012). In 2015 six new applications for geothermal exploration were submitted, with the total number of geothermal licences in effect reaching 58 as of January 2016 (Ministry of Economic Affairs, 2016). This highlights the increased interest for geothermal applications, even though only 14 doublets have been realized to date. In the majority of the licences, the heat is planned to be used for greenhouses (more than three quarters), followed by electricity and building heating (Kal, 2013; Ministry of Economic Affairs, 2016).

The first deep wells for geothermal energy became operational in 2008 showing a gradually increasing number over time (**Figure 1.1**a) while in the last few years the installed capacity has increased more than twofold (**Figure 1.1**b). During 2015 heat production exceeded 2400TJ/year (circa 0.06 mtoe/year)(**Figure 1.1**c) with significant co-production of gas in several projects, amounting to 4.3 mcm for the same year (EBN et al., 2016).

Most geothermal systems produce from Upper Jurassic or Lower Cretaceous sediments, followed by Rotliegend intervals (Ministry of Economic Affairs, 2016). The majority of developed geothermal reservoirs are located at depth shallower than 2.5km with the exception of two deeper projects that reach a depth of 2.7km (EBN et al., 2016).

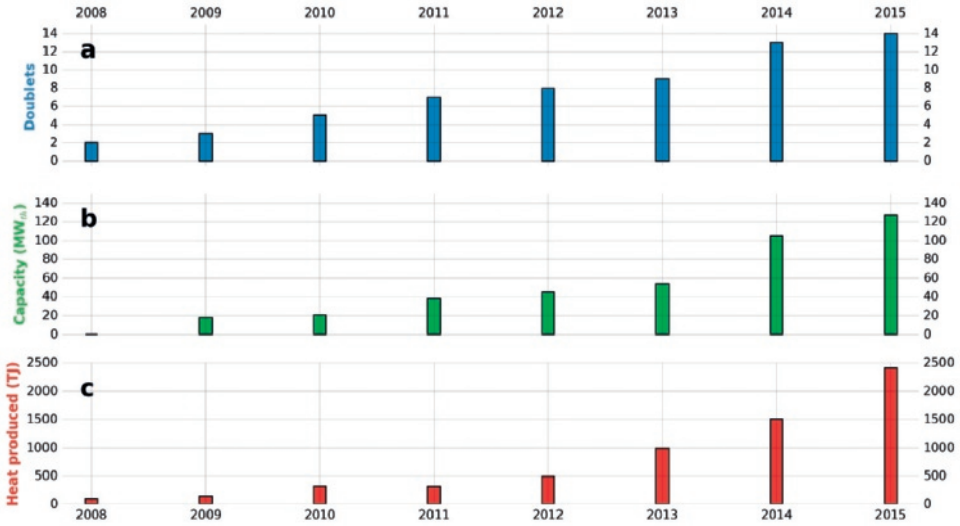

Figure 1.1 Number of doublets (a), respective installed capacity (b) and heat produced (c) for deep geothermal systems in the Netherlands. Source: (Bakema and Schoof, 2016; Ministry of Economic Affairs, 2016).

In 2013 the legal framework was clarified for geothermal applications; feed in tariffs for geothermal heat and guarantees for unsuccessful drilling operations were established during Phase 3 of the governmental geothermal support program (Kal, 2013). Nonetheless, the subsidy scheme of SDE+ (Stimulering Duurzame Energy) has become more substantial in recent years, while the drilling guarantees were further improved (Bakema and Schoof, 2016). Recently the aim of the Dutch government was set at 5 PJ of deep geothermal energy production in 2020 (Bakema and Schoof, 2016); this is a downward revision compared to the previous goal of 11PJ for the same period (Kal, 2013), possibly due to the economic performance and technical success of systems in place.

Despite these promising developments in terms of policy and the interest shown in terms of licences, the running projects remain few. This can be partly attributed to problems with production, such as the presence of gas or oil. Another bottleneck appears to be the high investment cost in the initial phase of the projects, mostly related to drilling, resulting in long investments return times. Lastly, possible interference or overlap between other subsurface activities (gas, oil, salt production, gas storage etc) further complicates the design, implementation and operation of geothermal applications (TNO, 2012, April; van Os et al., 2017). Nevertheless, the established policy framework and accelerating learning curve from various projects is expected to foster an increasing number of geothermal systems for direct use in the coming years.

Geological background

This section provides an overview of the geological history and features of the area in which the geothermal systems discussed in chapters 2,3,4 and 5 are situated. Three different levels are examined from a regional to a more local scale: the Southern Permian Basin, the Netherlands and the Groningen area.

Basin and Netherlands

The Netherlands is part of the Southern Permian Basin, which has been extensively studied and explored for hydrocarbons (Doornenbal *et al.*, 2010). The subsurface of the Netherlands has been affected by all the major orogenies of Europe (Caledonian, Variscan and Alpine), by Mesozoic rifting and by the Rhine Graben rift system (Doornenbal et al., 2010; Herngreen and Wong, 2007; Lokhorst and Wong, 2007).

Depositional environments and tectonic evolution

During the Paleozoic era, Caledonian and Variscan orogenies formed Pangea. The area of the Netherlands was at the time located close to the meeting points of the Laurentia, Baltica and Gondwana continental plates (Lokhorst and Wong, 2007).

In the late Carboniferous, the Westphalian coals were deposited, at a time that the Southern Permian Basin was located just north of the Equator (Glennie, 2007). The early Permian (Rotliegend), under thermal subsidence, marked the development of the Southern Permian Basin (Bachman and Hoffman, 1995; Bachman and Hoffman, 1997) and sedimentation started taking place in what is today central and north west Europe (Gast *et al.*, 2010). The Rotliegend sandstone sediments were deposited under an aeolian desert regime with increasing aridity, while saline lakes developed in the deeper parts of the basin (Gast *et al.*, 2010). The Westphalian coals and the Permian sandstones are separated by a stratigraphic hiatus, referred to as the Saalian unconformity (Glennie, 1998).

Periodic marine ingressions affected the late Rotliegend and were followed by a transgression that rapidly flooded the entire basin resulting in full marine conditions during the late Permian, creating the Zechstein sea (Gebhardt, 1994; Legler et al., 2005; Legler and Schneider, 2008; Peryt et al., 2010). As a result of cyclic chemical precipitation, sediments associated within a saline basin were deposited (Richter-Bernurg, 1955a; Richter-Bernurg, 1955b); five Zechstein evaporate formations and one claystone formation are identified within the Netherlands (Geluk, 2007a). Salt depositions are of importance to petroleum geology, serving as seals for hydrocarbons (Geluk *et al.*, 2007) and their high thermal conductivity is of importance for geothermal energy as is further discussed in Chapter 2.

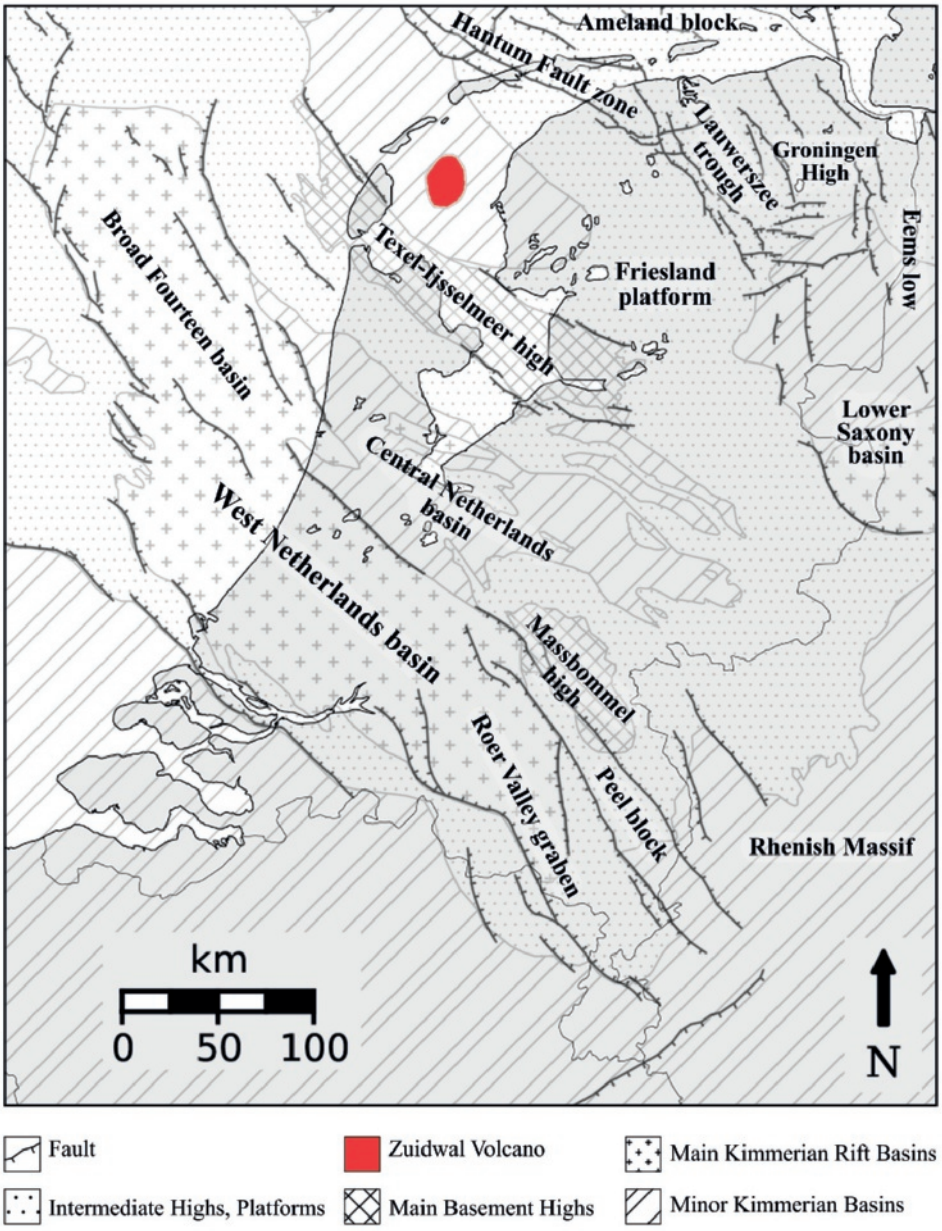

Figure 1.2. Main structural elements of the Netherlands and surrounding territories. Adapted from: (Herngreen and Wong, 2007).

The breaking up of Pangea in the Mesozoic was initiated by rifting during the early Triassic (Herngreen and Wong, 2007; Pharaoh et al., 2010). Continued extension, as late as the Late Cretaceous, evolved into the opening of the Atlantic Ocean (Pharaoh *et al.*,

2010). In the area of the Netherlands the sediment deposition occurred under thermal subsidence conditions (Pharaoh *et al.*, 2010). A Lower and Upper Trias group are separated by the base Solling or Hardegsen unconformity (Geluk, 2007b). The lower group consists of silicaclastic deposits (lacustrine environment) with sandstone (fluvial and aeolian environment) and oolite intercalations (Geluk, 2007b). The upper group consists of silicaclastics, carbonates and evaporites (lacustrine environment) (Geluk, 2007b). During this period, extensional forces have triggered local halokinesis of the Zechstein salt deposits (Geluk *et al.*, 2007), resulting in large present day thickness variations.

Jurassic sediments were deposited in a shallow epicontinental basin (Lott *et al.*, 2010) adjacent to sea-floor spreading and rifting in the central Atlantic Ocean (Pharaoh *et al.*, 2010). This period includes four lithostratigraphic groups: the lower group is mainly argillaceous (marine environment), while the other three groups are made of coarser silicaclastic formations of mainly marine, continental and continental to restricted marine environments (Wong, 2007). Cretaceous sediments were mostly formed in marine environments as a result of regional subsidence, comprised mostly of silicaclastics (Herngreen and Wong, 2007). Fading rifting and a gradual transition to lithospheric cooling and subsidence comprised the tectonic regime for this period (Lott *et al.*, 2010).

During the late Cretaceous and early Cenozoic the compressional regime of the Alpine orogenetic phase was established, resulting in extensive inversion of existing basins (Pharaoh *et al.*, 2010). Tertiary sediments, silicaclastic in nature, make up three North Sea groups, deposited at a single large epicontinental basin on top of the rift structures of the Mesozoic era (Knox *et al.*, 2010; Wong *et al.*, 2007).

Resulting from the tectonic history, several structural elements can be identified in the Dutch subsurface. The most important features are the Dutch Central Graben, the Broad Fourteens, West Netherlands Basins and Roer Valley Graben, the Lower Saxony Basin, the Friesland platform and the Groningen High (de Jager and Geluk, 2007)(**Figure 1.2**).

Groningen

Dealing with the subsurface of the north-east Netherlands, the biggest gas field in Europe stands out as a major feature. The Groningen gas field is situated in the sub-salt Rotliegend system and forms a substantial contribution to the world's oil and gas reserves (Grötsch *et al.*, 2011). The larger part of the gas reserves of the Groningen gas field was generated by Westphalian coals and Carboniferous shales (Laier *et al.*, 1997; van Gent *et al.*, 2009). The gas is trapped in the Rotliegend reservoir rocks and is sealed by Zechstein evaporites, which have been subjected to halokinesis (de Jager and Geluk, 2007; van Gent et al., 2009).

Discovered in 1959, it remains today the biggest gas field in Europe and the 9th biggest gas field in the world with recoverable reserves of 2,067 bcm (Sandrea, 2006; Whaley, 2009). Production from the Groningen gas field has led to the development of several new technologies, most notably extended reach drilling from cluster points, currently a wide spread technique for reducing both cost and environmental impact (Grötsch *et al.*, 2011). Additionally, gas production has also caused a depletion of the field pressure levels. This has in turn led to compaction and subsidence and ultimately to the occurrence of seismic events along pre-existing faults (Nepveu et al., 2016; Van Wees et al., 2014). The largest recorded seismic event had a local magnitude $M_L = 3.6$ (Nepveu et al., 2016) and occurred in August 2012. Ever since, gas production levels and related seismicity have been widely discussed on a political, social and economic level (van der Voort and Vanclay, 2015).

Stemming from the interest in hydrocarbons stored in the field, the Groningen gas field and consequently the north of the Netherlands, as well as the Dutch offshore have been extensively explored (van Ojik *et al.*, 2011). This has resulted in circa 56.000 km^2, or 56% of the total Dutch territory, being surveyed with high quality 3D seismic data (de Jager and Geluk, 2007; Grötsch et al., 2011).

The area of Groningen belongs to the structural Groningen High and is surrounded by the Lauwerszee Trough in the west-southwest, the Lower Saxony Basin in the south and the Ems Graben in the east (**Figure 1.2**). The area of Groningen has been a structurally positive element since the Late Carboniferous, while vitrinite reflectance data and magnetic anomalies suggest the presence of an intrusive body during the Kimmerian (de Jager and Geluk, 2007). The Groningen block has not evolved significantly since the latest Jurassic when the Groningen High was formed (de Jager and Geluk, 2007; Duin et al., 2006; NITG, 2004; Ziegler, 1982). **Figure 1.3** shows a cross section through the Groningen gas field, revealing the basic geological structure of the area.

Relatively thin deposits with a maximum thickness of 800m were deposited during Triassic to Lower Cretaceous and have been subjected to partial erosion or to a depositional hiatus (de Jager and Geluk, 2007; NITG, 2004; Ziegler, 1982). On top of them, the Chalk of Upper Cretaceous age (thickness 400 to 1200m) is formed by carbonates and marls (NITG, 2004). Overlying the Chalk, the North Sea supergroup of Cenozoic age consists of mainly silicaclastics with a thickness between 500 and 1250m and was deposited from the Early Paleocene onwards (NITG, 2004; van Adrichem-Boogaert and Kouwe, 1993-1997).

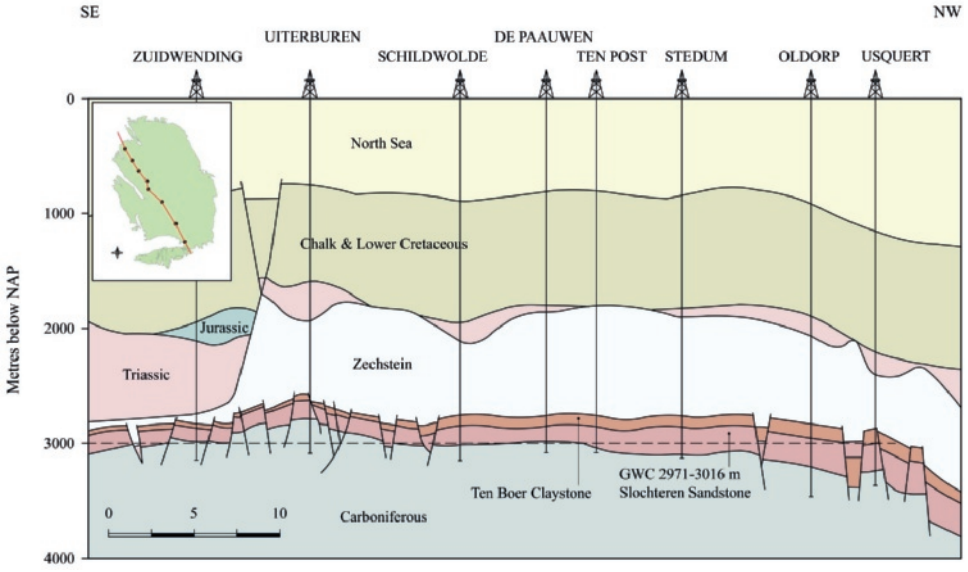

Figure 1.3. SE to NW simplified cross section, representing a generalized stratigraphy of the Groningen gas field. The upper left inset depicts the Groningen gas field. Adapted from: (Grötsch *et al.*, 2011)

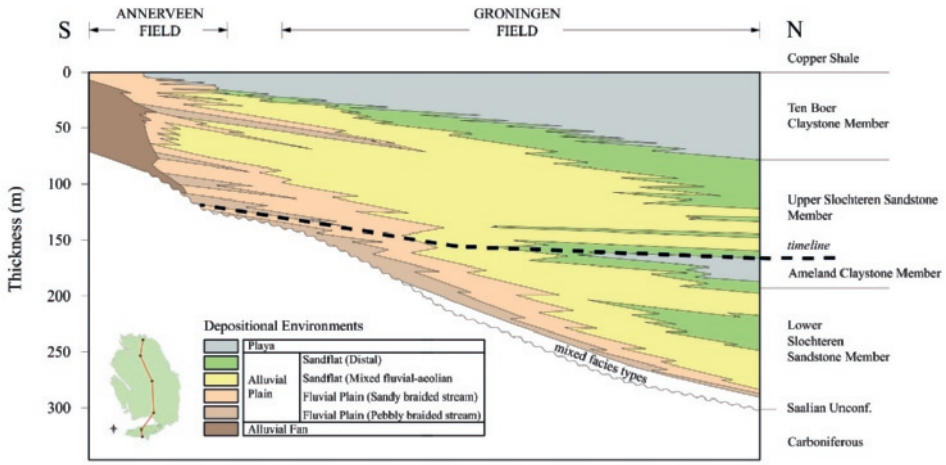

Figure 1.4. S to N cross section depicting a concept of the lithofacies and the different depositional environments. The lower left inset depict the Groningen gas field. Adapted from: (Grötsch *et al.*, 2011)

Subhercynian tectonism has eroded the Chalk group at some locations. Adjacent areas have been subjected to uplift, truncation, erosion, inversion and fault reactivation by the Laramide inversion during the Late Cretaceous (van Gent *et al.*, 2009). The north-west part of the block has been relatively stable, with only a slight uplift, which has eroded the top part of Cretaceous deposits and caused a minor inversion (mainly in the southern part)

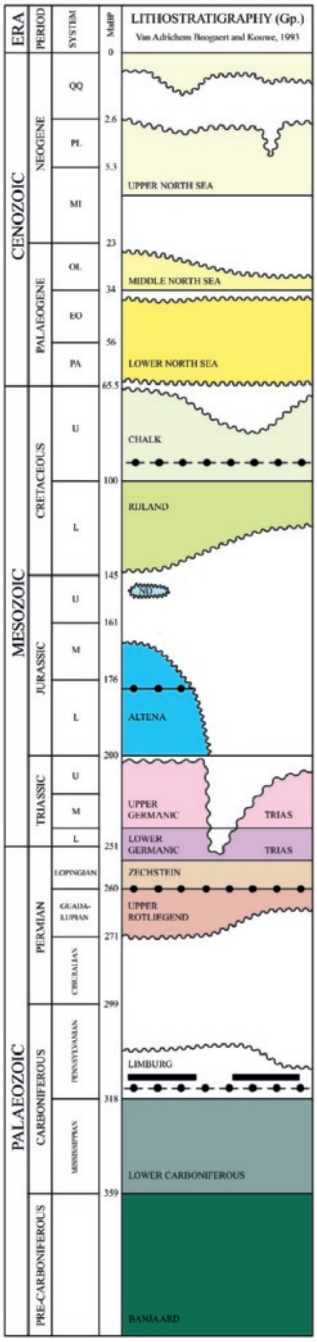

Figure 1.5. Generalized stratigraphic column of the Groningen petroleum system. Adapted from: (Grötsch *et al.*, 2011)

(de Jager and Geluk, 2007; de Jager, 2003; Dronkers and Mrozek, 1991; Duin et al., 2006; Gras and Geluk, 1999; NITG, 2004; Stäuble and Milius, 1970; van Adrichem-Boogaert and Kouwe, 1993-1997; Van Wijhe, 1987; Worum and Michon, 2005; Ziegler, 1982). A recent study on the stress states has concluded that the earlier phase occurred during the Late Permian – Triassic with extensional stresses on the NE-SW axis (van Gent *et al.*, 2009). During the late Cretaceous, further extension took place with E-W direction, while during the Tertiary extension along the E-W (Early Eocene) and NE-SW (Miocene) has been recognized (van Gent *et al.*, 2009).

Table 1.2 Stratigraphic sequence suggested by van Gent et.al. (van Gent *et al.*, 2009) using only wells with bio-stratigraphic data

Group	Age	Thickness (m, avg)	References
North Sea	Tertiary: Priabonion (19Ma)	600	(van Gent *et al.*, 2009)
	Tertiary: Ypresian to Lutetian (52Ma)	400	
	Tertiary: Early Lutetian (~45-48Ma)	50	
	Tertiary: Thanetian (60Ma)	250	NAM/(van Gent *et al.*, 2009)
Chalk	Late Cretacious: Middle-Upper Campanian (75-80Ma)	400	(van Gent *et al.*, 2009)
	Late Cretacious: Lower Campanian (82-84Ma)	200	
Rijnland	Late Cretaceous: Cenomanian (97Ma)	300	NAM/(van Gent *et al.*, 2009)
	Early Cretaceous: Latest Ryazanian (140Ma)	50	
Upper Germanic Trias	Triassic, Early Anisian (245Ma)	550	NAM
Zechstein	Late Permian: Thuringian (251Ma)	500-1500	
Upper Rotliegendes	Early Permian: Saxonian (258Ma)	-	

The complexity of the stratigraphy and poor biostratigraphic data (due to the arid deposition climate) do not allow for a single, overarching genetic stratigraphic framework for the Rotliegend (van Ojik *et al.*, 2011). **Figure 1.4** depicts the lateral differentiation in the Groningen gas field area, showing the complexity of the various lithofacies. However, a simplified cross section and a generalized lithostratigraphic column are suggested for the greater Groningen area (**Figure 1.5**). Furthermore, seismic interpretation and seismic-to-well ties suggest the stratigraphy presented in **Table 1.2** as a general sequence in the area.

The upper Rotliegend lithological composition was created under retreats and advances of several desert lake systems, reworked by aeolian sands attributed to the active play system in the centre of the basin (Fryberger *et al.*, 2011; van Ojik *et al.*, 2011). The sediment range gets broader towards the North, and includes fluvial, aeolian, playa and lacustrine facies (McKie, 2011).

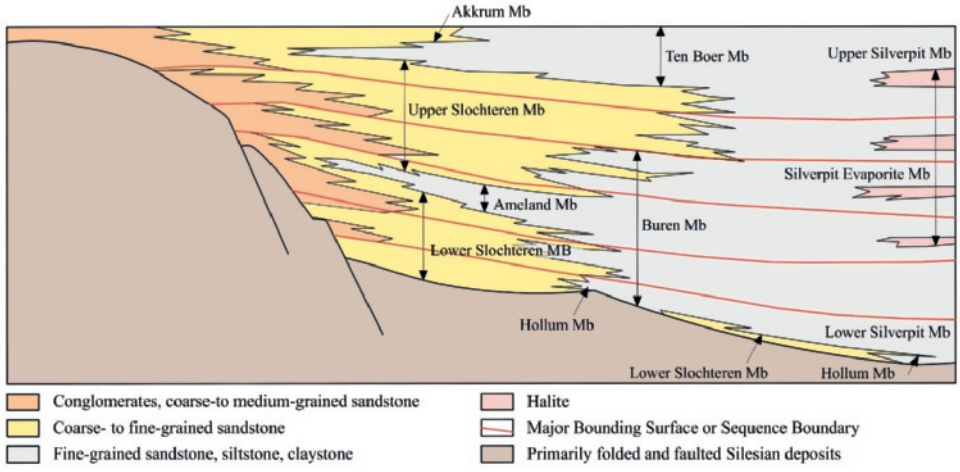

Figure 1.6. Lithostratigraphy of the upper Rotliegend. Adapted from: (van Ojik *et al.*, 2011)

The lithostratigraphic units in the upper Rotliegend can be divided in two major formations, the Silverpit and the Slochteren, which can be further subdivided in members (**Figure 1.6**). (van Ojik *et al.*, 2011). The Ten Boer member consists of red-brown sandy clays. Towards the South they laterally shale out into sandstones (Slochteren), while towards the North they turn to a more fine-grained siltstone (Silverpit). The Ameland member consists of red-brown sandy claystones and siltstones that fade out towards the North. This strata is only identifiable when both Upper and Lower Slochteren are present and remains indistinguishable where they are merged together. The Upper and Lower Slochteren sandstone members bear the gas and cannot be further subdivided. The Hollum member consists of thin bedded red claystones of small thickness that are present locally, below the Lower Slochteren. The Silverpit Evaporite member consists of evaporitic beds of halite and anhydrite that intercalate in the Silverpit formation. Lastly, the "Weissliegend" member consists of white to grey sandstones, resulting from reworked aeolian dunes that are found above the Rotliegend and below Copper Shale.

Thesis outline

This thesis is divided in two major parts. The first part includes **Chapter 2**, where a novel geothermal target is substantiated. The second part, **Chapter 3** to **Chapter 5**, concerns

the study of the Groningen geothermal field starting from outlining the reservoir and assessing the resource, all the way to identifying the economic outlook of the field.

Chapter 2 outlines a new geothermal exploration target for conduction dominates fields. Harvesting higher temperatures at shallower depths due to increased heat conductivity of salt bodies is substantiated as a proof of concept. A salt intrusion is delineated and five thermal conductivity scenarios are used for the lithostratigraphic units to compute the temperature field. The differences in temperature at a depth of 1,600m can be up to 25°C on top of the thickest part of the salt intrusion. Envisioning a suitable reservoir at this location, up to 40% more energy can be extracted causing only a 13% longer recovery time in the field.

Chapter 3 introduces the Groningen geothermal field and assesses it as heat resource. The integrated analysis of seismic interpretation, reservoir engineering and uncertainty generated quantitative results from an ensemble of 4,536 unique, 3D reservoir simulations. Additionally, a qualitative matrix for the Gronigen geothermal system identifies major risk aspects stemming from the uncertainties in the reservoir initial state, reservoir geology and operational parameters. The Groningen geothermal field in Rotliegend sandstone can produce energy of up to 21MW and production can be sustained in excess of 60 years.

Chapter 4 builds on this assessment and presents the geochemical implications of a tighter integration between the geothermal field and the surface heat network. A Model Predictive Control (MPC) is used to predict the seasonal heat demand in real time. This demand pattern is then coupled offline with a 2D reactive transport reservoir model. The model uses 243 iterations to account for uncertainty in pressure depletion, reservoir permeability, production flowrate, injection temperature and pH. The MPC is well suited as a controller of a geothermal system due to its ability to account for several hard constraints. The Groningen geothermal field can be produced at a seasonally variable rate without adverse geochemical effects at the reservoir. Reactive transport is principally affected by injection temperature and pH and the key minerals are Anhydrite and Dolomite.

Chapter 5 complements the uncertainty and findings of the resource assessment and the reactive transport with economic and project development uncertainties of the Groningen geothermal system. A probabilistic techno-economic model is developed. Using 20,000 iterations the economic indexes of Levelised Cost Of Heat (LCOH), Net Present Value (NPV) and Expected Monetary Value (EMV) are employed over a 40 year project period. The EMV exhibits a 50% chance for marginal profits and a 90% chance of 18M€ deficit. The LCOH is principally affected by geological and operational parameters.

Finally, **Chapter 6** discusses the overview and the synthesis of the potential for geothermal energy in the province of Groningen. Moreover, a reflection and future outlook is presented with regard to this and future geothermal energy developments in the Netherlands and beyond.

Chapter 2

Higher energy recovery at shallower depths

This chapter is published as:

Daniilidis, A., Herber, R., 2017, “Salt intrusions providing a new geothermal exploration target for higher energy recovery at shallower depths”, Energy, 118, 658-670.

Abstract

Direct use of geothermal energy can present challenges of financial feasibility in a low-enthalpy setting. The average temperature gradients in sedimentary basins make it necessary to reach larger depths for meaningful heat production, thus increasing the drilling cost. Therefore, full realization of geothermal projects in low-enthalpy environments has been difficult and not widely deployed. The concept of harvesting the positive temperature anomalies caused by the increased heat conductivity of salt bodies could enable access to higher temperatures at a shallower depth, thus reducing the necessary depth of drilling. In a potential site in NE Netherlands, temperature differences of up to 25°C close to the top of a salt body are modeled. Substantiating this concept, we show that the energy benefits can result to up to 40% more energy extracted, while the temperature recovery of the field is only prolonged by 13%. This opens up new possibilities for geothermal applications in sedimentary basins.

Introduction

The use of geothermal energy for industrial or domestic purposes has been the subject of scientific focus in various different contexts (Alberg Østergaard et al., 2010; Atlason and Unnthorsson, 2013; Mathiesen et al., 2012). However, direct use of energy from low-enthalpy geothermal sources can present challenges for financial feasibility, especially in areas where shallow, high temperature conditions are absent. The average geothermal gradient in sedimentary basins and the economic competition with fossil fuels are the main reasons for these challenges. In sedimentary basins, drilling has been identified as the highest cost contributor for geothermal projects (Barbier, 2002; Beckers et al., 2014; Goldstein et al., 2011b; Johnston et al., 2011), whereas the possible thermal energy output is largely determined by local temperature gradients and reservoir characteristics (van Wees et al., 2012). The above-mentioned challenges could be overcome by harnessing the energy channelled through the high heat conductivity of salt bodies (Geluk et al., 2007), giving rise to locally higher temperatures at shallower depths, thus reducing drilling costs. This principle could outline potential geothermal targets through regional models using data generated by the hydrocarbon industry. Uncertainty remains pertinent despite high data availability in mature hydrocarbon basins (Daniilidis et al., 2016). Nonetheless the use of such data has been exemplified in different geothermal contexts before as a means to identify geothermal potential (Trumpy et al., 2016). In this paper we substantiate the concept of harvesting the positive thermal anomalies caused by the heat conductivity of salt in the Eemshaven area in the NE Netherlands.

Salt bodies have a lower density than most rocks below 500m burial depth (Geluk et al., 2007). When pressure levels exceed the formation strength, salt behaves in a visco-plastic way (Zhang et al., 2013); through this process, called halokinesis, salt flows towards the surface creating various structural shapes (Strozyk et al., 2014). After halokinesis took place in Permian (Zechstein) evaporite sequences in the North of the Netherlands (de Jager and Geluk, 2007; van Gent et al., 2009), several salt intrusions and domes have formed (Strozyk et al., 2014).

In sedimentary basins, away from tectonic plate margins and in the absence of significant crustal extension, the heat flow maintains its average continental plate values (Pollack et al., 1993). In such settings the geothermal gradient is dominated by conductive processes (Moeck, 2014; Scheck-Wenderoth et al., 2014) if significant vertical heat convection through fracture systems is absent (Ondrak et al., 1998). The importance of conduction in the temperature distribution has also been identified in regional studies within the Southern Permian Basin (SPB) (Agemar et al., 2012; Noack et al., 2013). Consequently, stratigraphic intervals with high conductivity are of major importance for the temperature field.

The thermal conductivity of salt is two to four times higher than that of non-evaporitic sediments (Cacace et al., 2010; Nagihara et al., 1992; Petersen and Lerche, 1995; Nagihara, 2003). Heat is preferentially channeled through the salt, creating positive temperature anomalies around the top of a dome and negative ones at its base (Mello et al., 1995; Vizgirda et al., 1985; Ondrak et al., 1998; Zielinski et al., 2012; Nagihara et al., 1992; Noack et al., 2013).

Higher temperatures found at shallower depths could contribute to a more economically viable utilization of direct use geothermal heat, especially in the low enthalpy context of the Netherlands, which has an average geothermal gradient of 31.3°C/km (Bonté et al., 2012). Salt bodies have been found to influence the temperature gradient of existing nearby gas production wells in the greater southern Permian Basin (Cacace et al., 2010; Kaiser et al., 2013; Mello et al., 1995; Ondrak et al., 1998; Zielinski et al., 2012), as well as within the Netherlands (Bonté et al., 2012). Modelling of salt intrusions in Northern Germany, within the same basin, has also linked them to increased temperature levels (Agemar et al., 2012).

However, most studies examine an areas of tenths (Magri et al., 2008; Mello et al., 1995) , hundreds (Agemar et al., 2012; Bonté et al., 2012; Cacace et al., 2010; Kaiser et al., 2013; Zielinski et al., 2012) and sometimes thousands (Scheck-Wenderoth et al., 2014) of km with the underlying layer geometry sometimes based on large regional models. Such models are very insightful and identify temperature field anomalies on a larger scale. Nonetheless studies at a smaller scale could highlight details that are either missed or not pronounced in large regional studies. Using high resolution 3D seismic data for the geometry modelling and constraining the simulations with a temperature map as a lower boundary can increase the resolution of the temperature field. Such smaller scale models can help bridge the gap between the large scale regional models and models targeted at field development.

In this research, we substantiate the concept of harvesting higher temperatures at a shallower depth due to the increased heat conductivity of salt bodies. The energy benefits and possible economic impact of a direct-use geothermal installation is presented. To this end, 3D seismic data were used to delineate a salt body located in the North of the Netherlands above the currently producing Groningen gas field. Based on structural interpretation we have constructed a geological model of the salt body, covering an area of 5 km^2 at depths ranging from 1.6 to 2.0 km. At these depths, temperatures of ca. 65°C are predicted based on the average geothermal gradient. Using the geological model the specific temperature field has been calculated, using five thermal conductivity scenarios for the lithostratigraphic units. Furthermore, the effect of the computed temperature field on the performance of a conceptual geothermal aquifer positioned at the top of the salt

structure is analysed. Lastly, a comparison is made with an aquifer positioned in a standard geothermal gradient for the basin.

Background

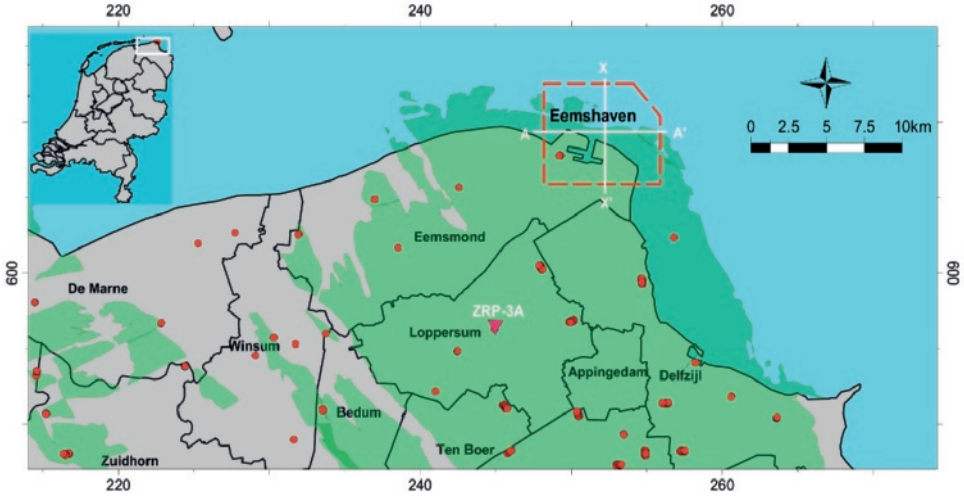

Figure 2.1 Study area in the North of the Netherlands. Axes are based on RD-New system coordinates, converted to distance (km). Red dots depict surface locations of existing gas wells, the black lines depict municipal borders and the coast line and gas fields are indicated in light green. The dotted red line outlines the area of interest around the Eemshaven port, where demand for geothermal heat is present. The cross section X-X' is presented in **Figure 2.2**, and cross section A-A' in **Figure 2.3**. Distributed Temperature Sensing (DTS) data of the ZRP-3A well are presented in **Figure 2.6**.

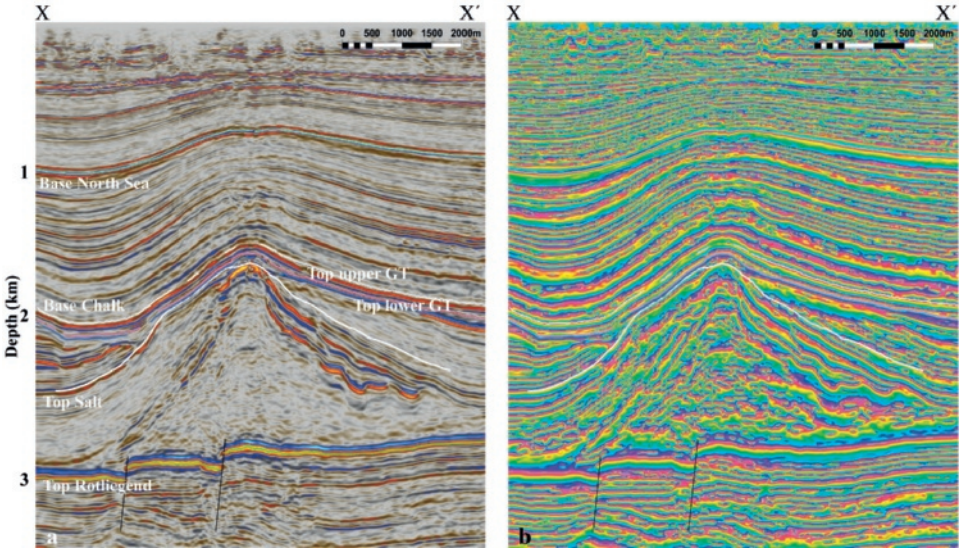

Figure 2.2. Section X-X' from **Figure 2.1** showing (a) seismic data and (b) instantaneous phase attributes. The abbreviation GT stands for the Germanic Trias group

The operator of the Groningen gasfield (NAM), provided the 3D Pre-Stack Depth Migrated (PSDM) reflection seismic data which were used for seismic interpretation. Crossline and inline interval is 25m, the vertical sample interval is 4m and the data reach to a depth of 4km. The available seismic data extends over an area of 27km by 26km, but interpretation focusses on the harbour area where there is demand for heat (**Figure 2.1**). Seismic interpretation was carried out on top and base horizons of the main geological units using Petrel (Schlumberger) supported by 3D autotracking (**Figure 2.2**a).

Furthermore, borehole lithostratigraphic data from 63 nearby wells (see Appendix A), publicly available from NL Olie-en Gasportaal (NLOG, 2014), were used to further constrain the geological model. To aid the interpretation of the salt, seismic attributes of Instantaneous Phase (**Figure 2**b), Amplitude Contrast, Relative Acoustic Impedance, Variance and Chaos were computed from the original seismic dataset.

Structural model

Geology

In the area of interest, a salt ridge was identified with a thickness of up to 1500m (**Figure 2.3**c). Within this area, the top of the salt exhibits a depth range between 1,600m and 2,000m covering circa 5 km^2 (**Figure 2.3**b). The geometry of the salt dome tightly matches the regional model by Strozyk et.al. (2014) for the Groningen High region. Furthermore, the shape of the salt ridge correlates strongly to the fault orientation in the underlying Rotliegend (**Figure 2.3**d). The salt structure is up to circa 1,000m thicker above the faulted Rotliegend basement, while it drops to its normal stratigraphic thickness of 500m to 600m away from the faults (**Figure 2.3**c). The halokinetic process therefore appears to have been triggered by fault movements, which is often seen elsewhere in the basin (Maystrenko et al., 2005; Geluk et al., 2007; Geluk, 2007a).

The presence of an anhydrite layer was interpreted within the salt ridge (**Figure 2.3**a). The layer was correlated with well data in the area and identified as the ZEZ3A formation. The anhydrite layer corroborates both the geometric shape, as well as the parallel to sub-parallel relation to the top of the salt in the area of the Groningen High; the anhydrite is closer to top salt in the upper parts of the salt body than on the sides (Strozyk et al., 2014). Due to its strong seismic reflection signature, the layer can be used as a phantom where the top salt reflection is weak.

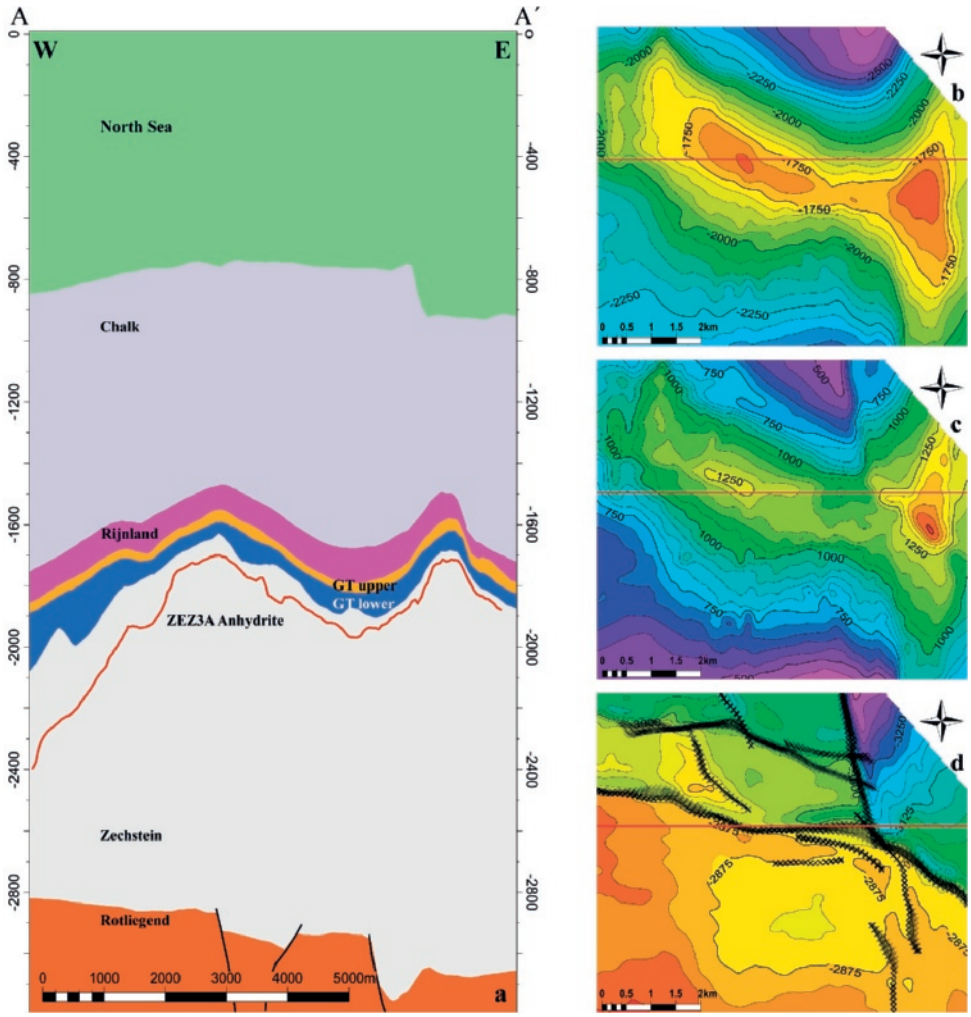

Figure 2.3. (a) Geological cross-section (b) top salt depth map, (c) salt isochore thickness map and (d) top Rotliegend depth map. Red lines on figures (b, c, d) indicate the location of the cross section (a), while the x marks on figure (d) delineate Rotliegend faults. The area covered in figures b, c and d is highlighted by the red polygon in **Figure 2.1**.The main orientation of the salt dome structure strongly correlates with the underlying Rotliegend faults (WWN-EES). The secondary elongated part of the dome on the east part of figure (b) also correlates with the faults oriented (NNW-SSE). Faults in the Rotliegend are considered to be of Jurassic age, related to the stress fields associated with opening up of the Atlantic Ocean (Pharaoh et al., 2010). Jurassic sediments are eroded at the Base Cretaceous unconformity, while there is another discontinuity between the lower Germanic Trias sediments and the underlying Zechstein salt.

Simulation models

Two types of models are used for the simulations. First a steady state temperature model that calculates the temperature field using different heat conductivity scenarios. One of the heat conductivity scenarios is also simulated using a different grid for comparison

purposes. Following this, and for each steady state temperature model, a sub-model is extracted representing the conceptual reservoir model. Each conceptual reservoir model uses three different production scenarios for energy generation through a doublet setup. The steady state temperature models in combination with the reservoir models provide an overview of the energy generation and reservoir behaviour in all the considered heat conductivity and production scenarios.

Steady state temperature model

A steady state model was built in the PetraSim/TOUGH2 (Rockware, 2014) reservoir simulator. Two different grids were considered to rule out the influence of grid resolution to the results. Both models have been optimized to balance between resolution and computational time. To this end the findings of previous temperature studies were taken into account, where for conductive settings the mesh has been found convergent as long as it manages to resolve the structural complexity (Kaiser et al., 2013).

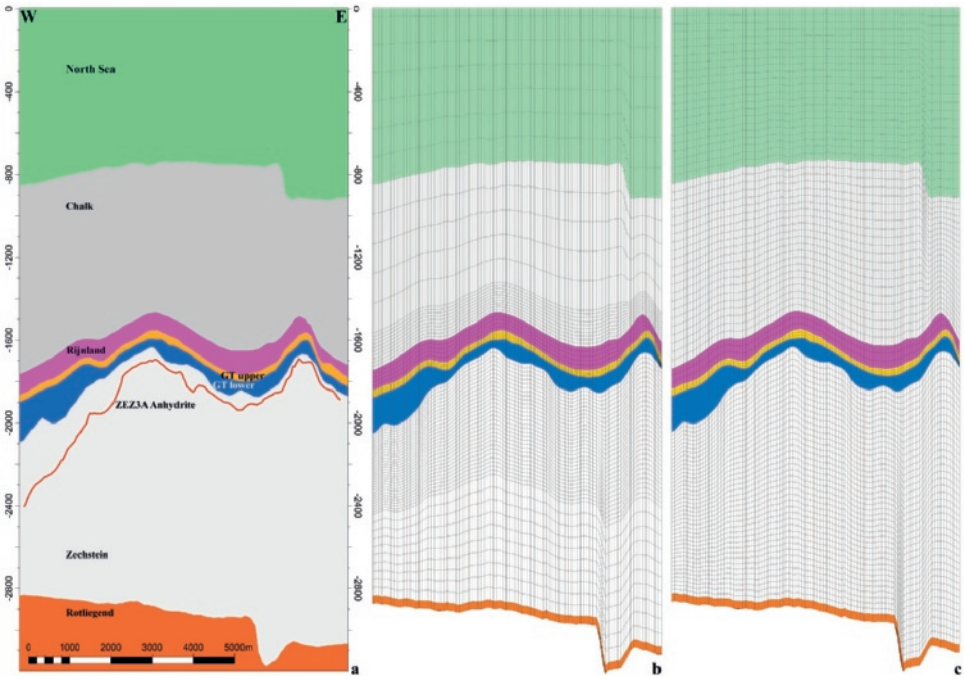

Figure 2.4. Different meshes applied in the steady state models. The geological model constructed in Petrel (a) exhibits a complex geometry above the crest of the dome, as well as thickness variations of the overburden. Nonetheless both the grid 1 (b) and the grid 2 (c) models are able to capture these geometrical variations by closely outlining the changes in thickness. The scenarios were run using the grid 1 model, while the MIN scenario was also run using grid 2 for comparison.

Figure 2.4 illustrates the ability of both models to capture the geometry in one of the most complex parts of the geological model. Horizontal discretization is 93 x 79 cells, while

vertically the model extends from the top part of the Rotliegend to the surface, using the structural framework interpreted in Petrel. The horizons represent the major contacts between the lithostratigraphic groups. The characteristics of both models are presented in **Table 2.1**.

Table 2.1. Architecture and characteristics of the steady state models. The PetraSim grid 1 uses higher vertical resolution around the top of the dome, while the grid 2 model ensures that there are no cells with a thickness larger than 50m. The boundary condition at the base is derived from the temperature map of the top of the Rotliegend in the Groningen gas field (NAM, 2015). Both models do not include faults and use the thermal inputs presented in **Table 2.2**, while their lithostratigraphic inputs and their hydraulic characteristics are presented in **Table 2.3**.

	PetraSim (TOUGH-MP)	
	Grid 1	**Grid 2**
Dimensions	6.9km x 6.0km x 3.3km	
Horizontal discretization	75m x 75m (93 x 79 cells)	
Horizontal cell count	7270	7270
Layers	87	103
Total cell count	623,790	747,162
Lithostratigraphic units	7	
Boundary conditions top	Temperature (10°C)	
Boundary conditions base	Temperature (map)	

Heat conductivities for the lithostratigraphic units were based on literature from comparable temperature models and are summarized in **Table 2.2**. Five scenarios were devised (NOTSALT-MIN-MED-MAX-XTRM) to account for the variation of literature input. In all scenarios, the model was allowed to reach a steady state temperature distribution constrained by the boundary conditions (**Table 2.1**). The structural characteristics of the models are identical for all simulations and only the heat conductivity values are different.

The hydraulic and thickness characteristics of the model layers are presented in **Table 2.3**. The top of the model is formed by ground level so that a temperature boundary condition can be applied. Any convection effects that would require a chemical species characterization to describe thermohaline flow (Magri et al., 2009) are beyond the focus of this study.

Table 2.2. Heat conductivity values found in literature for temperature modelling studies in the greater area of the Netherlands and Germany and values for the lithostratigraphic groups used in the simulations. The data are sourced from: Set 1 (Ondrak et al., 1998), Set 2 (Norden et al., 2008), Set 3 (Fuchs and Förster, 2010), Set 4 (Noack et al., 2012), Set 5 (Mello et al., 1995) and Set 6 (Mottaghy et al., 2011). The extreme and NOTSALT scenarios are devised as the absolute limits that could be encountered. The NOTSALT scenario assumes medium values for all groups and a Zechstein group conductivity the same as the overlying Germanic Trias group. The extreme scenario assumes that all layers have the lowest values of heat conductivity while the

Zechstein layers have the maximum. The MIN, MED and MAX scenarios use the respective data from the above listed sources.

	Literature thermal conductivity values (W/m·k)						**Simulation scenario values (W/m·k)**				
Lithostratigraphic group	Set 1	Set 2	Set 3	Set 4	Set 5	St 6	NOTSALT	MIN	MED	MAX	XTRM
North Sea	-	-	-	-	-	2.3			2.3		
Chalk	1.9	1.8	2.8	1.9	-	2.2	2.1	1.8	2.1	2.8	1.8
Rijnland	2.0	2.0	3.0	2.0	-	2.5	2.3	2.0	2.3	3.1	2.0
Germanic Trias	2.0	2.2	2.0	2.0	-	2.8	2.2	2.0	2.2	3.7	2.0
Zechstein (salt)	3.5	4.5	-	3.5	-	3.1	2.2	3.1	4.0	5.5	5.5
Rotliegend	2.1	3.3	-	2.2	-	4.0	2.5	2.1	2.5	4.0	2.1

Table 2.3. Hydraulic and thickness values of the lithostratigraphic groups. Vertical permeability is an order of magnitude lower (10% of horizontal) than the respective horizontal permeability of each group (Carlson, 2003). The grid 1 model is not equidistant but is refined around the top of the salt dome (see **Figure 2.4**). * a generic reservoir is assumed with a permeability representative of a sandstone body is used in order to evaluate the concept of harvesting the higher heat flow on top of the dome.

Lithostratigraphic group	Horizontal permeability (mD)	Porosity (%)	Thickness		Model layers	
			min	max	Grid 1	Grid 2
North Sea	101.3	10.00	671	1037	7	22
Chalk	0.1	10.00	492	1023	15	22
Rijnland	1.0	12.00	5	166	5	3
Germanic Trias upper	1.0	18.00	2	136	5	3
Germanic Trias lower*	101.3	18.00	1	482	13	11
Zechtein (salt)	1e-8	0.01	404	1551	40	41
Rotliegend	101.3	18.00			1	1

Conceptual reservoir model

The reservoir model has dimensions of 1.5 km by 1.7 km and uses a horizontal discretization of 75m. Vertically, the model extends from the top of the Upper Germanic Trias down to 50 meters inside the salt layer. The layer characteristics remain the same as the grid 1 steady state model (see **Table 2.1**). An overview of the model characteristics

can be found in **Table 2.4**, while **Figure 2.5** shows the outline of the model in relation to the initial state models and the well locations.

Table 2.4. Overview of the conceptual reservoir model characteristics and the production scenarios

	Value
Dimension XY	2391m by 1656m
Depth	1553m to 2204m
Reservoir thickness (min – avg – max)	24m - 62m - 170m
Well separation at reservoir depth	995m
Cell count	14,080
Production scenarios	100m^3/hr - 175m^3/hr - 250m^3/hr
Re-injection temperature	40°C

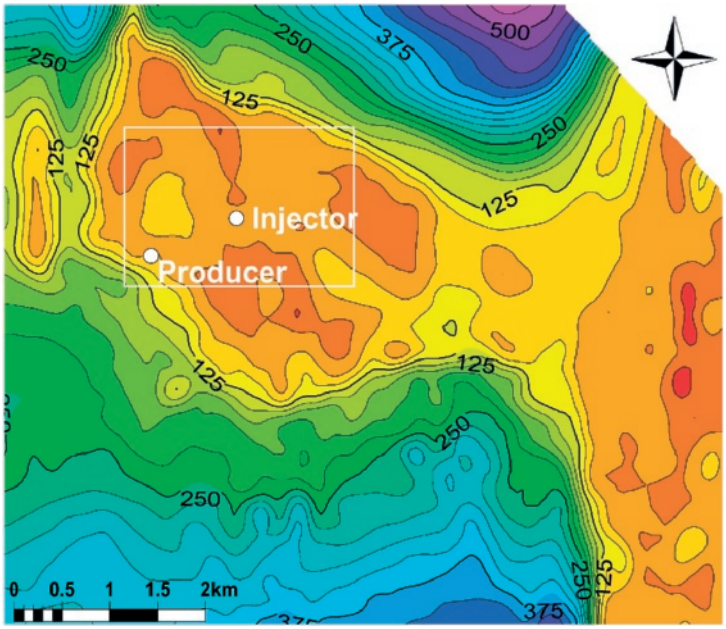

Figure 2.5. Outline of the conceptual reservoir model boundaries, location of the injector and producer well and the thickness of the reservoir (lower Germanic Trias lithostratigraphic layer).

The well positioning takes into account the geometry of the lower Germanic Trias reservoir and ensures as much as possible a continuous reservoir thickness (**Figure 2.5**). The temperature distribution is also considered and therefore, the injector is positioned where the highest temperatures are encountered (see **Figure 2.7**). Production is sustained for 50 years, after which the reservoir is allowed to recover.

Results and discussion

The results of the steady state temperature simulations are presented first. Following, a vertical temperature profile in two locations, a depth slice at the top of the salt ridge and the difference between heat conductivity scenarios on an N-S plane are discussed. Additionally, the results of the dynamic reservoir simulations are discussed. In these, for each conductivity scenario the temperature at the middle layer of the reservoir model is plotted, followed by the producer well temperature over time.

Steady state temperature simulations

Figure 2.6 depicts the steady state temperature model results. The vertical temperature profiles are plotted at two different locations representing the highest (1227m) and lowest thickness (497m) of the Zechstein salt lithostratigraphic group (for overview see **Figure 2.7**). The fixed top and bottom temperature boundaries constrain the possible temperature field solutions to identical top and bottom points for all scenarios in each location. Differences between scenario results stem from the thermal conductivity values used (see **Table 2.2**). Differences between locations can be attributed to geometrical (i.e. thickness) differences of the lithostratigraphic units.

In location 1 we observe two discrete parts of the temperature profile: a steep part through the salt interval and a less steep in the overlying sediments. The steep profile is caused by heat channeled to the surface faster due to the higher heat conductivity of salt and its large thickness in location 1. The two sections of the profile remain discrete for four of the thermal conductivity scenarios and their slopes change at the top of the salt. Only the NOTSALT scenario is not following this trend, due to the heat conductivity of the "salt" layer interval being similar to the overlying Germanic Trias sediments. No model differences between grid 1 and grid 2 are distinguishable, as the MIN and MINGRID datasets perfectly overlap. The XTRM scenario exhibits the highest temperature at the top of the salt, while the NOTSALT scenario exhibits the lowest. The difference between the XTRM and NOTSALT scenarios is up to ~17°C at the crest of the structure (**Figure 2.6**a, see also **Figure 2.8**c). Lastly, it is important to note that even though the XTRM scenario exhibits the highest temperature at the top of the salt, it results in lower temperature levels than the MAX scenario for depths shallower than ca. 1350m. This result could be explained by the lower conductivity of the XTRM scenario layers above the salt compared to the MAX scenario, which leads to higher temperature contrast at the top of the salt but lower temperatures in the overlying layers.

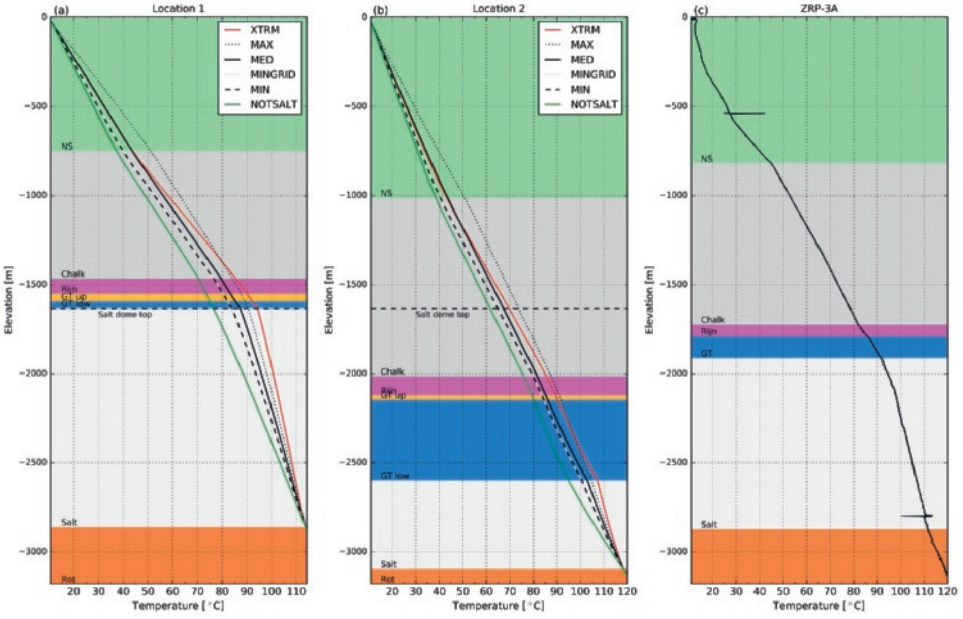

Figure 2.6. Vertical temperature profile at the two locations highlighted in **Figure 2.7**: (a) location 1, (b) location 2 and (c) DTS data from the ZRP-3A well. For ZRP-3A well location see **Figure 2.1**. Background colour highlights the lithostratigraphic group intervals. All scenarios make use of grid 1 except for MINGRID that makes use of grid 2 (see **Table 2.1**). Temperature profiles in figures (a) and (b) stop at the top of the Rotliegend since that is the base boundary of the model.

In location 2 we see a much more linear temperature gradient irrespective of the thermal conductivity scenario. A small change in the angle of the temperature profile can be observed but it is not as pronounced as in location 1 (**Figure 2.6**b). The stratigraphic thickness of the salt is not enough to create a distinct temperature anomaly in location 2. The scenarios show the same order in terms of temperature for a given depth as in location one. Notably, the MAX scenario exhibits higher temperatures than the XTRM scenario already at a depth of ca. 2350m. The model differences between MIN and MINGRID are again not distinguishable, corroborating previous research where horizontal grid resolution was found to be more important than vertical resolution for the conductive field (Kaiser et al., 2013).

A temperature difference of circa 20°C can be observed between the two locations for the same scenario at a depth of 1634m (top of the dome at location 1) as seen in **Figure 2.6**a&b. This difference can be attributed to the different salt thickness between the locations and is present for all conductivity scenarios (see also **Figure 2.7**). Similar temperature levels as location 1 in areas where salt exhibits its bedded thickness (like location 2) are encountered 500-600m deeper.

The ZRP-3A well, drilled as part of the Groningen gas field monitoring program, is situated 15km away from our study area in the same geological setting. The well encounters a salt layer thickness of 960m, which falls between the salt thickness of locations 1 and 2, but closer to location 1 (**Figure 2.6**c). The Distributed Temperature Sensing (DTS) method provides high resolution temperature measurements with little uncertainties (Hermans et al., 2014). The ZRP-3A well DTS temperature measurements clearly depict the steeper temperature flow through the Zechstein layers. The steepness of the slope through the salt is between the MED and MAX scenarios for location 1.

Figure 2.7 depicts the temperature of a depth slice at 1600m (top part of the salt structure) for all conductivity scenarios. Locations 1 and 2 exhibit the highest and lowest temperatures respectively for all heat conductivity scenarios used (see also **Figure 2.6**). Nonetheless, the temperature values at these locations differ. The NOTSALT (**Figure 2.7**f) scenario represents the absence of the increased heat conductivity of the salt lithostratigraphic interval and can therefore be used as a basis for comparison. The other lithostratigraphic intervals of the NOTSALT scenario have average heat conductivity values (see **Table 2.1**).

For all scenarios, the lower temperatures are situated in the areas of the lowest stratigraphic thickness of the salt lithostratigraphic group. The difference between the NOTSALT and the MIN, MED, MAX and XTRM scenario for low temperatures is 4°C, 7°C, 13°C and 9°C respectively (**Figure 2.7**). The MAX scenario (**Figure 2.7**b) exhibits higher temperatures than the XTRM (**Figure 2.7**a) one, in this case in the areas of low stratigraphic salt thickness. This can be attributed to the contributions from the other layers being higher under the MAX scenario, since all layers use the maximum respective heat conductivity.

Compared to the NOTSALT scenario (**Figure 2.7**f), the difference of the MIN, MED, MAX and XTRM scenarios for high temperatures is 7°C, 10°C, 14°C and 17°C respectively. In the areas around the top of the salt ridge (salt thickness > 1200 m) the temperature differences for all scenarios increase. For these high temperatures the XTRM scenario exhibits the biggest contrast with the NOTSALT base scenario.

Under the MAX heat conductivity scenario we observe a higher overall temperature throughout the domain for both low and high temperature locations compared to all other scenarios. The XTRM scenario only shows higher temperatures than the MAX scenario at the top of the salt structure. The temperature observed in the MIN scenario around location 2 (62°C) is in line with the predicted temperature for this depth (~60°C) for an average geothermal gradient of 31.3°C/km (Bonté et al., 2012) for North Netherlands. The differences between the MIN (**Figure 2.7**e) and MINGRID (**Figure 2.7**d) scenario is not more than 0.5°C. Between these two scenarios some differences on the contours

can be observed in the areas where the lower temperatures are encountered (around location 2), but the grid differences do not alter the overall temperature field

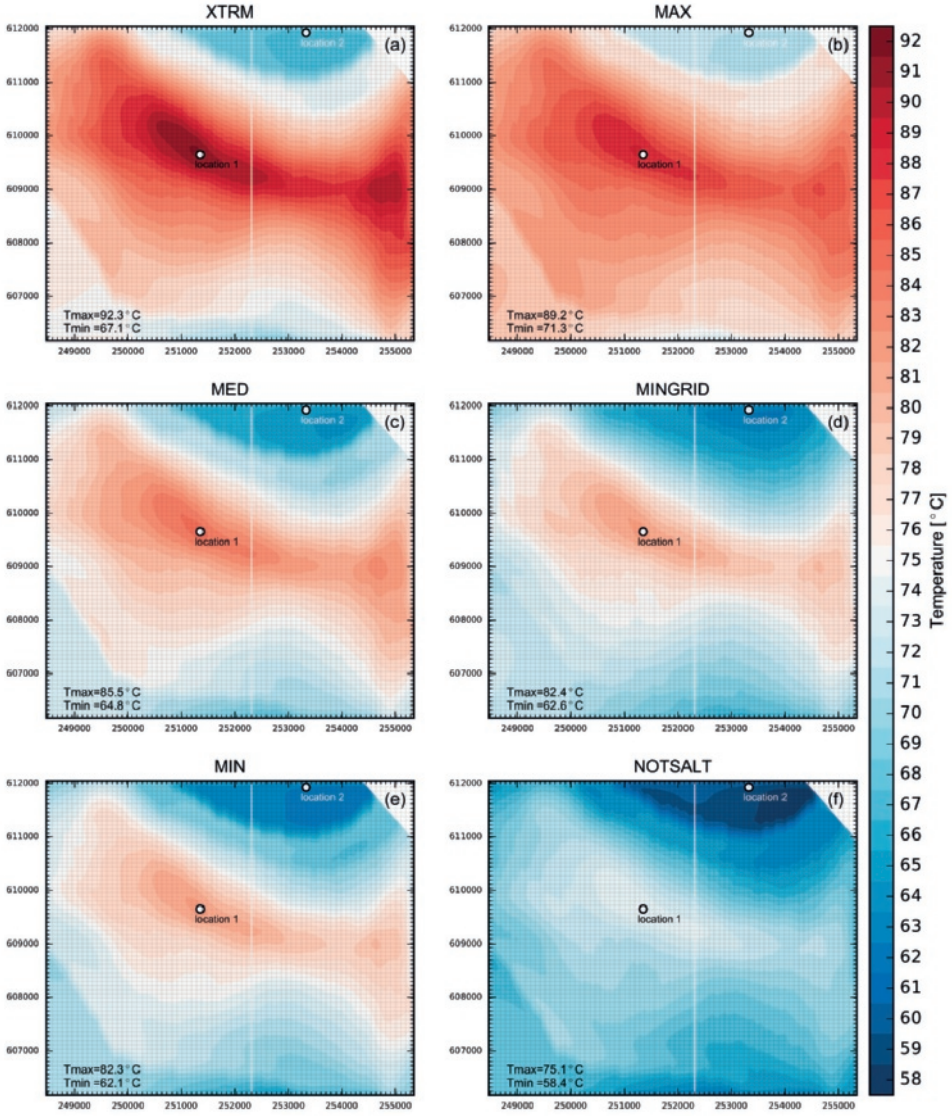

Figure 2.7. Depth slice through the temperature field at 1600m. All plots make use of the same temperature colour legend to allow cross comparison, while the minimum and maximum temperature values for each scenario are denoted on the lower left corner of each plot. The grid lines represent the simulator mesh. The marked locations represent the vertical temperature profiles shown in **Figure 2.6**, while the white line represents the N-S section shown in **Figure 2.8**. All scenarios make use of grid 1 except for MINGRID that makes use of grid 2 (see **Table 2.1**).

At its lowest stratigraphic thickness (location 2) the salt causes a positive temperature anomaly between 4°C (MIN scenario) and 13°C (MAX scenario) compared to the base NOTSALT scenario. In the area of the salt ridge top (location 1) the positive temperature anomaly of the salt is between 7°C (MIN scenario) and 17°C (XTRM scenario). For all scenarios, the temperature distribution closely matches the relief of the top salt surface as depicted in **Figure 2.3**b. Additionally within each individual scenario we can consistently observe a temperature difference of circa 20°C between the highest and the lowest temperature at the same depth. Therefore, this temperature difference stems from the thickness difference in the salt lithostratigraphic interval. The fact that this observation is consistent in all scenarios highlights the importance of the salt layer thickness and its higher heat conductivity in shaping the temperature field.

However, the highest temperature difference does not strictly correlate with the thickest salt (located in the western part of the model) for a given depth level. The shape of the dome there is narrower hence the heat accumulation is not as concentrated as in the elongated, conical shape part of the structure in the centre of the domain. Although the effect of salt thickness is apparent, the geometrical characteristics of salt structures are also of importance. Therefore, thickness alone is not sufficient to predict the temperature field around salt bodies. This could also explain the differences in temperature levels presented here in comparison with previous work (Magri et al., 2008), where differences of 17.5 °C were observed between the top of a salt structure with similar thickness and the surroundings that were undisturbed by the salt intrusion. Nonetheless, deriving a generalized relation between salt thickness and temperature differences would require a systematic examination of an ensemble of salt structures.

Figure 2.8 depicts the temperature difference on a N-S section (see also **Figure 2.7**) between the resulting temperature fields of different scenarios. The MED and the NOTSALT scenario differ only in the salt layer thermal conductivity (**Figure 2.8**d), while the other differences (between XTRM-NOTSALT and MAX-MIN) have different heat conductivity in all layers (**Figure 2.8**e&f respectively). For all plots, the temperature difference between the scenarios is zero at the top and base of the model since the same boundary conditions apply.

The only difference between the MED and the NOTSALT scenario is the heat conductivity of the salt and therefore temperature distribution dissimilarities are solely attributed to this difference (**Figure 2.8**d). The temperature contours stop following the geometry of the Rotliegend basement around a salt layer thickness of just below 600m (**Figure 2.8**a). From there on, the heat anomaly is sharply centred around the contact of the top salt, increasing with thickness.

The difference between the XTRM and NOTSALT scenario is a higher heat conductivity

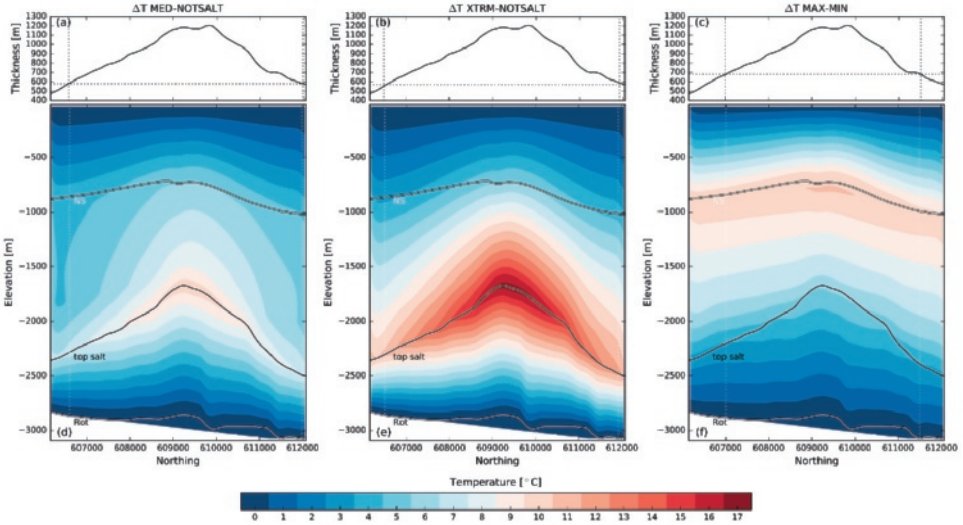

Figure 2.8. Salt thickness (a), (b) and (c) and temperature difference between the MED and the NOTSALT scenario (d), between the XTRM and NOTSALT scenario (e) and between the MAX and MIN scenarios (f) on a N-S section of the temperature model. The N-S section is marked as a white line in **Figure 2.7**. The stratigraphic contacts of Rotliegend, top Salt and North Sea (NS) are marked.

of the salt and lower for all other layers for the XTRM scenario (see also **Table 2.2**). Again, the temperature difference is centred the salt layer (**Figure 2.8**e) and becomes very prominent already at a thickness of about 600m (**Figure 2.8**b). The extent to which this heat anomaly propagates vertically beyond the salt layer is also a function of the salt thickness, since the positive heat anomaly propagates further with higher salt thickness. As a result, it is causing temperature disturbances above 10°C, more than 700m shallower than the top of the salt structure. The peak of the temperature difference between the two scenarios coincides with the crest of the salt structure. The effect of the heat anomaly caused by the salt is amplified compared to **Figure 2.8**d due to the fact that the other layers have lower heat conductivity values than the NOTSALT scenario. As a result, even though the differences show similar patterns centred around salt thickness, the absolute values are higher compare to **Figure 2.8**d.

The relative temperature difference contours between the MAX and MIN scenarios closely follow the flanks of the dome up to a thickness of circa 680m (**Figure 2.8**f). Above this thickness, the temperature domain is affected proportionally by the salt thickness, exhibiting a maximum difference at the top of the structure of 7°C (see also **Figure 2.7**). The largest difference between the two scenarios is observed around the depth of 800m where the temperature of the MAX conductivity scenario is up to 11 °C higher than the MIN scenario. The highest temperature appears to be strongly related to the base lithostratigraphic contact of the North Sea group, which exhibits the lowest heat

conductivity (**Table 2.2**) and is therefore trapping the heat below it causing a thermal blanketing effect. However, a higher temperature field could lead to higher temperatures observed at surface level, making the application of the surface boundary less realistic.

The differences between the scenarios demonstrate a consistency in their results, meaning that temperature field differences of similar level correlate to similar salt thickness (**Figure 2.8**a,b&c). Consequently, salt thickness is the causal mechanism for the temperature field differences, even though the thickness levels are not perfectly matching.

Dynamic reservoir simulations

The temperature of the middle reservoir layer for all different conductivity and production scenarios is depicted in **Figure 2.9**. The temperature levels of the undisturbed surroundings are dictated by the respective conductivity scenario used as input (see **Table 2.2**). The cold front propagation between production scenarios shows very similar patterns, but the front propagates progressively further moving from the XTRM to the NOTSALT conductivity scenarios (top to bottom) for the same production level. Nonetheless, the XTRM scenarios generate circa 40% more energy than the NOTSALT scenario for the same flow rates and about 19% more energy compared to the MIN scenarios. These results are in accordance with a previous parametric study of thermal conductivity effects on power output (Poulsen et al., 2015). Lastly, comparing the mean power generated between the MIN and the NOTSALT scenarios, we see an average increase of about 17%. These findings are in line with previous research where only the initial temperature domain in which the field is situated is important and the thermal conductivity itself appears to be insignificant (Mottaghy et al., 2011).

Producer well temperature shows a decline analogous to the production scenario (**Figure 2.10**), for all conductivity scenarios. The NOTSALT scenario is able to recover the original temperature of any production scenario faster than the other conductivity scenarios. With the exception of the MAX scenario and regardless of the production level, the higher the initial temperature is the longer it takes for the reservoir to recover. The largest differences occur between the XTRM and NOTSALT scenarios and are 14 years (+12%) for the lower production level and 20 years (+13%) for the highest one. The fact that the MAX scenario recovers its initial temperature faster than the MED one, could be attributed to the higher conductivity of all formations including the reservoir itself. The higher heat conductivity helps the available heat to be redistributed faster, leading to a shorter recovery time, a process that has also been described for different geothermal applications (Templeton et al., 2014). The recovery period of the XTRM scenario is on average ~13% longer compared to the NOTSALT scenario, but the extracted energy is about 40% more. Accordingly, there is almost no difference in the recovery time between

MAX and MIN scenarios, while the extracted energy is about 13% higher for the MAX scenario for the same drilling depth.

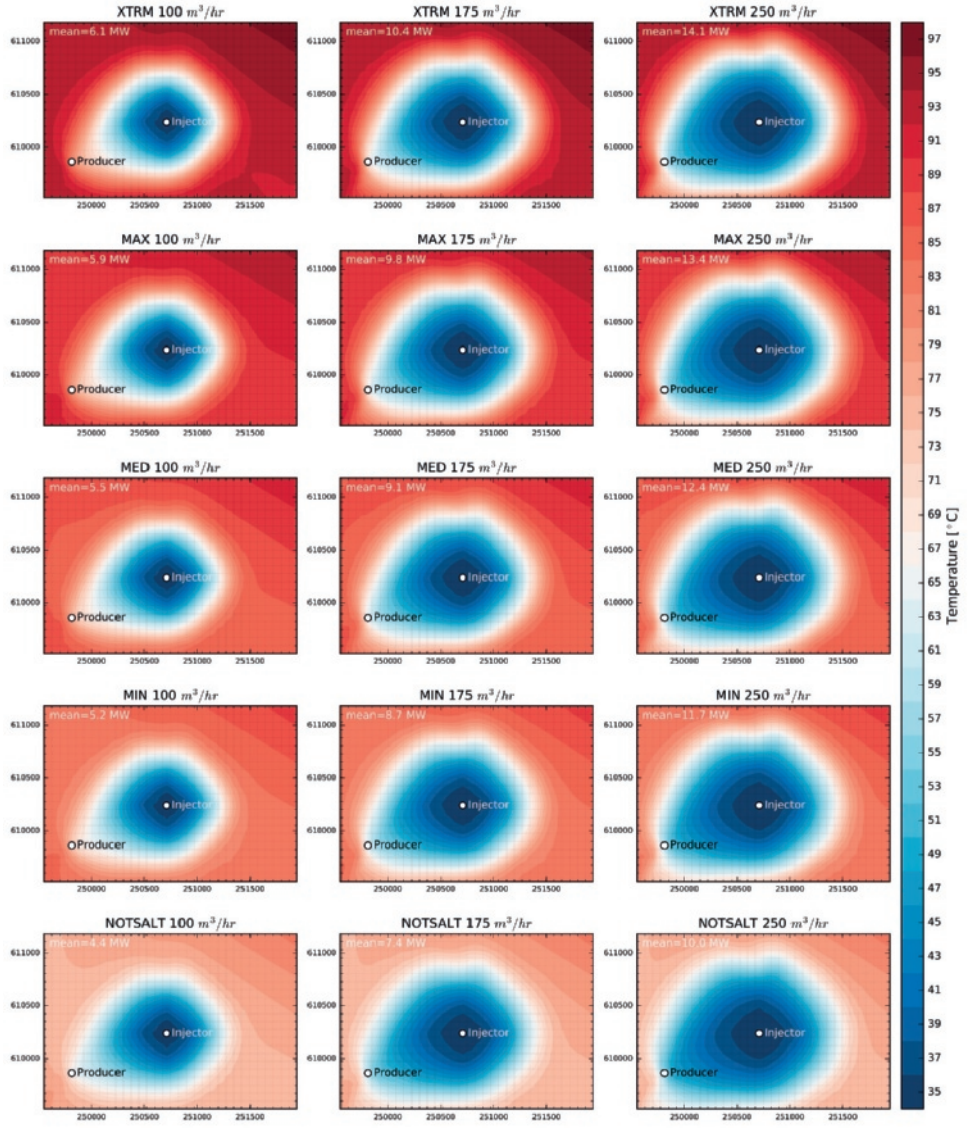

Figure 2.9. Temperature maps of the middle reservoir layer at time t=50years (end of production). All plots make use of the same temperature colour legend to allow cross comparison and the mean thermal power over the production period is denoted per plot.

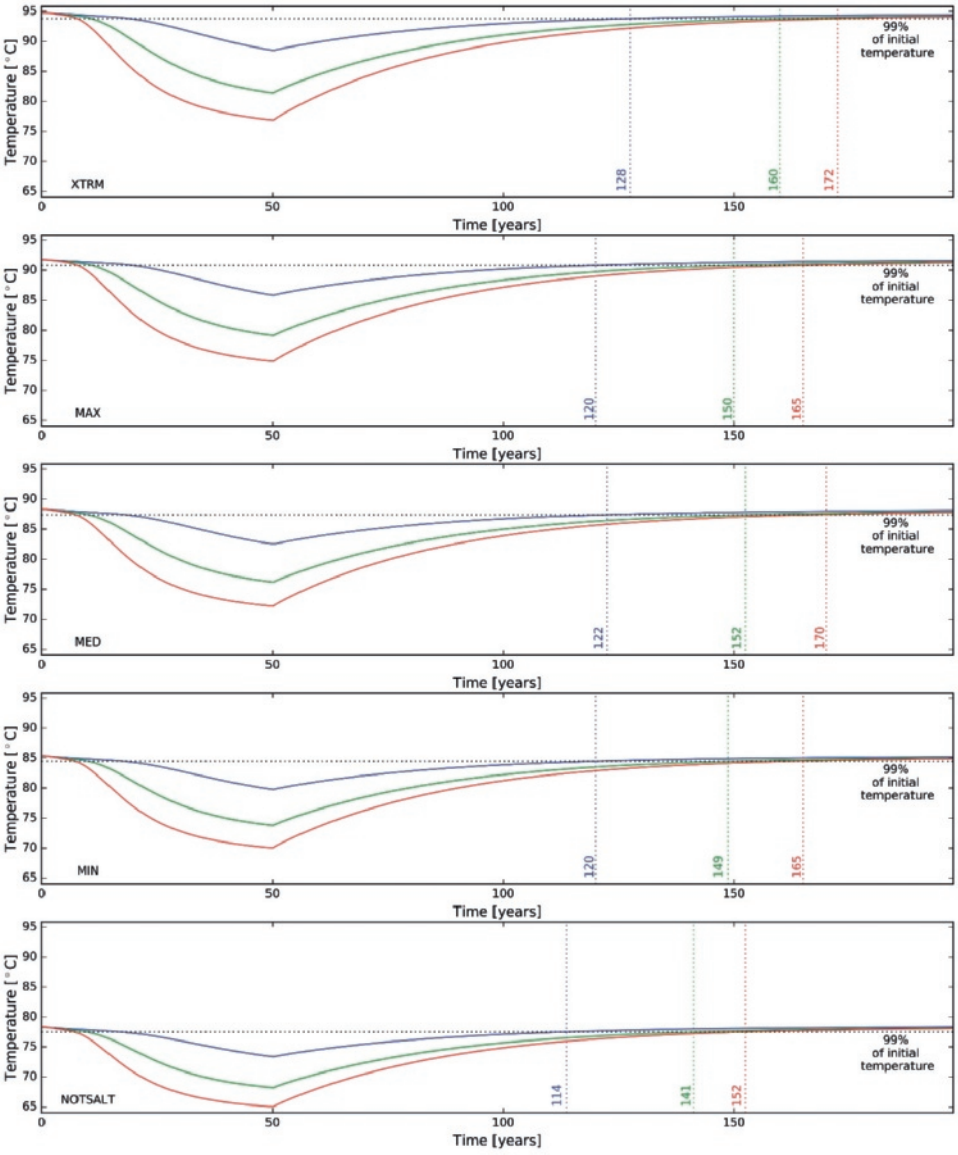

Figure 2.10. Producer temperature for all heat conductivity and production scenarios. The horizontal dashed line marks the level of 99% of the initial temperature. Blue, green and red lines designate a production flow rate of 100m^3/hr, 175m^3/hr and 250m^3/hr respectively. The vertical dashed lines mark the time at which the respective production scenario has recovered its original heat level by 99%.

Possible applications and implications

In several locations, especially in the North East Netherlands (particularly the provinces of Groningen and Drenthe), salt thickness exceeds 800m (**Figure 2.11**). In light of the results presented, these locations could potentially make use of the increased heat flow of

the salt for geothermal applications. Recoverable amounts of energy in these areas would be higher and at the same time the drilling depth required would be around 500m shallower compared to a location without salt structures for achieving similar temperature levels. However, there needs to be an appropriate permeable aquifer above the salt structure. Accordingly, site specific studies should be performed to quantify the available thermal energy amounts to be extracted (Procesi et al., 2015) in these potential interest areas.

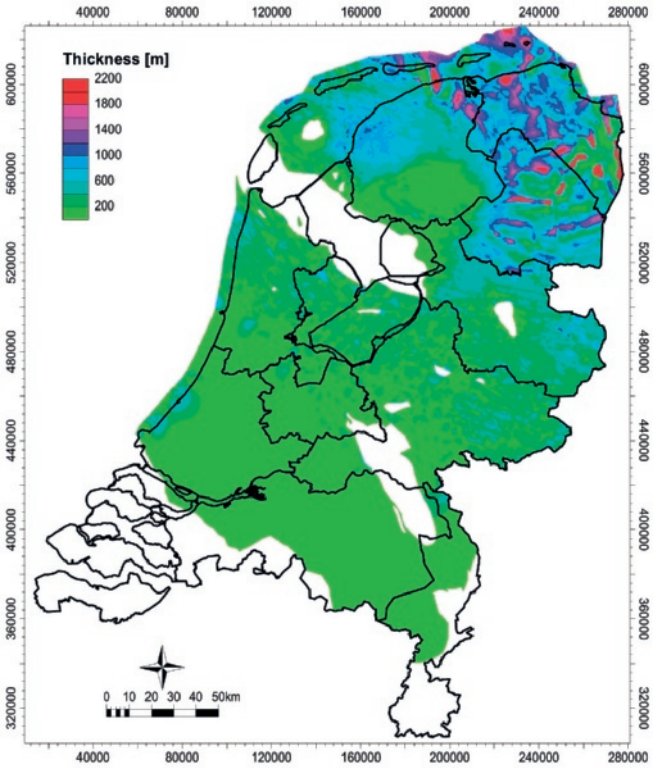

Figure 2.11. Thickness of the Zechstein layer in the Netherlands. Data source: Dinoloket (Dinoloket, 2014).

Conclusions

In this analysis, a new target for geothermal exploration is outlined. Anomalously high geothermal gradients within sedimentary basins in conductive environments can be caused by the increased thermal conductivity of salt. The associated variations in temperature gradients are proportional to the thickness of the salt but this is not the sole contributor to these higher temperature levels. The shape of the salt intrusion is also important.

Five different conductivity scenarios are considered for which the resulting temperature field is analyzed; the results are compared with DTS data from the nearby ZRP-3A well. The analysis reveals a temperature increase between 17°C and 25°C for the same depth between locations with normal stratigraphic salt thickness and those at the top of the salt structure.

The aforementioned differences in temperature levels correspond to a depth of 500m to 600m for the same thermal conductivity scenario. Therefore, these higher temperatures at the top of the salt structure can be more economically reached via drilling. Consequently, the financial feasibility of geothermal projects in conduction dominated settings can be improved.

Moreover, the combination of a sandstone body atop a salt structure is substantiated as a proof of concept for direct use geothermal production. Three production scenarios are evaluated in terms of doublet performance within the aforementioned temperature fields. The considered production scenarios show a range of up to 40% more energy extracted. The resulting increased energy causes only a 13% longer recovery time in the field.

As a continuation of these findings, an economic analysis to quantify the financial benefits from the avoided drilling depth could be envisioned. Furthermore, in the locations where substantial salt thickness (>800m) is present (e.g. the provinces of Drenthe and Groningen), specific studies could identify the presence of a suitable aquifer for geothermal production. Lastly, the overlap between the presence of thick salt layers, a suitable aquifer and demand for geothermal heat could outline favorable locations for geothermal development. The principle can be appropriate for any geological setting that exhibits thick salt sequences or doming and interest for geothermal energy is present.

Appendix A

List of wells used: Uithuizermeeden (UHM) cluster, Uithuizen (UHZ-01), De Hond (HND-01), Bierum (BIR) cluster, Farmsum (FRM) cluster, Delfzijl (DZL) cluster, Borgsweer (BRW) cluster, Amsweer (AMR) cluster, ‘t Zand (ZND) cluster

Chapter 3

Assessing the Groningen geothermal potential and uncertainty

This chapter is published as:

Daniilidis, A., Doddema, L. and Herber, R., 2016. "Risk Assessment of the Groningen Geothermal Potential: From Seismic to Reservoir Uncertainty using a Discrete Parameter Analysis", *Geothermics,* 64,271-288.

Abstract

Geothermal exploitation is subject to several uncertainties, even in settings with high data availability, adding to project risk. Uncertainty can stem from the reservoir's initial state, as well as from the geological and operational parameters. The interplay between these aspects entails irreducible risk prior to exploration drilling. Consequently, it is difficult to construct an indicative qualitative and quantitative depiction of the most prominent facets (e.g. pressure, permeability). This paper shows the classification of known unknowns to risks, while also providing numerical results. Starting from seismic data and arriving at a reservoir model using a discrete parameter analysis we assess the risks and uncertainties of a geothermal project near the city of Groningen (NE Netherlands). By simulating all combinations of the considered parameters, their relative importance can be mapped out. Findings suggest that the unique regime of possible pressure depletion due to neighbouring gas production can highly impact the feasibility of the project. Results demonstrate how an in depth analysis at the exploration phase can direct future efforts towards the most significant elements. Although the numerical results are field specific, the methodology can be readily applied to different locations.

Introduction

The municipality of Groningen has the ambition to realize a deep geothermal development as part of their CO_2 neutrality agenda for 2030. The geothermal source is envisioned as the baseload component of a heat network, serving some 10,000 households. The Permian Rotliegend sandstone is considered as the target aquifer with a proven good reservoir quality, as demonstrated by the nearby Groningen gas field. Based on a preliminary evaluation an exploration license has been awarded to the municipality in 2011 (**Figure 3.1**). Top reservoir depth of the Rotliegend Slochteren (ROSL) sandstone within the license is ca. 3400m, with an average thickness of ca. 250m.

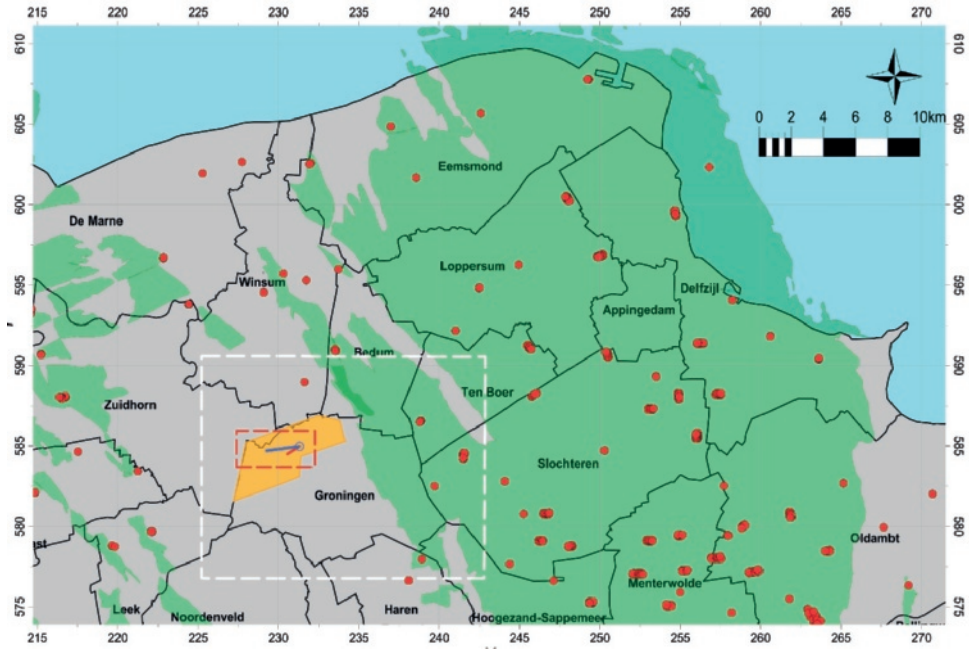

Figure 3.1. Area of interest in the north of the Netherlands. Gas fields are plotted in green, the orange surface indicates the geothermal license, white rectangle indicates the extent of the interpreted 3D seismic cube and the red dashed rectangle outlines the reservoir model. Proposed well trajectories are indicated with blue (injector) and red (producer) lines. Red dots mark the location of existing gas wells, while aggregated dots indicate the presence of a cluster. Map coordinates are in RD

Despite the good 3D seismic coverage and regional well control, some of the critical parameters for the performance of the geothermal doublet (e.g. permeability, pressure, compartmentalization, gas saturation) will remain subject to various degrees of uncertainty, irreducible prior to drilling. Several studies have analysed the effect of uncertainties on geothermal output. For low enthalpy fields various aspects have been considered, namely rock thermal properties (Vogt et al., 2010; Mottaghy et al., 2011),

rock properties together with well positioning (Vogt et al., 2013) and more recently flow rate, reservoir characteristics and temperature, injection temperature and well spacing (Saeid et al., 2015). The impact of different parameter uncertainties on power output has also been showcased analytically (van Wees *et al.*, 2012). Pressure profiles in particular are known to present difficulties for accurate simulation (Franco and Vaccaro, 2014).

Methodologically different approaches are applied to capture uncertainty, such as Monte Carlo (Mottaghy et al., 2011; Vogt et al., 2010; Vogt et al., 2013) and parameter analysis (Poulsen et al., 2015; Saeid et al., 2015). Reservoir simulation models are either based on a geological model (Mottaghy et al., 2011; Vogt et al., 2013) or use a representative geometry and a homogeneous, constant thickness reservoir (Saeid et al., 2015).

Five decades of gas production from the Groningen field have resulted in pressure depletion in the field itself and the aquifer in its surroundings (Breunese and van Thienen-Visser, 2014; TNO, 2014). Furthermore, some dissolved gas is also expected to be present in the targeted reservoir. To the best of our knowledge, the joint effect of uncertainty in initial pressure and gas saturation in geothermal doublet performance has not been investigated before.

Thus, this study focuses on the risk assessment of a low-enthalpy geothermal doublet in a Rotliegend aquifer, with consideration of the uncertainties at three different levels: initial aquifer state (pressure depletion and gas saturation), reservoir (rock and fault permeability) and lastly operational (flow rate and re-injection temperature) parameters. A comprehensive discrete parameter analysis makes it possible to consider all potential parameter combinations, analyzing the interaction between them through a numerical model. With this approach the amount of data and simulation time needed is reduced compared to a full Monte Carlo simulation. Furthermore, the analysis is based on a realistic reservoir geometry derived from interpretation of 3D seismic data.

Geological setting and background

The Netherlands is situated in the Southern Permian Basin which has been extensively studied for hydrocarbons (Doornenbal *et al.*, 2010; van Ojik *et al.*, 2011), based on a very large number of wells and seismic surveys (de Jager and Geluk, 2007; Grötsch et al., 2011). The Groningen gas field is the largest in Europe, situated on the crest of the Groningen structural high (de Jager, 2007; Ligtenberg et al., 2011), at depths ranging between ca. 2800m and 3000m (Grötsch et al., 2011). Its presence has led to an extensive exploration of the structural highs in the area, supported by numerous geological, structural and geophysical studies (Grötsch et al., 2011). The largest part of the gas reserves (more than 90%) of the Groningen gas field was generated by Westphalian coals and Carboniferous shales (Laier et al., 1997; van Gent et al., 2009). The gas is trapped in

the Permian Rotliegend sandstone reservoir, sealed by Zechstein evaporites which have been subjected to halokinesis (de Jager and Geluk, 2007; van Gent et al., 2009). The Rotliegend lithostratigraphy is the result of retreats and advances of desert lake systems in several cycles, reworked by aeolian sands (Fryberger et al., 2011; van Ojik et al., 2011). The range of depositional environments broadens towards the North and includes fluvial, aeolian, playa and lacustrine facies (McKie, 2011).

Despite the extensive exploration for gas, the use of the Rotliegend sandstone in the Netherlands for geothermal applications is not widespread. The only project in the North Netherlands region Koekoekspolder, that targeted the Rotliegend sandstone in aeolian dune facies, encountered lower than expected thickness, net-to-gross and permeability values (Henares *et al.*, 2014), the latter attributed to anhydrite cementation.

The Groningen geothermal concession area is located in the Lauwerszee Trough at the western margin of the gas field. It covers a graben of Rotliegend sandstone in fluvial/sabkha facies, surrounded by structural highs, many of which are gas-bearing. Hydrostatic pressure and temperature gradients in the region are well understood (Verweij et al., 2011; Bonté et al., 2012). Nonetheless, the Groningen gas field has been producing since 1963 (Grötsch *et al.*, 2011), resulting in pressure depletion in the field and surroundings (Breunese and van Thienen-Visser, 2014; TNO, 2014). Pressure depletion and accompanying reservoir compaction and subsidence have been identified as the governing processes of recent seismicity events in the region (Van Wees et al., 2014; van Thienen-Visser and Breunese, 2015).

The extent to which pressure depletion propagates through the aquifer beyond the gas field is not well understood, making the pressure levels within the license area uncertain. The pressure regime can therefore be expected to range between hydrostatic (340-350 bar) and a depletion down to 115 bar (current pressure level of the gas field, NAM personal communication 2015). Furthermore, due to proximity to the Groningen and smaller gas fields and the presence of the underlying carboniferous source rock, the aquifer in the considered reservoir target could hold amounts of gas (NLOG, 2015). The percentage of gas in the reservoir remains uncertain but is expected to be mostly dissolved.

Geological uncertainty does not only relate to reservoir quality and characteristics, but also to the sealing or non-sealing nature of the faults which are abundantly present in the area. Some faults are documented to act as flow barriers thus compartmentalizing the Rotliegend reservoirs (Leveille et al., 1997; Van Hulten, 2010; Ligtenberg et al., 2011). Lastly, the effect of the operating conditions and their prediction is essential for designing a geothermal installation and its long-term deployment (Franco and Vaccaro, 2014).

Operating conditions (e.g. flow rate and re-injection temperature) for the Groningen project remain undecided at this point, adding to the uncertainty.

Methods

Overview

Our analysis employs a streamlined workflow from seismic data to reservoir parameter assessment, as depicted in Figure 2. The Petrel software suite (Schlumberger, 2012) was used for seismic interpretation and geological modeling. The PetraSim software (Rockware, 2014) combined with PyTOUGH (Florian Wellmann et al., 2012; Croucher, 2014) scripts was used for the simulations. PetraSim makes use of the TOUGH2 code family that utilizes the finite difference method (Pruess, 1991). The EWASG (Equation-of-State for Water, Salt and Gas) equation of state module was chosen as the most suitable, as it can accommodate three components in the pore-fill mixture, namely water, salt and a non-condensable gas (e.g. CH_4) (Battistelli et al., 1997). The EWASG equation of state was setup to accommodate non-isothermal CH_4 gas in two phase flow with brine.

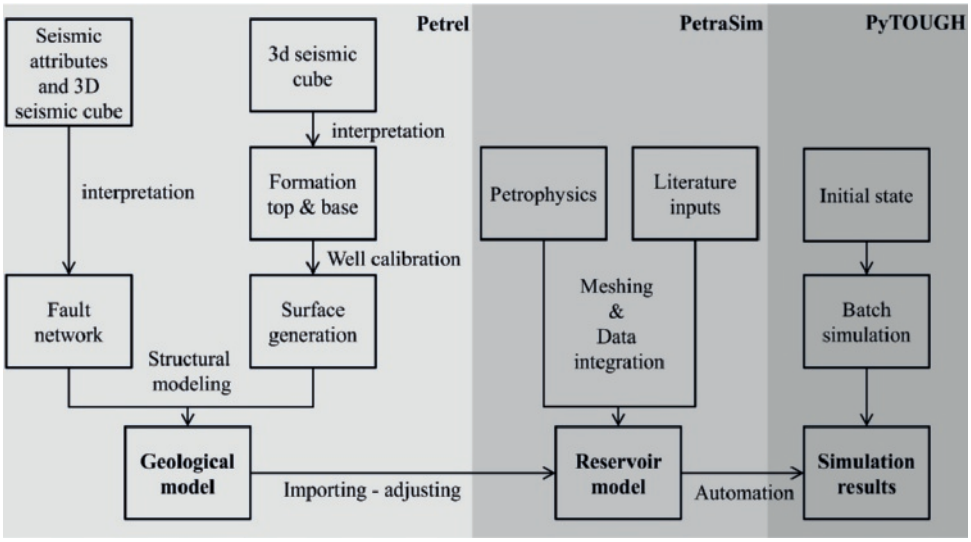

Figure 3.2 Work flow chart overview of the methodology. The PetraSim and PyTOUGH parts are further substantiated in **Figure 3.7**.

The inclusion of all combinations of discrete parameters deepens the understanding of their interrelation as opposed to varying one parameter at a time as in the work of Saied et.al. (2015). The focus is towards the reservoir potential and does not address well bore effects. Well geometry and trajectories are the same for all simulations.

Geological data

Seismic interpretation

A 3D Pre-Stack Depth Migrated (PSDM) seismic cube from NAM (Nederlandse Aardolie Maatschappij BV) was used to interpret the main stratigraphic units in the area. The dimensions of the cube are 17.5km (N-S) by 13.7km (E-W) by 4km (depth). The inline and crossline interval of the seismic data is 25m. Interpretation was carried out every 8th line (200m) in both directions.

The license area covers a surface of 17.9 km^2 where interpretation was carried out every 4th line (100m) in both directions. Interpretation was calibrated with the 22 wells present inside the seismic cube area[1].

Edge detection and dip illumination seismic attributes (**Figure 3.3**) were used together with the original seismic cube to aid fault interpretation, shown in **Figure 3.4**. The Saalian unconformity between the Carboniferous and the base of the overlying Rotliegend group was mapped after flattening the seismic at top Rotliegend. The resulting surfaces and fault planes served as input for the structural framework of the geological modelling.

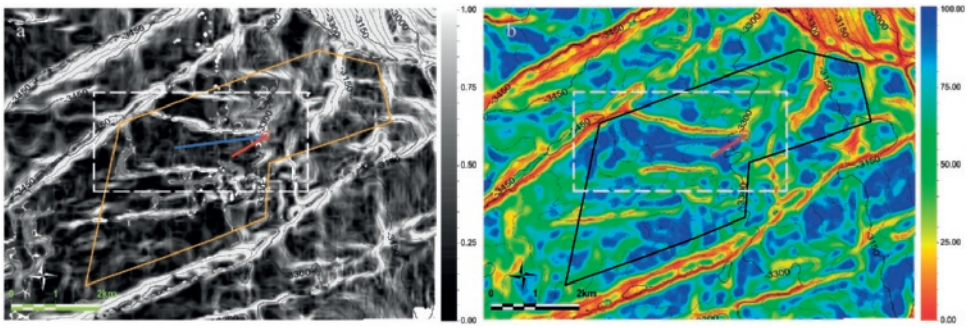

Figure 3.3. Dip illumination (a) and edge detection (b) attributes along the top reservoir surface. Dip illumination reveals signal discontinuities and noisy areas. It uses a gradient decent and dip estimation to compute volume curvature attributes. A search window of 20m with a zero offset was used without a direction. Edge detection highlights surface areas with subtle changes in topography and helps identify discrete sharp edges. This is achieved by a combination of dip and azimuth that is normalized to the noise surface of the signal. Both attributes highlight the fault patterns at top Rotliegend level. The white dotted rectangle outlines the extent of the reservoir model.

The spatial distribution and strike azimuth of the interpreted faults on the top reservoir surface is depicted in **Figure 3.4**a. Most faults have a NE-SW or NW-SE orientation, consistent with previous observations in the area (van Gent et al., 2009). The faults point cloud highlights the presence of sets of faults with conjugate azimuths, most of which show dip angles higher than 30° (**Figure 3.4**b). The prevailing fault orientation suggests

[1] Wells used for seismic interpretation: SAU-01, EKL-01 to EKL-13, HRS-01 to HRS-02-S2, TBR-01 to TBR-04

that N-S fault surfaces are less common. Therefore, sub-seismic resolution faults along the N-S axis between the wells are not likely to be present and well communication should not be affected.

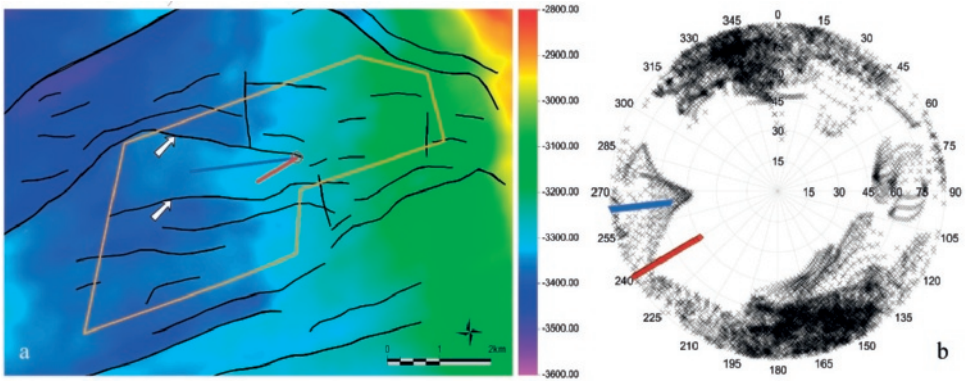

Figure 3.4. (a) top reservoir depth map with fault traces represented by black lines, license area in orange and injector and producer in blue and red respectively. The dominant orientation is NE-SW followed by NW-SE, while a few smaller faults show a roughly E-W orientation. The white arrows mark the two major bounding faults of the reservoir that were included in the simulations. (b) stereonet plot with dip and azimuth of regularly sampled points on the 3D fault surfaces around the concession. Most faults display a dip angle between 90° and 60°. Black marks represent points on fault surfaces while red and blue points represent producer and injector respectively.

Petrophysical data

Petrophysical data for poro-perm values were obtained from Panterra (van Leeuwen et al., 2014). Public data logs (gamma-ray, sonic, bulk density, bulk density correction, neutron porosity, caliper) from 8 wells (EKL-01, NRD-01, PSP-01, ROD-101, SSM-01, SSM-02, SAU-01, TBR-04) around the concession together with core measurements were used to infer layer characteristics within the target Rotliegend reservoir. Gross thickness, net sand, net-to-gross, porosity and P90-P50-P10 values of permeability per well and per layer were provided.

The petrophysical data were aggregated with equal weights of 1 for the wells, except for the SAU-01 well which is most proximal (ca. 4 km) to the concession (weight factor 2). The lack of data for vertical permeability was accounted for in the model by consistently assigning a vertical permeability which was one order of magnitude lower than the respective horizontal permeability (Carlson, 2003). This is a worst case estimate compared to the Kx/Kz ratio of 1.7 usually used for the Rotliegend (van Leeuwen et al., 2014). Angled contacts between deviated wells and reservoir cells are therefore taken into account.

Well location and trajectory

Following the fault interpretation, fault planes were used to extract points with dip azimuth and dip angle of the fault surfaces. Using these data in relation to the faulted

blocks in the license area, the targeted compartment was chosen together with a commercial project stakeholder (Well Engineering Partners, WEP). The objective of the well trajectories was to target the largest non-faulted block in the concession and ensure, as much as possible good communication between injector and producer wells (**Figure 3.4**). WEP further designed well trajectories and casing schemes (Boersma and Brinkgreve, 2014). The producer well trajectory takes into account the possibility of encountering a depleted reservoir, which would require placing the pump deeper in the well. For this reason, the producer exhibits an as much as possible vertical trajectory. The surface location was fixed, based on preliminary arrangements made by the project. Since the focus of this work is on the reservoir, only the well trajectories in terms of downhole targets and deviations were considered in the model. Distance between producer and injector at reservoir depth is ca. 1,250 m to ensure the desired doublet power output is met.

Geological modelling

The geological model includes the full stratigraphic interval from the top Rotliegend (ROCLT) to the base Saalian unconformity (**Figure 3.5**). The Rotliegend dips towards the W-SW with an average inclination of 7% (**Figure 3.4**). The top and base markers were interpreted from seismic together with the interface between the Silverpit formation (Ten Boer member - ROCLT) and the Slochteren members (ROSL) of the upper Rotliegend. The seismic signature of individual members within the reservoir is either too weak or not spatially continuous enough to allow 3D interpretation. Therefore, the weighted gross thickness of the petrophysical layers was converted to thickness percentage based on the interpreted variable thickness of the Rotliegend sandstone. It should be noted that the ROCLT layer of the reservoir is not perforated in the simulations.

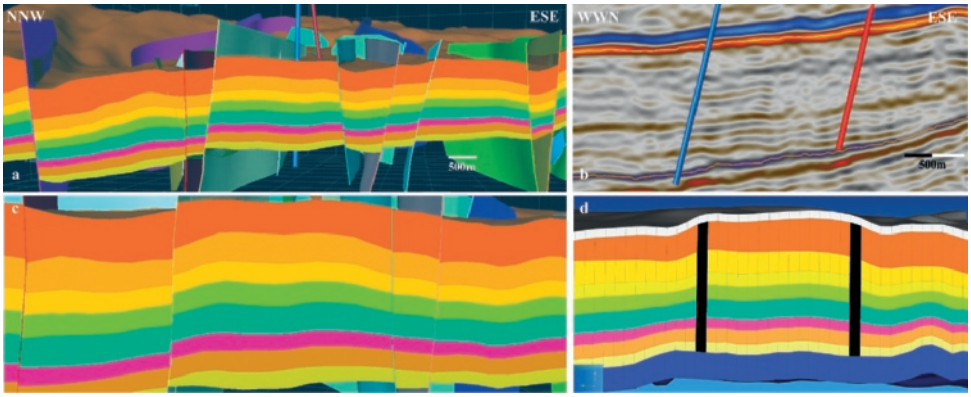

Figure 3.5 (a) geological model of the reservoir, view from W-SW, (b) seismic line along the well plane inside the reservoir. Top reservoir is interpreted in green and the Saalian unconformity in orange. Wells are highlighted in blue (injector) and red (producer) for both figures, (c) close up of the targeted block and (d) the reservoir model of the geological model from (c).

3D reservoir model

All surfaces were imported directly from the geological model. Nevertheless, the juxtaposition of the layers across faults is not maintained in the reservoir model since PetraSim cannot accommodate this. The initial state model domain is 4.85 km by 2.25 km, in a depth range of ca. 2.9 km to ca. 3.9 km (**Figure 3.6**). An overview of the inputs is depicted in **Table 3.1**. The horizontal cell dimension is 50 m x 50 m, while the vertical one is different for each stratigraphic zone, ranging between 24 m and 59 m (**Table 3.2**), which results in a total model size of 47,520 cells. The two major faults which bound the block (**Figure 3.4**) were incorporated in the model with a vertical geometry. Fault horizontal resolution was 50m x 50m to account for the fault influence zone and interpretation uncertainty. The discretization allowed efficient simulation times, while retaining the resolution of the geological model as high as possible. Additionally, this setup is able to accommodate all the different time-steps for the range of parameter values (presented in the next chapters) without causing model disruptions or unreasonable simulation time. In this way all presented results make use of the same mesh specifications and are therefore cross comparable.

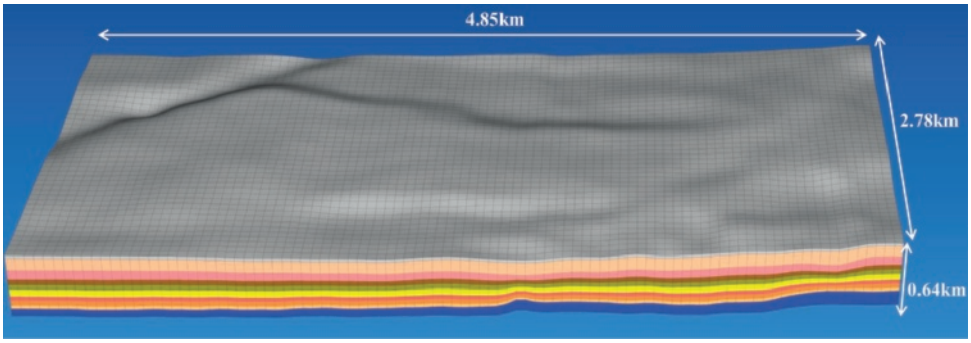

Figure 3.6. Generalized initial state model architecture and dimensions. Grey and blue colors represent the overlying salt and underlying carboniferous basement respectively. Reservoir layers are represented by the other colors.

The generalized initial state is computed based on the pressure and temperature gradients for the study area. All other initial state models are based on this version. Following this, the initial state for each pressure depletion and gas saturation scenario was computed for a 100 years period using a fixed pressure and temperature boundary at the interface between the Rotliegend reservoir and the overlying Zechstein salt. The fixed boundary allowed for the modelling of the pressure depletion values.

A geothermal gradient of 31.3°C/km (Bonté et al., 2012)(see also Appendix A) was used throughout the model, and a pressure gradient of 0.1bar/m for the domain above the reservoir (surface to base Zechstein). The brine in the overburden has a salt mass fraction

ratio of 0.03 and a very low gas saturation (1%.) For the reservoir part, nearby field data values indicated a NaCl concentration of 250,000 ppm (Bolourinejad and Herber, 2015), translating into a mass fraction of 17.31%.

Table 3.1 Initial state main inputs. Other porosity values for faults were also considered (5% and 15%) but proved to have little effect on the results, therefore a middle value of 10% was used throughout the analysis. Wet heat conductivity and specific heat values are based on data from several sources (Ondrak et al., 1998; Muntendam-Bos et al., 2008; Schön, 2011). Reservoir layer porosity and permeability data are detailed in **Table 3.2**.

Lithological group	Density (kg/m^3)	Porosity (%)	Permeability (horizontal) (mD)	Wet heat conductivity (W/m·K)	Specific heat (J/kg·K)
Zechstein salt (overburden)	2170	1	10^{-10}	3.5	1050
Rotliegend (reservoir)	2500-2700	variable	variable	2.9	827
Limburg (basement)	2900	1	10^{-2}	2.65	840
Faults	2800	10	variable	2.9	827

Uncertainty & PyTOUGH automating

Each initial state model consists of a combination of values for pressure depletion and gas saturation (21 versions). The initial state model is further diversified using a unique combination of the reservoir and fault permeability, flow-rate and re-injection temperature values. The set of all possible variations for the given initial state constitutes a batch (**Figure 3.7**).

Due to the number of simulations needed to capture the uncertainty, the handling of the input and result files had to be automated (**Figure 3.7**). The initial state (pressure depletion and gas saturation) for each simulation batch was prepared separately and inspected in PetraSim. After the initial state was prepared, the remaining parameters where automated using PyTOUGH scripts. The flow rate for both injector and producer was kept constant throughout the simulations. Simulation time was 100 years for all instances.

The first two classes (i.e. initial state and geological uncertainty) aim at capturing the uncertainties related to the reservoir conditions and properties, while the last one (operating uncertainty) evaluates the effect of possible development scenarios of the reservoir. All combinations of the discrete values were considered, amounting to 4536 unique full reservoir simulation runs. Data and graphs presented hereafter include all combinations of discrete values for all classes.

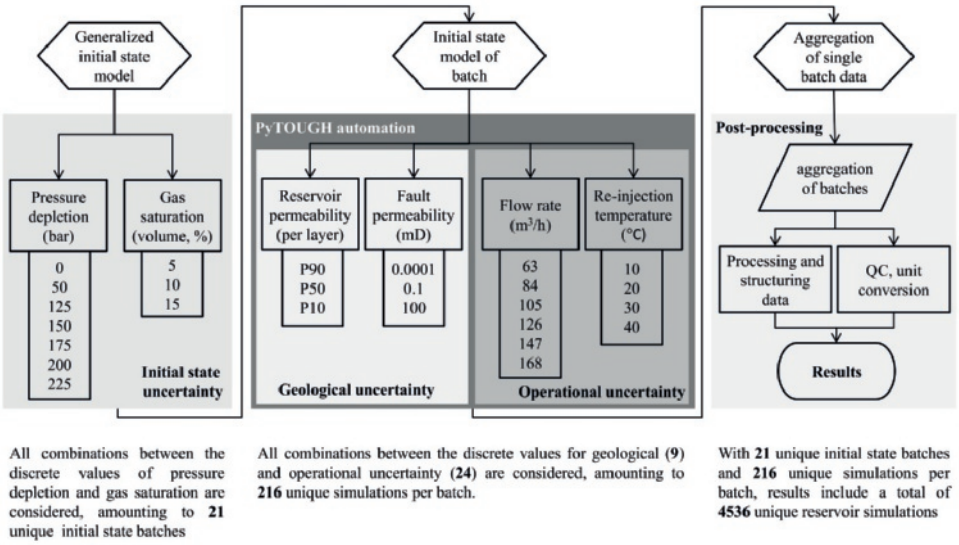

Figure 3.7 Discrete steps followed for the reservoir simulation workflow. Due the amount of data produced by the simulations, only the results on the injector and producer cells were stored and are included in the results.

Different initial conditions were applied to the two domains (inside the Rotliegend reservoir and above it) to accommodate the pressure depletion scenarios. After the initial state of a batch is computed the fixed boundary (pressure and temperature) was removed so that pressure and temperature interactions could take place between reservoir and overburden. Within the reservoir, pressure depletion scenarios were accommodated by using the same gradient as the generalized initial state and a fixed value X for pressure depletion according to the formula Pressure = Z·(X-0.1bar/Z) (Z in m). Gas saturation in the reservoir was assigned three discrete values depending on the scenario, namely 5%, 10% and 15%.

Reservoir permeability values were arranged in three scenarios, namely P90, P50 and P10. The values are assigned discretely per layer based on the petrophysical data as detailed in **Table 3.2** and sub-chapter Petrophysical data. Fault characteristics are divided in three scenarios consisting of a sealing, transparent and conduit behaviour to flow. These scenarios contained three discrete values for fault permeability (i.e. 0.0001, 0.1 and 100 mD). Six discrete values were considered for the flow rate covering a range between 63 and 168 m^3/hr. Lastly, four re-injection temperature values were considered namely 10°C, 20°C, 30°C and 40 °C.

Table 3.2 Reservoir layer characteristics of the Rotliegend Slochteren members (ROSL). Grouping the permeability values in P90-P50-P10 scenarios, the permeability range of influence is taken into account as a worst-middle-best estimation, based on the petrophysical data presented. Any combination of heterogeneity between or distribution within the layers, should fall within the range of these scenarios. Consequently,

capturing further lateral permeability heterogeneity would not help to further differentiate between the range of permeability uncertainty influence and other uncertainty classes considered in the analysis.

Reservoir layer (top to base)	Vertical thickness (m, avg)	Porosity (%)	Permeability		
			P90	P50	P10
7	59	17.4	1	2	9
6	30	18.5	15	48	152
5	34	17.7	14	44	140
4	44	19.5	14	46	153
3	24	17.5	11	35	114
2	32	18.3	3	11	42
1	25	14.9	4	15	48

Results

Model output is subdivided in four main categories: power, pressure, temperature and gas content. These constitute the major areas of interest towards a project realization, revealing the effects of the uncertainty levels on performance and operation as well as in terms of field management. Data from all parameters are depicted in the graphs and together with the sensitivity plots, help to classify the most influential inputs. A small number (159 or 0.035%) of the simulations did not complete successfully (for details see Appendix B). Result data are compiled from the 4377 completed simulations.

Power

The thermal power output of the doublet is mostly controlled by the flow rate (**Figure 3.8**). This is supported by previous researchers (Saeid et al., 2015). The flow rate controlled range of the thermal power output amounts to about +/- 1MW. Differences smaller than 1MW are controlled by the remaining parameters (i.e. pressure depletion, gas saturation and re-injection temperature).

The effect of the re-injection temperature remains important, as the extracted power is always the difference between output and input of power. For the same flow rate, reducing the re-injection temperature results in a power output increase in steps of 0.5MW to 2MW. Higher flow rate levels result in higher increases caused by reducing the re-injection temperature (**Figure 3.8**). This relationship creates a counterbalance between flow rate and re-injection temperature. The same power can be extracted by simultaneously reducing the flow rate by one single step and reducing the re-injection temperature by 1.75 to 2.25 discrete steps. A thermal power of e.g. 10.5MW can be generated with three different combinations of flow rata and re-injection temperature ($84m^3/h$ and 10°C, $105m^3/h$ and 30°C and lastly $126m^3/h$ and 40°C respectively in the case of 100mD fault permeability).

The effect of fault permeability becomes more pronounced over time (**Figure 3.8**). More specifically, sealing faults reduce the affected reservoir volume and lead to an earlier drop in power. This effect is not distinguishable for flow rates up to 84 m^3/hr. From there onwards it becomes increasingly more noticeable and appears to occur earlier in time for higher flow rates. For the highest considered flow rate, the effect of fault permeability is noticeable after 60 years and reduces the output by up to 6 MW, depending on the re-injection temperature.

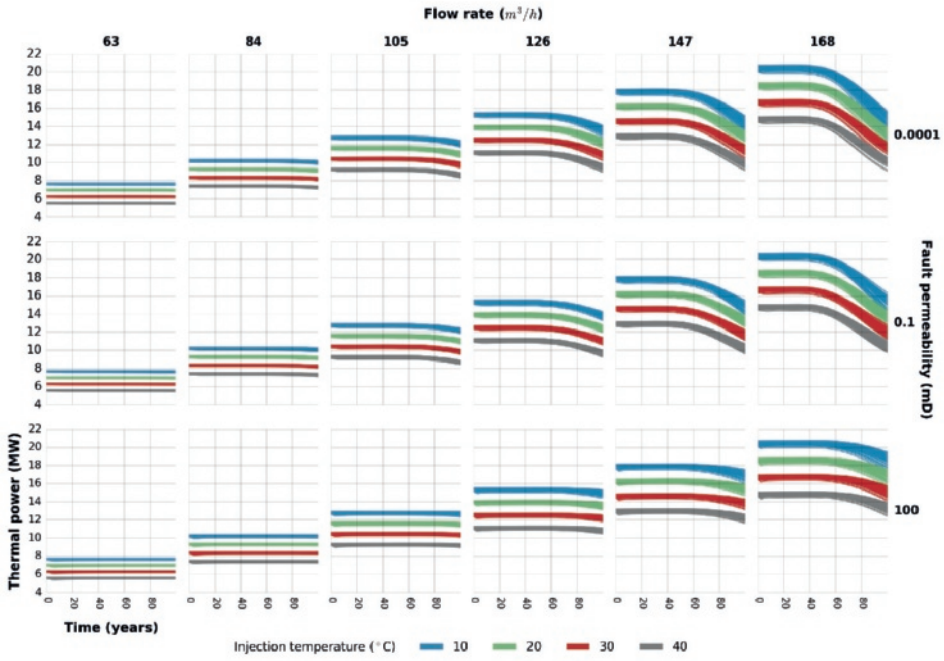

Figure 3.8. Thermal power output (MW) as a function of time, flow rate, fault permeability and injection temperature. "Spread" between the injection temperature effect increases with higher flow rates. Breakthrough occurs sooner (curves bend) with higher flow rates and sealing faults. Permeable faults extend the lifetime of the system.

It should be noted that although pressure depletion has no direct impact on the thermal power output of the reservoir, the reduced pressure implies that more energy will be needed for pumping, hence the net power output or Coefficient of Performance (CoP) will be lowered. Since pressure is a function of depth, the required pumping energy will be proportional to the amount of depletion. This could present technical limitations depending on the design specifications of the pump.

The mean output for each parameter group and respective inputs is depicted for some specified fixed times in **Figure 3.9**. By computing the mean output of each parameter, the sensitivity of the thermal power to each of them is highlighted. It should be noted that

since the parameter values are partly dependent and rather represent a set of combinations, the mean values do not capture the full range of power output as presented in **Figure 3.8**.

The power output is mostly controlled by flow rate, which shows the highest spread in values. Over time the significance of flow rate is diminished, as can be seen from the 100 years data. Re-injection temperature reveals a fairly linear effect on power output which increases over time (30, 65 and 100 years). Nonetheless, the reduction of power output retains a linear relationship until the end of the simulation time. The temporal effect of fault permeability only becomes significant for lower permeability values.

The effect of both initial state parameters (pressure depletion and gas saturation) uncertainties is minor. The temporal effect on output increases, but seems unrelated to the discrete values of the parameters. The lower power output over time for initial state uncertainty can be explained by the other variables, most prominently flow rate.

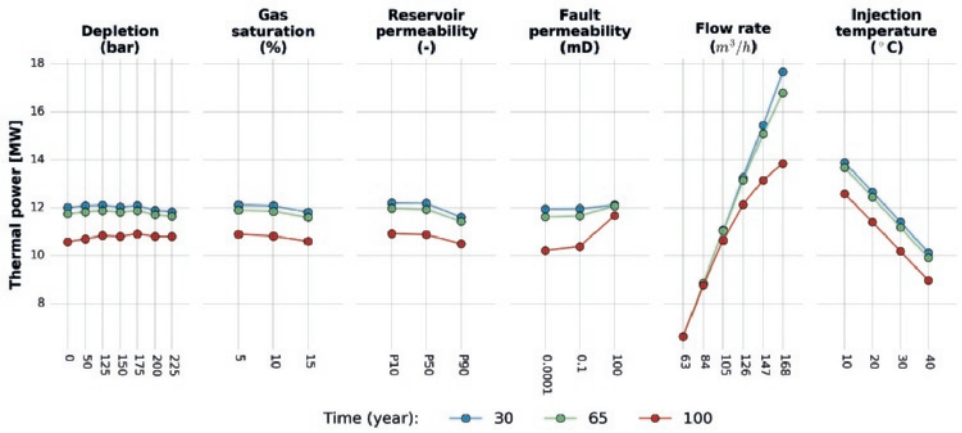

Figure 3.9. Mean values of thermal output (MW) for all uncertainty classes. The co-dependency of the variables causes the mean values presented to be different (lower) than the absolute values of the individual simulations presented in **Figure 3.8**.

Pressure

Power against Δp producer-injector

The pressure difference between producer and injector is indicative of the pumping energy that is required to extract the thermal power from the reservoir. The pressure difference between the wells is mostly controlled by the reservoir permeability, grouping the results in three discrete clusters (**Figure 3.10**a & b). The evolving pressure difference at low reservoir permeability (P90) rises to very high values, up to 500 bar in some instances. For the P50 and P10 clusters this effect is much less pronounced. Within each cluster, a further grouping based on fault permeability can be observed. Lower

permeability faults result in higher pressure differences, although the difference between 0.001 mD and 0.1 mD is not very pronounced, it is still discernible especially over a longer time period (**Figure 3.10**b). This effect is enhanced at lower reservoir permeability values (P90). Consecutively, higher Δp values are observed, while the thermal power output decreases, especially for the high flow rates (**Figure 3.22**b in Appendix C). Alternative cross-plots of the same datasets can be found in Appendix C.

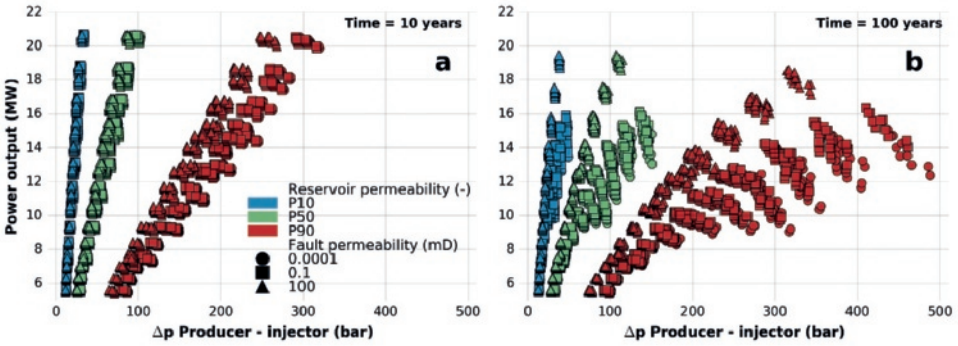

Figure 3.10 Thermal power output against well producer and injector Δp, coded based on reservoir and fault permeability. Two different time interval are shown: 10 years (a) and 100 years (b). A video with a time series animation and a step of 1 year is digitally available.

Δp producer - injector

For lower reservoir permeability (P90) the pressure build up between injector and producer progresses slower but still increases significantly over time. Higher reservoir permeability values demonstrate proportionally faster pressure build up in the first simulation years, albeit with little increase over time. This mechanism seems to be mostly controlled by fault permeability, as a sealed reservoir compartment amplifies pressure development. At low reservoir permeability (P90), highest flow rate (168 m^3/h) and lowest fault permeability the minimum Δp at 100 years is just below 300 bars. Nonetheless, all reservoir permeability values exhibit a similar proportional increase of their minimum values with higher flow rates. Minimum values increase by a factor of approximately five between the lowest and the highest flow rate for the whole dataset.

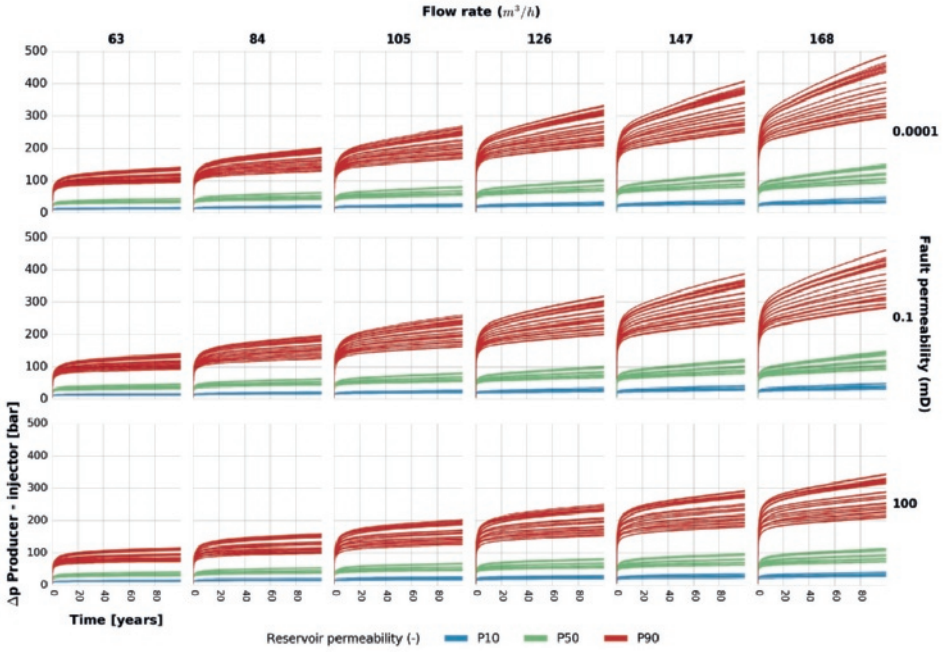

Figure 3.11. Pressure difference between producer and injector as a function of time, flow rate, reservoir permeability and fault permeability.

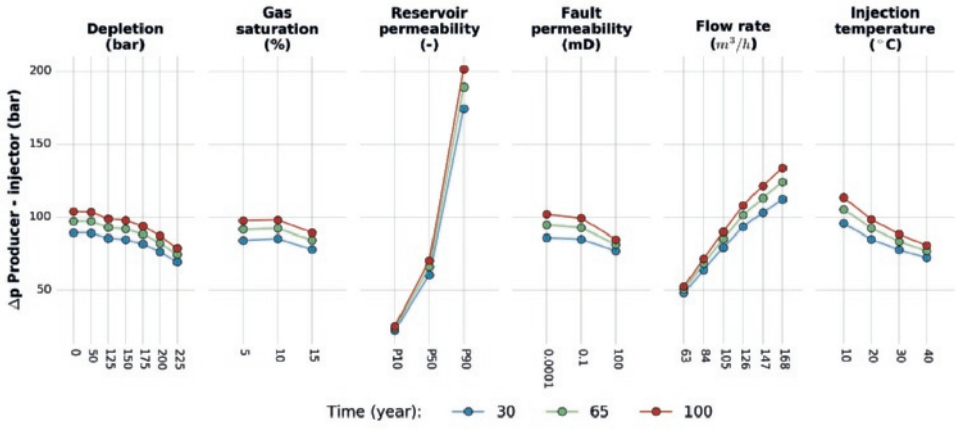

Figure 3.12. Mean values of Δp between injector and producer for all uncertainty classes. Variable co-dependency causes the mean values presented to be different (lower) than the absolute values of the individual simulations presented in **Figure 3.11**.

Within the envelope defined by the flow rate, reservoir permeability and the temporal effect of the faults, further differentiation is invoked by the remaining parameters (depletion, gas saturation and re-injection temperature). The sensitivity of output values

to variation in these input parameters is depicted in **Figure 3.12**. The major influencing factor is reservoir permeability followed by flow rate, as was also evident from the individual simulation results (**Figure 3.11**). These are closely followed by injection temperature. Over time the lower injection temperature values have an increasing effect on the Δp. Pressure depletion and gas saturation follow the same trend. Lastly, the effect of fault permeability is smaller in high permeability faults as pressure is not built up along fault surfaces over time.

Pressure difference between producer and hydrostatic reservoir pressure

Pressure depletion in the aquifer has a strong effect on the performance of the geothermal doublet, since it determines the pumping power required to bring the water to the surface.

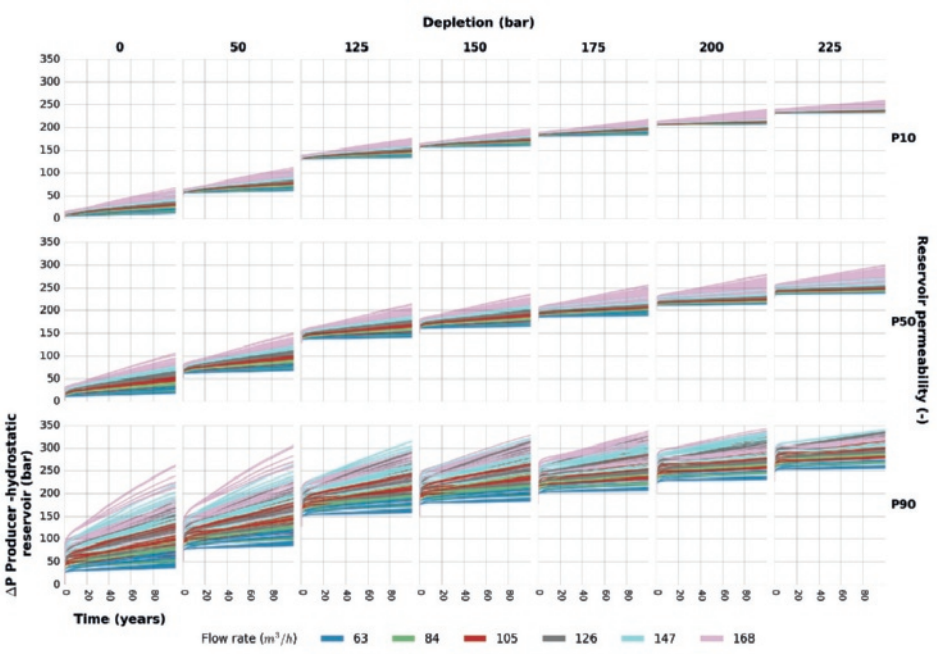

Figure 3.13. Pressure difference between producer and hydrostatic reservoir pressure (no depletion). The pressure values represent the pumping pressure needed in the producer for the water to reach the surface. The lowest value in each subplot represents the equivalent depth at which the pump needs to be installed.

This is analysed with the help of **Figure 13** for a series of depletion scenarios. Using an average pressure of 360 bar (hydrostatic pressure level at the average reservoir depth), the Δp between the producer and the hydrostatic reservoir pressure can be computed (**Figure 3.13**). The absolute pressure values are controlled by the degree of depletion in the aquifer due to nearby gas production in the Groningen field. The flow rate level controls a smaller range for each subplot as the depletion levels increase. The effect of reservoir permeability is a bit more complex. High and medium reservoir permeability

values (P10 and P50 respectively) result in a smaller pressure envelope with a clear stratification based on the flow rate. Low reservoir permeability values (P90) result in a much broader envelope with higher absolute pressure values and significant overlap between the different flow rates. Furthermore, low reservoir permeability increases the pressure drop for the same flow rate, due to the resistance to flow within the reservoir. This results to higher minimum and maximum (increase of both) values per subplot.

The sensitivity of the Δp between the producer and hydrostatic reservoir clearly demonstrates the dominance of pressure depletion (**Figure 3.14**). Reservoir permeability appears to be the second most influential factor with lower values leading to higher pressures. The effect of flow rate is also pronounced, further causing an increasing Δp over time. The remaining parameters of gas saturation, fault permeability and injection temperature have a minor effect.

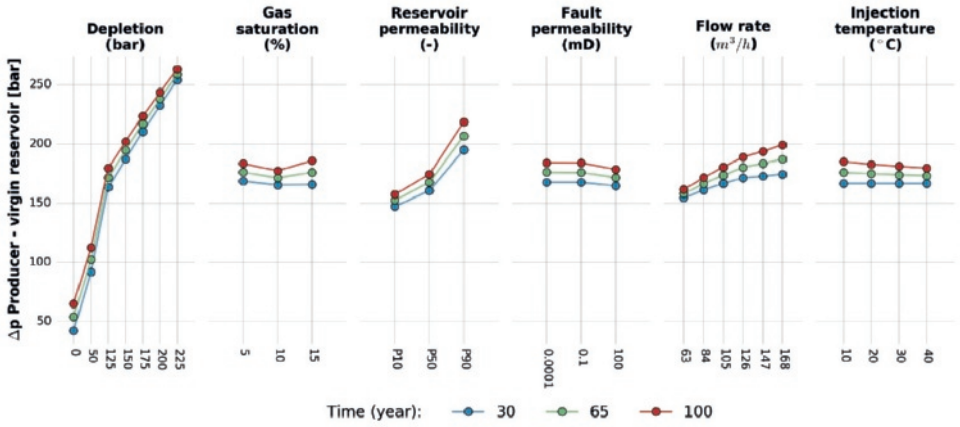

Figure 3.14. Mean values of Δp between producer and hydrostatic reservoir (360 bar) for all uncertainty classes. The pressure difference values in the graph represent the hydraulic head that a producer pump would need to overcome.

Pressure across the fault plane

The maximum pressure build up along a fault surface is presented in **Figure 3.15**. The data show the pressure development between the reservoir compartment and the juxtaposed fault block. The pressure levels are controlled by the combination of flow rate and reservoir permeability. The flow rate has a smaller effect on pressure development for high permeable faults, becoming stronger at lower fault permeabilities. Maximum values increase by a factor 3 for high fault permeability, a factor 4 for medium fault permeability and a factor 6 for low fault permeability. The range of pressures across the fault plane is clustered according to reservoir permeability. Higher differences between reservoir and fault permeability leads to an increased pressure difference.

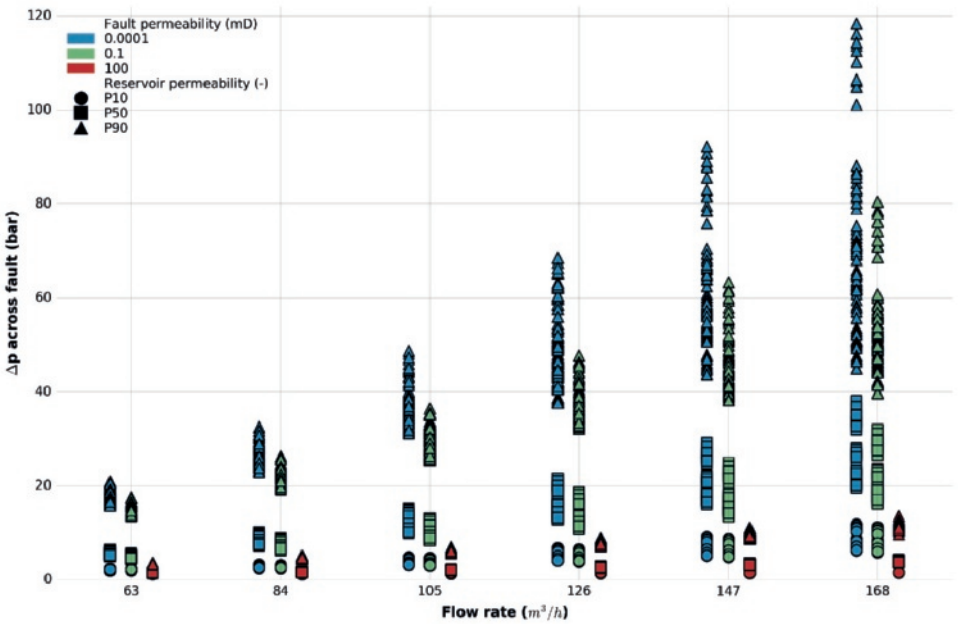

Figure 3.15. Maximum Δp across fault against flow rate. Higher flow rate increases the range of maximum Δp. The effect is smaller for permeable faults and significantly higher for medium and low permeability faults. Reservoir permeability further amplifies this effect with higher permeability values leading to higher pressure values for the same flow rate. The spread becomes smaller for lower permeability values, but remains controlled by reservoir permeability. Data shown are from the cell pair across the fault surface that exhibits the highest Δp after 100 years of simulation.

Temperature

The producer well temperature is indicative of the rate at which the field is depleted of thermal energy. The producer temperature for all 4536 simulations is depicted in **Figure 3.16**. No temperature decrease is observed before 45 years of simulation. Past 45 years, the temperature drops for the higher flow rate simulations. Nonetheless the temperature only drops by about 5°C around 60 years of production and remains higher than 100°C even after 80 years.

The slight temperature increase over 120°C that is observed between years five and forty can be attributed to the additional input of deeper lying layers to the producer well (see **Table 3.2**). These layers have a lower permeability hence the flow through them starts to communicate to the producer at a latter state in time.

As observed from the producer temperature values displayed in **Figure 17**, the temperature doesn't deviate from the initial value of ca. 120°C during the first 30 years

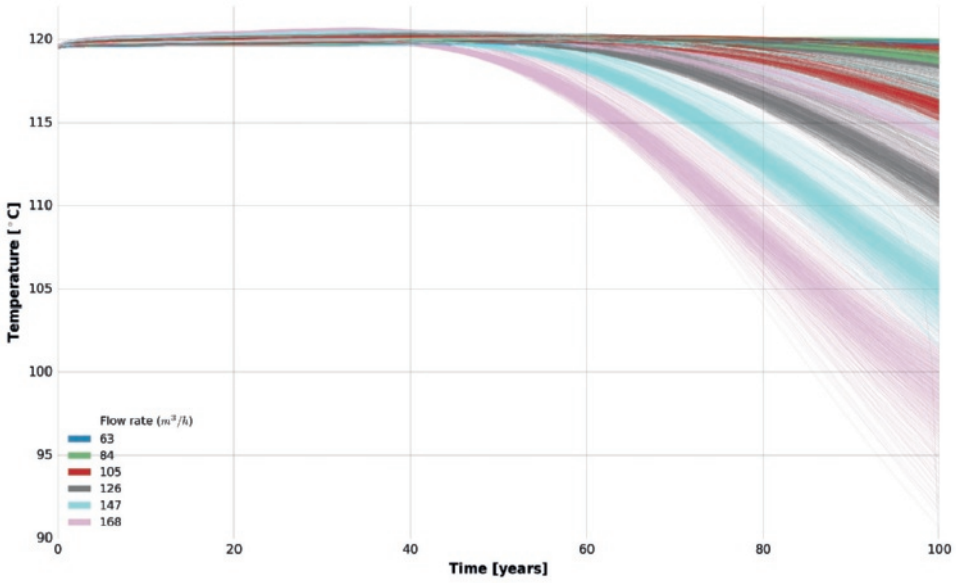

Figure 3.16. Producer well temperature data for all 4377 simulation scenarios. Temperature drops by 10% of the initial production temperature only after around 75 years of simulation. A drop in produced water is not observed in any case before 45 years of production. Breakthrough time is not a significant parameter for the operations design.

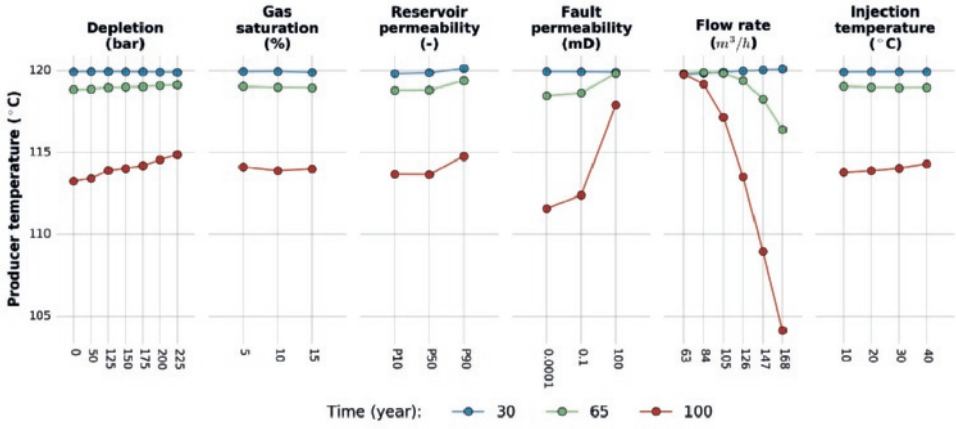

Figure 3.17. Mean values of producer temperature for all uncertainty classes.

of simulation and is not affected by any of the parameters. At year 65 flow rate has the highest impact, while most other parameters, such as re-injection temperature have little to no effect. An exception is the high fault permeability that shows a positive effect, i.e. it does not lead to a temperature drop. After 100 years of simulation, flow rate remains the dominant parameter. High permeability faults do not contain the flow inside the faulted compartment, therefore the rock volume connected to the producer is larger and

temperature remains high for a longer period of time. Over time hydrostatic reservoir pressure reduces the temperature slightly more than strong pressure depletion. Reservoir permeability does not seem to significantly affect the producer water temperature. Lastly, gas saturation and injection temperature seem to have almost no effect to the produced water temperature even after 100 years of simulation.

Gas

Gas production is usually reported in m^3 per day, but for geothermal applications, co-production of gas is more commonly referred to in terms of gas to brine ratio at surface conditions (**Figure 3.18**). Within the range of parameters used in this analysis, the gas production in this setting varies between close to zero and almost 90 m^3/m^3.

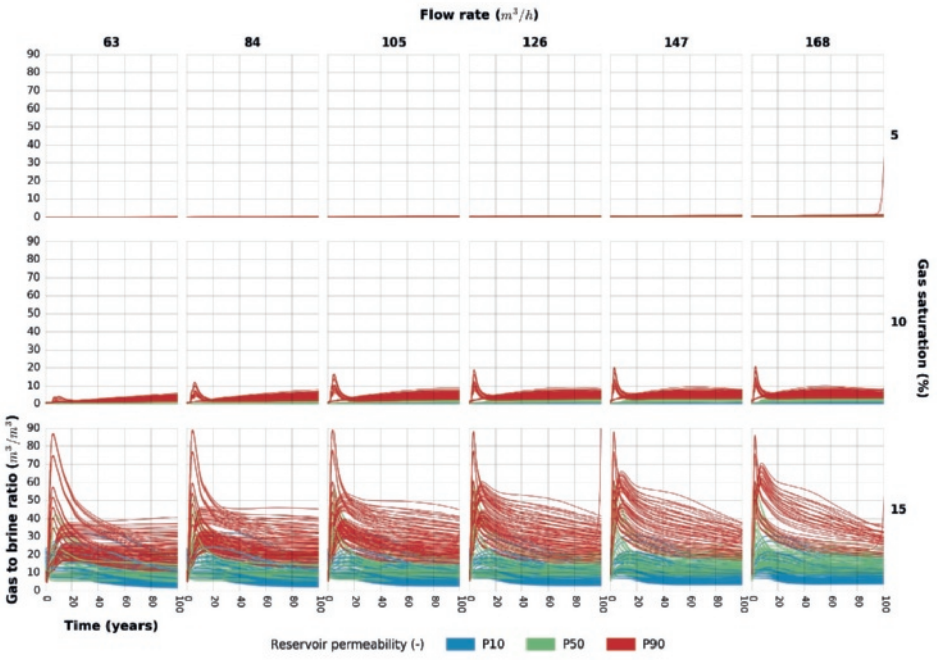

Figure 3.18. Amount of gas m^3 produced for every m^3 of water at surface conditions. Gas saturation has a major effect and more gas is produced at higher initial gas saturation. Production further increases with higher flow rates. The effect of permeability is relatively low for lower saturations but becomes more significant with higher flow rates and gas saturations.

The spike on the all graphs within the first ten simulation years can be attributed to the pressure front from the injector reaching the producer and displacing the gas. This is followed by a drop in gas production which stabilizes over time. Low initial gas saturation leads to minor amounts of gas at the producer well. For the middle and high initial gas saturation (10% and 15% respectively) there is a clear ordering, with lower reservoir permeability (P90) generally leading to higher gas production. Lower reservoir permeability results in a higher gas to brine ratio through the increase of absolute

permeability of the gaseous phase as described by the Klinkenberg effect (Tanikawa and Shimamoto, 2009) which is included in the TOUGH2 code (Pruess et al., 2012). As reservoir permeability increases (P50 and P10), smaller amounts of gas are produced and the gas is not displaced as effectively.

Based on the results of the sensitivity analysis (**Figure 3.19**), the production of gas seems to be the most complex component. Even though the produced gas to brine ratio is dominated by the initial gas saturation, all parameters affect this ratio. The degree of depletion is also crucial, since at a given gas saturation at reservoir level, it determines the volume of the gas at reservoir conditions as well as the expansion factor when the gas is transferred to standard conditions at the surface. Higher reservoir pressure depletion therefore progressively leads to a lower ratio of gas being produced. Low reservoir permeability values help the displacement and production of gas significantly more than medium and high values. High fault permeability also results in higher gas to brine ratios, but over time this effect is minimized. Flow rate has a modest increasing effect up to 126 m^3/hr, after which a lowering and plateau is observed. Lastly, high injection temperature decreases the amount of produced gas over time, while lower injection temperatures cause a smaller reduction.

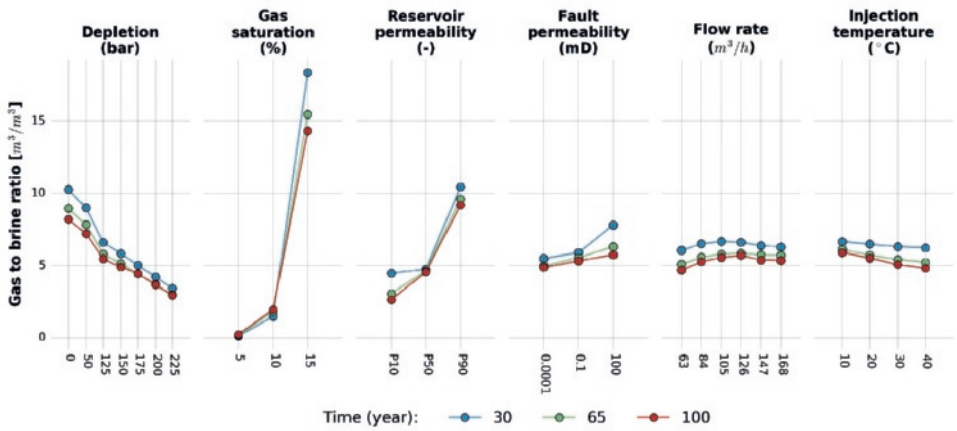

Figure 3.19. Mean values for gas to brine ratio for all uncertainty classes.

Discussion

Uncertainty of the parameters determining the initial state of reservoir and porefill has the largest impact on pressure output between well and reservoir, as well as the amounts of gas produced. More specifically, *pressure depletion* in the reservoir is most influential to the Δp between the producer well and a hypothetical undisturbed reservoir pressure level (**Figure 3.14**). This effectively controls the depth at which the production pump

needs to be installed and may have further implications regarding well trajectory. The producer well trajectory used in this study was designed to accommodate some level of pressure depletion, by means of a vertical hole (down to 2500 m) to allow for the pump installation. Spatial restrictions apply to the surface location of the wells, the optimal target at depth and the extent of the concession which limits the drainage area. Pressure depletion further constricts the installation design. Additionally, the deeper installation of the production pump complicates its design characteristics and even project feasibility. Furthermore, the reported Δp here might even be higher when a finer mesh is used in the model around the wells to better capture near wellbore effects and the dynamic level of the water table. It should be noted that if pressure depletion is present in the aquifer, it will progress during the production period (Van Wees et al., 2014) since the causal mechanism (gas production in the neighbouring gas field) is still active. Thus, the evolution of the pressure depletion levels in time in relation to geothermal energy production requires further investigation.

Uncertainty of the level of *gas saturation* in the reservoir has a dominant effect on the produced gas to brine ratio. A high gas to brine ratio could serve as an additional energy and income source for a geothermal project (van Heekeren and Bakema, 2015). Simultaneously, the presence of gas can further complicate the technical feasibility of the pump installation (i.e. gas coming out of solution) and the surface facilities (Frick et al., 2011; van Heekeren and Bakema, 2015).

Geological uncertainty pertains mostly to pressure output and secondly to gas production levels and thermal and temperature output. Thermal power seems to be the least affected. *Reservoir permeability* dominates the Δp between the wells. It further determines the pumping energy needed to extract a certain amount of energy. The extremely high pressure resulting from low reservoir permeability will significantly reduce the CoP. Nonetheless, limitations related to low reservoir permeability could be offset by hydraulic stimulation as has been demonstrated in Rotliegend sediments at the Groß Schönebeck field (Legarth et al., 2005; Zimmermann and Reinicke, 2010) or by a hybrid system between the two versions of natural and stimulated reservoir (Blöcher et al., 2015). Alternatively, a different perforation scheme could selectively target the layers with better flow characteristics.

Fault permeability has a medium to low temporal effect on the producer well temperature and thermal power, but it does further affect the gas to brine ratio. Effectively, the presence and permeability of faults influence the fluid volume connected to the producer well. Sealing faults alter both heat extraction and gas production on a temporal level by confining the volume and accelerating resource depletion. This effect highlights the importance of 3D geometric reservoir modeling, as this aspect would have been overlooked using a more simplified 2D model. Furthermore, the inclusion of the faults

themselves allows examining the pressure front development around them. This aspect remains highly pertinent as induced seismicity relates closely to existing faults (Van Wees et al., 2014) . The relevance of this is important since high overpressures (>200 bar) are present in the Lauwerszee Trough (Verweij et al., 2011). Results presented in **Figure 3.15** do not constitute an exhaustive analysis of the effect of pressure on faults. In-situ mechanical stress and full fault geometry need to be part of the analysis to provide a broad understanding of the interrelation between fluid injection and seismic activity (Moeck et al., 2009). Earthquakes in sedimentary geothermal settings have been documented to be negligible in magnitude (Evans et al., 2012). However, cyclic production could also aid to mitigate the pressure build up, allowing for pressure redistribution within the reservoir, thus reducing Δp across faults. Still, this project involves a more complex geological setting where advancing pressure depletion and geothermal production might lead to different results. For this purpose, further input is needed, as well as different meshing and simulating tools that can better handle complex fault geometry. Nonetheless, this highlights a crucial point for geothermal development and a parameter which needs to be considered as a starting point for a comprehensive analysis of the effects of geothermal energy production on fault behaviour.

Operational uncertainty has an important influence on most outputs with the exception of gas to brine ratio. *Flow rate levels* govern thermal power, producer temperature and doublet pressure difference. There is however a certain degree of freedom which allows a trade-off, such that the same power output can be achieved through more than one combination of flow rate levels and re-injection temperatures. This finding is supported by similar outcomes for geothermal power plants (Franco and Villani, 2009). Since direct use of geothermal heat does not operate under the optimized and fine-tuned conditions needed for binary electricity plants (Franco and Villani, 2009), this trade-off becomes more valuable. Flow rate still remains important for pressure differences between producer and hydrostatic reservoir. Nonetheless, this aspect needs further research since the applied mesh resolution might underestimate the pressure levels in close proximity to the wells and the difference between static and dynamic fluid level (Frick et al., 2011).

The *reinjection temperature* indirectly controls the amount of extracted heat from the reservoir and is the second most important parameter determining doublet power; this is most notable in the temporal dimension and corroborates previous analytical findings (van Wees et al., 2012). This aspect strongly dictates the mode of operation, as well as the design of surface facilities and should be considered when deciding on the size of the doublet. Reinjection temperature does not significantly shorten project life since the first effects are observed only after 60 years in the worst case. Pressure difference between producer and injector is only affected moderately by the reinjection temperature, relating to density and viscosity differences caused by temperature (Francke and Thorade, 2010).

Table 3.3 Risk assessment overview through the effect of uncertainty parameters to simulation output.

		Output impact				
		Thermal power (MW)	Δp producer – injector (bar)	Δp producer – hydrostatic reservoir (bar)	Producer temperature (°C)	Gas to brine ration (m^3/m^3)
Uncertainty parameter	Depletion (bar)	low	low	high	low	medium
	Gas saturation (%)	low	low	low	low	high
	Reservoir permeability (-)	low	high	medium	low	medium
	Fault permeability (mD)	low (temporal)	low	low	medium (temporal)	medium-low
	Flow rate (m^3/h)	high	high	medium	high	low
	Injection temperature (°C)	medium	medium	low	low	low

The applied workflow enables the establishment of a comprehensive risk matrix (**Table 3.3**) with regard to the three uncertainty levels discussed (initial state, geological and operational). The input levels, value ranges and outputs presented in this analysis constitute an extension of previously considered uncertainties. More significantly, the parameter co-dependency demonstrates the relative importance of each input to the different analysis outputs. The assessment can serve as starting point to identify critical project aspects and steer the focus of further research needed prior to drilling the exploration well. The breadth of the analysis is underpinned by 3D field geometry and 3D numerical reservoir simulations and can therefore support both quantitative as well as qualitative insights.

The methodology can be further expanded to include other parameters or broader value range of uncertainty where appropriate. The number of simulations however would increase dramatically. The ensemble of 4536 simulations highlights that uncertainties still remain, even in a mature hydrocarbon basin with a wealth of available subsurface data. Decisions on doublet sizing or data and engineering requirements can decrease the uncertainty range included in the analysis before the applied methodology, thereby reducing the number of simulations needed. The proposed workflow can contribute to risk comprehension and lead to more successful implementation of direct use geothermal projects.

The number of parameters and their co-dependent arrangement create a six-dimensional solution space on top of the four dimensions of reservoir simulation. The difficulty to visualize these data can be circumvented through the sensitivity analysis that highlights the relative importance of the parameters. In the absence of available data, a careful selection of the parameters and their values can still generate useful results and insights through the same mechanism. This widens the applicability of the paradigm presented.

Some limitations of the study are still relevant. Retaining the geological model resolution to the reservoir simulator was suboptimal. The added definition especially related to fault geometry could further fine-tune the findings. Furthermore, the complexity of the workflow highlights the need for integrated geothermal assessment tools.

Conclusion

The employed methodology results in a comprehensive reservoir risk assessment of a geothermal direct use installation. Three levels of uncertainty are included in the discrete parameter analysis, namely initial state, geological and operational uncertainty. The analysis is based on a 3D geological model and is carried out through an ensemble of 4536 unique numerical 3D reservoir simulations extending over 100 simulation years. All possible combinations of the discrete parameters are considered. The relative effect of each parameter class is extracted by means of a sensitivity analysis. A risk assessment matrix provides a qualitative overview, while the wealth of generated data deliver quantitative output ranges. While the methodology is transferable to other geothermal fields, the numerical results are restricted to the Groningen concession.

Making use of available data and uncertainty ranges with the methodology, we conclude that the thermal energy in the envisioned Groningen geothermal doublet (Rotliegend reservoir) can be sustained beyond 60 years (5°C temperature drop) under all simulations.

Regarding initial state uncertainty, pressure depletion can significantly affect the production pump installation depth. A pressure head of up to 325 bar could be required by the pump, resulting in major technical challenges. Therefore, reservoir pressure depletion is a major risk for geothermal projects. Reservoir gas saturation levels control the amount of gas that might be co-produced. Volumes of up to 90 m^3 of methane per m^3 of produced brine can be expected for a gas saturation of 15%.

Pressure difference within the reservoir is controlled by reservoir permeability. Low permeability (P90) can generate pressure differences up to 500 bar, while medium permeability (P50) only reaches up to 150 bar. Fault permeability, the second geological uncertainty parameter, affects the produced water temperature. Sealing faults start to affect the produced temperature after 60 years of simulation time.

Operational uncertainty parameters present trade-offs between them and the same power output can be achieved with more than one flow rate and re-injection temperature combinations. Flow rate impacts both pressure and the thermal power outputs significantly. The Groningen geothermal doublet can produce power in excess of 21 MW at the pressure penalty of up to 300 bars. Additionally, injection temperature impacts power output and pressure. For the same flow rate up to 5 MW more can be extracted by reducing the injection temperature from 40°C to 10°C.

Appendix A

Temperature data for the top of the Rotliegend (Ten Boer formation) from a basin model in the Groningen area where available to us from NAM (NAM, 2015). The dataset makes use of borehole temperature data from the Groningen gas field and surrounding wells.

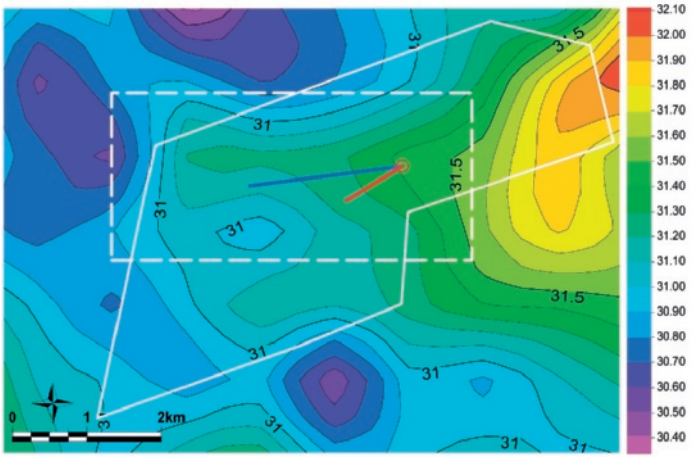

Figure 3.20. Temperature gradient calculated using the NAM temperature top Rotliegend temperature and the interpreted depth. A surface temperature of 10°C is used. The dotted line outlines the extent of the reservoir model, while the continuous line the extent of the Groningen license.

Using the dataset a temperature gradient map was produced (**Figure 3.20**). Assuming a temperature of 10°C at the surface, the average temperature gradient around the concession is 31.3°C/m which is in agreement with the dataset from literature (Bonté et al., 2012).

Appendix B

Non-complete simulations

Some simulations have not completed due to very high pressures that cannot be accommodated by the TOUGH2 simulator. The crashed simulations and their respective input parameter values are presented in **Figure 3.21**.

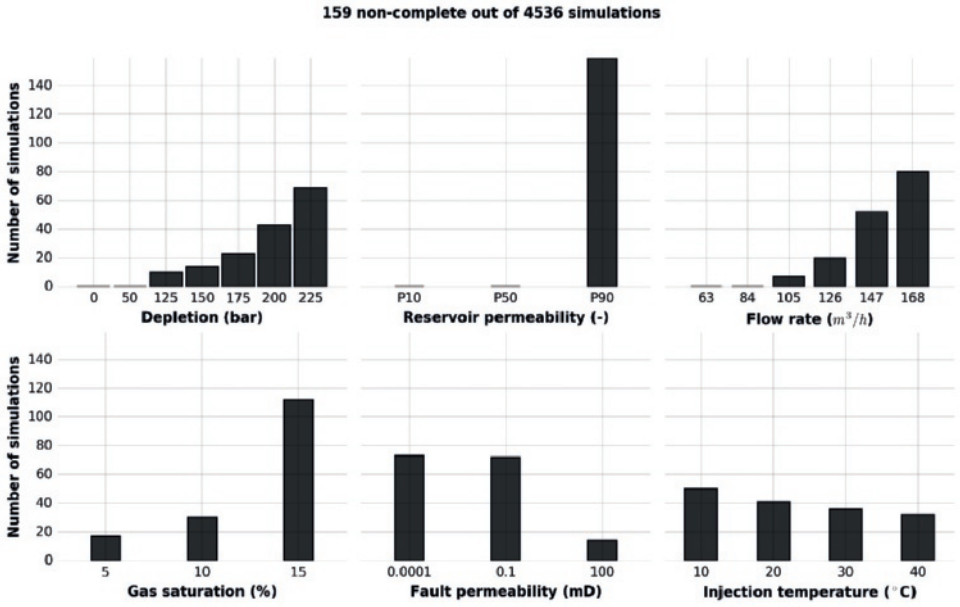

Figure 3.21. Simulations that have not completed the full simulation time of 100 years amount to a total of 159 (0.035% of the total 4536). It should be noted that the numbers in the subplots are not cumulative. Each subplot amounts to 159, as a single simulation has a value for each parameter.

All simulations that have not completed share low reservoir permeability values (P90). Higher values of depletion, gas saturation and flow rate show an increasing number of incomplete simulations. Opposite to this, higher fault permeability and injection temperature reduce the number of simulations that have not reached full simulation time. Since there is not a clear physical reason why this might occur (though pressure built up is the most prominent one), crashed simulations do not necessarily mean that such scenarios cannot be realized. Nonetheless, the lower reservoir permeability values (P90) can be seen as an important factor for failure. Since all crashed simulations exhibit low reservoir permeability values, all abovementioned results have a more poorly represented effect of low permeability (P90).

Appendix C

The dataset depicted in **Figure 3.22** is identical to the one presented in **Figure 3.10**. The effect of flow rate and injection temperature defines the clustering regarding the thermal power output (operational uncertainty parameters). This effect can be also followed on the temporal dimension, in **Figure 3.22**b. The effect on pressure difference is not clear using this coding. The scatter patterns of the geological uncertainty do not allow for a meaningful interpretation of the results.

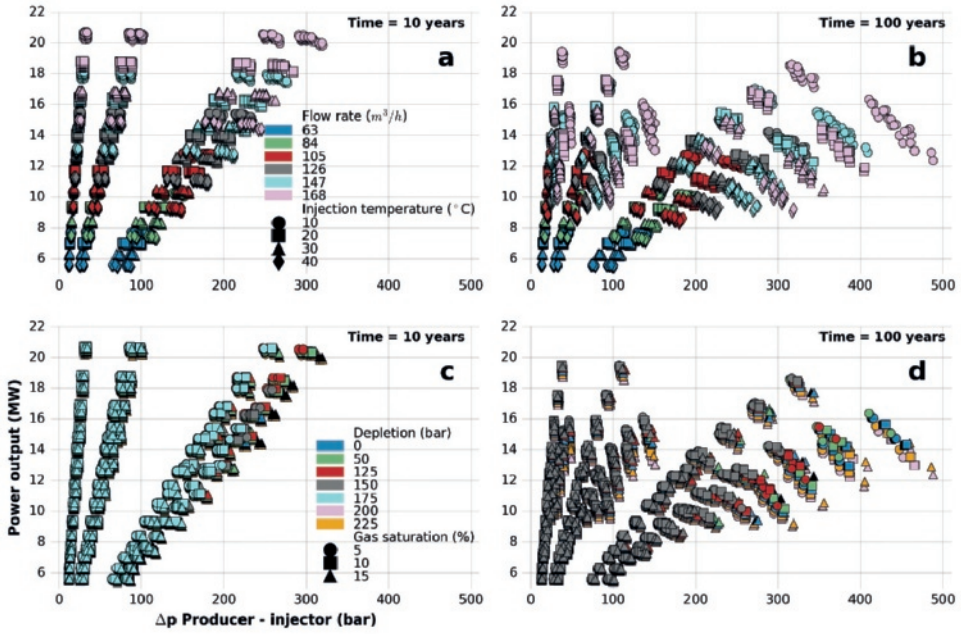

Figure 3.22. Power output plotted against producer and injector Δp. but coded based on operational (a & b for 10 and 100 years respectively) and initial state uncertainty (c & d for 10 and 100 years respectively).

Chapter 4

GEOCHEMICAL IMPLICATIONS OF COUPLING A DIRECT USE GEOTHERMAL SYSTEM WITH SURFACE DEMAND

This chapter is based on the publication:

Daniilidis, A., Scholten, T., Hoogheim, J., De Persis, C. and Herber, R., 2017, "Geochemical implications of production and storage control by coupling a direct use geothermal system with heat networks. ", *Applied Energy*, 204, 254-270.

Abstract

This paper outlines a method in which the heat production of a geothermal system is controlled in relation to the demand from a district-heating network. A model predictive control strategy is designed, which uses volume measurements in the storage tank, and predictions of the demand, to regulate the production of the geothermal system in real time. The implications of such time-varying production for the reservoir are investigated using a 2D reactive transport reservoir model. As a case study, the Groningen geothermal project is considered. The numerical data generated by the controller, in closed loop with a modelled district-heating network, are used as inputs for the reservoir simulations. The latter make use of discrete parameter analyses to evaluate the effect of pressure depletion, reservoir permeability, flow rate, re-injection temperature and injection pH on the geothermal reservoir, and also mitigate possible risks during development. Using a model predictive control does not create adverse geochemical effects in the reservoir; instead, the controller is able to improve the efficiency of the geothermal heat extraction. The findings pave the way for stronger integration between elements of heat networks and a more sustainable development of geothermal resources.

Introduction

Currently heat demand constitutes the largest part (~78%) of household energy consumption in the EU (European Commission, 2016b). Renewable heat from geothermal systems can aid the reduction of CO_2 emissions associated with conventional heat production (Eicker et al., 2015; Østergaard and Lund, 2011; Tokimatsu et al., 2016). Geothermal district heating systems have been used since the 14th century (Lemale and Jaudin, 1999), but were challenged by the wide use of cheap fossil fuels. However, due to global warming and a revived focus on renewable energy sources, district heating and heat energy networks are gaining importance in the provision of renewable energy (Lund et al., 2014; Rezaie and Rosen, 2012; Sayegh et al., 2016). The spatial topology and integration of a heat network in an urban setting has been recently analyzed in a comprehensive manner (Unternährer et al., 2017). The complexity and challenges related to geothermal heat distribution have been previously outlined (Gelegenis, 2009), while the efficient production and use of geothermal resources has been identified as an important aspect of their sustainable development (Shortall et al., 2015). Such insights are relevant for all geothermal fields. Nonetheless, the nature and impact of the challenges cannot be fully generalized and should be addressed by means of project-level studies (Shortall et al., 2015).

In a conventional setup, a geothermal system provides the baseload heat supply, while backup systems cover any excess demand (Huculak et al., 2015; Sayegh et al., 2016). Recently, it has been shown that periods of high and low geothermal heat production can lead to more sustainable utilization of the geothermal resource (Axelsson, 2010). Global historical data on direct-use geothermal systems suggest that there is a capacity factor drop over time (Lund and Boyd, 2016). This drop could be partly attributed to a better utilization of the geothermal heat produced by means of coupling supply and demand.

It is important to match the heat supply and demand (Eicker et al., 2015) in district heating systems, and daily discrepancies can be bridged with the use of a storage component (Kyriakis and Younger, 2016; Sayegh et al., 2016), while the geothermal production level can be adjusted to match the seasonal changes. However, applying a seasonally variable production rate to the geothermal system can have several consequences at reservoir level, among which are changes in chemical composition, pressure and possibly also temperature. Moreover, a seasonally variable production rate could also affect the cold front breakthrough time of the reservoir, when compared with a constant production level. Salt dissolution or precipitation can affect reservoir permeability (Zhang and Liu, 2016) and therefore needs to be addressed with location-specific modelling. Recent experimental studies presented geochemical interactions (Schmidt et al., 2017; Wolff-Boenisch and Evans, 2013) in conduction-dominated geothermal settings (Moeck, 2014). Moreover, chemical implications, in the form of salt precipitation during geothermal

production using CO_2 as the energy carrier, have also been recently highlighted (Cui et al., 2016). It was demonstrated that a dynamic production rate can lead to clogging of the reservoir due to salt precipitation. To avoid this, the production rate of change should be constrained. Obtaining realistic values for these constraints is often difficult, as they are dependent on the characteristics of the geothermal system and therefore case specific. Furthermore, a geothermal system has upper and lower production constraints determined by reservoir properties and engineering specifications.

In order to satisfy all previously mentioned constraints while supplying a time varying heat demand, a storage device can be used to shift loads in time (Kyriakis and Younger, 2016). To provide the geothermal system with time-varying production rates, a controller should be designed that takes the production and storage capacity constraints into account. In case the demand has a periodic structure, an internal model controller can be used, as is shown in (Scholten et al., 2015). In (Rosander, 2012) several other controller designs are presented that do not require a periodic demand, among which well-tuned proportional-integral-differential (PID) controllers and model predictive controllers (MPC) are the most promising. The PID controllers are very easy to implement and guarantee stability, but cannot guarantee that the constraints are always met. Conversely, an MPC does have the capacity to guarantee that the constraints are always satisfied but the stability of these controllers is hard to prove. Moreover, these MPC mostly rely on ad-hoc tuning and experimental analysis (Široký et al., 2011). Despite these drawbacks, MPC received a lot of attention (Allgöwer et al., 1999; Campo and Morari, 1989; Mayne et al., 2000; Široký et al., 2011) and are also applied to the control of pressure control of geothermal systems (Darup and Renner, 2016) and thermal energy storage for buildings (Ma et al., 2012).

An MPC solves an optimal control problem over a finite discrete time horizon, returning a sequence of control inputs of which only the first one is implemented. After this implementation, the process is reiterated using a new finite horizon that is shifted one step forward. Since the future demand is often unknown, a prediction can be made to solve the optimization problem. These predictions can be based on, for example, historical data and weather predictions. Also, a dynamic model of the system that is to be controlled is required to implement an MPC. Such a model relates flow rates and storage level (Scholten et al., 2016), and is well suited to modeling a district-heating network.

The importance of direct-use, deep geothermal systems to renewable heat supply was recently highlighted (Østergaard and Lund, 2011; Tokimatsu et al., 2016). However, for the simulation of such geothermal reservoirs, the implications and complexity of the geothermal system are usually simplified (Østergaard and Lund, 2011) or not discussed (Tokimatsu et al., 2016). Moreover, demand pattern changes are either not taken into consideration (Chen et al., 2015), or only described by a maximum (Barkaoui et al., 2016;

Muñoz et al., 2015) or annual demand level (Eicker et al., 2015; Unternährer et al., 2017). Additionally, direct use geothermal systems often exhibit risks that are difficult to estimate (e.g. uncertainties as discussed in **Chapter 3**), particularly at the early phases of development (Huculak et al., 2015). The effect of a variable geothermal production resulting from the coupling between demand and supply to the reservoir geochemistry has not been studied before, possibly impeding the application of such systems.

In this work, the heat demand is delivered using a district heating system that includes a storage device. An MPC is designed that regulates the production of the geothermal system. Although the design of MPC is not new, such a design has not been applied before to a geothermal system. The controller uses a storage level measurement and demand prediction as inputs and takes constraints into account for the production level, change in production level and storage level. A realistic, yearlong demand pattern for an equivalent of 10,000 households is used as input.

The resulting MPC production levels for the geothermal system have a realistic time-varying behavior, which is used as input for geochemical reservoir simulations. In this paper both the implications and complexity of the geothermal system and the changes in demand pattern are taken into account. Moreover, to take uncertainties in reservoir pressure depletion, permeability, flow rate, injection temperature and pH into account, multiple simulations are performed which helps to mitigate possible risks during the development phase.

The reservoir simulations are performed using a 2D model to obtain several insights. Firstly, it is investigated whether the geothermal doublet is able to provide the demanded energy (i.e. feasibility of delivery). Secondly, the long-term effects of a variable, demand driven, seasonal production pattern on the reservoir behavior (i.e. pressure, power, permeability and chemical changes) is compared to constant production rate data. Lastly, the interaction between the chemical and physical parameters of the reservoir is outlined. The analysis makes use of the Groningen geothermal project (NE Netherlands) data and features.

An analysis of the performance of the controller in closed loop with the district heating network is carried out. This is followed by an analysis of the geochemical implications for the reservoir. Finally, a discussion of the findings, and the conclusions that can be drawn are presented.

Methods/background

The possibility and implications of a time-varying production of a geothermal system that is controlled in real-time are evaluated. To this end, an MPC is designed that regulates

the production of the geothermal system. This controller is connected to a modelled storage device in order to analyze its performance. The demand pattern is predicted based on historical demand data. The MPC uses such predictions, in combination with measurements from the storage device, as its inputs. Additionally, the MPC takes into account the predetermined limitations of the reservoir in the form of constraints on the change in production rate. This control structure is depicted in the upper part of **Figure 4.1**. The controller design, equations and constraints, storage model and their respective results and discussion is presented in detail in the journal publication (Daniilidis et al., 2017). The reader is referred there for further details on the controller mathematical formulations and the MPC implementation.

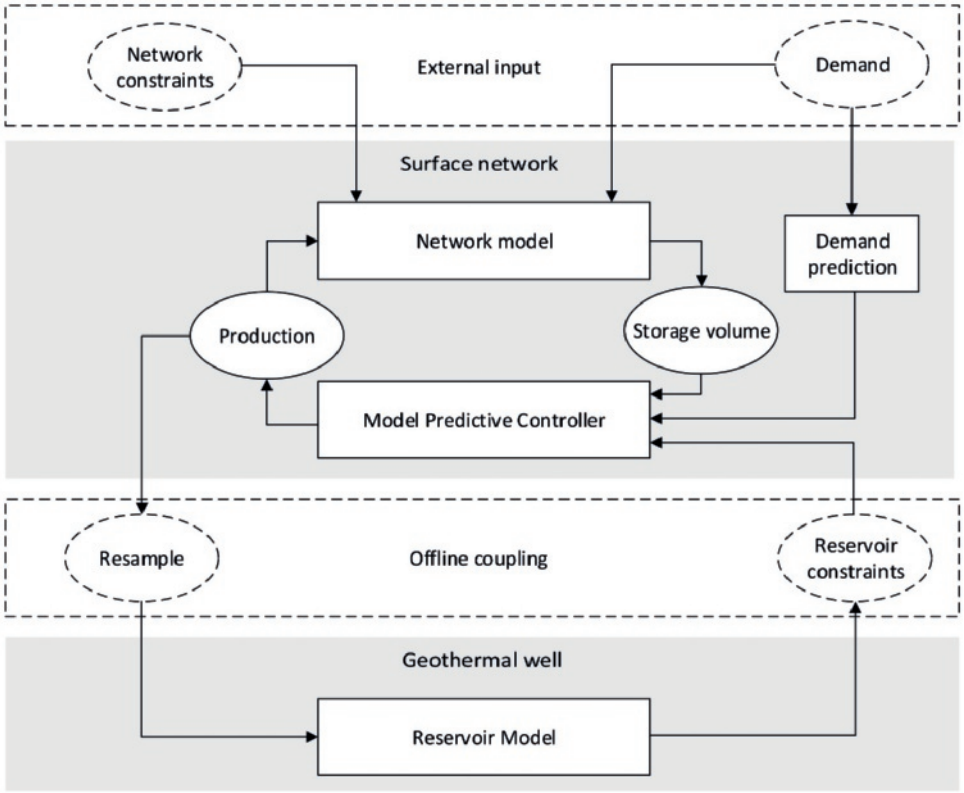

Figure 4.1 Overall flow chart. The storage model and the MPC are connected in closed loop for the simulation where the static constraints from the reservoir model and storage are used. The aggregated demand in the heat network is predicted using historical data and used as input for the MPC and the actual demand is used as input for the storage model. The resulting production levels are used (offline) as an input for the reservoir simulations.

To investigate the consequences of this time-varying production, a 2D reservoir model of the Groningen geothermal project is used. The production levels that are generated using

the heat network were converted from an hourly to a monthly demand and used as input for a 50-year reservoir simulation. The lower part of **Figure 4.1** shows the model of the reservoir for which 243 scenarios were considered, each one corresponding to a different uncertainty parameter combination. The results of the reservoir behavior in terms of pressure, permeability, chemical and power changes are investigated.

Reactive flow model

In order to evaluate the impact on the reservoir of fluctuating production, a reservoir model was used. Since project-level studies are needed to understand geothermal systems and gain insights, the model is based on data from the Groningen geothermal project (Daniilidis et al., 2016). The reactive flow model is discussed in further detail below.

Reservoir model

The model was built in the PetraSim pre-post processor (Rockware, 2014), using the TOUGHREACT (Xu et al., 2006) code for chemically reactive, non-isothermal flow and utilizing the EOS1 (Equation of State) (Pruess et al., 2012). The TOUGHREACT code uses space discretization through Internal Finite Difference (IFD) (Narasimhan and Witherspoon, 1976). The solver uses a sequential iteration approach for coupling between fluid and reactive flow (Yeh and Tripathi, 1991).

The chemically reactive flow model used is largely based on the model geometry and characteristics of the Groningen 3D reservoir model (Daniilidis et al., 2016), adapted to 2D. Overall characteristics and architecture are presented in **Table 4.1** and **Figure 4.2**, respectively. It should be noted that the EOS1 does not consider the viscosity aspects of the brine, contrary to the 3D reservoir model presented earlier. Therefore, differences in the pressure behavior of the reservoir between the two models can be attributed to the different EOS. Lastly, the model does not consider any effects inside the wellbores or the surface facilities.

Stratigraphy, geometry, wells and mesh

The model characteristics can be found in **Table 4.1**. The stratigraphy represented in the model is an adapted version of the Groningen 3D geological and reservoir model (Daniilidis et al., 2016). For the purposes of examining reactive flow through the reservoir, a 2D model is considered sufficient since there is no supporting data for a spatial, 3D variation of chemical characterization. Therefore, the 2D model assumes radial symmetry around the wells. A 2D model has the added benefit of reducing the simulation time.

Simplifications had to be made to adapt the model from 3D to 2D. The contacts of the stratigraphic layers in the model are now horizontal, using the average depth of the respective 3D model layers; furthermore, the thickness of the layers is also averaged for

Table 4.1. Characteristics of the reservoir model. A visual representation of the mesh can be found in **Figure 4.2**.

	Value
Dimensions (X, Y, Z)	1275m x10m x 900m
Lithostratigraphic units	10
Vertical discretization	according to layer
Vertical layers	35
Horizontal discretization	5m, successively increasing
Horizontal cell increment factor	1.138
Reservoir layer height	≥10m and ≤12.5m
Total cell count	1,785
Average reservoir depth	3595m
Reservoir thickness	248m
Temperature gradient	31.3°C/km
Pressure gradient	hydrostatic*

*The depletion scenarios apply only inside the domain of the Rotliegend.

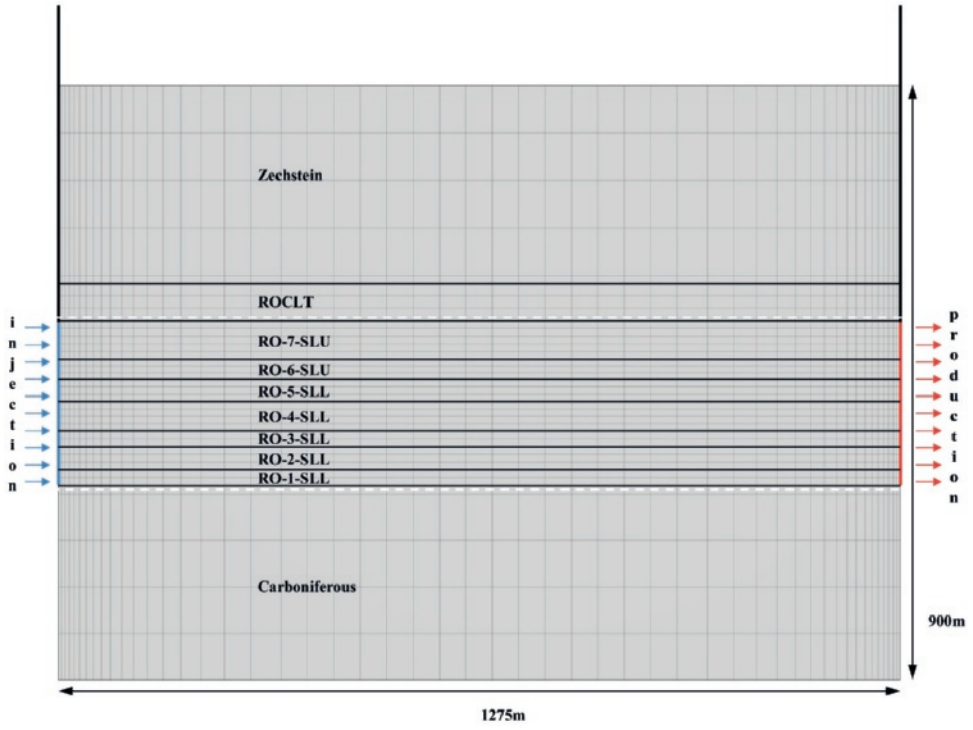

Figure 4.2. Reservoir model mesh. The productive layers consist of the SLU and SLL members, which are outlined by the white dashed lines.

uses a finer mesh (5m), close to the wells, that gradually coarsens (40m) towards the middle part of the reservoir (**Figure 4.2**). The Rotliegend Slochteren layers (upper and

lower members) were used as the reservoir body for the injection of cold, and production of hot, water. Vertical discretization ensures a constant thickness of the layers inside the producing interval.

Petrophysical inputs and boundary conditions

Petrophysical data for porosity and permeability were obtained from Panterra (van Leeuwen et al., 2014) and were scaled with respect to the most proximal well to the project area as presented in previous research (Daniilidis et al., 2016). Probability levels 90%, 50% and 10% are derived per reservoir layer and are denoted by P90, P50 and P10 (summarized in **Table 4.2**).

Table 4.2. Model layer characteristics. Grouping the permeability values in P90-P50-P10 scenarios, the permeability range is taken into account as a worst-middle-best estimation, based on the petrophysical data presented. Vertical permeability is an order of magnitude lower than horizontal permeability for all layers (Carlson, 2003).

	Permeability ($m^2 \cdot 10^{-14}$)			Porosity	Density	Wet heat conductivity	Specific heat	Thickness
	P90	P50	P10	(%)	(kg/m^3)	(W/m·K)	(J/kg·m)	(m)
Zechstein	0.987	0.987	0.987	1.0	2170	3.5	1050	300
ROCLT	0.010	0.010	0.010	12.0	2625	3.0	840	56
RO-7-SLU	0.098	0.222	0.913	17.4	2700	2.9	840	59
RO-6-SLU	1.474	4.700	14.946	18.5	2515	2.9	827	30
RO-5-SLL	1.357	4.336	13.829	17.7	2625	2.9	827	34
RO-4-SLL	1.413	4.565	15.100	19.5	2590	2.9	827	44
RO-3-SLL	1.049	3.411	11.239	17.5	2728	2.9	827	24
RO-2-SLL	0.265	1.073	4.133	18.3	2596	2.9	827	32
RO-1-SLL	0.426	1.437	4.743	14.9	2853	2.9	827	25
Carboniferous	9.87e-17			1.0	2900	2.7	840	400

The top and bottom cells were used as boundary conditions for the numerical simulation. The values for the temperature and pressure in the boundary cells were computed based on the respective pressure and temperature gradients (**Table 4.1**). Their distance to the production layers ensures that they do not interfere with the reactive flow in the reservoir cells. Furthermore, the boundaries remain valid in this geothermal setting, which is dominated by conductive heat transfer (Moeck, 2014).

Chemical characterization

The mineralogy of the reservoir layers was adapted from the X-Ray Diffraction (XRD) and Scanning Electron Microscopy (SEM) analysis of core samples (Bolourinejad et al., 2014) (**Table 4.3**). The TOUGHREACT code requires the specification of secondary minerals that might form as intermediate products of the chemical reactions. The primary

Table 4.3. Chemical composition of the Slochteren reservoir rock. Volume fraction values are computed using densities after (Waples and Waples, 2004a) for all minerals; for illite density values used are after (Barthelmy, 2014).

Mineral	Slochteren sandstone (% vol)
Quartz	87.18
Kaolinite	5.01
K-feldspar	2.55
Dolomite	1.87
Albite	1.52
Illite	0.96
Anhydrite	0.91

Table 4.4. Brine composition. Data obtained from (Bolourinejad et al., 2014). The initial reservoir pH is set at 7. Additionally to the minerals shown here, a thin layer of iron was also introduced to the model in the location of the well cells to account for the well casing. As in other geochemical studies, petroleum exploration and production data are usually the only data available to geothermal studies (Wolff-Boenisch and Evans, 2013) in conduction dominated geothermal fields.

Chemical species	Molality
Cl^-	4.11
Na^+	2.96
Ca^{2+}	0.463
Mg^{2+}	0.081
K^+	0.048
Sr^{2+}	0.006
Fe^{2+}	0.00485
HCO_3^-	0.00384
SO_4^{2-}	0.00178
Zn^{2+}	0.00115
Ba^{2+}	1.16e-4
Pb^{2+}	1.14e-4
H^+	4.75e-7
AlO_2^-	1.0e-20
$SiO_2(aq)$	1.0e-20
$O_2(aq)$	1.0e-20

and secondary minerals considered and their respective reactions as implemented in TOUGHREACT can be found in Appendix A. The kinetic rate parameters need to be specified for both the primary and secondary mineral phases. They are reported in

Appendix B, together with the general rate expression and kinetic rate constant formulations used in the TOUGHREACT code.

The brine composition is derived from gas field data, as presented in previous geochemical studies of the Permian Rotliegend sandstone (Bolourinejad et al., 2014) in the area of Groningen. Concentration levels presented in **Table 4.4** represent the equilibrated values with the initial rock mineral composition. The Carman-Kozeny porosity-permeability relation is used in TOUGHREACT to account for changes in the flow properties due to chemical processes.

Simulation parameters

To account for the uncertainty inherent in such geological data, but also to evaluate operational possibilities a discrete parameter analysis is used, similar to recent studies for geothermal systems (Adams et al., 2015). Uncertainty is taken into account regarding the initial reservoir pressure, the reservoir permeability, flow rate control strategy, re-injection temperature and injection pH (**Table 4.5**). The uncertainty classes cover the initial reservoir state (pressure depletion) and geological uncertainty (mainly permeability related), which are determined by the field conditions and are beyond project control. Additionally, the operational parameters of the flow rate control strategy, the re-injection temperature and the injection pH provide some degree of freedom in designing the geothermal system (Daniilidis et al., 2016),

Table 4.5. Uncertainty classes and respective discrete parameters considered. In total 243 unique reservoir simulation realizations are computed (3^5). The flow rate levels are unique for each re-injection temperature level as the heat content of the injected water changes. Therefore MPC, constant min and constant max flow rate levels are adjusted accordingly to reflect this (see also **Figure 4.4**). Geothermal systems for direct use are usually utilized for a period of a few decades, if the produced heat levels are not diminished. For this reason all simulations are carried out over a 50 year period to identify a possible cold front breakthrough.

Pressure depletion (bar)	Permeability (-)	Flow rate control strategy (m^3/h)	Re-injection temperature (°C)	Injection pH (-)
0	P90	MPC output	40	4
100	P50	constant max	55	5.5
200	P10	constant min	70	7

Results

For the case study of Groningen, a simulation of the MPC, using appropriately chosen parameters, is first performed and presented. This is followed by the results of the reservoir simulations. The effects of the 243 scenarios on reservoir pressure, permeability change, power output chemical changes at the injector and 2D property changes are analyzed.

Controller and MPC

In order to simulate the district heating network in closed loop with the MPC, the demand pattern for the Groningen case study is firstly introduced. This heat demand pattern is depicted in **Figure 4.3**a and is obtained from a statistical model representing 10,000 households. For further details on the MPC results the reader is referred to the journal publication (Daniilidis et al., 2017).

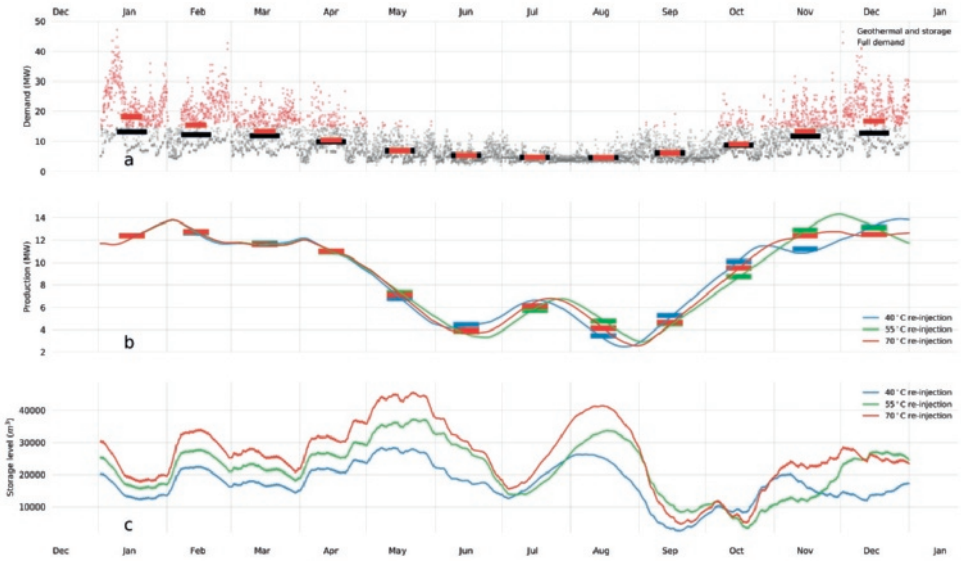

Figure 4.3. Model heating energy demand data per hour from the geothermal project of Groningen city (a). An upper limit of 15MW is used in the MPC for the geothermal system that is sufficient for 77% of the demand points; the demand in excess of this limit is expected to be delivered by other means, namely bio-gas burners. The markers represent the monthly averages of full and geothermal supplied demand. Production levels of the geothermal system resulting from the MPC (b). The markers represent resampled monthly averages of the data series and are used as flow rate levels in the reactive flow simulations. The rate constraints in are set close to zero, resulting in slowly varying production levels of the geothermal system. For this reason, a monthly averaging is a good approximation of the production levels. The increased production in July with respect to June and August can be attributed to an overshoot of the controller in combination with the limited prediction horizon and the various constraints. This behaviour could be avoided by considering better predictions, relaxing the constraints and adopting a longer control horizon. Storage levels for the respective scenarios (c). The storage helps to ensure that the demand is met by accounting for the rapid fluctuations of the demand. Moreover, the capacity of the storage is not exceeded in the simulation, resulting in a feasible control signal (*i.e.* a control signal that satisfies all the constraints at all time).

Geochemical reservoir simulations

Changes in pressure, temperature, permeability and chemical composition could affect the output of the geothermal system. It is therefore important to investigate what the consequences of time varying production are for the reservoir. For these reasons 2D reservoir simulations are carried out comparing constant and time varying production. In order to take the uncertainty of the reservoir parameters into account the simulations are

performed for several scenarios, as discussed in the methods section. The results shown hereafter include data from all the performed simulations with the exception of the two-dimensional plots.

The production rates that result from the MPC simulation are used as input for the reservoir simulation. However, due to the large timespan of the simulation (50 years) and increased number of simulations (243) a lower resolution is used by extracting the monthly averages (**Figure 4.4**). One needs to keep in mind that the resampling might affect the simulation results. That is, due to low frequency resampling, the high frequency behaviour of the production flow rate is neglected in the geochemical analysis of the reservoir. The yearly pattern obtained is then used as input for each of the 50 years of the reservoir simulations.

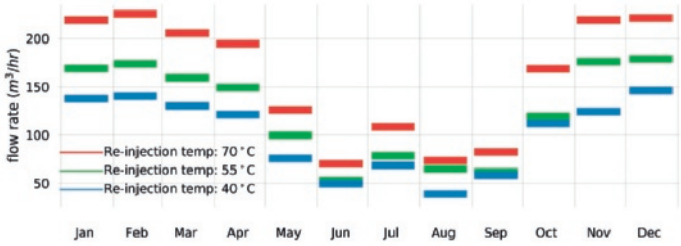

Figure 4.4. Flow rate levels for the different re-injection temperatures. Since the demand curve is expressed in MW (and it is unique for each re-injection temperature, the flow rates have to be adjusted accordingly when using different re-injection temperatures. Consequently, min and max flow rate control strategy levels for different re-injection temperatures are different for each scenario.

In these simulations the changes in the pressure difference between the producer and injector, the permeability around the injector, the power production and chemical composition in the reservoir are investigated. In the following sections, a comparison between the different flow rate control strategies (MPC, constant max and constant min) with regard to the temperatures in the reservoir is presented.

Pressure difference producer-injector

First the influence of the re-injection temperature, permeability and flow rate control strategy on the pressure is investigated. The pressure difference between the wells is mainly determined by reservoir permeability as seen by the distinct grouping of the results (**Figure 4.5**). A high permeability value (P10) results in a small Δp while for a low permeability (P90) we observe higher levels of pressure difference between the wells. The MPC controlled flow rate levels appear to fall between their respective max and min flow rate intervals. Moreover, the range of Δp is broader for the P90 permeability scenarios; this range is attributed to the other parameters (injection pH and depletion).

A low re-injection temperature (40°C) results in a lower pressure difference compared to a high re-injection temperature. This effect is not very pronounced as the differences are in the order of a few bars. Causally the re-injection temperature effect on the pressure could be explained by the permeability changes in the reservoir, which is presented in the next section (**Figure 4.7**).

All flow rate levels exhibit a slight increase of pressure over time, but this increase is more prominent for the P90 scenarios. Where present, the pressure increase is gradual and never exceeds 50% of the initial pressure. The highest pressure increase is observed in the case of a constant max flow rate and less so for the MPC flow rate levels. The pressure increase for the min flow rate levels is only marginal. These results are consistent with the permeability results presented hereafter.

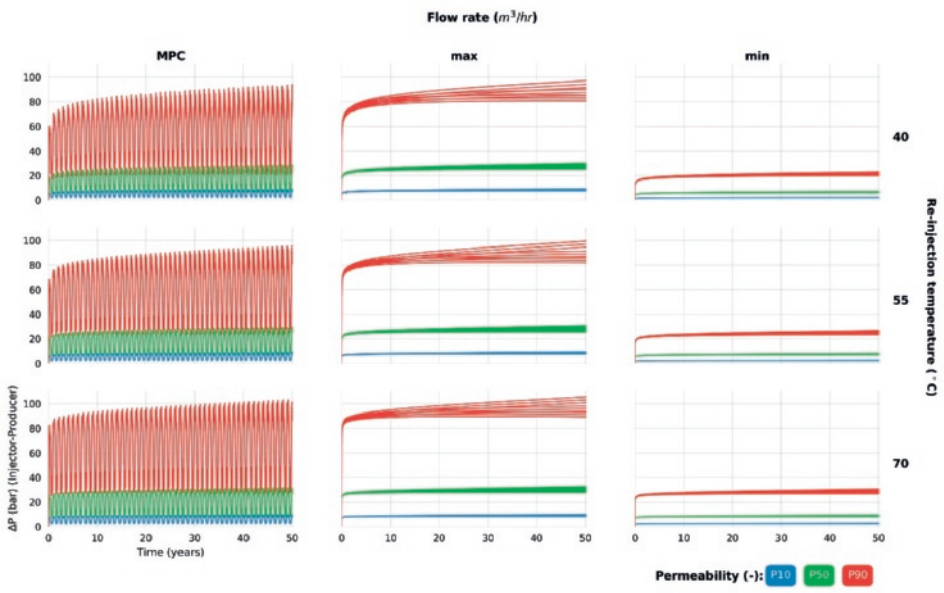

Figure 4.5. Pressure difference between the wells for all simulations. The data series are colored based on their permeability specifications. The subplot horizontal axis differentiates the flow rate levels (MPC, max, min), while the subplot vertical axis differentiates the re-injection temperature (40, 55 and 70°C). All subplots use the same scale and are therefore cross-comparable.

Doublet power production and energy reserve

The power production P (in Watt) of the geothermal system is derived from:

$$u_g(k) = \frac{C_P \rho \Delta T}{60^2} u(k)., \tag{4.1}$$

Where d is the demand covered by the geothermal well in m^3/h, C_P is the specific heat in $J/Kg \cdot K$, ρ is the density of the water in Kg/m^3 and ΔT is the temperature difference between the production and return pipes in the reservoir in Kelvin (K). However, the temperature and pressure are not necessarily constant which can result in a deviation from the desired power output; this deviation can be attributed to enthalpy changes, according to:

$$\Delta H = C_{pw} \cdot \Delta T + V \cdot (1 - \beta T) \cdot \Delta p, \tag{4.2}$$

where ΔH is the enthalpy change, ΔT the temperature change, V the volume, β the coefficient of thermal expansion, T the temperature and Δp the pressure change in the system. The simulations show that the deviations from the desired power output can be attributed to changing pressure levels inside the reservoir (**Figure 4.6**b). This is because these changes ultimately affect the producer T_p causing small temperature variations resulting in these minor changes in produced power.

The simulation results illustrate the dependency between the flow rate, temperature and power output (**Figure 4.6**). A first observation is that the power output in all simulations that use the MPC flow rate control strategy, is contained within power production levels corresponding to minimal and maximal flow rate (see also **Figure 4.4**). Secondly, we observe a small decrease in the power output is observed, when moving from no depletion to 200 bar of depletion in the initial reservoir conditions (**Figure 4.6**b). Although small (between 1 MW and 1.7 MW), this decrease needs to be considered in designing and sizing the installation to accommodate for the uncertain level of pressure depletion. Lastly, the re-injection temperature levels cause minor changes (~0.5MW) in the power output (**Figure 4.6**c).

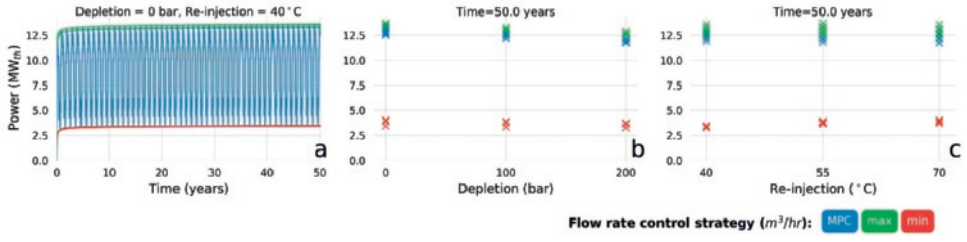

Figure 4.6. Doublet power production. The data series are coloured based on their flow rate levels. The time series data reveal no drop of power over time (a). Depletion level at year 50 reveal small differences between the power outputs (b), while re-injection temperature shows only marginal differentiation (c) for all simulations.

Permeability and chemical changes around the injector

The permeability in the reservoir is not necessarily constant; changes in permeability are related to changes in mineral volume fraction, which are in turn affected by the simulation input parameters like the initial mineral compositions and their reaction mechanisms (see Appendix A). Therefore, permeability changes and chemical changes are presented together in this section. Due to the large number of minerals only the ones with significant changes are discussed. Permeability and chemical changes around the injector well are presented for all the simulations to derive comprehensive insights.

The changes in permeability or mineral volume fraction are, however, not limited to the area around the injector well but also exhibit spatial differences within the reservoir; the two dimensional changes in permeability and for the minerals that proved significant around the injector are discussed for a sub-set of input parameters in the following sub-chapter. Nonetheless, it is evident that the injector well is very important as the first point at which the major physical (e.g. temperature) and chemical (e.g. composition, pH) changes are taking place.

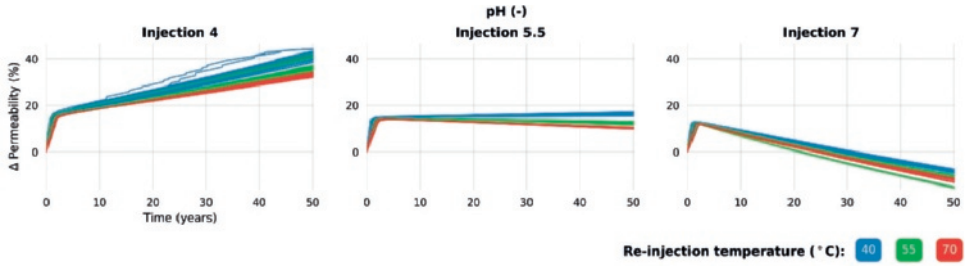

Figure 4.7. Permeability change at the injector for all simulations. The data series are coloured based on the re-injection temperature. The subplot horizontal axis differentiates between the injection pH levels. All subplots use the same scale and are therefore cross-comparable.

All simulations share an initial permeability increase of about 10% within the first 3-4 years of injection, irrespective of the injection pH and the re-injection temperature (**Figure 4.7**). The temporal volume fraction of Anhydrite closely matches this time interval, where an increase in permeability is observed for all simulations (see **Figure 4.7**). The volume fraction of anhydrite simultaneously reduces down to almost zero for all simulations (**Figure 4.8**); it therefore presents a direct link to the permeability increase, since no other mineral volume fraction changes in any of the simulations within the first 3 years. There exists a clear positive correlation between the rate of Anhydrite dissolution and the flow rate control strategy; higher flow rates lead to faster dissolution. However, these differences only affect the time at which the final volume fraction is reached; the value of the final volume fraction is the same for all flow rate control strategies. The changes in Iron concentration levels are very low (6^{th} decimal) and appear to be affected by flow rate levels.

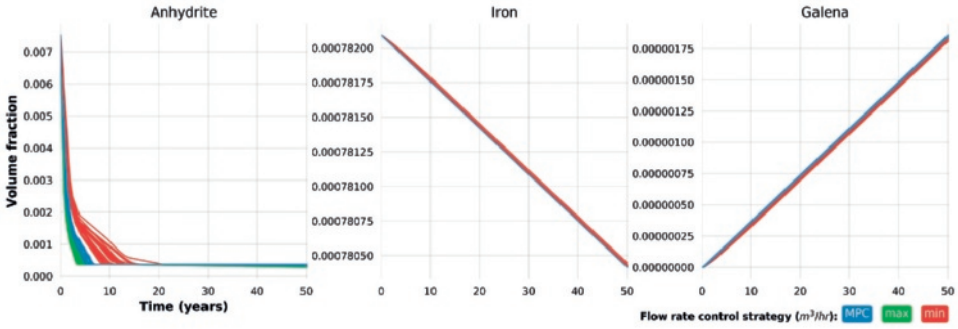

Figure 4.8. Changes in mineral volume fraction at the injector cells for all simulations for the minerals mostly affected by the flow rate control strategy. Minerals are presented in order of decreasing initial volume fraction.

Beyond the initial permeability increase, simulation results show that the permeability is mainly affected by the pH value and temperature of the injected fluid (**Figure 4.7**). Notably, following the initial increase of permeability, which occurs in all simulations, the changes caused by an injection pH of 4 and 7 are of the same order of magnitude, but in opposite directions. In both cases a permeability change of an additional 17%-27% takes place. For a pH of 4, the permeability continues to increase, reaching values between 32% and 45% higher compared to the initial values. For a pH of 5.5 the changes of permeability over time are relatively small; For an injection pH of 7 and after the initial increase, shared by all simulations, a sharp decrease follows. Between the production years 20-40, the permeability change decreases. The effect is large enough to reduce the overall permeability to -5% to -15%, with respect to the starting values.

The characteristics of the Dolomite plots, together with its high initial volume fraction, indicate that Dolomite could be the cause of the permeability changes observed in all simulations following the first increase caused by Anhydrite dissolution. Dolomite concentration exhibits a linear change over time, which is caused by the pH level of the injected fluid (**Figure 4.9**). Also, the initial volume fraction of Dolomite is the fourth highest after Quartz, making it the fourth most abundant mineral in the reservoir. Additionally, the volume fractions changes of Dolomite are the highest of all minerals compared to the initial concentration, indicating significant relative changes in its volume.

With an injection pH of 4 Dolomite dissolves, leading to further increases in permeability (in addition to the trends observed during the first 2-3 years, **Figure 4.7**). An injection pH of 5.5 causes small increases or decreases of the initial Dolomite concentration and corresponding effects (i.e. both decreases and increases respectively) to the permeability. A pH of 7 triggers Dolomite precipitation, which is in turn reflected in the permeability

decrease; this effect follows the initial increase (attributed to Anhydrite dissolution) observed in all simulations.

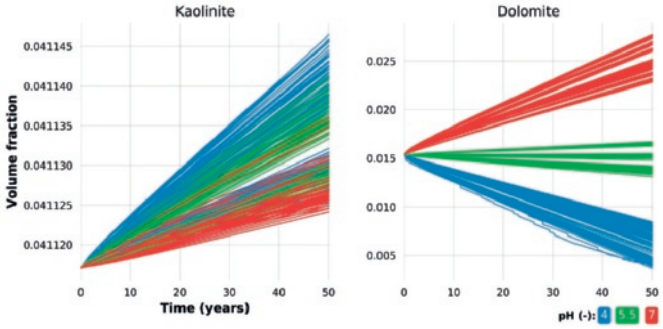

Figure 4.9. Changes in mineral volume fraction at the injector cells for all simulations for the minerals mostly affected by the injection pH. Minerals are presented in order of decreasing initial volume fraction.

Beyond the initial changes common to all simulations and the subsequent differentiation of permeability caused by the injection pH, a third factor of influence can be distinguished based on the re-injection temperature (**Figure 4.7**). Consistently, lower re-injection temperatures lead to greater increases in permeability than the higher re-injection temperatures for each level of injection pH.

For an injection pH of 4, the range of increase is influenced by the re-injection temperature; lower injection temperatures lead to higher permeability increases. For a pH of 5.5 the changes in permeability over time are relatively small; following the initial increase of about 14%-15%, minor increments lead up to an overall level of circa 16%-17% at a re-injection temperature of 40°C. For a re-injection temperature of 55°C and 70°C a slight permeability decrease compared to the initial increase of 14%-15% takes place. This reduces the permeability change to an overall increase of 12%-13% and 10%-11% for the 55°C and 70°C degrees re-injection, respectively. Lastly, for an injection pH of 7 an overall decrease in permeability is observed at the end of the simulation time. These levels are once again causally linked to the re-injection temperature, with higher re-injection temperature (70°C) resulting in a stronger decrease (~15%).

The volume fraction of Albite and Illite is dependent on the re-injection temperature (**Figure 4.10**). Albite dissolves under all scenarios, but changes are more drastic for 70°C and minimal for 40°C of injection temperature. Contrary to Albite, Illite precipitates under all scenarios. The changes in Illite volume fraction are however very low (5th decimal). An injection temperature of 40 °C causes only minor changes, while 70°C more significant ones. The volume fraction changes caused by the re-injection temperature do not seem to be of sufficient magnitude to explain the changes in permeability associated

with the re-injection temperature. Moreover, the marginal increase or decrease that is affected by the re-injection temperature for an injection pH of 5.5 would imply dissolution or precipitation affected by the temperature level. A more plausible explanation is the marginal changes in the volume fraction of Dolomite, for an injection pH of 5.5, which are further differentiated by the re-injection temperature (Appendix C).

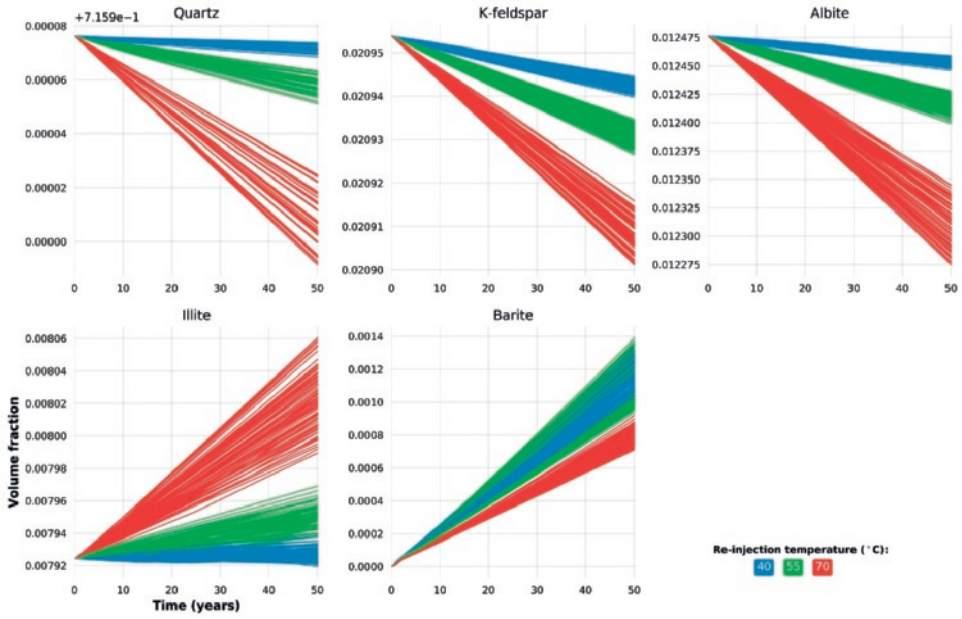

Figure 4.10. Changes in mineral volume fraction at the injector cells for all simulations for the minerals mostly affected by the re-injection temperature. Minerals are presented in order of decreasing initial volume fraction.

Minerals with high initial abundance (e.g. Quartz, k-Feldspar and Kaolinite) exhibit little volume fraction change over the 50 years of the simulations. Quartz and K-feldspar volume fractions are mainly affected by the injection temperature (**Figure 4.10**) while the change in Kaolinite volume is caused by the injection pH level (**Figure 4.9**). For all three minerals however, the changes can be considered minor, in comparison to their initial levels.

Barite and Galena are the only minerals that are not present in the initial state of the reservoir. Barite precipitates under all simulations and the mechanism of precipitation appears to be affected by the re-injection temperature (**Figure 4.8**). Although Barite precipitates under all scenarios considered, its volume fraction is lower for higher injection temperature. This is in line with observations in other Rotliegend geothermal sites, where lower temperatures favor Barite precipitation (Regenspurg et al., 2015). Similarly, Galena also precipitates under all scenarios, although the volume fractions for Galena are the smallest of all minerals (7^{th} decimal). It is also notable that Galena

precipitation seems to be independent of temperature, pH level and only small differences can be explained through flow rate levels (**Figure 4.8**).

Inside the reservoir and at the injection well, no changes are observed of the minerals Calcite, Pb (elemental), Halite, Magnesite, Gypsum, Anglesite and Siderite (Fe^{+2}).

Two-dimensional property changes

In order to compare the differences between the flow rate levels of the MPC and the max scenarios in terms of lifetime expectancy of the geothermal system, the 2D heat distribution in the reservoir is analyzed. Under the MPC control strategy and after 50 years of production the cold front propagates to about a quarter of the distance between the injector and producer wells (**Figure 4.11**a). Using the max flow rate levels for the same re-injection temperature the cold front propagates further to about a third of the well distance (**Figure 4.11**b). The difference between the two scenarios (**Figure 4.11**c) highlights the benefits in terms of a more sustainable use of the geothermal resource when

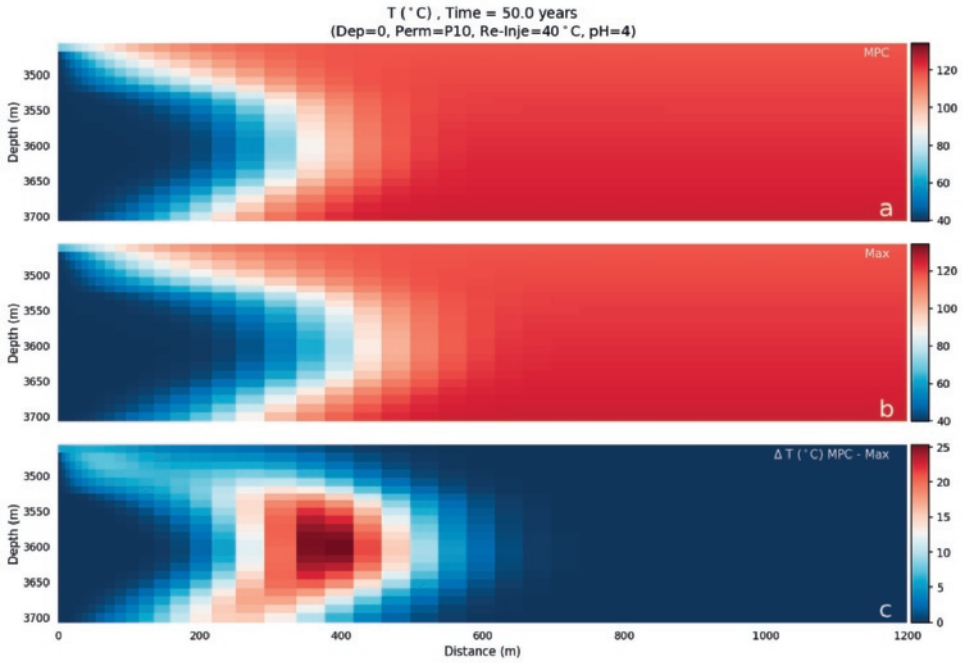

Figure 4.11. Reservoir temperature for (a) MPC flow rate, (b) Max flow rate and (c) the difference between the two scenarios. Other simulations parameters are the same for both flow rates.

without a cold front breakthrough under any of the considered scenarios.

Similar to permeability changes, alterations in mineral composition are not limited around the injector but propagate further inside the 2D space of the reservoir model. Due to the

large number of simulations, a selection is made to illustrate the changes in the two-dimensional space (see **Figure 4.12**).

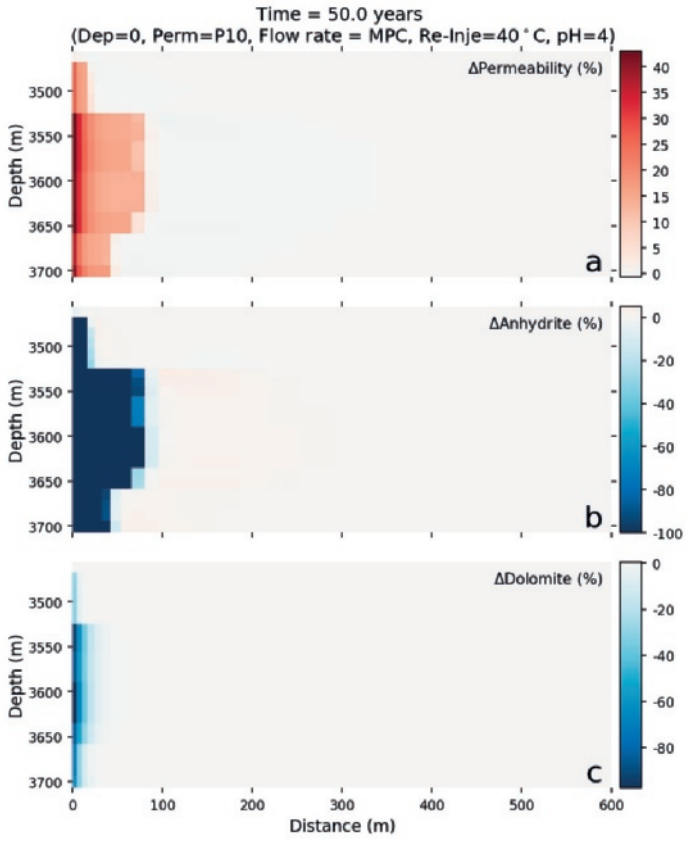

Figure 4.12. Change of parameters in the two-dimensional space of the reservoir for permeability (a), Anhydrite (b) and Dolomite (c) concentration change. A video file with a time series animation of the two dimensional space for the most relevant parameters is digitally available

The link between the dissolution of Anhydrite in the injector well as the affecting mechanism for the permeability increase is further corroborated by the 2D reservoir plots. A direct relationship can be observed between the spatial distribution of Anhydrite volume fraction change and the changes in permeability (**Figure 4.12**a). A decrease in Anhydrite volume fraction (**Figure 4.12**b) results in a permeability increase (**Figure 4.12**a). This connection also exists between the Dolomite volume fraction (**Figure 4.12**c) and the changes in permeability, but it is less strongly correlated spatially. Changes in Dolomite volume fraction also appear at a later stage in time (see also supporting time animation video) and therefore have a second order effect on the permeability.

Moreover, precipitation (positive volume fraction change) of Anhydrite occurs further away from the injector. This spatially coincides with the changes in permeability, which decreases in this part of the reservoir. It appears that precipitation is stronger at the contact between the upper, less permeable, layers than the middle ones. Similar behavior is observed for Dolomite. Thus, it can be concluded that Anhydrite and Dolomite are dissolved by the water injection and are partly re-precipitated further inside the reservoir. In these simulations, we have not observed a cold-water breakthrough, but in the event that production continues for a longer period we could see the deposition of these two minerals close to the injector. In this event, the deposition of Anhydrite and Dolomite close to the injector might introduce them to the production water cause problems in the well or surface facilities.

Discussion

The coupling of the controller to the reservoir model provides new insights on the energy network to which they are both connected. These insights can facilitate a stronger integration between the different parts of the system, if they are analyzed and developed in tandem. Furthermore, possible incompatibilities can also be mapped out. The production of heat becomes constrained by the geothermal system specifications, while the geothermal system itself is also more efficiently utilized as it can respond to changes in demand.

The designed controller is able to generate real-time production levels, using demand predictions and storage level measurements as inputs. It is guaranteed that these productions levels will satisfy several hard constraints. These include storage capacity constraints, minimal and maximal production levels and production rate constraints.

With regard to the geothermal system, the relative changes in pressure levels can be explained by the geochemical changes in the reservoir. The changes in pressure over time appear to be minor; this is in line with the mostly increasing permeability around the injector well. Only when using an injection pH of 7 we observe a decrease of the initial permeability levels, and this change only occurs after 25 years of production; thus, such an issue can be identified in time before it affects production. The increase under all other scenarios is attributed to the initial dissolution of Anhydrite.

The geochemical behavior of the reservoir is impacted primarily by flow rates, followed by injection pH and injection temperature. Notably the variable production rates of the geothermal system (resulting from the MPC control strategy) alter only the rate and not the nature of the changes in the chemical reservoir properties. A prominent example is the dissolution of Anhydrite, which appears to be affected by the flow rate. The dissolution or precipitation of other minerals is mainly affected by either re-injection

temperature or pH. Nonetheless, the effect of the variable production is beneficial with regards to the utilization of the geothermal resource. This is exemplified by the volume of rock that remains less affected by production using an MPC production rate as opposed to a constant production level (see **Figure 4.11**). The absence of adverse geochemical effects combined with the improved efficiency of heat extraction opens up possibilities for a more sustainable development of geothermal resources (Shortall et al., 2015).

Initial pressure depletion in the Groningen case history does not appear to have a significant effect in any of the results. Especially the geochemical behavior and the precipitation or dissolution of minerals is unaffected by possible pressure depletion. This is unlike the importance of the pressure depletion to the physical aspects of the 3D reservoir in previous research (Daniilidis et al., 2016). These differences can be ascribed to the different model setup, namely the inclusion of methane and the use of a different Equation of State in the 3D model compared to the 2D model presented in this work. The 2D model does not include the physical implications of the brine viscosity, as this was a limitation of the EOS1 that was used. This could change the behaviour of some of the minerals discussed here.

Due to the nature of the coupling between the two models (i.e. the input for the reservoir simulations is pre-defined for the whole simulation period of 50 years), the effect of varying either the injection pH or the injection temperature during the production lifetime could not be evaluated. This could, however, be of interest for a further study. Several of the minerals discussed are affected by either the injection pH or the injection temperature and altering the injection temperature could be an interesting scenario from the operator perspective.

Analyzing a geothermal system with a time-varying production can lead to a better utilization of the reservoir and helps balancing demand and supply in a heat network, resulting in lower CO_2 emissions. The analysis in this paper allows for identifying potential geochemical risks in the development of heat networks which utilize a deep geothermal system. That is, at an early stage of project development and in the absence of production data, this study provides an indication of the temporal behavior with regards to reactive transport at the reservoir level. Moreover, the discussed geochemical implications expand on previously presented risk analysis in literature (Daniilidis et al., 2016). The model setup and results could be refined once data from the exploration well become available and the system development progresses. The presented method can assist in the implementation of a demand driven heat network utilizing a geothermal system.

Conclusions

The combined use of an MPC controller and scenario analysis enable a more efficient integration of a geothermal system in a heating or energy network. An MPC is well suited to controlling the production of a geothermal system due to its ability to take several hard constraints into account. The performance of the controller depends greatly on the demand pattern, the tuning of the controller and the quality of the prediction. Furthermore, the performance is also affected by the lower and upper bound for the rate of change of a geothermal reservoir. Since these bounds are usually unknown, obtaining a method to find these bounds is an interesting open problem. The controller is designed such that new values can easily be implemented once they become available. Since a better performance leads to a smaller storage size it is desirable to investigate how this performance can be optimized.

With respect to the energy production, no cold front breakthrough is encountered after 50 years of production under any considered scenario. The findings further suggest that for the case study of the Groningen geothermal project in Rotliegend sandstone, the use of a variable production rate has no adverse geochemical effects on the reservoir. Moreover, it enables a more efficient use of the geothermal resource by limiting the heat extraction to levels dictated by existing demand.

Reservoir geochemical behavior is affected primarily by flow rate levels, followed by injection pH and injection temperature. The key minerals that affect the injector area are Anhydrite during the first years of production and Dolomite in the following years. Anhydrite dissolution is strongly correlated to an increase in permeability around the injector and is the only considered mineral for which the rate of change is influenced by the flow rate control strategy; higher flow rates lead to faster dissolution but all flow rates eventually cause the same volume fraction to dissolve. Dolomite affects the evolution of the permeability and its change rate is primarily affected by the pH and secondarily by the temperature. An acidic pH favors dissolution and neutral pH precipitation of Dolomite, while lower temperature reduces precipitation and increases dissolution. Consequently, Dolomite becomes a crucial mineral for the temporal system behavior.

The geochemical results are representative of a geothermal system in Rotliegened sandstone in the area of Groningen, NE Netherlands. Nonetheless, the controller design, the simulation of the storage device, the simulation of the reservoir model and the analysis that integrates the control engineering and geochemistry domains is readily applicable to other geological contexts and can aid in a more widespread integration of such systems.

Appendix A

Supporting chemical data for the minerals considered in the geochemical simulations (**Table 4.6**).

Table 4.6. Primary and secondary minerals and their respective reaction mechanisms as described in the TOUGHREACT thermodynamic database.

Mineral	Chemical formula	TOUGHREACT reaction mechanism
Primary		
Quartz	SiO_2	$SiO_2(aq) \rightleftharpoons Quartz$
Albite	$NaAlSi_3O_2$	$Na^+ + 3SiO_2(aq) + AlO_2^- \rightleftharpoons Albite$
K-feldspar	$KAlSi_3O_8$	$K^+ + 3SiO_2(aq) + AlO_2^- \rightleftharpoons K-feldspar$
Dolomite	$CaMg(CO_3)_2$	$Mg^{2+} + Ca^{2+} + HCO_3^{2-} \rightleftharpoons H^+ + Dolomite$
Kaolinite	$Al_2Si_2O_5(OH)_4$	$2H^+ + 2SiO_2(aq) + H_2O + 2AlO_2^- \rightleftharpoons Kaolinite$
Illite	$K_{0.6}Mg_{0.25}Al_{1.8}(Al_{0.5}Si_{3.5}O_{10})(OH)_2$	$1.2H^+ + 0.25Mg^{2+} + 0.6K^+ + 3.5SiO_2(aq) + 0.4H_2O + 2.3AlO_2^- \rightleftharpoons Illite$
Halite	NaCl	$Na^- + Cl^- \rightleftharpoons Halite$
Calcite	$CaCO_3$	$Ca^{2+} + HCO_3^- \rightleftharpoons Calcite + H^+$
Anhydrite	$CaSO_4$	$Ca^{2+} + SO_4^{2-} \rightleftharpoons Anhydrite$
Secondary		
Magnesite	$MgCO_3$	$HCO_3^- + Mg^{2+} \rightleftharpoons H^+ + Magnesite$
Siderite	$FeCO_3$	$Fe_2^+ + HCO_3^- \rightleftharpoons H^+ + Siderite$
Barite	$BaSO_4$	$Ba^{2+} + SO_4^{2-} \rightleftharpoons Barite$
Galena	PbS	$Pb^{2+} + SO_4^{2-} \rightleftharpoons 2O_2(aq) + Galena$
Gypsum	$CaSO_4 \cdot 2H_2O$	$Ca^{2+} + SO_4^{2-} + 2H_2O \rightleftharpoons Gypsum$
Anglesite	$PbSO_4$	$Pb^{2+} + SO_4^{2-} \rightleftharpoons Anglesite$
Iron	Fe	$H^+ + Fe^{2+} + H_2O \rightleftharpoons 0.5O_2(aq) + Iron$
Lead	Pb	$H^+ + Pb^{2+} + H_2O \rightleftharpoons 0.5O_2(aq) + Lead$

Appendix B

The rate expression in TOUGHREACT is described as (Lasaga et al., 1994):

$$r_n = \pm k_n A_n \left| 1 - \left(\frac{Q_n}{K_n} \right)^{\theta} \right|^{\eta} \tag{4.3}$$

with n the mineral kinetic index, k_n the rate constant in moles per unit mineral surface are and unit time (temperature dependent), A_n the specific reactive surface area per kg of $H_2 0$, K the equilibrium constant for the mineral water interaction written for the destruction of one mole of mineral n and Q_n is the reaction quotient. Parameters θ and η must be determined by experiments; most commonly they are taken equal to one. Positive values indicate mineral dissolution and negative values precipitation. A complete mathematical description is documented in (Xu et al., 2006). The required rate constants for equation (4.3) are computed according to (Palandri et al., 2004):

$$\begin{aligned} k = {} & k_{25}^{nu} \exp\left[\frac{-E_a^{nu}}{R} \left(\frac{1}{T} - \frac{1}{298.15} \right) \right] + k_{25}^{H} \exp\left[\frac{-E_a^{H}}{R} \left(\frac{1}{T} - \frac{1}{298.15} \right) \right] a_H^{n_H} \\ & + k_{25}^{OH} \exp\left[\frac{-E_a^{OH}}{R} \left(\frac{1}{T} - \frac{1}{298.15} \right) \right] a_{OH}^{n_{OH}} \end{aligned} \tag{4.4}$$

with k_{25} the rate constant at 25°C, R the gas constant, T the absolute temperature, α the activity of the species and n a constant exponent. Superscripts or subscripts nu, H and OH indicate neutral, acidic and base mechanisms respectively.

The kinetic rate parameters need to be specified for the both the primary and secondary mineral phases that are constrained to kinetic conditions, in order to evaluate equations (4.3) and (4.4). The kinetic data presented are obtained from (Palandri et al., 2004) and are presented in **Table 4.7**. Reactive surface area and grain radius data is obtained from (Xu et al., 2006) and (Bolourinejad et al., 2014). Since the reaction rates of anhydrite and calcite are fast compared to the modelling time, they are assumed to react at equilibrium (Zheng et al., 2009). Additionally, the thermodynamic properties of the chemical species are obtained from the EQ3/6 database (Wolery, 1992). The database data cover a temperature range of 0°C to 300 °C, a pressure range up to several hundreds of bars and is applicable for a brine concentration equivalent of up to 6 molal. Thermodynamic data for the minerals anglesite, barite and lead were further added, obtained from the Thermoddem database (Blanc et al., 2012).

Table 4.7. Relevant parameters for the evaluation of the kinetic rate laws according to equations (4.3) and (4.4) . The rate constant k_{25} is in mol/m^2 , the activation energy E_a in kJ/mol ,the reactive surface A in

cm^2 / g. Where the acidic and/or base mechanisms are not present, the corresponding reaction mechanisms are not considered. Data are obtained from (Palandri et al., 2004).

Mineral	Acid			Neutral		Base			A
Primary	k_{25}	E_a	n(H^+)	k_{25}	E_a	k_{25}	E_a	n(H^+)	
Quartz				1.02e-14	87.7				9.1
Albite	6.92e-11	65	0.457	2.75e-13	69.8	2.51e-16	71	-0.57	9.1
K-feldspar	8.71e-11	51.7	0.5	3.89e-13	38.0	6.31e-22	94.1	-0.823	9.1
Dolomite	0.000646	36.1	0.5	2.95e-08	52.2				9.1
Kaolinite	4.9e-12	65.9	0.777	6.61e-14	22.2	8.91e-18	17.9	-0.472	108.7
Illite	1.05e-11	23.6	0.34	1.66e-13	35.0	3.02e-17	58.9	-0.4	108.7
Halite				0.616595	7.4				9.1
Calcite									
Anhydrite									
Secondary									
Magnesite	4.17e-07	14.4	1	4.57e-10	23.5				9.1
Siderite	0.000646	36.1	0.5	1.26e-09	62.76				9.8
Barite	1.26e-07	30.8	0.22	1.26e-09	30.8				9.1
Galena				4E-11	62.76				12.9
Gypsum				0.001622	0				9.1
Anglesite	2.63e-06	31.3	0.298	3.16e-07	31.3				9.1
Iron				2.0e-12	0				121.8
Lead									

Appendix C

Dolomite dissolution/precipitation is primarily affected by the pH (**Figure 4.9**) by secondarily also by the injection temperature (**Figure 4.13**). Higher injection temperature leads to more precipitation and less dissolution.

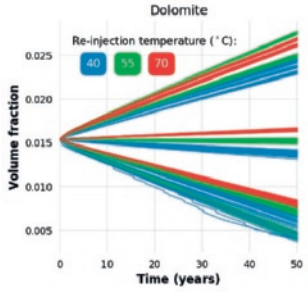

Figure 4.13. Alternative coding of the dolomite volume fraction.

Chapter 5

TECHNO-ECONOMIC UNCERTAINTY

This chapter is published as:

Daniilidis, A., Alpsoy, B. and Herber, R., 2017, "Impact of technical and economic uncertainties on the economic performance of a deep geothermal heat system", *Renewable Energy,* 114B, 805-816.

Abstract

This paper presents a techno-economic analysis of a deep, direct use geothermal heat system in a conductive geological setting (Groningen, NE Netherlands). The model integrates the previously discussed uncertainties of the initial reservoir state, geological and operational conditions with the economic uncertainties. These uncertainties are incorporated in the form of probability distributions and 20,000 iterations of the model are performed over a project lifetime of 40 years. A combination of Ex-Ante and Ex-Post criteria are used to evaluate the economic performance of the system based on the Net Present Value (NPV), Levelised Cost of Heat (LCOH) and Expected Monetary Value (EMV). The sensitivity analysis highlights the load factor (effective flowrate) as the most important parameter for the economic performance and energy costs. However, the differences between the NPV and LCOH sensitivities highlight the importance of using both metrics for the economic performance of such systems. The presented project remains economically challenging, exhibiting a 50% probability of marginal revenues over its lifetime. Systematic insights are drawn with regard to potential improvements of technical and economic aspects of such geothermal heat systems.

Introduction

District heating and heat energy networks are gaining importance in the provision of renewable energy (Lund et al., 2014; Rezaie and Rosen, 2012; Sayegh et al., 2016). At the same time market penetration of direct use geothermal energy remains relatively restricted (Tselepidou and Katsifarakis, 2010) and a large potential for direct use geothermal remains untapped (Agemar et al., 2014).

Being largely in its implementation phase, geothermal energy is now considered a mainstream technology. It is however still expected to accelerate in the near future (Lund and Boyd, 2015) and possibly saturate by 2030 (Zheng et al., 2015). The number of direct use installations for geothermal energy and investments in geothermal projects have continuously increased in the 21st century, but the development rates are deemed slow (Lund and Boyd, 2015).

As the scientific understanding of a diversity of low enthalpy fields and analysis methods are evolving (Mottaghy et al., 2011; Saeid et al., 2014; Saeid et al., 2015; Vogt et al., 2013; Willems et al., 2017b), the interaction between the technical and the economic aspects becomes more pertinent for successful project implementation and wider dissemination of installed deep geothermal systems for direct use. The importance and impact of technical and economic parameters remains crucial for the realization of planned systems.

Promoting the sustainability agenda within renewable energy projects encourages the efficient use of geothermal resources (Shortall et al., 2015). Previous research has highlighted points of exergy destruction that are important for optimizing the energy efficiency of existing systems (Keçebaş, 2011; Yamankaradeniz, 2016). In order to expand installed geothermal capacity, project level studies are needed to address the complexities and inherent uncertainty of geothermal field development (Agemar et al., 2014; Shortall et al., 2015).

Economic feasibility is identified as the main hindering aspect of direct use geothermal systems, with payback periods extending up to 33 years (Thorsteinsson and Tester, 2010). Drilling is considered a major cost factor and increasing the success rates would benefit geothermal project developments (Thorsteinsson and Tester, 2010). Additionally, the economics of geothermal energy production (electricity or heat) are usually addressed in a top down manner (Goldstein et al., 2011b; Limberger et al., 2014; van Wees et al., 2012), contrary to the commonly accepted need for project level geotechnical studies. Thus, while the insights from a top down analysis are valuable, they do not clarify the interplay between the geological context, the specific economic conditions of a project

and the contextual parameters, such as the regulatory framework with its possible incentives and restrictions (Sayegh et al., 2016).

Due to the high initial costs and uncertainties related to geothermal development (Beckers et al., 2014), scenario analysis is essential for understanding the economic viability of projects (Gelegenis, 2009; Limberger et al., 2014). A recent study has analysed the effect of doublet well spacing on the Net Present Value (NPV) of a geothermal doublet in the West Netherlands Basin (WNB) (Willems et al., 2017a). However, literature on direct use, deep geothermal projects lacks an analysis that incorporates both technical and economic uncertainty to the assessment of energy generation costs. Moreover, there is no clear prioritization between the two in the form of a sensitivity analysis at the project level; no bottom-up cost estimation is presented.

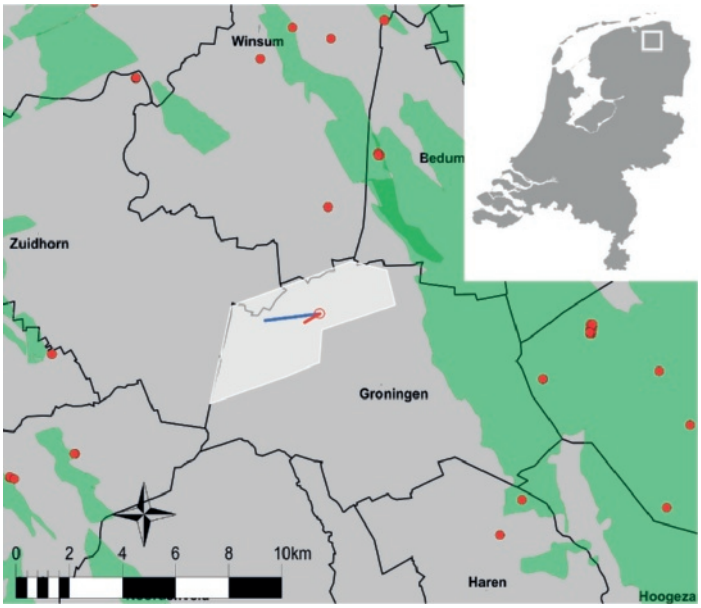

Figure 5.1. Location of the Groningen geothermal project. The white shaded area outlines the geothermal concession, the red and blue lines the injector and producer respectively, the green shaded areas are existing gas fields and the red dots represent existing gas wells.

In this paper a techno-economic model is presented based on the Groningen geothermal project (**Figure 5.1**). It builds on previous work regarding initial state, geological and operational uncertainty (Daniilidis et al., 2016) and incorporates the insights regarding resource efficiency and coupling of a direct use geothermal system to heat networks (Daniilidis et al., 2017). In this work economic and project development uncertainties are further included in order to establish a tighter linkage between technical and economic aspects for the Groningen geothermal project. This generates comprehensive insights on a project level, regarding the development of direct-use, deep geothermal systems in

conduction dominated geological settings. The analysis employs the Levelized Cost of Heat (LCOH), Net Present Value (NPV) and Expected Monetary Value (EMV) indexes; it is thus addressing the center of the renewable energy nexus, linking geothermal technology with the policy/incentive framework.

Methods and model description

The results are evaluated using Ex-Ante (beforehand) and Ex-Post (afterwards) criteria. The Ex-Ante criteria (well failure) lead to a project stop. After that point further computations are not carried out. Ex-Post criteria include the LCOH and the project NPV at the end of the project period, as well as the Expected Monetary Value (EMV) of the project.

The model is developed by making use of the Monte Carlo Simulation software GoldSim (GoldSim, 2017). Uncertainty regarding any of the technical or financial aspects considered is implemented in the model in the form of probability distributions. This allows for an Ex-Post overall evaluation of the outcomes. The probability characteristics of each input are detailed in the following sections.

Exploration

The Exploration phase is the initial reconnaissance phase of the project. Interest in generating geothermal energy is identified and initial studies commence. An application for an exploration-drilling license is made and detailed geological studies are carried out. During this phase modelling studies might also be carried out to locate prospective aquifers, estimate reservoir volume and characteristics, forecast energy production and to support system design and dimensioning. Two major elements are of importance, namely the duration of the exploration phase and the attributed cost (**Table 5.1**).

Table 5.1. Exploration phase inputs. Bold values indicate the base case for the sensitivity analysis presented in the results section.

Element	input type	distribution	resampled	value	Unit
Exploration phase duration	probability	triangular	once at iteration start	3-**4**-5	yrs
Exploration phase cost	probability	triangular	once at iteration start	180-**200**-280	k€/yr

Development

The Development phase includes the construction of the heat network, drilling the wells and purchasing equipment necessary for operating the system. The major capital expenditures for the project occur during this phase (see also LCOH sub-chapter). The model inputs used for this module are summarized in **Table 5.2**.

Heat network

The project heat network has a length between 20 and 30km and has an average cost of 1000 €/m of installed network, including materials.

Drilling

Two different formulas are considered for calculating the well drilling costs. The first is the ThermoGIS equation for well costs (Limberger et al., 2014; van Wees et al., 2012):

$$C_{well} = s \cdot (0.2 \cdot Z_R{}^2 + 700 \cdot Z_R + 25000) \cdot 10^{-6} \tag{5.1}$$

where s is a variable representing the well scaling factor, Z_R is the measured depth (MD) and costs are calculated in euros. An s value of 1.72 is used for the calculations.

The second formula is the geothermal well cost presented by Lukawski (Lukawski et al., 2014). The authors here mention that despite differences in complexity, geothermal and oil wells have similar costs. The authors do however provide a geothermal specific cost formula and recommend calculating cost on an individual well basis :

$$C_{well} = 1.72 \cdot 10^{-7} \cdot z^2 + 2.3 \cdot 10^{-3} \cdot z - 0.62 \tag{5.2}$$

where z represents measured depth (MD) and the costs are in million dollars. Dollars are converted to euros according to a rate of 0.93 €/$.

Due to the small differences between the two formulas in calculating the well drilling costs (**Figure 5.2**), only the ThermoGIS formula is used in the model in this paper.

In addition to the calculated well drilling costs, a contingency is added to cover possible delays or difficulties that could be encountered during drilling and could increase the overall cost. It is assumed that the injector is drilled first therefore the injector contingency can only increase the costs. The drilling of the producer that follows could potentially benefit from the insights of the first well, therefore the contingency could result in either a reduction or increase of its calculated costs (see also **Table 5.2**).

The wells are insured against technical failure and/or suboptimal performance after they have been drilled (Rijksdienst voor Ondernemend Nederland, 2015) and the insurance

premium is included in the cost. Additional to the well cost some expenses are also made for the preparation of the drilling location and surface facilities around the wells.

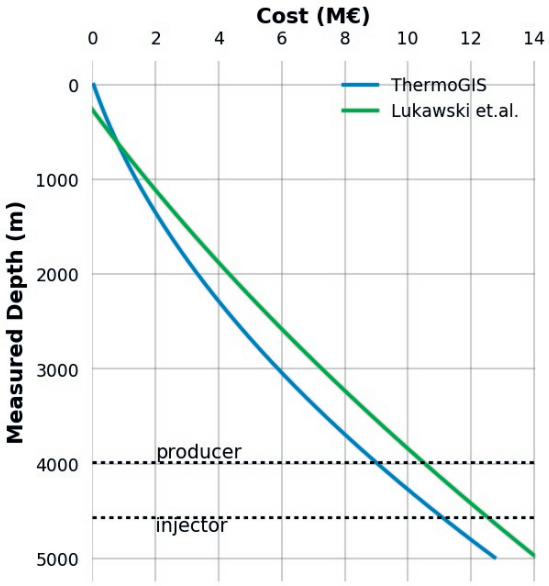

Figure 5.2. Well cost calculation formulas considered. Specifications of the wells, as well as their trajectories are derived from the Groningen project (Boersma and Brinkgreve, 2014; Daniilidis et al., 2016).

Furthermore, successful well drilling is assigned to a certain probability. This probability only takes into account the technical success rate (70% for successfully drilling to a Rotliegend target) in the Netherlands and is based on historical gas well data (EBN, 2015). After a successful first well (injector) we consider the success rate of the second well to increase to 90% (see **Table 5.2**). The combined Probability Of Success (POS) for the doublet is therefore 63%. In the event of a failure for the first well, or of a successful first well and a failed second well, the project stops a year later.

Equipment

Necessary for the operation of the geothermal system are an Electrical Submersible Pump (ESP), a heat exchanger and a gas separation unit and these units are acquired during the development phase.

Production and operation

This module computes the generated heat, the possible gas produced by the system and the doublet pressure levels. Reservoir permeability, gas saturation and pressure depletion are differentiated in three values each, as discussed in previous work (Daniilidis et al., 2016).

Table 5.2. Development phase inputs and specifications. Bold values indicate the base case for the sensitivity analysis presented in the results section.

Element	input type	distribution	resampled	value	Unit
network length	probability	uniform	once at iteration start	20-30	km
network cost	probability	triangular	once at iteration start	800-**1000**-1200	€/m
ESP cost	data	-	-	800	k€
heat exchanger	data	-	-	100	k€
gas separation unit	data	-	-	210	k€
producer well contingency	probability	triangular	once at iteration start	100-**120**-120	%
injector well contingency	probability	triangular	once at iteration start	92.5-**100**-107.5	%
production well MD	data	-	-	3980	m
injection well MD	data	-	-	4562	m
production well success	probability	boolean	once at iteration start	70% success	%
injection well success	probability	boolean	once if successful production well	90% success	%
drilling insurance	data	-	-	1	M€
abandonment cost per well	data	-	-	1	M€
drilling location cost	probability	triangular	once at iteration start	1.5-**1.5**-2	M€
development duration	probability	triangular	once at iteration start	2-**3**-4	yrs

Heat production

The capacity of the doublet is defined according to:

$$Cap_{eff} = Cap_{inst} \cdot (\eta_{exch} \cdot \eta_{transm}) \tag{5.3}$$

where Cap_{eff} the effective maximum power output of the doublet (after the efficiency losses), Cap_{inst} is the doublet capacity, η_{exch} the heat exchanger efficiency and η_{transm} the transmission efficiency.

In addition to the efficiency losses in the exchanger and transmission the heat demand exhibits a seasonal variation on a yearly basis. The predicted hourly demand is shown in **Figure 5.3**a. In accordance with the doublet capacity, only part of the demand is covered by the geothermal system; for this part, the average monthly values are computed and the ratio of the monthly demand to the maximum demand covered by the geothermal system (**Figure 5.3**b) is used to scale the production level accordingly by regulating the flow rate.

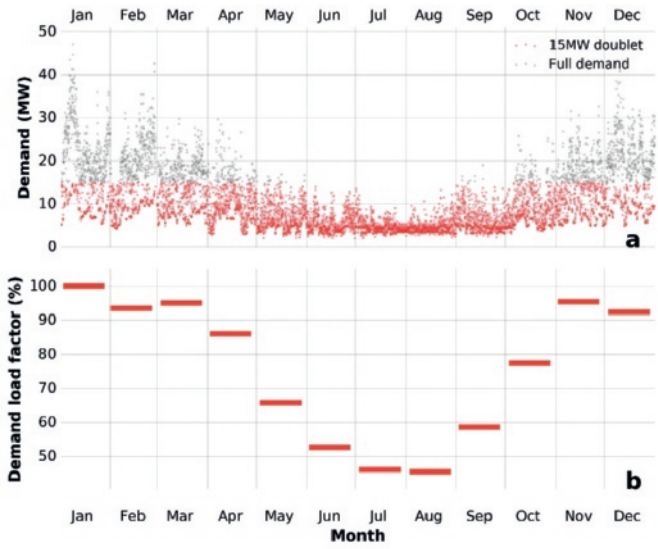

Figure 5.3. Hourly demand from the Groningen city project and the part covered by the doublet (a) and respective monthly demand load factor (b). The latter is calculated as the ratio of the average production level per month, divided by the maximum production level.

Consequently, the required flow rate level is calculated according to:

$$Q = \left(\frac{Cap_{eff}}{\Delta T \cdot C_{brine}} \right) \cdot f_{m_{seasonal}} \tag{5.4}$$

where Q is the flowrate (m^3/s), ΔT is the temperature difference between producer and injector wells, C_{brine} the volumetric heat capacity of the brine $\left(J/m^3 \cdot K\right)$ and

$f_{m_{seasonal}}$ is the seasonal demand at month m. The brine volumetric heat capacity calculations are detailed in **Appendix A**.

Pump and pressure

The pressure of the doublet is calculated as a function of the flow rate and the reservoir permeability. The mean values and standard deviations for each discrete flow rate value are inferred through statistical analysis of the dataset in Daniilidis et.al. (2016), presented in Appendix B (**Figure 5.12**). For the same reservoir permeability value, a second order polynomial regression analysis is performed on the dataset **(Figure 5.4)**. The derived formula is used to calculate the effective pressure difference between the wells, depending on the reservoir permeability input selected.

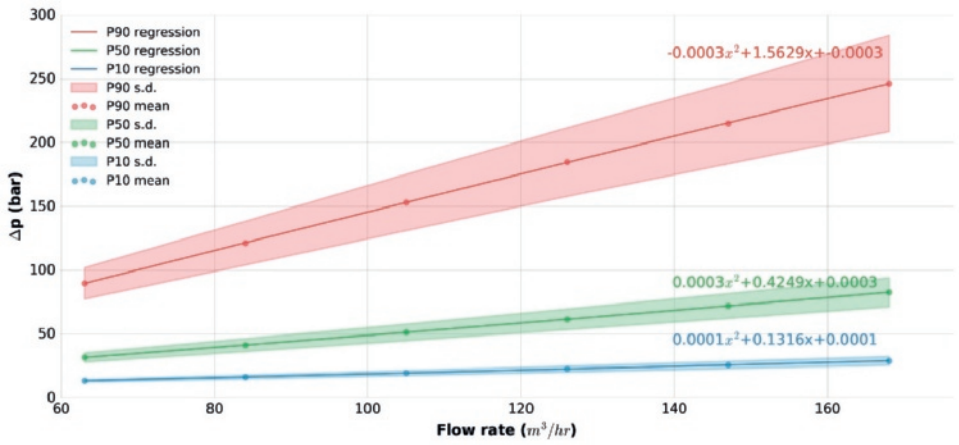

Figure 5.4. Analytical formulas for calculating the pressure difference levels in the model. The data are based on the output of the 3D reservoir model for Groningen (Daniilidis et al., 2016).

The ESP power requirement (in Watts) is calculated as follows:

$$P_{power} = \frac{\rho \cdot g \cdot Q \cdot \Delta p}{p_{hydro} \cdot \eta} \tag{5.5}$$

In which ρ is the fluid density (kg/m^3), g is the gravity acceleration (m/s^2), Q is the flow rate (m^3/s), Δp is the pressure difference (bar), p_{hydro} the hydrostatic pressure gradient (bar/m) and η the pump efficiency. The ESP is replaced when a failure occurs and the replacement results in a downtime of 15 days during which no energy is being produced. The income not generated due to the downtime is added as part of the pump replacement costs.

Table 5.3. Production module inputs. Bold values indicate the base case for the sensitivity analysis presented in the results section.

Element	input type	distribution	resampled	value	Unit
Injection temperature	probability	discrete	once at iteration start	equal probability **40**/55/70	°C
Reservoir Permeability	probability	discrete	once at iteration start	25%:P90 50%: **P50** 25%: P10	-
Production temperature	data			120	°C
Doublet temperature loss	probability	uniform	daily	min: 2 max: 10	°C
Desired capacity	probability	discrete	once at iteration start	equal probability 10/**12.5**/15	MW
High temperature household equivalents	data	-	-	10000	-
Low temperature houses (fraction of HT houses)	data	-	-	15	%
transmission efficiency	probability	normal	daily	mean: **85** s.d.: 3.5	%
Heat exchanger efficiency	probability	normal	daily	mean: **90** s.d.: 1.5	%
Pump efficiency	probability	normal	daily	mean: **65** s.d.: 2.5	%
Pump failure rate	probability	normal	resampled when an ESP is installed	mean: **0.2** s.d.: 0.04	1/yr
Reservoir gas saturation	probability	discrete	once at iteration start	equal probability **5**/10/15	%
Reservoir pressure depletion	probability	discrete	once at iteration start	equal probability **0**/100/200	bar
Gas production	probability	normal	daily	based on permeability and gas saturation (see Appendix B)	(m^3/m^3)

Gas production

Gas production as a function of permeability and flow rate is calculated according to the statistical analysis of the dataset in Daniilidis et.al. (2016), presented in Appendix B. Data points and their mean values and standard deviations are presented in **Figure 5.13**. Depending on the reservoir permeability, gas saturation input and the production duration, the corresponding mean values and standard deviations are applied.

Economics

The Economics module computes all financial indexes based on the inputs regarding expenses and the computed revues and annuities. A 40 year period is chosen for the model, considering that no production temperature drop is expected within this period (Daniilidis et al., 2016); furthermore, the production duration of circa 35 year is considered as a minimum length for developing a geothermal system. Economic inputs are summarized in **Table 5.4**.

Levelised Cost Of Heat

The economic outlook of the project is evaluated based on the Levelised Cost Of Heat (LCOH) index and the Net Present Value (NPV) of the project. The LCOH is defined as:

$$LCOH = \frac{\sum_{t=1}^{n} \frac{CapEx_t + OpEx_t}{(1+r)^t}}{\sum_{t=1}^{n} \frac{Heat_t}{(1+r)^t}} \tag{5.6}$$

where $CapEx$ and $OpEx$ are the respective Capital and Operational expenses in year t, r is the discount rate and $Heat$ is the generated energy in year t.

Net Present Value

The NPV is calculated as:

$$NPV = \sum_{t=0}^{n} \frac{CF_t}{(1+r)^t} \tag{5.7}$$

where CF is the net cash flow (expenses- revenues), t is the year and r is the discount rate..

Table 5.4. Economic module inputs. Bold values indicate the base case for the sensitivity analysis presented in the results section.

Element	input type	distribution	resampled	value	Unit
OpEx%	data	-	-	5	%/yr
inflation rate	data	-	-	1.5	%
discount rate	data			7	%
interest rate	data			2.5	%
depreciation rate	data			5	%/yr
gas heat price	probability	normal	daily	mean: **23.19** s.d.: 0.10	€/GJ
geothermal to gas heat price ratio	data	-	-	90	%
natural gas producer price	probability	normal	daily	mean: **0.25** s.d.: 0.01	€/m^3
subsidy amount	data	-	-	0.045	€/kWh
electricity price	probability	normal	daily	mean: **0.08** s.d.: 0.01	€/kWh
connection fee	data			1000	€
usage fee	data			300	€/yr

Expected Monetary Value

The Expected Monetary Value (EMV)is defined as (Rose, 1993; Wellmer et al., 2007):

$$EMV = POS \cdot NPV + (1 - POS) \cdot COF \tag{5.8}$$

Where POS is the Probability of Success for the doublet drilling (with a value of 0.63, see also sub-section drilling and Table 5.2) and NPV and Cost Of Failure (COF COF) are the monetary values for a successful and a failed doublet drilling respectively. The COF has a negative value (see also **Table 5.5**).

Expenses

The expenses are the sum of the capital and operational expenses. Capital Expenses (CapEx) are discrete investments; these include the costs for the exploration phase, the drilling of the wells, the construction costs for the heat network and drilling facilities, equipment (heat exchanger, gas separator) and the recurring costs for the ESP. The

Operational Expenses (OpEx) are computed as a percentage of the CapEx with the pump power electricity added; this is purchased at the electricity price for industrial use (**Figure 5.5**a). The discounted project cash-flow is corrected for inflation, as well as financing interest rate costs. Lastly the depreciation period is calculated based on the depreciation rate. No funding or taxing scheme is considered in our calculations and therefore, depreciation costs are not re-financed.

Revenues

The revenue sources include the income from the delivered heat, possible produced gas, as well as the income from the SDE+ (Sustainable Duurzame Energieproductie) subsidy scheme for renewable energy in the Netherlands (Rijksdienst voor Ondernemend Nederland, 2016). The subsidy for the delivered heat is for up to 5500 full-load equivalent

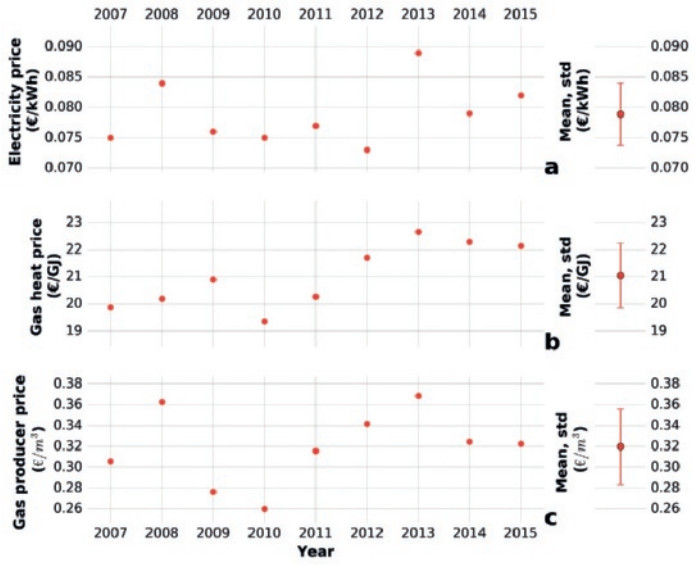

Figure 5.5. Electricity prices for industrial use (a), gas generated heat prices (b) and gas producer prices (c). Data source:(CBS, 2016)

hours and is available for a maximum period of 15 years (Rijksdienst voor Ondernemend Nederland, 2016). The delivered heat is cascaded at two different levels: high temperature (HT) and low temperature (LT). The cascading scheme assumes that a percentage of the HT heat return temperature is still sufficient to be sold for LT heat usage at half the HT price. Additionally, there is a fixed one-off connection fee and a usage fee per year for the service.

In the Dutch context the heat price of any energy source cannot be higher than the gas produced heat (ACM, 2017). Therefore the geothermal heat prices are computed as 90%

of the cost for heat generated by gas combustion. The household prices for gas generated heat, gas price for producers and electricity prices are derived statistically from historical data (**Figure 5.5**b&c).

Results

The model is run in using 20,000 iterations. Firstly, the energy production and system performance indicators are presented, followed by the economic indexes. Lastly, for a selection of the result indexes a sensitivity analysis is presented.

Energy production

The annually produced heat demonstrates little variation over the years, with the mean and percentile values exhibiting a clear annual pattern that remains constant throughout the production lifetime (**Figure 5.6**a). Consequently, the cumulative heat production (**Figure 5.6**b) also manifests a narrow range for the 90% to Max percentiles. Contrary to this, the annual and cumulative gas production levels respectively (**Figure 5.6**c&d) prove to be highly uncertain, exhibiting a wide range of values for the percentile interval 90% to Max. This result is in line with the uncertainty level present in the model with regard to gas related variables (e.g. gas saturation, gas production volume, see also **Table 5.3**). The COP of the system exhibits a mean value that varies seasonally between 5 and 10 (**Figure 5.6**e), again demonstrating very thick percentiles between 90% and Max values. These wide percentiles are attributed to the impact of pressure depletion and reservoir permeability on the required pumping energy (Daniilidis et al., 2016).

The narrow range of values in the 90% to Max percentile band for the heat production compared to the gas production (**Figure 5.6**b&d respectively) can also better explain the percentiles of the economic parameters; gas production related uncertainty heavily affects the value range of the economic percentiles, despite the fact that heat revenues remain more important than gas revenues throughout the production time (see also next sub-chapter).

Economic results

The cumulative discounted cashflow provides a comprehensive overview of the project finances taking into account all financial parameters and annuities. The mean includes all possible input variable values including the occasions for which any of the two wells has failed during drilling. A large decrease is observed during the construction phase before

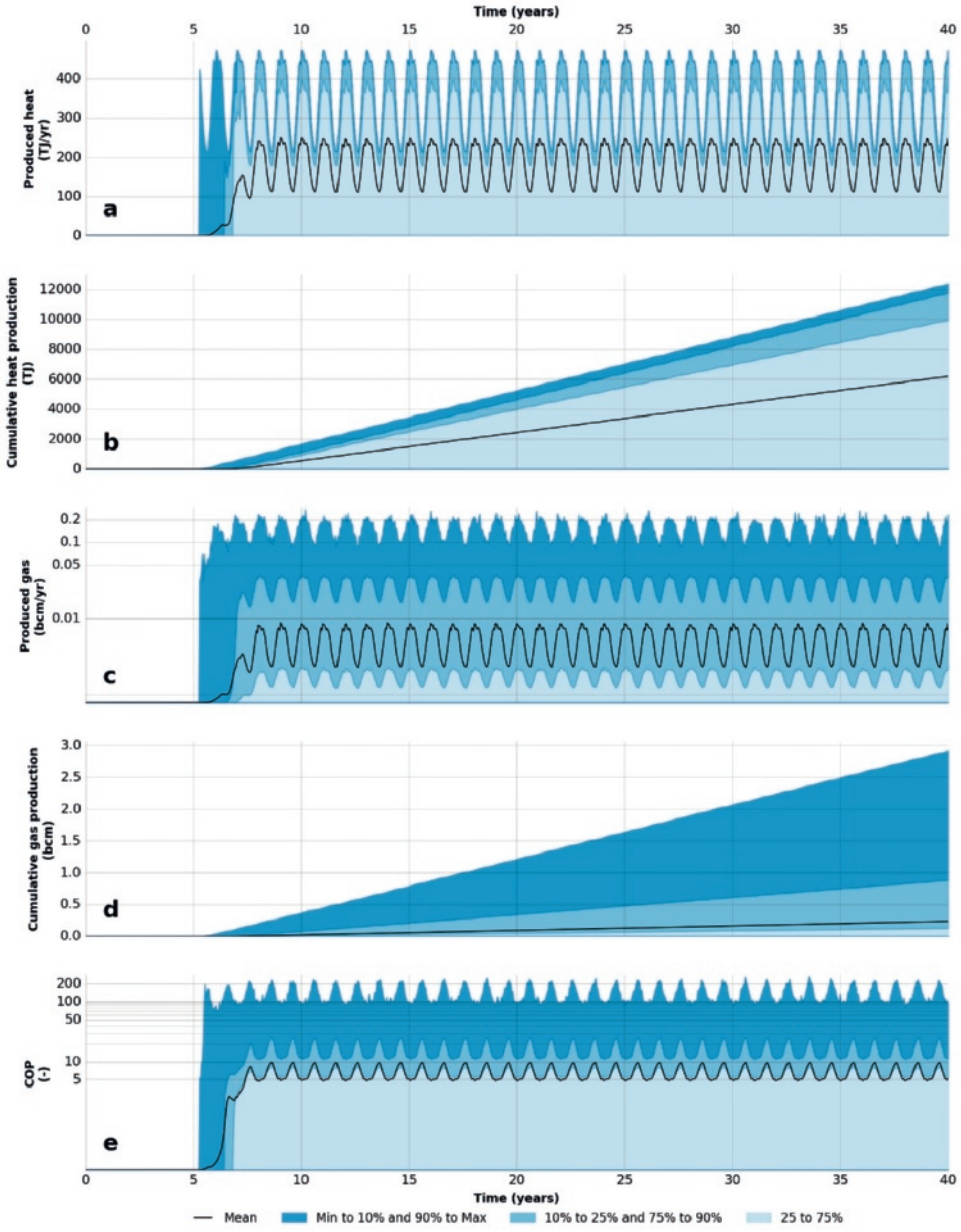

Figure 5.6. Heat production per year (a), cumulative heat production (b), yearly gas production (c), cumulative gas production (d) and Coefficient Of Performance (COP), defined as the ratio of generated heat to pumping energy (e). Note that the scale on (c) and (e) is not linear.

the first 5 years of production, after which the cashflow starts to slowly recover as energy and income is generated. Under the most favorable conditions profitability is achieved around year 10, while the mean of the ensemble achieves profitability around year 27.

The lower part of the range remains flat; this is caused by the failure of any of the two wells that ultimately leads to a project halt and no further economic calculations (see also sub-chapter Drilling).

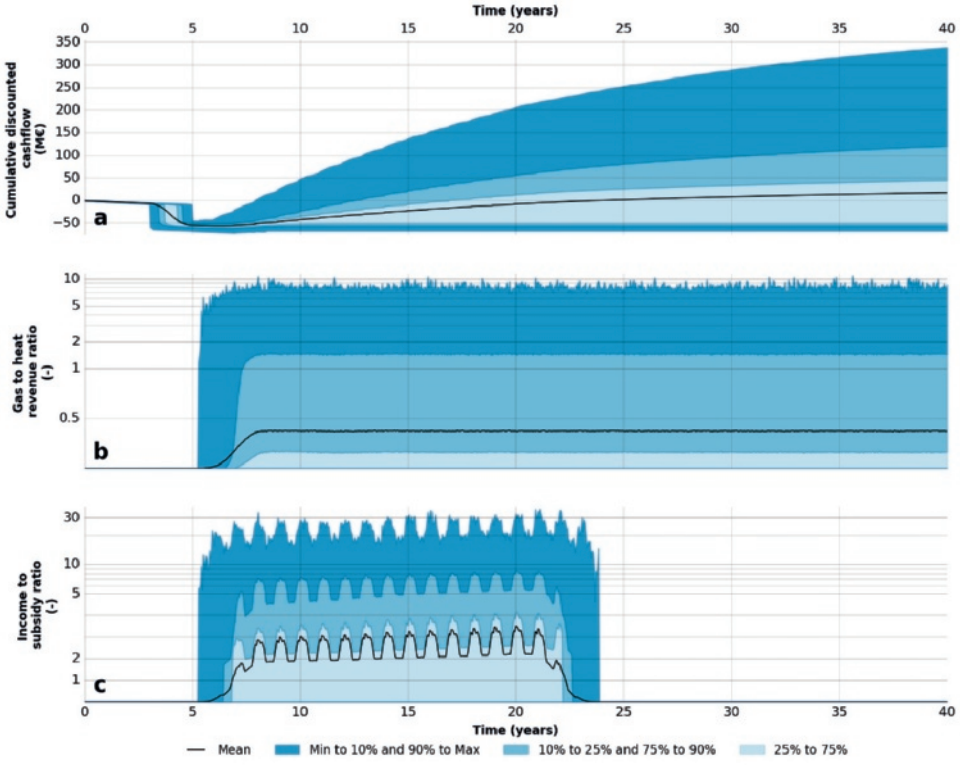

Figure 5.7. Economic analysis with cumulative discounted cashflow (a), the ratio of gas revenues to heat revenues (b) and the ratio of income to subsidy (c) with their respective percentiles for 20,000 iterations. Note that the scale on (b) and (c) is not linear. The gas to heat revenue ratio does not include any income that might be generated as a result of subsidized heat generation; only the direct income from heat delivery is considered. The ratio of income to subsidy includes both heat and gas generated income.

When production of heat and gas is initiated the ratio of gas to heat revenues reveals that for the mean of the ensemble heat remains the dominant income source (**Figure 5.7**b); the mean ratio exhibits a heat generated income that is about 2.5 times more than that of gas generation. The sharp transitions of the index are attributed to the daily sampling interval of the gas production volumes (see **Figure 5.13**). Nonetheless and for all percentiles the ratio remains constant throughout the lifetime.

Once production begins the income to subsidy ratio is also computed for a period of up to 15 years following the initial production time (see also Revenues sub-section). The generated income remains the main source of revenue and is up to circa threefold larger than the provided subsidy (**Figure 5.7**c). The seasonal load factor is clearly observed in

the results (see also **Figure 5.3**b); during periods of low load factors (i.e. centered around the summer period) the subsidy proves more important, as exhibited by the lower income to subsidy ratio. The larger peaks are attributed to the possibility to produce higher gas volumes together with the heat. The heat and gas income becomes progressively more important over subsidy as a revenue source; this is evident by the marginal upward trend of the mean over time within the 15 years for which the subsidy is available (**Figure 5.7**c).

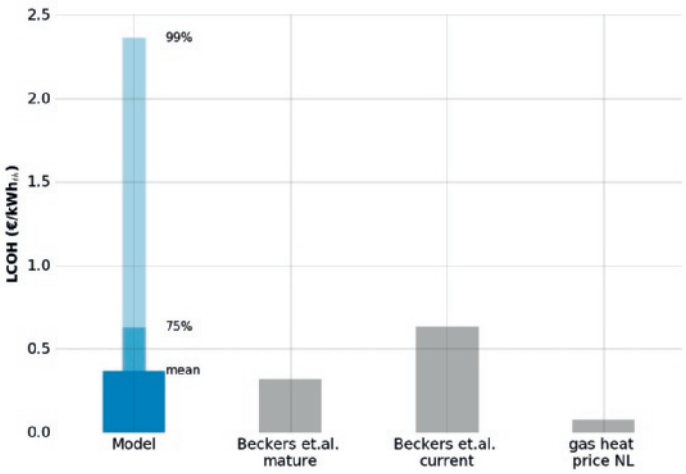

Figure 5.8. LCOH index from the model compared to literature sources and gas heat price in the Netherlands. For district heating systems of medium grade geothermal gradients an LCOH of 0.32€/kWh_{th} is reported for a commercially mature technology and 0.63€/kWh_{th} for current technology (Beckers et al., 2014). The gas heat price for the Netherlands is the average over the last 9 years (period between 2007 and 2015, see also **Figure 5.5**)(CBS, 2016).

The LCOH index shows a mean value of 0.36€/kWh_{th} which is not very different from the projected LCOH of commercially mature district heating systems (**Figure 5.8**). Nonetheless, the LCOH remains fivefold more expensive than gas generated heat in the Netherlands. The cumulative discounted cashflow is also alternatively displayed by discriminating the iterations with both wells successful and those with any of the two wells having failed (**Figure 5.9**a). The adjacent frequency histogram reveals that for both successful wells, most iterations are clustered in the interval with NPV's between zero and 50M€, while for any failed well values are clustered slightly lower than -50M€ (**Figure 5.9**b). Part of the assemblage for the successful wells (circa 5%) still generates a negative NPV after 40 years. The Cumulative Distribution Function (**Figure 5.9**c) reveals the respective probability of occurrence for the two cases. The EMV values highlight that at 50% probability the project will yield marginal profit (**Table 5.5**), while at 90% probability the deficit will be greater than 8M€. A positive value of 71M€ or higher only has a 10% probability of occurring.

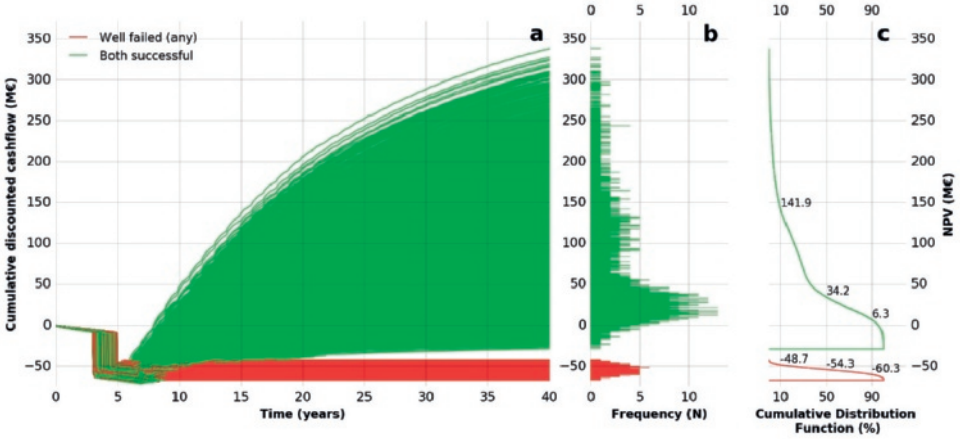

Figure 5.9. Cumulative discounted cashflow of 20,000 iterations over the 40 year duration (a), their respective frequency histogram for the NPV at year 40 (b) and the Cumulative Distribution Function (CDF) at year 40 (c) presented separately for the case of both wells being successfully drilled and any of the two wells having failed.

Table 5.5. Calculation of the EMV considering the CDF values of P10, P50 and P90 (10%, 50% and 90% probability) as presented in **Figure 5.9**.

	Probability		
	P10	P50	P90
POS / (1-POS)		0.63 / 0.37	
NPV	141.9	34.2	6.3
COF	-48.7	-54.3	-60.3
EMV	71.4	1.5	-18.4

Sensitivity

The sensitivity analysis allows for a relative ranking of the input effects and their respective probability ranges or values. It should be noted that the POS of the wells is not part of the sensitivity analysis since by definition it does not exhibit a continuous value range and therefore would not yield a ranged outcome. The absence of the POS in the sensitivity analysis accounts for the slightly different central values for both the NPV and the LCOH compared to the mean values presented earlier (**Figure 5.7** and **Figure 5.8**).

The importance of the load factor, indirectly reflected in the range of the effective flowrates, is the most dominant; higher flowrate can increase the NPV by more than threefold, while a lower one can decrease it down to deficit levels. This aspect highlights the importance of a carefully selected load factor profile throughout the year. The sensitivity of the NPV to the reservoir gas saturation is also prominent, with higher saturation leading to a higher NPV. The volume of gas can significantly affect the

available income (**Figure 5.10**). The fact that the NPV is more sensitive to heat production (directly related to flow rate level) compared to gas corroborates the ratio of gas to heat income being lower than one (see **Figure 5.7**).

The significance of the load factor and consecutively the flow rate is in line with previous findings where the flow rate level was the second most significant parameter to affect the NPV (Willems et al., 2017a); it should be noted that the considered system was different in several ways (most notably production temperature, drilling depth and well spacing).

For the next three inputs (discount rate, OpEx percentage, injection temperature) an increasing value leads to an NPV decrease. At the same time their influence range is almost symmetrical to the central value of the input range. The same can be said for the following four inputs (HT households, network length, gas heat consumer price and network cost). The ranking of the gas heat price which indirectly affects the price of the geothermal heat through the geothermal to gas heat price ratio (see also sub-section Revenues and **Table 5.4**), together with that of the reservoir gas saturation, can explain the high values for the 90% to Max percentiles of the cumulative discounted cashflow results (**Figure 5.7**). The network length and reservoir pressure depletion that follow have very similar influence ranges (+/-35%).

The LCOH sensitivity plot reveals a slightly different influence ranking of the inputs, since the LCOH is not affected by any gas related parameters (see also sub-chapter LCOH). The effective flowrate, which directly corresponds to the produced amount of heat, proves the most influential (**Figure 5.11**) just like for the NPV. Higher flowrate reduces the LCOH by ~35% compared to the 50% increase it exhibited on the NPV index. This could be attributed to the fact that the NPV index also considers the revenues while the LCOH does not; therefore, since flow rate is related to the amount of heat generated and sold it

has an impact on the revenues. Injection temperature follows, with an injection temperature of 40°C increasing the extracted energy and thus reducing the LCOH by circa 20%. A lower injection temperature increases the extracted energy and the overall COP, thereby improving the ratio of expense to generated energy. The percentage of OpEx, reservoir permeability and transmission efficiency follow.

The OpEx percentage has the second highest potential to further reduce the LCOH after flowrate. Moreover, the OpEx percentage together with the inflation rate and network costs are the only economic parameters with a large influence in the LCOH; this highlights the fact that the LCOH index is mostly controlled by the operational, geological and technical aspects. The network cost and the temperature loss of the doublet complete the most significant influencing inputs, after which the impact becomes less significant.

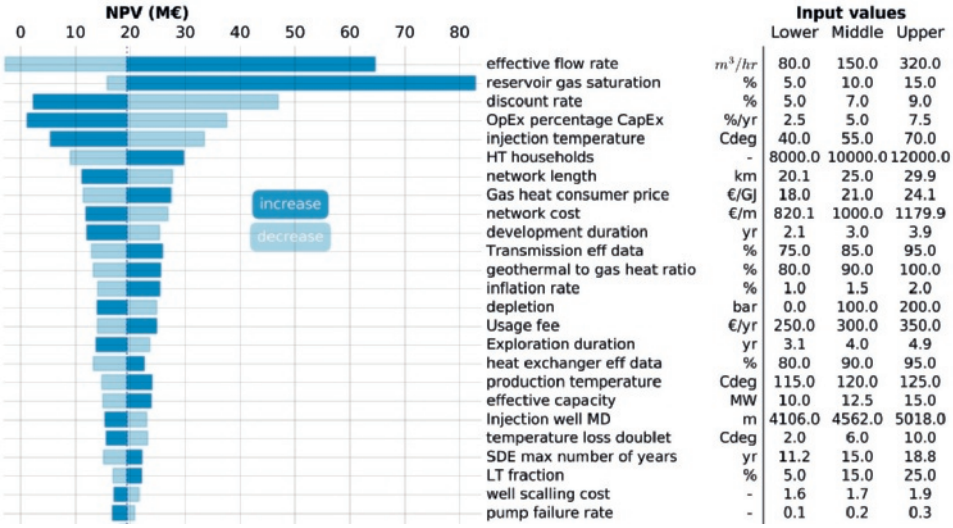

		Input values		
		Lower	Middle	Upper
effective flow rate	m^3/hr	80.0	150.0	320.0
reservoir gas saturation	%	5.0	10.0	15.0
discount rate	%	5.0	7.0	9.0
OpEx percentage CapEx	%/yr	2.5	5.0	7.5
injection temperature	Cdeg	40.0	55.0	70.0
HT households	-	8000.0	10000.0	12000.0
network length	km	20.1	25.0	29.9
Gas heat consumer price	€/GJ	18.0	21.0	24.1
network cost	€/m	820.1	1000.0	1179.9
development duration	yr	2.1	3.0	3.9
Transmission eff data	%	75.0	85.0	95.0
geothermal to gas heat ratio	%	80.0	90.0	100.0
inflation rate	%	1.0	1.5	2.0
depletion	bar	0.0	100.0	200.0
Usage fee	€/yr	250.0	300.0	350.0
Exploration duration	yr	3.1	4.0	4.9
heat exchanger eff data	%	80.0	90.0	95.0
production temperature	Cdeg	115.0	120.0	125.0
effective capacity	MW	10.0	12.5	15.0
Injection well MD	m	4106.0	4562.0	5018.0
temperature loss doublet	Cdeg	2.0	6.0	10.0
SDE max number of years	yr	11.2	15.0	18.8
LT fraction	%	5.0	15.0	25.0
well scalling cost	-	1.6	1.7	1.9
pump failure rate	-	0.1	0.2	0.3

Figure 5.10. Sensitivity analysis for the NPV index with respect to the model inputs in decreasing order of importance. The respective values of the NPV are shown on the left-hand side, while the respective input ranges are denoted on the right hand side.

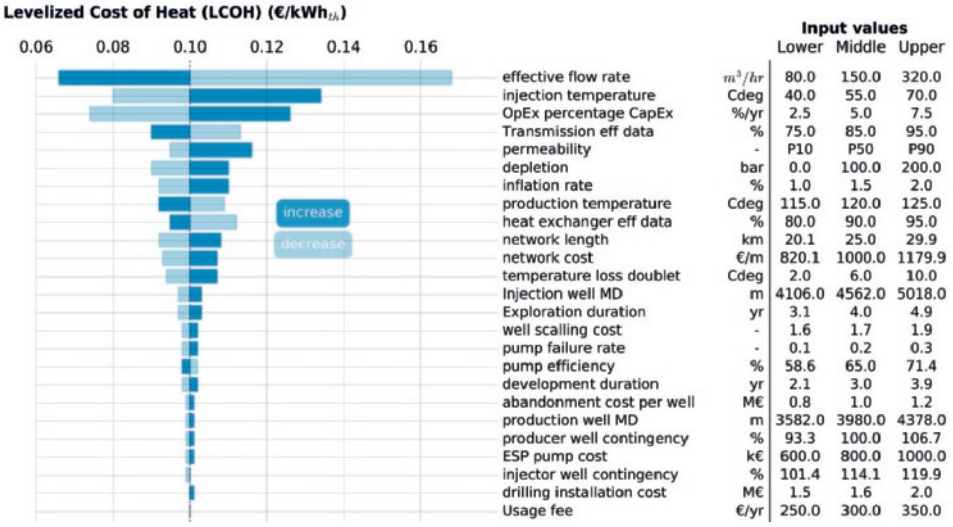

		Input values		
		Lower	Middle	Upper
effective flow rate	m^3/hr	80.0	150.0	320.0
injection temperature	Cdeg	40.0	55.0	70.0
OpEx percentage CapEx	%/yr	2.5	5.0	7.5
Transmission eff data	%	75.0	85.0	95.0
permeability	-	P10	P50	P90
depletion	bar	0.0	100.0	200.0
inflation rate	%	1.0	1.5	2.0
production temperature	Cdeg	115.0	120.0	125.0
heat exchanger eff data	%	80.0	90.0	95.0
network length	km	20.1	25.0	29.9
network cost	€/m	820.1	1000.0	1179.9
temperature loss doublet	Cdeg	2.0	6.0	10.0
Injection well MD	m	4106.0	4562.0	5018.0
Exploration duration	yr	3.1	4.0	4.9
well scalling cost	-	1.6	1.7	1.9
pump failure rate	-	0.1	0.2	0.3
pump efficiency	%	58.6	65.0	71.4
development duration	yr	2.1	3.0	3.9
abandonment cost per well	M€	0.8	1.0	1.2
production well MD	m	3582.0	3980.0	4378.0
producer well contingency	%	93.3	100.0	106.7
ESP pump cost	k€	600.0	800.0	1000.0
injector well contingency	%	101.4	114.1	119.9
drilling installation cost	M€	1.5	1.6	2.0
Usage fee	€/yr	250.0	300.0	350.0

Figure 5.11. Sensitivity analysis for the LCOH index with respect to the model inputs in decreasing order of importance. The respective values of the LCOH are shown on the left-hand side, while the respective input ranges are denoted on the right hand side.

Discussion

The presented techno-economic model enables a comprehensive understanding of the interplay between economic and technical uncertainty. The model uses probability

distributions for most inputs addressing previously raised concerns with regard to capturing uncertainty in doublet capacity (Willems et al., 2017a), and even goes beyond by employing a probabilistic approach in all aspects of the analysis. Therefore, the complexity and interdependence of the variables shaping the energy output and economic performance of a direct-use geothermal system is structured and analysed comprehensively. This is done through utilizing the understanding of geological and technical aspects of the geothermal system as the foundation, now combined with economic aspects. The analysis could be further fine-tuned when project or technical limitations are more sharply defined. Effectively, the insights from the analysis could be refined as the project advances and reservoir initial state, geological, operational and economic uncertainty are further reduced following the drilling of the exploration well.

When considering financial profitability, both the NPV and EMV results indicate that this remains a challenge. This is in contrast to the relatively competitive LCOH index generated through the 20,000 model iterations. This discrepancy, rooted in the fact that the LCOH index does not consider the revenues generated, highlights that using solely the LCOH as an economic indicator could be misleading. Considering the NPV and LCOH indexes together provides a more comprehensive understanding of the economic outlook. However, the LCOH is still an insightful index for comparing energy generation costs from different sources. It should be noted that possible funding or taxing expenses could further deteriorate the financial outlook of such a project. Additionally, financial profitability seems to be more related to the possible gas production rather than the production of geothermal heat.

Nonetheless, the load factor remains extremely pertinent for improving profitability. Storage could reconcile discrepancies in the demand and supply balance on a seasonal basis, thus improving the effective load factor of the system (Daniilidis et al., 2017); This however means that the energy efficiency highlighted in previous research (Daniilidis et al., 2017) is countered by the energy extraction rate (see sub-chapter Sensitivity). Thus, a fine balance between resource efficiency and economic viability is required to ensure a profitable deployment of geothermal direct-use utilization; for the Groningen data presented here the load factor must be such that it ensures flowrates above circa 100 m^3/h to result in a positive NPV with all other variables being constant. This would require either a seasonal storage or additional load to the system for the lower load factor periods. Moreover, sequencing the network construction to follow the drilling of the well could reduce the exposure and financial risk; if the wells are successfully drilled then further investments could commence.

Furthermore, even though drilling costs were identified before as the most impactful to LCOH for geothermal projects, followed by plant lifetime (Beckers et al., 2014), this claim can be challenged. Even though drilling costs together with the grid deployment

costs remain the biggest capital expenditures, the LCOH index is mostly sensitive to operational (i.e. load factor and injection temperature), geological (i.e. permeability and depletion) and technical inputs (i.e. transmission and heat exchanger efficiency, network length and cost). This is in part because drilling and network deployment costs are not expected to become significantly lower, therefore, cost reduction options should be sought elsewhere. Inputs related to drilling costs (well scaling factor, drilling depth and well contingencies) rank low on the sensitivity analysis of both indexes; moreover, for the LCOH their influence is in the order of ~3-4% or lower.

Within the first ten most influential inputs to the LCOH the OpEx percentage and inflation are the only inputs of economic origin; consequently, the LCOH is not so heavily influenced by the economic context in which a project is deployed. On the contrary, for the NPV sensitivity the discount rate, OpEx percentage, gas heat price and inflation are encountered in the first ten influential inputs, implying that project profitability is more tightly linked to the deployment context.

Regarding the provided subsidy scheme in the Netherlands for deep geothermal projects, it would appear that the financial support provided is not sufficient to ensure a profitable outcome. While the generated income exceeds the provided subsidy amount, leading in principle to a healthy project, the projected outcome implies that under these conditions a project like this would not be realized (see also EMV and NPV). Therefore, the intended scope of the subsidy scheme could benefit from some revision, if the policy goal is to stimulate deep direct-use geothermal projects. While the 15 year duration of the support scheme is generous, the cashflow curve suggests that a shorter but more substantial subsidy scheme would aid similar projects in overcoming the high amount of initial investments required. The amount of renewable, locally generated heat (a mean of ~250TJ/year) is substantial enough from a regional scale perspective to be further pursued. A similar analysis for multiple projects from a bottom up perspective could be envisioned as complementary to the top-down economic analysis usually carried out in future research.

Conclusions

A probabilistic, techno-economic model for direct-use, deep geothermal systems is introduced based on the insights of the Groningen geothermal project. The model makes use of previous work on initial state, geological and operational uncertainty (Daniilidis et al., 2016) and incorporates the insights regarding resource efficiency and coupling a direct-use geothermal system to heat networks (Daniilidis et al., 2017). Furthermore, the model considers economic uncertainty over a period of 40 years using 20,000 iterations.

The use of detailed 3D reservoir simulations allows for a robust estimation of the produced heat and gas from the geothermal system, with low uncertainty levels. The inclusion of the seasonal heat demand enables a more comprehensive evaluation of the COP and its importance and influence to the economic analysis.

The EMV results reveal a 50% chance of marginal profits over the period of 40 years and a 90% chance of an 18 M€ deficit. This distribution is mostly attributed to the probability of both wells being successfully drilled. Nonetheless, the analysis suggests that a small part of the iterations with both wells being successful could still yield a net deficit. Therefore, for the Groningen dataset profitability is challenging.

Drilling and network deployment costs remain the main capital expenditures but the sensitivity reveals that the NPV is mostly influenced by flow rate and gas saturation. Constructing the grid only after the wells are successfully drilled would reduce the economic risk. Additionally, since the NPV is strongly linked with the reservoir gas saturation levels (and consequently the gas volume produced), the produced gas uncertainty in combination with the price at which it is sold results in high values for the 90% to 100% NPV percentiles.

Nonetheless, the NPV retains a high sensitivity to economic parameters related to the deployment context, such as discount and inflation rate; this is in contrast to the LCOH which is mostly affected by geological and operational parameters. It is therefore recommended to use both indexes when performing techno-economic analysis of deep geothermal projects.

The load factor of geothermal heat production emerges as the second most important parameter affecting the financial outlook. In view of previous insights regarding resource efficiency through coupling supply and demand, a strong divide exists between a more sustainable development and economic profitability of deep, direct-use geothermal systems in conductive settings. Since the load factor varies seasonally, the importance of seasonal storage or additional seasonal loads can significantly improve the economic outlook of such projects.

Lastly, the current Dutch subsidy scheme proves insufficient to overcome the challenging technical nature of this particular project. A support scheme with a shorter duration but more impact in the post-development phase would be more efficient in outweighing the high initial investment costs.

Appendix A

The volumetric heat capacity of the brine is calculated in steps. First the water and halite volumetric heat capacities are computed, after which their brine mixture volumetric heat capacity is calculated.

The coefficient of thermal expansion of water is expressed as (Waples and Waples, 2004b):

$$\beta_w = 0.0002115 + 1.32 \cdot 10^{-6} \cdot T + 1.09 \cdot 10^{-8} \cdot T^2 \tag{5.9}$$

where T is the temperature in $°C$. Following, the water density is expressed by (Waples and Waples, 2004b):

$$\rho_w = \frac{\rho_{w20}}{\left[1 + (T - 20) \cdot \beta_w\right]} \tag{5.10}$$

w here ρ_{w20} is the water density at $20\,°C$. The specific heat capacity for temperatures up to $290\,°C$ is then described as (Waples and Waples, 2004b):

$$C_p(J/Kg/K) = \frac{(4245 - 1.841 \cdot T)}{\rho_w} \tag{5.11}$$

Accordingly, the volumetric heat capacity of water is then computed as:

$$V_{heatcap} = \rho_w \cdot C_p \tag{5.12}$$

Halite density is computed as (Allen and Allen, 2005b):

$$\rho = \rho_{ref} \cdot (1 - a_0 \cdot (T - T_{ref})) \tag{5.13}$$

where ρ_{ref} is the reference density corresponding to the reference temperature T_{ref} and a_0 is the volumetric coefficient of thermal expansion (experimentally derived).

For Halite the normalized specific heat at temperature T is calculated according to (Waples and Waples, 2004a):

$$C_{pn_T} = 8.95 \cdot 10^{-10} \cdot T^3 - 2.13 \cdot 10^{-6} \cdot T^2 + 0.00172 \cdot T + 0.716 \tag{5.14}$$

for any temperature T_i the specific heat of Halite can then be computed as (Waples and Waples, 2004a):

$$C_{p_{T_2}} = \frac{C_{p_{T_1}} \cdot C_{pn_{T_2}}}{C_{pn_{T_1}}} \tag{5.15}$$

where $C_{pn_{T_1}}$ and $C_{pn_{T_2}}$ are the normalized specific heat values for temperatures T_1 and T_2 respectively and $C_{p_{T_1}}$ is the measured specific heat capacity at T_1.

The brine specific heat is then computed as (Dimoplon, 1972):

$$C_{brine} = (C_{w_{Tprod}} \cdot w_w + C_{H_{Tprod}} \cdot w_H) \cdot \rho_{brine} \tag{5.16}$$

where C_i and w_i are respectively the specific heat and mass fraction of component i in the solution and ρ_{brine} the brine density.

Appendix B

The pressure difference (**Figure 5.12**) and gas to brine data (**Figure 5.13**) are derived after 35 years of production from a total of 4536 unique 3D reservoir simulations (Daniilidis et al., 2016). The thick red line represents the mean value and the thinner red lines one standard deviation. The mean values and respective standard deviations of the pressure difference data are used to derive an analytical formulation between flowrate and pressure difference inside the reservoir presented in **Figure 5.4**.

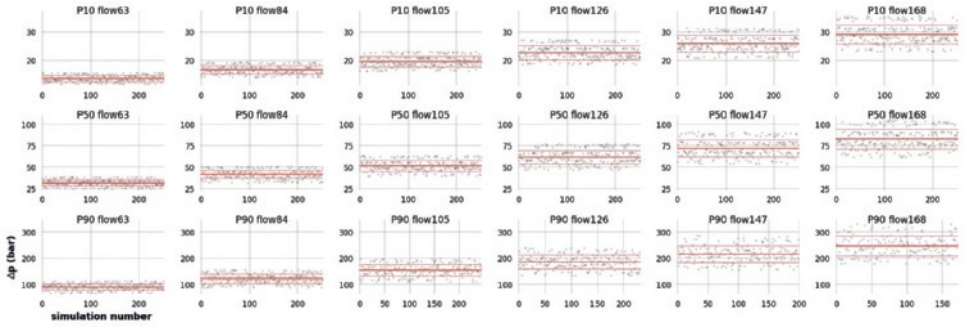

Figure 5.12. Pressure difference between injector and producer for the respective input parameters of reservoir permeability and flow rate of the model. Thick red lines represent mean values and thinner ones one standard deviation

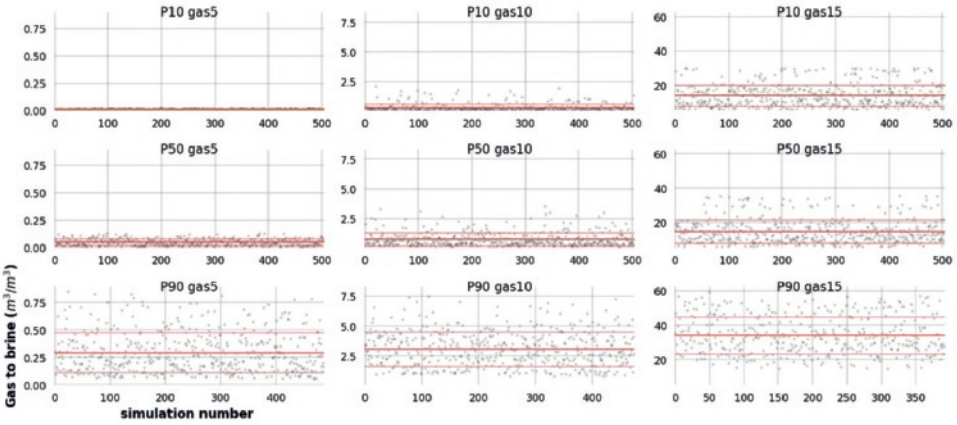

Figure 5.13. Gas to brine production during the first 35 years for the respective input parameters of permeability and gas saturation of the model. Thick red lines represent mean values and thinner ones one standard deviation

Chapter 6

Discussion and outlook

Thesis: An overview of findings

This thesis is aimed at identifying and analyzing potential geothermal fields in the conduction-dominated geological setting of NE Netherlands. The study followed two different paths. The first path consisted of exploring, substantiating and quantifying the concept of harvesting the high heat flow through salt. The second path was a step-wise, incremental approach in outlining, assessing, characterizing and evaluating the development of the Groningen geothermal system.

Harvesting conduction

In Chapter 2, a new target for geothermal exploration is outlined and substantiated. The high thermal conductivity of salt in comparison with other sediments becomes significant for the temperature field in a conductive geological setting. Outlining and quantifying the phenomenon of these, potentially significant, temperature anomalies in conductive settings opens up new possibilities for geothermal exploration. Documenting higher temperatures at shallower depths essentially describes a higher geothermal gradient in an otherwise tectonically inactive geological setting. The presence of this anomaly, if harvested, has a dual effect. Firstly, it lowers the threshold for accessing the heat resource (in terms of resources, time and, most critically for geothermal projects, cost). Secondly, the renewability of the resource is also enhanced, owing to the same mechanism that generated the anomaly, namely the heat conductivity of the salt.

In the examined salt intrusion, the associated variations in temperature gradients were found to be proportional to the thickness of the salt and a critical minimum thickness was identified (~600m). Nonetheless, thickness is not the sole contributor to these higher temperature levels. The shape of the salt intrusion is also important and therefore a more systematic study of other salt bodies would yield a more complete understanding of the phenomenon.

Temperature differences up to 25°C were modelled between the top of the salt structure and the surrounding strata at the same depth. These temperature differences correspond to an additional equivalent depth of 500m to 600m for the same conductivity scenario if the salt structure would be absent. This makes the top of the salt structures a sweet spot for geothermal heat production in conductive settings. If a suitably permeable formation is overlaying this sweet spot, up to 40% more energy can be extracted, while at the same time the recovery time of the field will only be prolonged by 13%.

Therefore, in conductive settings two spatial criteria need to be met for this concept to be applicable. In the subsurface a permeable aquifer must immediately overlie the salt intrusion. This principle could be applied in any geological setting where thick salt sequences or doming have taken place and interest for geothermal energy is present. In

the Dutch context, the provinces of Drenthe and Groningen are likely candidates as local salt thickness can exceed 800m.

Irreducible uncertainty

A major problem for geothermal development worldwide is the lack or scarcity of available subsurface data. In that sense, the Dutch practice of publicizing all subsurface activity data is a remarkable asset for geothermal development within the Netherlands. Nonetheless, and despite the good 3D seismic coverage and regional well control, some of the critical parameters for the performance of a geothermal system (e.g. permeability, pressure, compartmentalization, gas saturation) remain subject to various degrees of uncertainty, irreducible prior to drilling. Several studies, making use of a diversity of methodologies, have analysed the effect of uncertainties on geothermal output. This thesis however, provides insights of the combined uncertainty in reservoir initial state (pressure and gas saturation levels), geological uncertainty (reservoir and fault permeability) and operational uncertainty (flow rate levels and re-injection temperature). These insights stem from a streamlined workflow that yields a comprehensive qualitative risk matrix, underpinned by quantitative data from 3D reservoir simulations. The Groningen geothermal system is used as a case study in **Chapter 3**.

The parameter co-dependency reveals the relative importance of the input parameters to the different analysis outputs, thus enabling the ranking of inputs according to their importance. This ranking serves as a starting point for identifying critical project aspects for which further research is needed prior to drilling the exploration well. The qualitative and numerical results in this thesis are restricted to the Groningen geothermal system, but the methodology can be adjusted accordingly and applied readily to other locations.

For the Groningen geothermal system, the reservoir initial state principally affects the pressure difference between the producer well and a hydrostatic reservoir, as well as the produced gas volume. Pressure depletion controls the pressure difference between the producer and a hypothetical, virgin-pressure reservoir and therefore dictates the depth at which the pump would need to be placed. Gas saturation is known to affect the efficiency of water production. At the same time, it also has a dominant effect on produced gas volume, potentially adding to the project finances but also complicating the pump installation and operation.

Of the geological parameters, reservoir permeability is tightly connected to the pressure difference between the wells. Fault permeability affects the drainage area and thus has a temporal effect on the produced temperature. Of the operational parameters, the used flow rate controls the produced thermal power, the well pressure difference and the producer temperature. The injection temperature also affects the produced thermal power over time.

Surface interfacing

System complexity is increased when the geothermal resource is coupled with the demand pattern of the surface system. This introduces seasonal load factors, together with uncertainty regarding the supply robustness and possible geochemical implications.

Offline coupling between a Model Predictive Control (MPC) and a 2D reactive transport reservoir model, as presented in **Chapter 4**, allows for an integrated evaluation of the linkage between the surface and subsurface part of a geothermal energy network. Using an hourly demand pattern over a yearly period, the MPC controls the production of the geothermal system by taking into account hard constraints. A storage unit is included in the system to ameliorate demand peaks and to help shift loads in time. The 2D reactive transport model considers the effects of pressure depletion, reservoir permeability, a constant or variable (MPC defined) flow rate control strategy, injection temperature and pH.

For the case study of the Groningen geothermal project the use of a seasonally variable production rate has no adverse geochemical effects on the reservoir and energy generation during a production time of 50 years. Moreover, the seasonally variable production enables a more efficient use of the geothermal resource by only extracting the heat required from the surface demand. This variability affects only the rate and not the nature of the changes in the chemical reservoir properties. The absence of adverse geochemical effects combined with the improved efficiency of heat extraction opens up possibilities for a more sustainable development of geothermal resources. Nonetheless, the geochemical behavior enables some systematic observations.

The geochemical behavior of the reservoir is mostly affected by flow rate, and secondarily by the injection pH and injection temperature. In the Rotliegend Sandstone, anhydrite and dolomite are identified as the two key minerals. Anhydrite dissolves during the first years of production leading to increased permeability around the injector well. The flow rate control strategy influences the rate of dissolution, but all investigated flow rate control strategies result in the dissolution of the same volume fraction. Dolomite has a temporal effect on the permeability and its change rate is primarily affected by pH and secondarily by temperature. Acidic pH and lower temperatures favor dolomite dissolution while a neutral pH and higher temperatures favor precipitation.

Uncertainty monetized

The third integration level in this thesis was aimed at bringing together technical and economic uncertainties to provide a comprehensive overview of geothermal field development (**Chapter 5**). Resulting from the findings of the reservoir geochemical behavior (i.e. no adverse effects in terms of reservoir geochemistry after 50 years of

production), the technical uncertainty could be simplified to not include geochemical aspects. A probabilistic, techno-economic model for direct-use, deep, low enthalpy geothermal systems is introduced based on the findings of the Groningen project. The model makes use of the findings on initial state, geological and operational uncertainty (**Chapter 3**) and incorporates the insights from coupling a direct-use geothermal system to heat networks with regard to a seasonally variable production (**Chapter 4**). The produced heat and possibly gas levels are underpinned by the 3D reservoir simulations, while the seasonal heat demand enables a more comprehensive evaluation of the COP and its importance and influence to the economic analysis. Economic uncertainty is further incorporated in the model. The complexity and interdependence of the variables shaping the energy output and economic performance of a direct-use geothermal system is structured and analyzed comprehensively. A period of 40 years is simulated using 20,000 iterations.

The Expected Monetary Value (EMV) shows a 50% probability for marginal profits at the end of the 40 years period, mostly affected by the success rate of drilling the wells. However, even if both wells are successfully drilled, a net deficit remains as a possibility. The Net Present Value (NPV) is mostly sensitive to operational and initial state parameters. Specifically, the load factor (which in turn dictates flow rate) and the gas saturation of the reservoir are the most significant ones. Economic parameters such as discount and inflation rate remain germane for the NPV sensitivity, in contrast with the Levelised Cost of Heat (LCOH) that is mostly affected by geological and operational parameters. This difference further suggests that the LCOH and NPV indexes should be used in tandem for a more insightful financial assessment.

The seasonality of the load factor and its importance on the economic outlook highlight the significance of seasonal storage or additional seasonal loads. These together with the temporal decoupling of the surface and subsurface capital investments can significantly improve the economic outlook of similar projects. Another conclusion stemming from the economic outlook is that the current Dutch subsidy scheme is not sufficient to overcome the challenging technical nature of this particular project. A support scheme structure with a shorter duration but more impact directly after the drilling phase would be more effective in offsetting the high initial investment costs.

Anti-thesis: deconstruction and critical reflection

In this subchapter, an attempt is made to deconstruct the argumentation presented in the two paths of the thesis and the individual chapters. The aim of this exercise is to critically reflect on the presented work, put it into a wider context and possibly identify future directions for research.

On harvesting conduction

The initial scope of **Chapter 2** was to harvest the higher heat conductivity of salt using the fracture network of the anhydrite layers in the Zechstein sequence. Specifically, the ZEZ3A interval, a strong reflector, floats close to the top of the salt structures. The anhydrite interval is subject to brittle deformation, in contrast with the ductile behavior of the surrounding halite matrix. This in turn generates a neck fracture network and boudinage. The density and fracture characteristics still need to be determined to establish a realistic model. Nonetheless, the research was reoriented towards a sedimentary interval on top of the salt dome as the reservoir body of the geothermal system, mostly due to the inability to characterize the fracture network in any meaningful way.

The new geothermal exploration target presented in **Chapter 2** was meant as a proof of concept. Some ideas that could refine and possibly increase its robustness emerge while reflecting on that same concept. A more precise thermal conductivity characterization possibly utilizing the IMAGE petrophysical database (Bär et al., 2016), which is in development at the time of writing, would further sharpen the analysis. At the moment, the characterization of the considered layers is based on lithostratigraphy; depositional facies based analysis would be beneficial, data supply permitting. Potential benefits from such a refinement of the temperature model could come in the form of improved precision of the temperature distribution and also sharper outlining of the aquifer zone that is affected by the higher temperature.

Additionally, as partly discussed with the NAM, coupling of such a temperature model with the DTS temperature data would validate the modelling results and increase confidence in the applicability of the paradigm discussed. Since most data are derived from petroleum wells, which generally are not directed at crestal units above the salt dome as they form no hydrocarbon play, the spatial overlap between a high quality DTS temperature dataset and a salt structure crest is unlikely. Another DTS dataset from the ZRP-03A well might become available from NAM; this could enable a better evaluation of the effect of the salt to the temperature field (at least along the well trajectory) and possibly a better correlation method between logging temperature data and DTS derived data. Should this better correlation be achieved, an improvement of the temperature data quality of existing wells could be enabled, reducing uncertainty in existing temperature datasets overall for further geothermal modelling. Additionally, utilizing such an improved temperature dataset could potentially enable a geographically wider assessment of the proof of concept discussed, including a variety of different salt shapes.

On outlining and assessing a geothermal field

The assessment of the Groningen geothermal system in this thesis includes a multitude of aspects and gives a comprehensive overview of associated risks (**Chapter 3**).

Nonetheless, some improvements could be further incorporated in the analysis. A facies analysis of the reservoir layers could complement the identification of layers based on flow characteristics according to the petrophysical data presented; the importance of facies analysis was recently shown in another study (Crooijmans et al., 2016). The seven reservoir layers can be clustered in two groups; the first group includes three layers with relatively lower transmissivity (<600mDm), whereas the second group includes four layers that exhibit a relatively higher transmissivity (>1300mDm). Currently, each individual layer thickness is a constant fraction of the overall gross reservoir thickness. However, any spatial thickness variation in these layer groups could affect both the break through time, as well as pressure levels developed during production. Additionally, the volumetric uncertainty resulting from the seismic interpretation is not included and could potentially further refine mostly the duration for which the heat production can be sustained. Its impact however should not be too significant as high-quality 3D seismic data have been used for the interpretation.

Another aspect that could further refine the insight from the presented analysis is the inclusion of the detailed design of the wells and surface facilities. The engineering aspects related to change in flow patterns inside the pipes and heat exchanger, together with possible mineral precipitation from the highly saline brine could alter the pressure levels of the system and the required pumping energy. Furthermore, long term effects from the circulation of the said brine in a closed looped with regard to scaling should also be investigated.

The degree of freedom between reinjection temperature and flow rate might also be worth investigating; determining the balance between the two could have economic and system sizing implications. This might actually be more relevant once a more concrete profile of the heat demand is established, as the temperature levels needed to supply that demand might restrict the options. The possibility to seasonally vary the injection temperature could also be considered. The abovementioned improvement points might only be possible after the exploration well has been drilled and some of the uncertainty is reduced.

The coupling of supply and demand via a MPC controller is a first step towards integrating the geothermal system to the energy system at large (**Chapter 4**). A coupled Thermal Hydraulic Mechanical Chemical (THMC) simulator, coupled online with the surface MPC controller would generate an all-encompassing output in terms of reservoir implications due to demand pattern changes. While for the chemical part examined in **Chapter 4**, 2D modelling is sufficient, using a THMC model would also require a 3D model to fully utilize the ability to capture the possible mechanical implications due to pressure levels and temperature shocks to the rock and faults. Furthermore, it could incorporate the effects of brine viscosity that are currently not accounted for in the presented results.

A significant improvement in the flexibility of the analysis, even without the use of a coupled THMC simulator, would be the use of an online coupling between the demand and the reservoir simulator. This would require the development of a simulator capable to accommodate this complex task. In such a case, changing demand patterns over time, as well as temporal variations in injection pH and temperature could be analyzed. Last but not least, the estimation of the HCl amounts needed to achieve the injection pH levels discussed in **Chapter 4** would put the feasibility aspects in perspective both in terms of technical and environmental issues, as well as the economic impact of the chemical treatment.

Regarding the techno-economic analysis presented in **Chapter 5** some minor aspects can be discussed. Inclusion of the taxing and financing expenses would result in an exhaustive list of economic aspects to consider. On the technical side the chemical costs would also round off the analysis.

Overall

Concluding the reflection on the research presented in this thesis, one aspect remains regretfully absent, even though originally it was part of the scope of this work. This aspect is related to the social side of geothermal development. Especially for the Groningen project such interdisciplinary research, on a project basis and from the early stage of development would have been valuable. It would also highlight the societal aspect, often neglected among people with a natural science background. Rationality is not necessarily the only way to make decisions (for better or worse); therefore, a study related to people's perception of geothermal energy in Groningen could provide some contextual background that potentially transcends the locality of the case study. Juxtaposition of the societal perception of geothermal heat provision in relation to the recent debate regarding gas production in the province would have been of particular interest.

Furthermore, the adaptation of the energy system itself, but also the perception of that same energy system by the people could be followed over time. Since the drilling for the geothermal project in Groningen is almost contemporary to the writing of this thesis, the opportunity for similar studies during and past project development could ascribe the non-monetary value of geothermal energy to the citizens of the province and city. The dipole of locally produced - internationally consumed (gas) and locally produced and consumed (geothermal) also emerges as an interesting aspect to examine, also with regard to NIMBY reactions.

Meta- and synthesis: freethought and vista

One can argue that all applied research is normative by nature. This work cannot pretend to escape this inevitability, but rather chooses to reveal it. As such, this final reflection is normative. It is rooted in the opinion that renewable energy is preferable above fossil energy. Nonetheless, the actual value of geothermal development is currently underestimated.

The status of geothermal development is affected by and subjected to political and economic conditions of today. In the aftermath of the economic crisis the renewable agenda has been notably delayed. The price fluctuations of fossil fuels and their levels in the past few years have also reduced the financial feasibility windows for renewable sources (**Figure 5.14**). The dominance of economic elements on the political agenda has pushed back energy supply and environmental concerns. Indicatively, in recent years key statistics with regards to renewable energy indicators of EU member states are no longer available by Eurostat (e.g. country energy mix factsheets with renewable energy contributions).

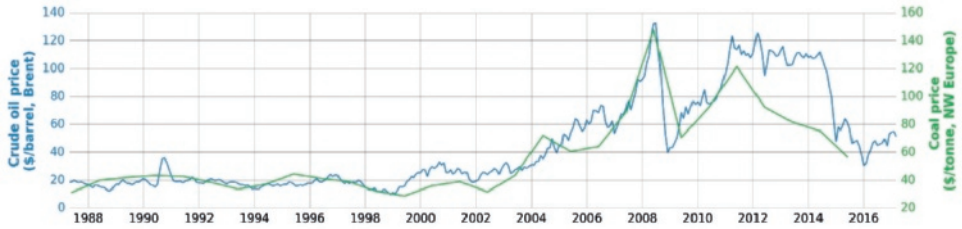

Figure 5.14. Historical data price for Brent crude oil and coal. Data sources, Crude oil: (Energy Information Administration (EIA), 2017), coal: (BP, 2016)

At the same time, the renewable energy discourse remains skewed towards electricity. Electricity is often considered the only form of energy used and accordingly most of the focus with regards to renewable supply has been dominated by power generation, while heat remains a secondary thought. Ironically, currently 50% of the EU energy consumption (European Commission, 2016b) is related to heating and cooling, while for households this amounts to 78% (European Commission, 2016a); about 75% of this energy is supplied by fossil fuels. In this context, direct-use geothermal heat can have a significant impact in the transition towards a more sustainable energy production. The current market cost of energy sources does not necessarily reflect their value and contribution to such strategic goals. The technological challenges with regard to grid stability from large scale implementation of renewable sources (mostly intermittent) and the difficulty of translating strategic goals to quantified, articulated policy and applications are impeding the wider dissemination of renewable energy. While the Paris

Agreement receives proper attention at the highest political level, with the recent exception of the US, this attention has not yet found its way to actual implementations towards its goals.

Nonetheless, for the larger part of the world, away from tectonic margins and volcanic or igneous activity the possibility of geothermal electricity generation is both limited and not as economically competitive in comparison with other renewable electricity sources. Geothermal energy can however make a significant contribution to the energy mix with direct heat usage, as there is a worldwide availability of geothermal systems suitable for such direct-use utilization. Currently such systems, as discussed and exemplified also in this thesis, are economically not always profitable.

The Groningen geothermal system is a particular case for several reasons. The aquifer is located quite deep which makes for an expensive drilling plan, but it is not hot enough to produce steam and drive electricity generation. A binary system could be utilized to generate electricity through an Organic Rankine Cycle (Vélez et al., 2012). Nonetheless, it should be noted that if a challenging project like the Groningen geothermal system manages to achieve economic profitability, it would make other conduction dominated systems more attainable.

Economic feasibility can be further improved by pursuing new techniques that will reduce cost and maybe enable a more cost effective combined production of heat and power from low temperature geothermal resources; at the same time a better design and development practice will enable more successful geothermal projects. It would appear that several geothermal developments are underway across Europe for both heat and power (Angelino et al., 2017). Since the scientific background and technological solutions, although not without problems, are widely available today, the only obstacle for further low enthalpy geothermal development appears to be the economic performance. Two aspects can be identified here: regulation of the heat market and reduction of drilling costs. Even so, direct evaluation of the economic outlook of geothermal systems is not necessarily comprehensive in all aspects of their value. The added value resulting from the contribution to strategic goals (e.g. CO_2 emission reduction) and possible local development is not included.

However, since geothermal energy (be it heat or electricity), is usually consumed at the regional level and not internationally, the characterization of geothermal systems remains heavily geographically dependent and therefore fragmented. A wider adaption of the geothermal play catalog could help to streamline the characterization of geothermal systems in a way that transcends the local definitions. This goal appears to be actively pursued by the International Geothermal Association (IGA) and would especially benefit geothermal developments in conductive settings.

In addition, possible improvements in understanding the complexity of geothermal systems can be derived at a higher level, if a structured, systematic, real-time, data supply becomes available. In such a case, the whole of the subsurface as a resource and its geothermal contribution to the energy supply could be more comprehensively evaluated, utilizing the data streams and also incorporating the spatial (three dimensional) placement of existing, producing geothermal systems.

The Dutch geothermal developments are already moving towards this direction. All the prerequisites are either present or in development for the refinement and streamlining required for this to be achieved. The Dutch geothermal scientific community and development sector have therefore the potential to pioneer this integrated assessment and monitoring of geothermal resources.

A coupled subsurface - surface THMC model that includes the dipole demand-supply, as well as economic and societal implications can be outlined as a means of an integrated assessment of a geothermal system. Real time data flow and projection of the field recovery time once a system is in place would ensure comprehensive follow up and monitoring. This could firstly be achieved at the national level and potentially later deployed to the EU level, across national scales.

Returning to the topic of scales, this time from the perspective of renewable energy, geothermal is not a goal in itself; it is however a means to an end. The way the end goal is achieved remains as important as the goal itself. There is, still, a lot of work to be done.

References

ACM, 2017. Besluit tot vaststelling van de maximumprijs en de berekening van de eenmalige aansluitbijdrage en het meettarief warmteverbruik per 1 januari 2017 16.1166.52, 1-19.

Adams, B.M., Kuehn, T.H., Bielicki, J.M., Randolph, J.B., Saar, M.O., 2015. A comparison of electric power output of CO2 Plume Geothermal (CPG) and brine geothermal systems for varying reservoir conditions. Applied Energy 140, 365-377.

Agemar, T., Schellschmidt, R., Schulz, R., 2012. Subsurface temperature distribution in Germany. Geothermics 44, 65-77.

Agemar, T., Weber, J., Schulz, R., 2014. Deep Geothermal Energy Production in Germany. Energies 7, 4397-4416.

Alberg Østergaard, P., Mathiesen, B.V., Möller, B., Lund, H., 2010. A renewable energy scenario for Aalborg Municipality based on low-temperature geothermal heat, wind power and biomass. Energy 35, 4892-4901.

Allen, P.A., Allen, J.R., 2005a. The Petroleum Play, in: Allen, P.A., Allen, J.R. (Eds.), Basin Analysis - Principles and Applications. Wiley-Blackwell Science Ltd., pp. 309-396.

Allen, P.A., Allen, J.R., 2005b. The physical state of the lithosphere, in: Allen, P.A., Allen, J.R. (Eds.), Basin Analysis - Principles and Applications. Wiley-Blackwell Science Ltd., pp. 20-51.

Allgöwer, F., Badgwell, T.A., Qin, J.S., Rawlings, J.B., Wright, S.J., 1999. Nonlinear Predictive Control and Moving Horizon Estimation --- An Introductory Overview, in: Frank, P.M. (Ed.), Advances in Control: Highlights of ECC'99. Springer London, London, pp. 391-449.

Angelino, L., Dumas, P., Garabetian, T., Pinzuti, V., 2017. 2016 EGEC Geothermal Market report - key findings, 1-18.

Atlason, R.S., Unnthorsson, R., 2013. Hot water production improves the energy return on investment of geothermal power plants. Energy 51, 273-280.

Axelsson, G., Stefánsson, V., Björnsson, G., Jiurong, L., 2005. Sustainable Management of Geothermal Resources and Utilization for 100 – 300 Years. Proceedings World Geothermal Congress 2005.

Axelsson, G., 2010. Sustainable geothermal utilization – Case histories; definitions; research issues and modelling. Geothermics 39, 283-291.

Bachman, G.H., Hoffman, N., 1995. Bildung und Entwicklung des Norddeutschen Rotliegend-Beckens, in: Plein, E. (Ed.), Stratigraphie von Deutschland I - Norddeutsches Rotliegend-becken. Courier Forschungsinstitut Senckenberg, Frankfurt Am Main, Germany, pp. 156-169.

Bachman, G.H., Hoffman, N., 1997. Development of the Rotliegend Basin in Northern Germany. Geologisches Jahrbuch D 103, 9-31.

Bakema, G., Schoof, F., 2016. Geothermal Energy Use, Country update for the Netherlands, 1-8.

Banks, D., 2012. An Introduction to Thermogeology: Ground Source Heating and Cooling, 2nd ed. John Wiley & Sons.

Bär, K., Strom, A., Reinsch, T., Sippel, J., Freymark, J., Mielke, P., 2016. IMAGE petrosphysical catalogue - an international database of rock properties for reservoir characterization EGC2016-T-EP-84, 1-5.

Barbier, E., 2002. Geothermal energy technology and current status: an overview. Renewable & Sustainable Energy Reviews 6, 3-65.

Barkaoui, A., Boldyryev, S., Duic, N., Krajacic, G., Guzović, Z., 2016. Appropriate integration of geothermal energy sources by Pinch approach: Case study of Croatia. Applied Energy 184, 1343-1349.

Barthelmy, D., 2014. Illite mineral data.

Battistelli, A., Calore, C., Pruess, K., 1997. The simulator TOUGH2/EWASG for modelling geothermal reservoirs with brines and non-condensible gas. Geothermics 26, 437-464.

Beckers Koenraad F., Lukawski, M.Z., Anderson, B.J., Moore, M.C., Tester, J.W., 2014. Levelized costs of electricity and direct-use heat from Enhanced Geothermal Systems. JOURNAL OF RENEWABLE AND SUSTAINABLE ENERGY 6.

Beckers, K.F., Lukawski, M.Z., Anderson, B.J., Moore, M.C., Tester, J.W., 2014. Levelized costs of electricity and direct-use heat from Enhanced Geothermal Systems (vol 6, 013141, 2014). Journal of Renewable and Sustainable Energy 6, 059902.

Bertani, R., 2012. Geothermal power generation in the world 2005–2010 update report. Geothermics 41, 1-29.

Bertani, R., 2016. Geothermal power generation in the world 2010–2014 update report. Geothermics 60, 31-43.

Blanc, P., Lassin, A., Piantone, P., Azaroual, M., Jacquemet, N., Fabbri, A., Gaucher, E.C., 2012. Thermoddem: A geochemical database focused on low temperature water/rock interactions and waste materials. Applied Geochemistry 27, 2107-2116.

Blöcher, G., Cacace, M., Reinsch, T., Watanabe, N., 2015. Evaluation of three exploitation concepts for a deep geothermal system in the North German Basin. Computers & Geosciences 82, 120-129.

Boersma, K., Brinkgreve, D., 2014. GRN-GT-01 & GRN-GT-02 detailed design 2.2, 1-87.

Bolourinejad, P., Herber, R., 2015. Experimental investigation of porosity and permeability variations in reservoirs and caprock following co-injection of sulfur dioxide and hydrogen sulfide with carbon dioxide. Journal of Petroleum Science and Engineering 129, 137-144.

Bolourinejad, P., Shoeibi Omrani, P., Herber, R., 2014. Effect of reactive surface area of minerals on mineralization and carbon dioxide trapping in a depleted gas reservoir. International Journal of Greenhouse Gas Control 21, 11-22.

Bonté, D., Van Wees, J.D., Verweij, J.M., 2012. Subsurface temperature of the onshore Netherlands: new temperature dataset and modelling. Netherlands Journal of Geosciences-Geologie en Mijnbouw 91, 491-515.

BP, 2016. Statistical Review of World Energy June 2016 - data workbook, 1-48.

Breunese, J.N., van Thienen-Visser, K., 2014. Effecten van verschillende productiescenario's op de verdeling van den compactie in het Groningen veld in de periode 2014 tot en met 2016 R10427, 1-29.

Cacace, M., Kaiser, B.O., Lewerenz, B., Scheck-Wenderoth, M., 2010. Geothermal energy in sedimentary basins: What we can learn from regional numerical models. Chemie Der Erde-Geochemistry 70, 33-46.

Campo, P.J., Morari, M., 1989. Model predictive optimal averaging level control. AIChE Journal 35, 579-591.

Carlson, M.R., 2003. Practical reservoir simulation: using, assessing, and developing results. PennWell Books.

Cataldi, R., 2001. Sustainability and renewability of geothermal energy, 4pp.

CBS, 2016. Aardgas en elektriciteit, gemiddelde prijzen van eindverbruikers.

CBS, November 16, 2012. Energy balance sheet; key figures 2013.

Chen, M., Tompson, A.F.B., Mellors, R.J., Abdalla, O., 2015. An efficient optimization of well placement and control for a geothermal prospect under geological uncertainty. Applied Energy 137, 352-363.

Crooijmans, R.A., Willems, C.J.L., Nick, H.M., Bruhn, D.F., 2016. The influence of facies heterogeneity on the doublet performance in low-enthalpy geothermal sedimentary reservoirs. Geothermics 64, 209-219.

Croucher, A., 2014. PyTOUGH user's guide 1.4.0, 1-99.

Cui, G., Zhang, L., Ren, B., Enechukwu, C., Liu, Y., Ren, S., 2016. Geothermal exploitation from depleted high temperature gas reservoirs via recycling supercritical CO2: Heat mining rate and salt precipitation effects. Applied Energy 183, 837-852.

Daniilidis, A., Scholten, T., Hoogheim, J., De Persis, C., Herber, R., 2017. Geochemical implications of production and storage control by coupling a direct use geothermal system with heat networks 204, 254-270.

Daniilidis, A., Doddema, L., Herber, R., 2016. Risk assessment of the Groningen geothermal potential: From seismic to reservoir uncertainty using a discrete parameter analysis. Geothermics 64, 271-288.

Darup, M.S., Renner, J., 2016. Predictive pressure control in deep geothermal systems. Proc. of the 2016 European Control Conference, 605-610.

de Jager, J., 2007. Geological development, in: Wong, T.E., Batjes, D.A.J., de Jager, J. (Eds.), Geology of the Netherlands. Royal Netherlands Academy of Arts and Sciences, Amsterdam, Netherlands, pp. 5-26.

de Jager, J., Geluk, M.C., 2007. Petroleum Geology, in: Wong, T.E., Batjes, D.A.J., de Jager, J. (Eds.), Geology of the Netherlands. Royal Netherlands Academy of Arts and Sciences, Amsterdam, Netherlands, pp. 241-264.

de Jager, J., 2003. Inverted basins in the Netherlands, similarities and differences. Geologie en Mijnbouw/Netherlands Journal of Geosciences 82, 355-366.

Dimoplon, W., 1972. Estimating specific-heat of liquid mixtures. Chemical Engineering 79, 64-&.

Dinoloket, 2014. Digital Geological Model (DGM) v.4 2016.

DiPippo, R., 2005. Geothermal power plants: principles, applications and case studies. Elsevier, Oxford.

Doornenbal, J.C., Abbink, O.A., Duin, E.J.T., Dusar, M., Hoth, P., Jasionowski, M., Lott, G.K., Mathiesen, A., Papiernik, B., Peryt, T.M., Veldkamp, J.G., Wirth, H., 2010. Introduction, stratigraphic framework and mapping, in: Doornenbal, J.C., Stevenson, A. (Eds.), Petroleum Geological Atlas of the Southern Permian Basin Area. EAGE Publications b.v., Houten, The Netherlands, pp. 1-9.

Dronkers, A.J., Mrozek, F.J., 1991. Inverted basins of the Netherlands. First Break 9, 409-425.

Duin, E.J.T., Doornenbal, J.C., Rijkers, R.H.B., Verbeek, J.W., Wong, T.E., 2006. Subsurface structure of the Netherlands - results of recent onshore and offshore mapping. Netherlands Journal of Geosciences - Geologie en Mijnbouw 85, 245-276.

EBN, 2015. Focus on Dutch Oil and Gas, 1-60.

EBN, TNO, Ministry of Economic Affairs, 2016. Dutch geothermal development, 1.

Eicker, U., Monien, D., Duminil, E., Nouvel, R., 2015. Energy performance assessment in urban planning competitions. Applied Energy 155, 323-333.

Energy Information Administration (EIA), 2017. Spot Prices for Crude Oil and Petroleum Products.

European Commission, 2016a. Coomunication from the commission to the European Parliament, the Council, the European Economic and Social Committee and the Committee of the Regions on an EU strategy for Heating and Cooling - Review of available information COM(2016) 24 final, part 1 of 2, 1-101.

European Commission, 2016b. An EU Strategy on Heating and Cooling COM(2016) 51 final, 1-13.

Evans, K.F., Zappone, A., Kraft, T., Deichmann, N., Moia, F., 2012. A survey of the induced seismic responses to fluid injection in geothermal and CO2 reservoirs in Europe. Geothermics 41, 30-54.

Florian Wellmann, J., Croucher, A., Regenauer-Lieb, K., 2012. Python scripting libraries for subsurface fluid and heat flow simulations with TOUGH2 and SHEMAT. Computers & Geosciences 43, 197-206.

Francke, H., Thorade, M., 2010. Density and viscosity of brine: An overview from a process engineers perspective. Chemie der Erde - Geochemistry 70, Supplement 3, 23-32.

Franco, A., Vaccaro, M., 2012. An integrated "Reservoir-Plant" strategy for a sustainable and efficient use of geothermal resources. Energy 37, 299-310.

Franco, A., Vaccaro, M., 2014. Numerical simulation of geothermal reservoirs for the sustainable design of energy plants: A review. Renewable and Sustainable Energy Reviews 30, 987-1002.

Franco, A., Villani, M., 2009. Optimal design of binary cycle power plants for water-dominated, medium-temperature geothermal fields. Geothermics 38, 379-391.

Frick, S., Regenspurg, S., Kranz, S., Milsch, H., Saadat, A., Francke, H., Brandt, W., Huenges, E., 2011. Geochemical and Process Engineering Challenges for Geothermal Power Generation. Chemie Ingenieur Technik 83, 2093-2104.

Fridleifsson, I.B., Bertani, R., Huenges, E., Lund, J.W., Ragnarsson, A., Rybach, L., 2008. The possible role and contribution

of geothermal energy to the mitigation of climate change, 59-80.

Fridleifsson, I., 2001. Geothermal energy for the benefit of the people. Renewable & Sustainable Energy Reviews 5, 299-312.

Fryberger, S.G., Knight, R., Hern, C., Moscariello, A., Kabel, S., 2011. Rotliegend facies, sedimentary provinces, and stratigraphy, Southern Permian basin UK and The Netherlands: A review with new observations, in: Grötsch, J., Gaupp, R. (Eds.), The Permian Rotliegend of the Netherlands. SEPM (Society for Sedimentary Geology), Oklahoma, USA, pp. 51-88.

Fuchs, S., Förster, A., 2010. Rock thermal conductivity of Mesozoic geothermal aquifers in the Northeast German Basin. Chemie der Erde - Geochemistry 70, Supplement 3, 13-22.

Garg, S.K., Kassoy, D.R., 1981. Convective heat and mass transfer in hydrothermal systems, in: Rybach, L., Muffler, L.J.P. (Eds.), Geothermal Systems: Principles and Case histories. John Wiley and Sons Ltd, New York, USA.

Gast, R.E., Dusar, M., Breitkreuz, Z., Schneider, J.W., Stemmerik, L., Geluk, M.C., Geißler, M., Kiersnowski, H., Glennie, K.W., Kabel, S., Jones, N.S., 2010. Rotliegend, in: Doornenbal, J.C., Stevenson, A. (Eds.), Petroleum Geological Atlas of the Southern Permian Basin Area. EAGE Publications b.v., Houten, The Netherlands, pp. 101-121.

Gebhardt, U., 1994. Zur Genese der Rotliegend-Salinare in der Norddeutschen Senke (Oberrotliegend II, Perm). Freiberger Forschungshefte, 3-22.

Gelegenis, J.J., 2009. Use of a probabilistic model to design energy transmission and distribution networks for low enthalpy geothermal multiple use schemes. Applied Energy 86, 284-289.

Geluk, M.C., 2007a. Permian, in: Wong, T.E., Batjes, D.A.J., de Jager, J. (Eds.), Geology of the Netherlands. Royal Dutch Academy of Arts and Sciences, Amsterdam, Netherlands, pp. 63-83.

Geluk, M.C., 2007b. Triassic, in: Wong, T.E., Batjes, D.A.J., de Jager, J. (Eds.), Geology of the Netherlands. Royal Dutch Academy of Arts and Sciences, Amsterdam, Netherlands, pp. 85-106.

Geluk, M.C., Paar, W.A., Fokker, P., 2007. Salt, in: Wong, T.E., Batjes, D.A.J., de Jager, J. (Eds.), Geology of the Netherlands. Royal Dutch Academy of Arts and Sciences, Amsterdam, Netherlands, pp. 279-290.

Glennie, K.W., 1998. Petroleum Geology of the North Sea, Basic concepts and recent advances, 4th ed. Blackwell, Oxford.

Glennie, K.W., 2007. The Permo-Carboniferous Rotliegend of NW Europe, 10-16.

GoldSim, 2017. GoldSim User's Guide, Probabilistic simulation environment, version 12.

Goldstein, B., Hiriart, G., Tester, J., Bertani, B., Bromley, C., Gutierrez-Negrin, L., Huenges, E., Ragnarsson, A., Mongillo, M., Muraoka, H., 2011a. Great expectations for geothermal energy to 2100.

Goldstein, B., Hiriart, G., Bertani, R., Bromley, C., Gutierrez-Negrin, L., Huenges, E., Muraoka, H., Ragnarsson, A., Tester, J., Zui, V., 2011b. Geothermal Energy, in: IPCC Special report on Renewable energy sources and Climate Change Mitigation.

Grant, M., Donaldson, I.G., Bixley, P.F., 1982. Geothermal Reservoir Engineering. Academic Press, New York.

Gras, R., Geluk, M.C., 1999. Late Cretaceous–Early Tertiary sedimentation and tectonic inversion in the southern Netherlands. Geologie en Mijnbouw 78, 1-79.

Grötsch, J., Sluijk, A., van Ojik, K., de Keijzer, M., Graaf, J., Steenbrink, J.,

2011. The Groningen gas field: fifty years of exploration and gas production from a Permian dryland reservoir, in: Grötsch, J., Gaupp, R. (Eds.), The Permian Rotliegend of the Netherlands. SEPM (Society for Sedimentary Geology), Oklahoma, USA, pp. 11-33.

Hanano, M., 2004. Contribution of fractures to formation and production of geothermal resources. Renewable and Sustainable Energy Reviews 8, 223-236.

Henares, S., Bloemsma, M.R., Donselaar, M.E., Mijnlieff, H.F., Redjosentono, A.E., Veldkamp, H.G., Weltje, G.J., 2014. The role of detrital anhydrite in diagenesis of aeolian sandstones (Upper Rotliegend, The Netherlands): Implications for reservoir-quality prediction. Sedimentary Geology 314, 60-74.

Hermans, T., Nguyen, F., Robert, T., Revil, A., 2014. Geophysical Methods for Monitoring Temperature Changes in Shallow Low Enthalpy Geothermal Systems. Energies 7, 5083-5118.

Herngreen, G.W.F., Wong, T.E., 2007. Cretaceous, in: Wong, T.E., Batjes, D.A.J., de Jager, J. (Eds.), Geology of the Netherlands. Royal Netherlands Academy of Arts and Sciences, Amsterdam, Netherlands, pp. 127-150.

Huculak, M., Jarczewski, W., Dej, M., 2015. Economic aspects of the use of deep geothermal heat in district heating in Poland. Renewable and Sustainable Energy Reviews 49, 29-40.

Hurter, S., Schellschmidt, R., 2003. Atlas of geothermal resources in Europe. Geothermics 32, 779-787.

IGA, 2001. Clean Power from the Heart of the Earth.

Jalilinasrabady, S., Itoi, R., Valdimarsson, P., Saevarsdottir, G., Fujii, H., 2012. Flash cycle optimization of Sabalan geothermal power plant employing exergy concept. Geothermics 43, 75-82.

Johnston, I.W., Narsilio, G.A., Colls, S., 2011. Emerging geothermal energy technologies. KSCE Journal of Civil Engineering 15, 643-653.

Juliusson, E., Horne, R.N., 2010. Characterization of fractures in Geothermal Reservoirs.

Kaiser, B.O., Cacace, M., Scheck-Wenderoth, M., 2013. 3D coupled fluid and heat transport simulations of the Northeast German Basin and their sensitivity to the spatial discretization: different sensitivities for different mechanisms of heat transport. Environmental Earth Sciences 70, 3643-3659.

Kal, H., 2013. Geothermal Energy in the Netherlands.

Keçebaş, A., 2011. Performance and thermo-economic assessments of geothermal district heating system: A case study in Afyon, Turkey. Renewable Energy 36, 77-83.

Knox, R.W.O.B., Bosch, J.H.A., Rasmussen, E.S., Heilmann-Clausen, C., Hiss, M., de Lugt, I.R., Kasińksi, J., King, C., Köthe, A., Słodkowska, B., Standke, G., Vandenberghe, N., 2010. Cenozoic, in: Doornenbal, J.C., Stevenson, A. (Eds.), Petroleum Geological Atlas of the Southern Permian Basin Area. EAGE Publications b.v., Houten, The Netherlands, pp. 211-223.

Kramers, L., Van Wees, J.D., Pluymaekers, M.P.D., Kronimus, A., Boxem, T., 2012. Direct heat resource assessment and subsurface information systems for geothermal aquifers; the Dutch perspective. Netherlands Journal of Geosciences-Geologie en Mijnbouw 91, 637-649.

Kyriakis, S.A., Younger, P.L., 2016. Towards the increased utilisation of geothermal energy in a district heating network through the use of a heat storage. Applied Thermal Engineering 94, 99-110.

Laier, T., Kockel, F., Geluk, M.C., Pokorsky, J., Milaczewski, L., Lott,

G.K., 1997. Section A: Geology, in: Lokhorst, A. (Ed.), NW European gas atlas. Netherlands Institute of Applied Geoscience TNO - National Geological Survey, Harlem, The Netherlands.

Lasaga, A.C., Soler, J.M., Ganor, J., Burch, T.E., Nagy, K.L., 1994. Chemical weathering rate laws and global geochemical cycles. Geochimica et Cosmochimica Acta 58, 2361-2386.

Legarth, B., Huenges, E., Zimmermann, G., 2005. Hydraulic fracturing in a sedimentary geothermal reservoir: Results and implications. International Journal of Rock Mechanics and Mining Sciences 42, 1028-1041.

Legler, B., Gebhardt, U., Schneider, J.W., 2005. Late Permian non-marine–marine transitional profiles in the central Southern Permian Basin, northern Germany. International Journal of Earth Sciences 94, 851-862.

Legler, B., Schneider, J.W., 2008. Marine ingressions into the Middle/Late Permian saline lake of the Southern Permian Basin (Rotliegend, Northern Germany) possibly linked to sea-level highstands in the Arctic rift system. Palaeogeography, Palaeoclimatology, Palaeoecology 267, 102-114.

Lemale, J., Jaudin, F., 1999. La geothermie, une energie d'avenir, une realite en Ile de France [Geothermal heating, an energy of the future, a reality in Ile-de-France]. Report, IAURIF, Paris.

Leveille, G.P., Knipe, R., More, C., Ellis, D., Dudley, G., Jones, G., Fisher, Q.J., Allinson, G., 1997. Compartmentalization of Rotliegendes gas reservoirs by sealing faults, Jupiter Fields area, southern North Sea. Geological Society, London, Special Publications 123, 87-104.

Ligtenberg, H., Okkerman, J., de Keijzer, M., 2011. Fractures in the Dutch Rotliegend - An overview, in: Grötsch, J., Gaupp, R. (Eds.), The Permian Rotliegend of the Netherlands. SEPM (Society for Sedimentary Geology), Oklahoma, USA, pp. 229-244.

Limberger, J., Calcagno, P., Manzella, A., Trumpy, E., Boxem, T., Pluymaekers, M., van Wees, J., 2014. Assessing the prospective resource base for enhanced geothermal systems in Europe. Geothermal Energy Science 2, 55-71.

Lokhorst, A., Wong, T.E., 2007. Geothermal Energy, in: Wong, T.E., Batjes, D.A.J., de Jager, J. (Eds.), Geology of the Netherlands. Royal Netherlands Academy of Arts and Sciences, Amsterdam, Netherlands, pp. 341-346.

Lott, G.K., Wong, T.E., Dusar, M., Andsbjerg, J., Mönnig, E., Feldman-Olszewska, A., Verreussel, R.M.C.H., 2010. Jurassic, in: Doornenbal, J.C., Stevenson, A. (Eds.), Petroleum Geological Atlas of the Southern Permian Basin Area. EAGE Publications b.v., Houten, The Netherlands, pp. 175-193.

Lukawski, M.Z., Anderson, B.J., Augustine, C., Capuano Jr., L.E., Beckers, K.F., Livesay, B., Tester, J.W., 2014. Cost analysis of oil, gas, and geothermal well drilling. Journal of Petroleum Science and Engineering 118, 1-14.

Lund, J.W., Boyd, T.L., 2015. Direct Utilization of Geothermal Energy 2015 Worldwide Review.

Lund, H., Werner, S., Wiltshire, R., Svendsen, S., Thorsen, J.E., Hvelplund, F., Mathiesen, B.V., 2014. 4th Generation District Heating (4GDH): Integrating smart thermal grids into future sustainable energy systems. Energy 68, 1-11.

Lund, J.W., 2007. Development and utilization of geothermal resources. Proceedings of ISES Solar World Congress 2007.Solar Energy and Human Settlement, 87; 87-9595; 95.

Lund, J.W., Boyd, T.L., 2016. Direct utilization of geothermal energy 2015 worldwide review. Geothermics 60, 66-93.

Lund, J.W., Freeston, D.H., Boyd, T.L., 2011. Direct utilization of geothermal energy 2010 worldwide review. Geothermics 40, 159-180.

Ma, Y., Kelman, A., Daly, A., Borrelli, F., 2012. Predictive control for energy efficient buildings with thermal storage. IEEE Control system magazine 32, 44-64.

Magnusdottir, L., Horne, R.N., 2011. Characterization of fractures in geothermal reservoirs using resistivity.

Magri, F., Littke, R., Rodon, S., Bayer, U., Urai, J., 2008. Temperature fields, petroleum maturation and fluid flow in the vicinity of salt domes, in: Littke, R., Bayer, U., Gajewski, D., Nelskamp, S. (Eds.), Dynamics of Complex Intracontinental Basins. The Central European Basin System. Springer-Verlag, Berlin Heidelberg, pp. 323-344.

Magri, F., Bayer, U., Maiwald, U., Otto, R., Thomsen, C., 2009. Impact of transition zones, variable fluid viscosity and anthropogenic activities on coupled fluid-transport processes in a shallow salt-dome environment. Geofluids 9, 182-194.

Mathiesen, B.V., Lund, H., Connolly, D., 2012. Limiting biomass consumption for heating in 100% renewable energy systems. Energy 48, 160-168.

Mayne, D.Q., Rawlings, J.B., Rao, C.V., Scokaert, P.O.M., 2000. Constrained model predictive control: Stability and optimality. Automatica 36, 789-814.

Maystrenko, Y., Bayer, U., Scheck-Wenderoth, M., 2005. Structure and evolution of the Glueckstadt Graben due to salt movements. International Journal of Earth Sciences 94, 799-814.

McKie, T., 2011. A comparison of modern dryland depositional systems with the Rotliegend group in the Netherlands, in: Grötsch, J., Gaupp, R. (Eds.), The Permian Rotliegend of the Netherlands. SEPM (Society for Sedimentary Geology), Oklahoma, USA, pp. 89-103.

Mégel, T., Kohl, T., Hopkirk, R.J., 2006. The potential of the use of dense fluids for initiating hydraulic stimulation. Geothermics 35, 589-599.

Mello, U.T., Karner, G.D., Anderson, R.N., 1995. Role of Salt in Restraining the Maturation of Subsalt Source Rocks. Marine and Petroleum Geology 12, 697-716.

Ministry of Economic Affairs, 2010. Natural resources and geothermal energy in the Netherlands - Annual review 2009, 158.

Ministry of Economic Affairs, 2011. Natural resources and geothermal energy in the Netherlands - Annual review 2010, 1-156.

Ministry of Economic Affairs, 2012. Natural resources and geothermal energy in the Netherlands - Annual review 2011, 1-155.

Ministry of Economic Affairs, 2016. Natural resources and geothermal energy in the Netherlands - Annual review 2015, 1-166.

Moeck, I.S., 2014. Catalog of geothermal play types based on geologic controls. Renewable and Sustainable Energy Reviews 37, 867-882.

Moeck, I., Kwiatek, G., Zimmermann, G., 2009. Slip tendency analysis, fault reactivation potential and induced seismicity in a deep geothermal reservoir. Journal of Structural Geology 31, 1174-1182.

Mottaghy, D., Pechnig, R., Vogt, C., 2011. The geothermal project Den Haag: 3D numerical models for temperature prediction and reservoir simulation. Geothermics 40, 199-210.

Muñoz, M., Garat, P., Flores-Aqueveque, V., Vargas, G., Rebolledo, S., Sepúlveda, S., Daniele, L., Morata, D., Parada, M.Á, 2015. Estimating low-enthalpy geothermal energy potential for district heating in Santiago basin–Chile (33.5 °S). Renewable Energy 76, 186-195.

Muntendam-Bos, A.G., Wassing, B.B.T., Geel, C.R., Louh, M., Thienen-Visser, K., 2008. Burgemeer seismicity study 2008-U-R1071/B.

Murphy, H., Brown, D., Jung, R., Matsunaga, I., Parker, R., 1999. Hydraulics and well testing of engineered geothermal reservoirs. Geothermics 28, 491-506.

Nagihara, S., Sclater, J., Beckley, L., Behrens, E.W., Lawver, L.A., 1992. High heat flow anomalies over salt structures on the Texas Continental Slope, Gulf of Mexico. Geophysical Research Letters 19, 1687-1690.

Nagihara, S., 2003. Three-dimensional inverse modeling of the refractive heat-flow anomaly associated with salt diapirism. AAPG Bulletin 87, 1207-1222.

NAM, 2015. Personal communication: temperature map at the top of the Rotliegend in the area of the Groningen gas field.

Narasimhan, T.N., Witherspoon, P.A., 1976. An integrated finite difference method for analyzing fluid flow in porous media. Water Resources Research 12, 57-64.

Nepveu, M., van Thienen-Visser, K., Sijacic, D., 2016. Statistics of seismic events at the Groningen field. Bulletin of Earthquake Engineering 14, 3343-3362.

NITG, 2004. Geological altas of the subsurface of the Netherlands - onshore, 104.

NLOG, 2014. Netherlands Oil and Gas portal (NLOG) - Boreholes 2015.

NLOG, 2015. SAU-01 2015.

Noack, V., Scheck-Wenderoth, M., Cacace, M., 2012. Sensitivity of 3D thermal models to the choice of boundary conditions and thermal properties: a case study for the area of Brandenburg (NE German Basin). Environmental Earth Sciences 67, 1695-1711.

Noack, V., Scheck-Wenderoth, M., Cacace, M., Schneider, M., 2013. Influence of fluid flow on the regional thermal field: results from 3D numerical modelling for the area of Brandenburg (North German Basin). Environmental Earth Sciences 70, 3523-3544.

Norden, B., Förster, A., Balling, N., 2008. Heat flow and lithospheric thermal regime in the Northeast German Basin. Tectonophysics 460, 215-229.

Olasolo, P., Juárez, M.C., Morales, M.P., D´Amico, S., Liarte, I.A., 2016. Enhanced geothermal systems (EGS): A review. Renewable and Sustainable Energy Reviews 56, 133-144.

Ondrak, R., Wenderoth, F., Scheck, M., Bayer, U., 1998. Integrated geothermal modeling on different scales in the Northeast German basin. Geologische Rundschau 87, 32-42.

Orzol, J., Jung, R., Jatho, R., Tischner, T., Kehrer, P., 2005. The GeneSys-Project: Extraction of Geothermal Heat from Tight Sediments.

Østergaard, P.A., Lund, H., 2011. A renewable energy system in Frederikshavn using low-temperature geothermal energy for district heating. Applied Energy 88, 479-487.

O'Sullivan, M.J., Pruess, K., Lippmann, M.J., 2001. State of the art of geothermal reservoir simulation. Geothermics 30, 395-429.

Palandri, J.L., Kharaka, Y.K., Geological Survey (U.S.)., National Energy Technology Laboratory (U.S.)., 2004. A compilation of rate parameters of water-mineral interaction kinetics for application to geochemical modeling 2004 - 1068, 1-71.

Peryt, T.M., Geluk, M.C., Mathiesen, A., Paul, J., Smith, K., 2010. Zechstein, in: Doornenbal, J.C., Stevenson, A. (Eds.), Petroleum Geological Atlas of the Southern Permian Basin Area. EAGE Publications b.v., Houten, The Netherlands, pp. 123-147.

Petersen, K., Lerche, I., 1995. Quantification of thermal anomalies in sediments

around salt structures. Geothermics 24, 253-268.

Pharaoh, T.C., Dusar, M., Geluk, M.C., Kockel, F., Krawczyk, C.M., Krzywiec, P., Scheck-Wenderoth, M., Thybo, H., Vejbæk, O.V., Van Wees, J.D., 2010. Tectonic evolution, in: Doornenbal, J.C., Stevenson, A. (Eds.), Petroleum Geological Atlas of the Southern Permian Basin Area. EAGE Publications b.v., Houten, The Netherlands.

Pollack, H.N., Hurter, S.J., Johnson, J.R., 1993. Heat-Flow from the Earths Interior - Analysis of the Global Data Set. Reviews of Geophysics 31, 267-280.

Poulsen, S.E., Balling, N., Nielsen, S.B., 2015. A parametric study of the thermal recharge of low enthalpy geothermal reservoirs. Geothermics 53, 464-478.

Procesi, M., Buttinelli, M., Pignone, M., 2015. Geothermal favourability mapping by advanced geospatial overlay analysis: Tuscany case study (Italy). Energy 90, Part 2, 1377-1387.

Pruess, K., 1991. TOUGH2: A general-purpose numerical simulator for multiphase fluid and heat flow Report LBL-29400.

Pruess, K., Oldenburg, C., Moridis, G., 2012. TOUGH2 User's Guide, Version 2.1 LBNL-43134.

Regenspurg, S., Feldbusch, E., Byrne, J., Deon, F., Driba, D.L., Henninges, J., Kappler, A., Naumann, R., Reinsch, T., Schubert, C., 2015. Mineral precipitation during production of geothermal fluid from a Permian Rotliegend reservoir. Geothermics 54, 122-135.

Rezaie, B., Rosen, M.A., 2012. District heating and cooling: Review of technology and potential enhancements. Applied Energy 93, 2-10.

Richter-Bernurg, G., 1955a. Stratigraphische Gliederung des deutschen Zechsteins. Zeitschrift der Deutschen Geologischen Gesellschaft, 843-854.

Richter-Bernurg, G., 1955b. Über salinare Sedimentation. Zeitschrift der Deutschen Geologischen Gesellschaft, 593-645.

Rijksdienst voor Ondernemend Nederland, 2015. Regeling nationale EZ subsidies – risico's dekken voor aardwarmte, 1-16.

Rijksdienst voor Ondernemend Nederland, 2016. Handleiding haalbaarheidsstudie SDE+, 1-13.

Rockware, 2014. PetraSim.

Rosander, P., 2012. Averaging level control in the presence of frequent inlet flow upsets.

Rose, P.R., 1993. Expected Value and Chance of Success: Part 2. Economics and Risk Assessment, in: Morton-Thompson, D., Woods, A.M. (Eds.), Development Geology Reference Manual. AAPG Special Volumes, pp. 30-34.

Rybach, L., 2003. Geothermal energy: sustainability and the environment. Geothermics 32, 463-470.

Rybach, L., 2007. Geothermal sustainability, 1-5.

Saeid, S., Al-Khoury, R., Nick, H.M., Barends, F., 2014. Experimental–numerical study of heat flow in deep low-enthalpy geothermal conditions. Renewable Energy 62, 716-730.

Saeid, S., Al-Khoury, R., Nick, H.M., Hicks, M.A., 2015. A prototype design model for deep low-enthalpy hydrothermal systems. Renewable Energy 77, 408-422.

Salimi, H., Wolf, K., 2011. Compositional flow simulations of mixed CO_2-water injection into geothermal reservoirs: geothermal energy combined with CO_2 storage.

Sandrea, R., 2006. Global natural gas reserves – a heuristic viewpoint (Part 2 of 2). Middle East Economic Survey 49.

Sausse, J., Dezayes, C., Dorbath, L., Genter, A., Place, J., 2010. 3D model of fracture zones at Soultz-sous-Forêts based on geological data, image logs, induced microseismicity and vertical seismic profiles. Comptes Rendus Geoscience 342, 531-545.

Sayegh, M.A., Danielewicz, J., Nannou, T., Miniewicz, M., Jadwiszczak, P., Piekarska, K., Jouhara, H., 2016. Trends of European research and development in district heating technologies. Renewable and Sustainable Energy Reviews.

Scheck-Wenderoth, M., Cacace, M., Maystrenko, Y.P., Cherubini, Y., Noack, V., Kaiser, B.O., Sippel, J., Björn, L., 2014. Models of heat transport in the Central European Basin System: Effective mechanisms at different scales. Marine and Petroleum Geology 55, 315-331.

Schlumberger, 2012. Petrel 2012 Geology and modelling 12-IS-0333.

Schmidt, R.B., Bucher, K., Drüppel, K., Stober, I., 2017. Experimental interaction of hydrothermal Na-Cl solution with fracture surfaces of geothermal reservoir sandstone of the Upper Rhine Graben. Applied Geochemistry 81, 36-52.

Scholten, T., De Persis, C., Tesi, P., 2016. Optimal steady state regulation of distribution networks with input and flow constraints, 6953-6958.

Scholten, T., De Persis, C., Tesi, P., 2015. Modeling and control of heat networks with storage: The single-producer multiple-consumer case, 2242-2247.

Schön, J.H., 2011. Physical properties of rocks: A workbook. Elsevier.

Shortall, R., Davidsdottir, B., Axelsson, G., 2015. Geothermal energy for sustainable development: A review of sustainability impacts and assessment frameworks. Renewable and Sustainable Energy Reviews 44, 391-406.

Siratovich, P.A., Villeneuve, M.C., Cole, J.W., Kennedy, B.M., Bégué, F., 2015. Saturated heating and quenching of three crustal rocks and implications for thermal stimulation of permeability in geothermal reservoirs. International Journal of Rock Mechanics and Mining Sciences 80, 265-280.

Široký, J., Oldewurtel, F., Cigler, J., Prívara, S., 2011. Experimental analysis of model predictive control for an energy efficient building heating system. Applied Energy 88, 3079-3087.

Stäuble, A.J., Milius, G., 1970. Geology of Groningen gas field, Netherlands, in: Halbouty, M.T. (Ed.), Geology og giant petroleum fields. American Association of Petroleum Geologists, Tulsa, US, pp. 359-369.

Stefansson, V., 2005. World geothermal assessment. Proceedings World Geothermal Congress 2005.

Stefansson, V., Axelsson, G., 2005. Sustainable Utilization of Geothermal Resources through Stepwise Development. Proceedings World Geothermal Congress 2005.

Stefánsson, V., 1992. Success in geothermal development. Geothermics 21, 823-834.

Stefánsson, V., 2002. Investment cost for geothermal power plants. Geothermics 31, 263-272.

Strozyk, F., Urai, J.L., van Gent, H., de Keijzer, M., Kukla, P.A., 2014. Regional variations in the structure of the Permian Zechstein 3 intrasalt stringer in the northern Netherlands: 3D seismic interpretation and implications for salt tectonic evolution. Interpretation 2, SM101-SM117.

Tanikawa, W., Shimamoto, T., 2009. Comparison of Klinkenberg-corrected gas permeability and water permeability in sedimentary rocks. International Journal of Rock Mechanics and Mining Sciences 46, 229-238.

Templeton, J.D., Ghoreishi-Madiseh, S.A., Hassani, F., Al-Khawaja, M.J., 2014.

Abandoned petroleum wells as sustainable sources of geothermal energy. Energy 70, 366-373.

Tester, J.W., Anderson, B.J., Batchelor, A.S., Blackwell, D.D., DiPippo, R., Drake, E.M., Garnish, J., Livesay, B., Moore, M.C., Nichols, K., Petty, S., Nafi Toksöz, M., Veatch, R.W.J., 2006. The future of Geothermal energy - Impact of Enhanced Geothermal Systems (EGS) on the United States in the 21st century, 372.

Thorsteinsson, H.H., Tester, J.W., 2010. Barriers and enablers to geothermal district heating system development in the United States. Energy Policy 38, 803-813.

TNO, 2012, April. Informatiebladen aardwarmtewinning.

TNO, 2014. Toetsing van de bodemdalingsprognoses en seismische hazard ten gevolge van gaswinning van het Groningen veld Rl l953, 1-218.

Tokimatsu, K., Konishi, S., Ishihara, K., Tezuka, T., Yasuoka, R., Nishio, M., 2016. Role of innovative technologies under the global zero emissions scenarios. Applied Energy 162, 1483-1493.

Trumpy, E., Botteghi, S., Caiozzi, F., Donato, A., Gola, G., Montanari, D., Pluymaekers, M.P.D., Santilano, A., van Wees, J.D., Manzella, A., 2016. Geothermal potential assessment for a low carbon strategy: A new systematic approach applied in southern Italy. Energy 103, 167-181.

Tselepidou, K., Katsifarakis, K.L., 2010. Optimization of the exploitation system of a low enthalpy geothermal aquifer with zones of different transmissivities and temperatures. Renewable Energy 35, 1408-1413.

Ungemach, P., Antics, M., Papachristou, M., 2005. Sustainable geothermal reservoir management.

Unternährer, J., Moret, S., Joost, S., Maréchal, F., 2017. Spatial clustering for district heating integration in urban energy systems: Application to geothermal energy. Applied Energy 190, 749-763.

Uyeda, S., 1988. Geodynamics, in: Haenel, R., Rybach, L., Stegena, L. (Eds.), Handbook of terrestrial heat-flow density determination. Kluwer Academic Publishers, Dordrecht, Germany, pp. 486pp.

van Adrichem-Boogaert, H.A., Kouwe, W.F.P., 1993-1997. Stratigraphic Nomenclature of the Netherlands; revision and update by RGD and NOGEPA, 1-50.

van der Voort, N., Vanclay, F., 2015. Social impacts of earthquakes caused by gas extraction in the Province of Groningen, The Netherlands. Environmental Impact Assessment Review 50, 1-15.

van Gent, H.W., Back, S., Urai, J.L., Kukla, P.A., Reicherter, K., 2009. Paleostresses of the Groningen area, the Netherlands—Results of a seismic based structural reconstruction. Tectonophysics 470, 147-161.

van Heekeren, V., Bakema, G., 2015. The Netherlands Country Update on Geothermal Energy, 1-6.

Van Hulten, F.F.N., 2010. Geological factors effecting compartmentalization of Rotliegend gas fields in the Netherlands. Geological Society, London, Special Publications 347, 301-315.

van Leeuwen, L., Böker, U., van de Weerd, A., 2014. Geothermal Energy in Groningen Geological investigation (Groot Geologisch Onderzoek Groningen) G1111, 1-99.

van Ojik, K., Böhm, A.R., Cremer, H., Geluk, M.C., de Jong, M.G.G., Mijnlieff, H.F., Nio, S.D., 2011. The rationale for an integrated stratigraphic framework of the upper Rotliegend II depositional system in the Netherlands, in: Grötsch, J., Gaupp, R. (Eds.), The Permian Rotliegend of the Netherlands.

SEPM (Society for Sedimentary Geology), Oklahoma, USA, pp. 37-48.

van Os, H.W.A., Herber, R., Scholtens, B., 2017. Modular evaluation method for subsurface activities (MEMSA). A novel approach for integrating social acceptance in a permit decision-making process for subsurface activities. Environmental Impact Assessment Review 64, 97-122.

van Thienen-Visser, K., Breunese, J., 2015. Induced seismicity of the Groningen gas field: History and recent developments. The Leading Edge 34, 664-671.

van Wees, J.D., Kronimus, A., van Putten, M., Pluymaekers, M.P.D., Mijnlieff, H., van Hooff, P., Obdam, A., Kramers, L., 2012. Geothermal aquifer performance assessment for direct heat production—Methodology and application to Rotliegend aquifers. Netherlands Journal of Geosciences-Geologie en Mijnbouw 91, 651.

Van Wees, J.D., Buijze, L., Van Thienen-Visser, K., Nepveu, M., Wassing, B.B.T., Orlic, B., Fokker, P.A., 2014. Geomechanics response and induced seismicity during gas field depletion in the Netherlands. Geothermics 52, 206-219.

Van Wijhe, D.H., 1987. Structural evolution of inverted basins in the Dutch offshore. Tectonophysics 137, 171-219.

Vélez, F., Segovia, J.J., Martín, M.C., Antolín, G., Chejne, F., Quijano, A., 2012. A technical, economical and market review of organic Rankine cycles for the conversion of low-grade heat for power generation. Renewable and Sustainable Energy Reviews 16, 4175-4189.

Verweij, H., Simmelink, E., Underschultz, J., 2011. Pressure and fluid flow systems in the Permian Rotliegend in the Netherlands onshore and offshore, in: Grötsch, J., Gaupp, R. (Eds.), The Permian Rotliegend of the Netherlands. SEPM (Society for Sedimentary Geology), Oklahoma, USA, pp. 247-263.

Vizgirda, J., O'Brien, J.J., Lerche, I., 1985. Thermal anomalies on the flanks of a salt dome. Geothermics 14, 553-565.

Vogt, C., Mottaghy, D., Wolf, A., Rath, V., Pechnig, R., Clauser, C., 2010. Reducing temperature uncertainties by stochastic geothermal reservoir modelling. Geophysical Journal International 181, 321-333.

Vogt, C., Iwanowski-Strahser, K., Marquart, G., Arnold, J., Mottaghy, D., Pechnig, R., Gnjezda, D., Clauser, C., 2013. Modeling contribution to risk assessment of thermal production power for geothermal reservoirs. Renewable Energy 53, 230-241.

Waples, D.W., Waples, J.S., 2004a. A review and evaluation of specific heat capacities of rocks, minerals, and subsurface fluids. Part 1: Minerals and nonporous rocks. Natural resources research 13, 97-122.

Waples, D.W., Waples, J.S., 2004b. A Review and Evaluation of Specific Heat Capacities of Rocks, Minerals, and Subsurface Fluids. Part 2: Fluids and Porous Rocks. Natural Resources Research 13, 123-130.

Wellmer, F., Dalheimer, M., Wagner, M., 2007. Economic evaluations in exploration, 2nd ed. Springer Science & Business Media.

Whaley, J., 2009. The Groningen gas field 6.

Willems, C.J.L., Nick, H.M., Goense, T., Bruhn, D.F., 2017a. The impact of reduction of doublet well spacing on the Net Present Value and the life time of fluvial Hot Sedimentary Aquifer doublets. Geothermics 68, 54-66.

Willems, C.J.L., Nick, H.M., Donselaar, M.E., Weltje, G.J., Bruhn, D.F., 2017b. On the connectivity anisotropy in fluvial Hot Sedimentary Aquifers and its influence on geothermal doublet performance. Geothermics 65, 222-233.

Wolery, T.J., 1992. EQ3/6: A software package for geochemical modeling of aqueous systems: package overview and installation guide (version 8.0) UCRL-MA-110662, 1-262.

Wolff-Boenisch, D., Evans, K., 2013. Geochemical modelling of petroleum well data from the Perth Basin. Implications for potential scaling during low enthalpy geothermal exploration from a hot sedimentary aquifer. Applied Geochemistry 37, 12-28.

Wong, T.E., 2007. Jurassic, in: Wong, T.E., Batjes, D.A.J., de Jager, J. (Eds.), Geology of the Netherlands. Royal Dutch Academy of Arts and Sciences, Amsterdam, Netherlands, pp. 107-125.

Wong, T.E., de Lugt, I.R., Kuhlmann, G., Overeem, I., 2007. Tertiary, in: Wong, T.E., Batjes, D.A.J., de Jager, J. (Eds.), Geology of the Netherlands. Royal Netherlands Academy of Arts and Sciences, Amsterdam, Netherlands, pp. 151-171.

Worum, G., Michon, L., 2005. Implications of continuous structural inversion in the West Netherlands Basin for understanding controls on Palaeogene deformation in NW Europe. Journal of the Geological Society 162, 73-85.

Xu, T., Sonnenthal, E., Spycher, N., Pruess, K., 2006. TOUGHREACT—A simulation program for non-isothermal multiphase reactive geochemical transport in variably saturated geologic media: Applications to geothermal injectivity and CO2 geological sequestration. Computers & Geosciences 32, 145-165.

Yamankaradeniz, N., 2016. Thermodynamic performance assessments of a district heating system with geothermal by using advanced exergy analysis. Renewable Energy 85, 965-972.

Yeh, G., Tripathi, V.S., 1991. A Model for Simulating Transport of Reactive Multispecies Components: Model Development and Demonstration. Water Resources Research 27, 3075-3094.

Zhang, S., Liu, H., 2016. Porosity–permeability relationships in modeling salt precipitation during CO2 sequestration: Review of conceptual models and implementation in numerical simulations. International Journal of Greenhouse Gas Control 52, 24-31.

Zhang, Y., Krause, M., Mutti, M., 2013. The Formation and Structure Evolution of Zechstein (Upper Permian) Salt in Northeast German Basin: A Review. Open Journal of Geology 03, 411-426.

Zheng, B., Xu, J., Ni, T., Li, M., 2015. Geothermal energy utilization trends from a technological paradigm perspective. Renewable Energy 77, 430-441.

Zheng, L., Apps, J.A., Zhang, Y., Xu, T., Birkholzer, J.T., 2009. On mobilization of lead and arsenic in groundwater in response to CO2 leakage from deep geological storage. Chemical Geology 268, 281-297.

Ziegler, P.A., 1982. Geological Atlas of Western and Central Europe. Elsevier Scientific Publishing Company, The Hague, The Netherlands.

Zielinski, G.W., Poprawa, P., Szewczyk, J., Grotek, I., Kiersnowski, H., Zielinski, R.L.B., 2012. Thermal effects of Zechstein salt and the Early to Middle Jurassic hydrothermal event in the central Polish Basin. AAPG Bulletin 96, 1981-1996.

Zimmermann, G., Reinicke, A., 2010. Hydraulic stimulation of a deep sandstone reservoir to develop an Enhanced Geothermal System: Laboratory and field experiments. Geothermics 39, 70-77.

Acknowledgements

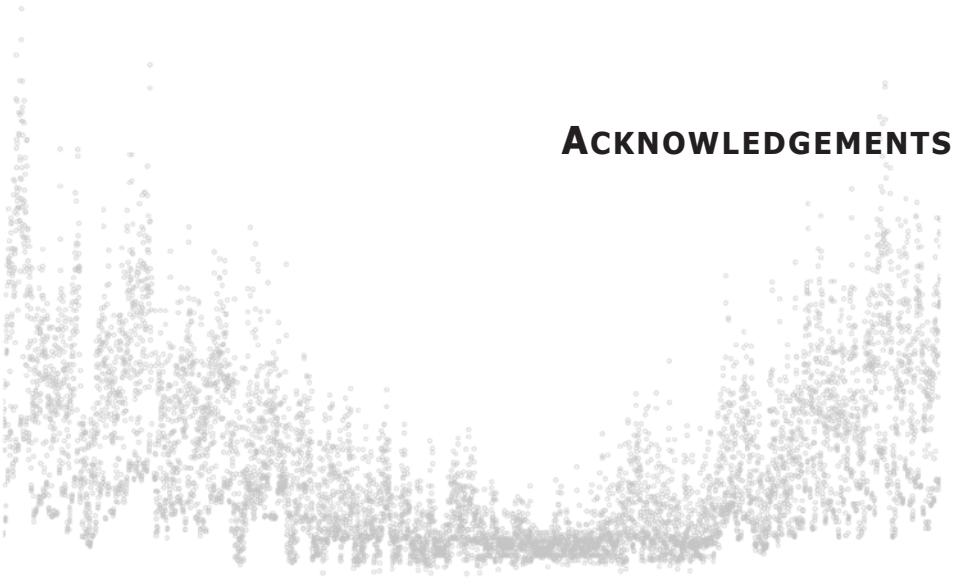

The work presented in this thesis would not have been completed without the help of several people who either contributed to the content of the work or where part of my social life. I would like to take the opportunity to thank them and acknowledge their support:

Firstly, I would like to thank my supervisor Rien Herber. His vast knowledge of the subsurface and his ability to communicate it in an integrated manner and with enthusiasm brought peace and confidence when the questions were too many. At the same time, his support and willingness to share his experience with issues beyond knowledge, but also his way of doing it will resonate for years to come. Rien as a supervisor has also been outstanding at maintaining the perfect balance between support and challenge for me throughout the years; anyone who has worked with him needs no further explanation to understand. The efficacy and efficiency of our meetings, the casual discussions on music and politics, but also the ability to address personal issues when needed set a high standard for future working relations.

More importantly, I am thankful to Rien for inspiring respect in an environment that tends to demand it. When the ripples of the global financial crisis started manifesting in Greece in 2010, some academic staff members engaged in mockery and disrespectful, poor jokes; Rien simply asked how was all this affecting my family and me and we then discussed the underlying reasons for the crisis. I do believe that his character has fostered an inclusive, respective and productive working attitude for the whole geo-energy group; the ethos he conveys should serve as an example for any working environment, particularly

so for other academic groups; it breeds motivation. Time and again I have stopped to reflect on his wise advice and insights. Looking back at the seven years we have been working together, I feel that he has helped me develop as a scientist and also as a person. Rien, it has been an honour and a privilege to work with you and to know you.

Additionally, I would like to thank the people with whom I have worked the most during my thesis work. With Tjardo Scholtens our collaboration has been exceptional and we have successfully managed to conclude it with great respect to both our critical spirits. Working with and learning from you has been a pleasure. Claudio de Persis I would like to thank for his constructive criticism, his effective discussion and the degree of freedom that he fostered in our work with Tjardo.

The collaboration with students in my PhD years has been important. I would like to acknowledge and thank: Leon Doddema for his help on the PyTOUGH automation of the 3D simulations and for introducing me to Python; Joram Hoogheim for his attention to detail with regards to the geochemical modelling and persistence in generating high quality results; Betul Alpsoy for her thorough investigation and overview in generating the first version of the economic model; Thom Postma for his help in evaluating the fractured rock equations for simulations.

With regards to the geothermal work, I specifically would like to acknowledge: Mariene Gutierrez for her continued support to my work and the geothermal agenda in general, even when it was difficult to do so; Rijksta Zwart for her support and confidence and for providing the much needed structure at the early stages of the project; Paul Corzaan for his openness in sharing project insights and information but also in giving feedback to the input provided to the project; Theo Venema for the information and context regarding the heating part of the project; Robert te Gussinklo Ohmann for our collaboration in identifying risks in the Groningen geothermal project, Floris Vegeer for his enthusiastic collaboration on the wells and pump installations; Andrew van de Weerd, Laura van Leeuwen and Cornelius Boersma for the discussions on geology and reservoir; Wen Liu for exchanging useful feedback on modelling and our fruitful collaborations at the project level; Marinus de Hartogh for the discussions on salt domes; Harmen Mijnlieff for his useful, constructive comments and encouraging attitude towards my work. Lastly, I would also like to acknowledge everyone who contributed to the Flexiheat project: Jacques Dam, Floris de Groot, Wim van Gemert, Julianna Montoya, Erika Zomerman and Marcel van der Werf

Moreover, I would like to thank the NAM and particularly Jan van Elk for his continued support to the Groningen geothermal project and the Eemshaven concept. His positive attitude and interest for the project has been pivotal. Making the high-quality 3D PSDM seismic data available to us set the geothermal part of the research on solid ground. His

later enthusiasm in sharing the DTS temperature data and pursuing the comparison between temperature logging accuracy could be a legacy to the geothermal community. I would also like to thank Pepijn Kole for sharing his insights and for introducing me to onshore logging at the Zeerijp well. I am grateful for your persistence and for embracing the scope and interest of my work, in spite of your busy schedule and personal obligations.

The petite geo-energy group was always a refreshing working space. Internal conspiracies, useful criticism and much needed fun distraction have been part of our repertoire. Sharing the office with someone with interests as diverse as Herman's has been a pleasure. On top of this, we have managed to remain brutally critical when reviewing each other's work without ever taking it personal. Panteha's joyful spirit, her sense of humour, her support and advise with my early geo-modelling steps, but also reminding me to control my temper were missed these last two years. Hannes has offered his insights and help in reflecting ideas and troubleshooting models and being always positive when discussing "the future of geothermal" and how we might fit in there. I know that you have helped me find my new place in the puzzle. Simon brought in his abroad experience and was keen on discussing geology.

The young geothermal community that I have met mostly through the EGPD platform was a pleasant surprise. I found out that we share not only our struggling with the same issues, but also a worldview and commitment to our work. Specifically, I would like to express my thanks to Cees Willems and Jon Limberger for successfully co-organizing the 6th EGPD and making the process fun at the same time.

David Bruhn invited me to the geothermal field trips to Italy and Iceland and gave me a broader, worldwide perspective on geothermal development and collaborations for which I am thankful. Through these trips I met Damien Bonte and Baptiste Lepillier. Discusing geology and geothermal in the field trips and sharing our enthusiasm for visiting such iconic geothermal locations with them was exciting, as was discussing work experiences over drinks.

Within the CIO I would like to acknowledge: Harro Meijer for his advice over the years, Henk Jansen for his joyful help with numerous technical problems fron installing printers to measuring alcohol levels of raki and to Dipayan, Steven, Charlotte, Truls, Linda, Katrin and Joram for their eagerness to keep lunch discussion away from work topics.

I would also like to extend my appreciation to the reading committee members Harro Meijer, David Smeulders and David Bruhn for their feedback and comments on this very book.

Maritina Markopoulou I wish to thank for adapting the figures in the introduction chapter.

I do feel the need to express my gratitude to the social group that has been my family over these years of master's studies and PhD work in Groningen.

Firstly, Andres for those long discussions where the argument consistency is preserved and discussions points are seen through to the end. Also, for being a friend that is impossible to insult. I will keep trying dude. Arguing and allowing yourself to be convinced is something rare and I am happy we have done just that on numerous occasions, between drinks, parties and personal life-changing situations. Nonetheless, we probably need to re-perform those late-night calculations regarding available time and required effort; we might need more sample points for that.

Herman is not just someone to help you put a floor in an apartment. The creator of the successful geo-ball game, has been there, hearing out work or personal problems, prepare lamb roasting designs, or have a beer and a casual conversation. His enthusiasm though is mostly coffee driven. But his gentle (almost subtle) sense of humor always set a nice tone to our encounters and has helped "saving the world" on occasions and among clinical environments.

Linda has always been up for new adventures and also for a joke or two, not just on other people but also on herself, which makes her unique. Together with Aggeliki, Maryam, Aidan, Hernan, Giannis, Britta, Adrianna, Javier, Athina, Dimitris, Tselios, Georgia, Kapinsky, Tassis, Despoina (Ser), Alekos, Despoina (Ant), Ilias, Jordi, David, Marina, Fons, Koen, Anne, Maja, Mayer, Mufty, Hessel, Saskia, Monica and Dore our escapades have been always eventful. I would particularly like to commemorate the biology community members for adopting me throughout these years and for compensating the lack of geologists in Groningen. It has always been comforting to doze off or daydream while you all geek out on some "scientific" theory battles.

Throughout these years there have been various groups that have formed by the people mentioned above that had a specific purpose. I could name the "zolder barflies", "suicide dinner squad", the "moving crew", the "Tuesday bball", the "silence of the lambs", the "DD grasshoppers", "movie club", "floor grillers", "music and alcohol gentlemen" and the "focus group". Plant pots and bowls have mysteriously been filled with food at the blink of an eye, hamsters have had birthday parties, parties have been had with a maximum 70 db of sound pressure level, pizzas have been eaten by floors, Tassis has danced, autopilots have kicked-in, cheeks have been numbed, beers have had icy baths, shirts have been set on fire, balloons have caused squeakiness, grandmother cooking aprons set ablaze, cuttlefish has been cleaned for hours, meat has been marbled, two meters was deemed the new standard, silver tape has been found everywhere and tired bottoms have missed the couch on their quest for solace.

As we all gradually disperse based on life choices in this absurd world of today, I do hope we manage to meet and stay in touch. Not to dwell on our past memories but to make new ones together.

My appreciation, respect and affection go to Dimitra and Stefanos for having first names and a sense of humour instead of being just parents; and to Voula for her silent care.

Insa, thank you for being next to me through all this and enabling me to dream again. And also for that basketball, it meant more than you might think. You keep on being my CPS.

List of publications

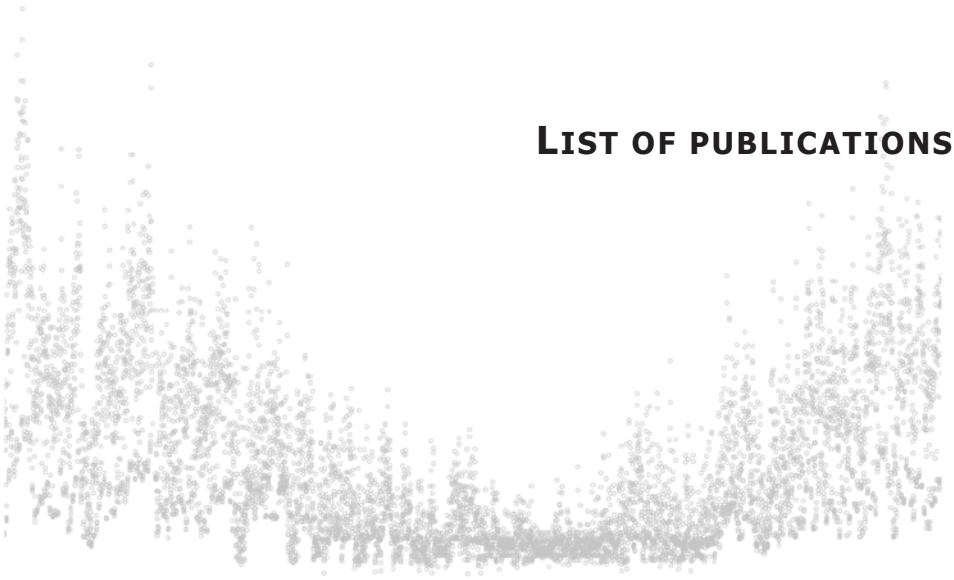

Daniilidis, A., Alpsoy, B., Herber, R., 2017, “Impact of technical and economic uncertainties on the economic performance of a deep geothermal heat system”, *Renewable Energy* 114B, 805-816

Daniilidis, A., Scholten, T., Hoogheim, J., De Persis, C., Herber, R., 2017, “Geochemical implications of production and storage control by coupling a direct use geothermal system with heat networks”, *Applied Energy* 204, 254-270.

Daniilidis, A., Herber, R., 2017, “Salt intrusions providing a new geothermal exploration target for higher energy recovery at shallower depths”, *Energy* 118, 658-670.

Daniilidis, A., Doddema, L. and Herber, R., 2016. "Risk Assessment of the Groningen Geothermal Potential: From Seismic to Reservoir Uncertainty using a Discrete Parameter Analysis." *Geothermics* 64,271-288.

Daniilidis, A., Herber, R., and Vermaas, D.A., 2014. "Upscale potential and financial feasibility of a reverse electrodialysis power plant." *Applied Energy* 119, 257-265.

Daniilidis, A., Vermaas D.A., Herber, R. and Nijmeijer, K., 2014. "Experimentally obtainable energy from mixing river water, seawater or brines with reverse electrodialysis." *Renewable Energy* 64, 123-131.

About the author

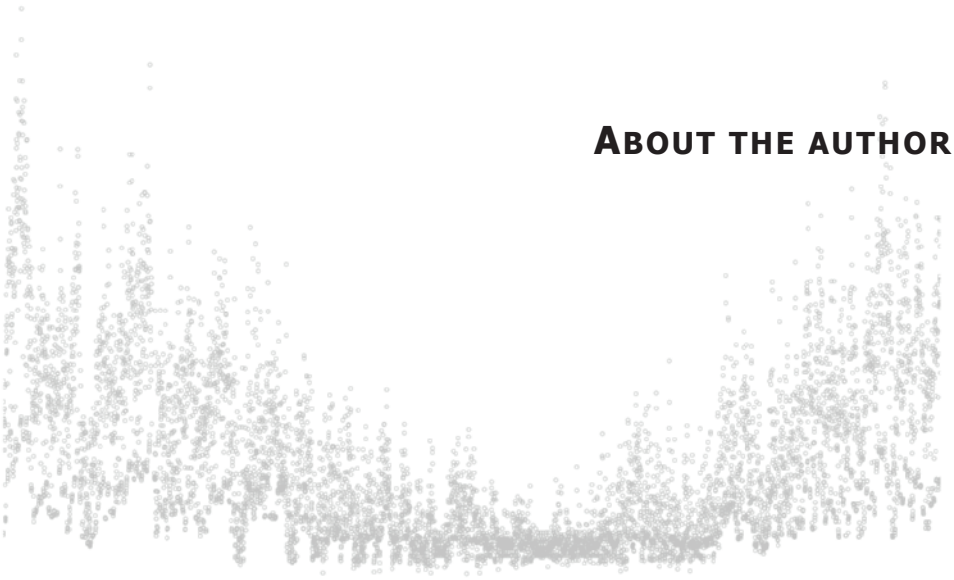

Alexandros Daniilidis was born in Stockholm, Sweden on September 26th 1983. He concluded his high school studies at I.M.Panagiotopoulos lyceum in 2001. He finished his bachelor studies in Geology and Geo-environment at the University of Athens in 2008.

He moved to the Netherlands and the University of Groningen to continue his master's studies in 2009. For his research Master in Energy and Environmental Science he performed lab experiments at Wetsus (European centre of excellence for sustainable water technology) and modelling at RuG on renewable electricity generation through reverse electrodialysis, utilizing different salinity gradients. For his Master in Environmental and Infrastructure Planning he worked on the socio-spatiality, power relations and the right to the city using Athens, Greece as a case study. He concluded the master's in 2012 and 2013 respectively.

In 2012 he started his PhD at University of Groningen on Geothermal energy. His doctoral work focused on two topics. The first was exploring, substantiating and quantifying the concept of harvesting the high heat flow through salt bodies. The second was a step-wise, incremental approach in outlining, assessing, characterizing and evaluating the development of the Groningen geothermal system. He concluded his PhD in October 2017.

In September 2017, he started working at the Delft University of Technology as a postdoctoral researcher. The focus of his research is to improve the utilization of geothermal energy through field development simulations.

"Take an eye for an eye
Take a tooth for a tooth
Just like they say in the Bible
Never leave a trace or forget a face
Of any man at the table
Any man at the table
When the moon is a cold chiseled dagger
Sharp enough to draw blood from a stone
He rides through your dreams on a coach
And horses and the fence posts
In the moonlight look like bones
…
He can turn himself into a stranger
Well they broke a lot of canes on his hide
He was born away in a cornfield
A fever beats in his head like a drum inside
Some say they fear him
Others admire him
Because he steals his promise
One look in his eye
Everyone denies
Ever having met him
Ever having met him"

Tom Waits, 1992